Structure-Property Relationships of Merocyanine Dyes in the Solid State: Charge Transport and Exciton Coupling

Dissertation zur Erlangung des
naturwissenschaftlichen Doktorgrades
der Julius-Maximilians-Universität Würzburg

vorgelegt von
Andreas Liess
aus Darmstadt

Würzburg 2017

Eingereicht bei der Fakultät für Chemie und Pharmazie am:
22.06.2017

Gutachter der schriftlichen Arbeit:
1. Gutachter: Prof. Dr. Frank Würthner
2. Gutachter: Prof. Dr. Jens Pflaum

Prüfer des öffentlichen Promotionskolloquiums:
1. Prüfer: Prof. Dr. Frank Würthner
2. Prüfer: Prof. Dr. Jens Pflaum
3. Prüfer: Prof. Dr. Anke Krüger

Datum des öffentlichen Promotionskolloquiums:
14.08.2017

Doktorurkunde ausgehändigt am:

_____

Für Anna

und

meine Eltern

List of Abbreviations, Physical Constants and Variables

Abbreviations

A	Acceptor
AFM	Atomic force microscopy
AM1	Austin Model 1
BFDH	Bravais-Friedel-Donnay-Harker
BHJ	Bulk heterojunction
BLA	Bond length alternation
CV	Cyclic voltammetry
D	Donor, Drain
DFT	Density functional theory
DNTT	Dinaphthothienothiophene
DOS	Density of states
EOAM	Electro-optical absorption measurement
Fc	Ferrocene
FET	Field-effect transistor
FWHM	Full width at half maximum
G	Gate
HOMO	Highest occupied molecular orbital
ITO	Indium tin oxide
LB	Langmuir-Blodgett
LUMO	Lowest unoccupied molecular orbital
MCH	Methylcyclohexane
MIS	Metal-insulator-semiconductor
MOSFET	Metal-oxide-semiconductor field-effect transistor
Nd:YAG	Neodymium-doped yttrium aluminium garnet
NIR	Near infrared
NLO	Nonlinear optics
NMR	Nuclear magnetic resonance
OD	Optical density
OFET	Organic field-effect transistor
OSC	Organic semiconductor
OTFT	Organic thin film transistor

PCE	Power conversion efficiency
PDA	Point dipole approximation
PEDOT:PSS	Poly(3,4-ethylenedioxythiophene):polystyrene sulfonate
PHJ	Planar heterojunction
PMHJ	Planar mixed heterojunction
PR	Photorefractivity
PTFE	Polytetrafluoroethylene
RMS	Root mean square
ROESY	Rotating frame nuclear Overhauser effect spectroscopy
S	Source
S_0	Singlet ground state
S_1	First singlet excited state
SAED	Selected area electron diffraction
SCFET	Single crystal field-effect transistor
SEM	Scanning electron microscopy
SHG	Second harmonic generation
TBAHFP	Tetrabutylammonium hexafluorophosphate
TC	Transition charge
TD-DFT	Time-dependent density functional theory
TEM	Transmission electron microscopy
TFT	Thin film transistor
THF	Tetrahydrofurane
TIPS	Triisopropylsilyl
TOF	Time of flight
TPA	*n*-Tetradecylphosphonic acid
UV	Ultraviolet
vdW	Van-der-Waals
Vis	Visible
XRD	X-ray diffraction

Variables

α, β, γ	Crystal lattice parameters, angles of unit cell
α	Rotational angle
α_{H}	Fraction of incorporated material
α_{ij}	Linear polarizability, tensor components
β, β_{ijk}	First hyperpolarizability, tensor components
γ_{ijkl}	Second hyperpolarizability, tensor components
$\Delta\mu$	Difference between dipole moment of ground and excited state
ε	Molar decadic extinction coefficient
ε_{max}	Molar decadic extinction coefficient at maximum of absorption
ε_{r}	Relative permittivity
θ	Slip angle
λ	Wavelength
λ_{max}	Wavelength at maximum of absorption
μ	Mobility
μ_{abs}	Absorption coefficient for X-ray radiation
μ_{e}	Excited state dipole moment
μ_{eg}	Transition dipole moment
$\boldsymbol{\mu}_{eg}$	Vector of transition dipole moment
μ_{g}	Ground state dipole moment
ν	Frequency
ν_{0}	Attempt-to-escape frequency
$\tilde{\nu}$	Wavenumber
ξ	Inverse radius of localization
ρ_{cal}	Calculated density
σ	Conductivity
φ	Angle between applied electric field and incident polarized light
χ	Reabsorption probability
a, b, c	Crystal lattice parameters, lengths of unit cell
B	Bandwidth of electronic band
BLA	Bond length alternation

c	Concentration
c^2	Resonance parameter
C_i	Capacitance per unit area
d	Thickness, height, interplanar distance
D	Degree of disorder
$\mathbf{E}$, E_{jkl}	Tensor of electric field, tensor components
E	Energy
$E_{1/2}$	Half-wave potential
$E_{1/2,Ox}$	Half-wave potential of oxidation
$E_{1/2,Red}$	Half-wave potential of reduction
E_A	Activation energy
E_{CB}	Energy of the conduction band
E_{eg}	Optical transition energy
E_F	Fermi energy
E_i	Intrinsic energy
E_M	Energy of the monomer
$E_{p,Red}$	Peak potential of irreversible reduction process
E_{VB}	Energy of the valence band
ΔE_{vdW}	Van-der-Waals energy term
f	Oscillator strength
$f(E)$	Fermi distribution
$F(000)$	Structure factor for Miller indices $h = k = l = 0$
FF	Fill factor
$\hat{H}$	Hamiltonian
I	Current
I_{DS}	Drain current
I_{on}/I_{off}	Current on/off ratio
J	Exciton coupling energy
J_C	Current density
J_{PDA}	Exciton coupling energy calculated by the point dipole approximation
J_{SC}	Short circuit current density

J_{TC}	Exciton coupling energy calculated by the transition charge method
$J_{TD\text{-}DFT}$	Exciton coupling energy calculated within time-dependent density functional theory
K_D	Dimerization constant
L	Length
M	Molar mass
n	Charge carrier density
p	Polarization
p_0	Equilibrium polarization
P	Power
PCE	Power conversion efficiency
Q	Charge
Q_i	Charge per unit area
$\mathbf{r}$	Vector of distance
r	Distance, also: bond length
R_1	Residual factor
R^2	Residual sum of squares
$R(I > 2\sigma(I))$	Residual factor for refinement with observed data
R(all data)	Residual factor for refinement with all data (also signals with intensity below noise)
t	Transfer integral
T	Temperature
T_S	Substrate temperature
T_{Subl}	Sublimation temperature
V	Voltage
$\hat{V}_{12}$	Perturbation term operator for two molecules 1 and 2
V_{DS}	Drain-source voltage
V_G	Gate potential
V_{GS}	Gate-source voltage
V_{OC}	Open circuit voltage
V_T	Threshold voltage
V_{UC}	Volume of unit cell

wR_2	Weighed residual factor
W	Width
X_H	Fraction of domains showing H-type coupling
X_J	Fraction of domains showing J-type coupling
X_{nHe}	Fraction of molecules nHe**D5**tBu**A5** in the thin film
Z	Number of molecules in unit cell

Physical Constants

ε_0	Permittivity of vacuum ($8.854 \cdot 10^{-12}$ A^2 s^4 m^{-3} kg^{-1})
c_0	Speed of light in vacuum ($2.998 \cdot 10^8$ m s^{-1})
h	Planck's constant ($6.626 \cdot 10^{-34}$ J s)
k_B	Boltzmann constant ($1.381 \cdot 10^{-23}$ J K^{-1})

Table of Contents

Chapter 1
-
Aim of Thesis

Consumer electronics are a part of our daily lives. According to the United Nations' *Broadband Commission*, almost half the world's population has access to the internet by 2016 and within the largest markets of North America and Europe, 90 % of the inhabitants already own a smartphone.[1] Alongside, next generation concepts like the smart home and virtual reality have already entered the markets,[2] while other future technologies such as autonomous driving or even the "internet of things" – with the interconnection of all objects with electronic devices, like cars, smart wearables or household appliances – are currently being investigated by industrial research due to their huge potential (Figure 1).[3]

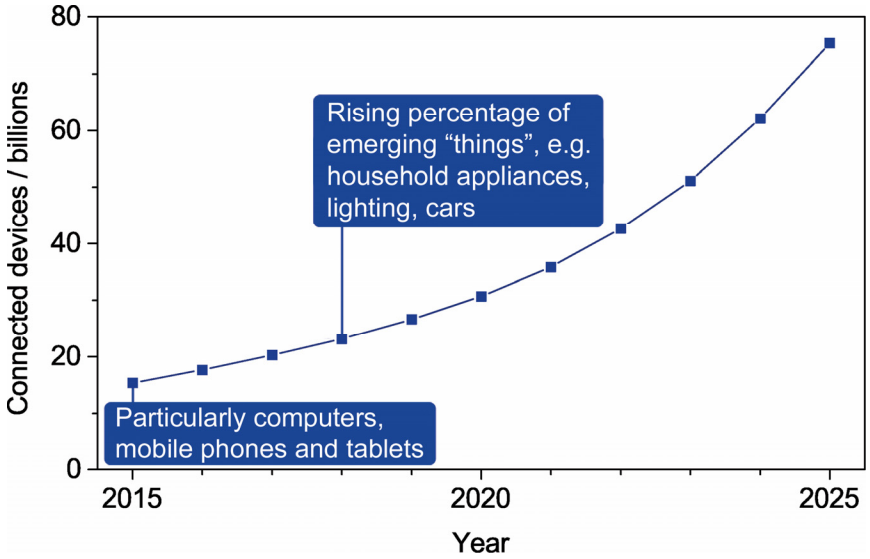

Figure 1. Projection of the number of connected devices and machines (in billions) within the "internet of things" until the year 2025 according to IHS Markit, Technology Group.[4]

In order to realize these technologies, (opto-)electronic devices and materials are crucial building blocks determining the scope and extend of their application. The field of electronics is still dominated by inorganic semiconductor devices and today amorphous silicon is the state-of-the-art material for applications, which do not require high computational performance. However, silicon-based technologies suffer from many drawbacks such as costly processing or brittle active material, making applications like flexible e-paper or cheap and disposable radio frequency identification tags impracticable.[5] At this point, organic semiconductors are investigated with regard to their ability for charge transport because of their possibility to be produced cheap as well as to be deposited as thin layers onto flexible substrates due to their low deposition temperature. Several materials could be identified in the recent years, which yielded high mobilities in organic field-effect transistors (OFETs) with values well above those of amorphous silicon with 0.5-1 $cm^2 V^{-1} s^{-1}$.[6] While the electronic part is only one side of the coin, an interconnected society requires also sensor devices which can be triggered e.g. by pressure or light. For highly specific light sensors, inorganic materials turn out to be disadvantageous as their absorption is typically very broad. On the other hand, organic materials can be easily designed to give a distinct and narrow absorption, which is a most indispensable property for this utilization.[7]

Both outlined application fields rely on electronic processes taking place at the frontier molecular orbitals of an organic material. The chemist's approach is to address these issues by the synthesis of specifically designed materials which can be either polymers or small molecules. In the field of organic electronics, low bandgap polymers have attracted much interest recently.[8] Here, their design is typically based on alternating donor (D) and acceptor (A) segments which provide strong electrostatic interactions between neighboring molecules, thus lowering the intermolecular distance and enhancing charge carrier hopping between the segments. The small molecule analogues to this design principle are the merocyanine dyes, which consist of a combination of a donor (D) as well as an acceptor (A) group (see Figure 2) and for this class of material, the electronic properties can be easily tuned by various D−A combinations.[9] Together with their easy synthetic accessibility and high extinction coefficients, these dyes might be regarded as ideal candidates for the outlined applications and accordingly were among the first molecules to be tested when the first organic solar cells and transistors were initially investigated in the 1970s and 1980s.[10] However, in the following years, research focused

on other promising material classes, e.g. acenes or bisthienobisthiophenes,[11] and merocyanines were almost absent in these fields, which can be explained with the belief that dyes with high ground state dipole moments should not be applied for high mobility applications: Amorphous films of such molecules will enlarge the density of states (DOS) due to a varying local environment of the single molecules and thus lower the charge carrier mobility because of larger energetic barriers within intermolecular hopping processes (see Figure 2).[12] It was only in 2008 when the groups of Würthner and Meerholz could demonstrate organic solar cells based on merocyanine absorbers with power conversion efficiencies of 1.7 %, comparable to solar cells with conventional organic semiconductors.[13] Additionally, in 2012 the group of Würthner showed that decent mobility values of 0.18 $cm^2\ V^{-1}s^{-1}$ were indeed achievable with such dyes despite their high ground state dipole moments.[14] Arguing that these dyes tend to form synthons and hence ordered structures rather than amorphous films due to their inherent dipolarity, Würthner and Meerholz proposed that merocyanines should not be overlooked regarding high mobility applications.[15]

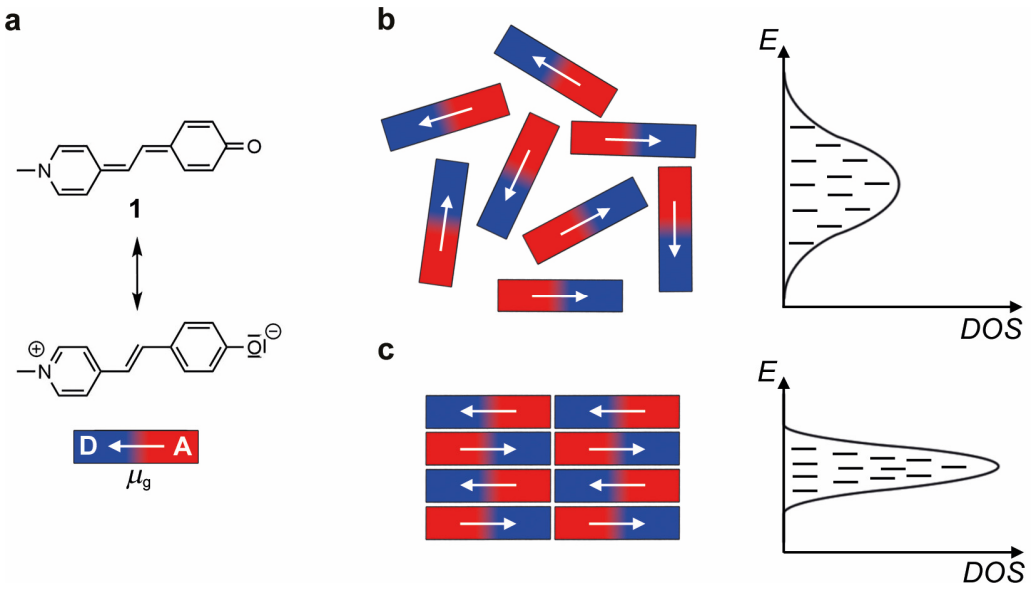

Figure 2. (a) Molecular structure of exemplary merocyanine dye **1** composed of a donor (D) and acceptor (A) moiety with two resonance structures giving rise to the inherent dipolarity with the dipole moment μ_g; (b,c) Schematic amorphous (b) and crystalline (c) ordering of dipolar merocyanine dyes with the effect of the packing on the density of states (DOS).

So far, some merocyanine dyes showed promising properties whereas others exhibited no charge carrier mobility and the reasons for this remained unclear. The aim of this thesis was to establish structure-property relationships in order to clarify how merocyanine dyes

need to be molecularly designed to provide high charge carrier mobilities as well as to achieve narrow and tunable absorption bands in the solid state. While their absorption can already be changed by aggregation into small dimer structures, the investigations of the charge transport, which was carried out in OFETs, demands for a charge transport along several micrometers. Therefore, two different series of merocyanine dyes with various donor and acceptor moieties were chosen to investigate the electronic and optical phenomena in the solid state. In addition, these dyes also varied in their sterics to specifically engineer beneficial crystal packing motifs.

For both series, the dyes were first investigated with regard to their molecular properties by UV-vis absorption, electro-optic absorption and cyclic voltammetry. To study the charge transport properties, organic thin film transistors (OTFTs) of twenty merocyanine dyes were built by vacuum deposition (see **Chapter 3.1**), as this technique usually yields the best performing devices compared to other processes, e.g. spin coating. From these results, a beneficial brickwork-type packing in the crystal structure enabling high mobility values was identified. Additionally, single crystal field-effect transistors (SCFETs) of the best performing dye were fabricated with nanocrystals grown from solution and the results are shown in **Chapter 3.2**. These devices were used to investigate charge transport directions as well as to determine the intrinsic charge carrier mobility without the influence of grain boundaries. With this approach, unprecedented mobility values for merocyanine dyes of up to 2.34 $cm^2 V^{-1} s^{-1}$ were achieved. For the studies on optical properties, which are described in **Chapter 3.3**, thin films were processed from solution for the investigated series of ten merocyanines which all exhibited the same chromophore backbone, but showed narrow and intense H- or J-type bands in the solid state. Again, for two chosen dyes with intriguing properties, nanocrystals were grown from solution to identify structural signatures yielding the observed absorption properties. The appearance of the H- or J-type bands was then shown to depend on the single crystalline packing into card stack (H) or zig-zag (J) type arrangements, which are the archetype arrangements described by Kasha in his exciton theory.

To conclude, **Chapter 4** and **Chapter 5** summarize this thesis in English and German and demonstrate that for both OFET and optical investigations, the effects are directly correlated to different single crystal structures, thus confirming the successful crystal engineering approach.

Chapter 2
-
State of Knowledge

2.1 Organic Field-Effect Transistors

The working principle of an organic field-effect transistor is based on the field effect. Here, a modulation of the current density by an applied voltage is possible and therefore the transistor can act as an electrical switch. In the following, this effect will be first explained in terms of the simplest device, the metal-insulator-semiconductor (MIS) diode, while then turning to OFETs.

2.1.1 MIS Diode

The schematic setup of a MIS diode is depicted in Figure 3a. It consists of a stack of an insulator and a semiconductor sandwiched between two (metal) electrodes, of which the contact at the dielectric is called “gate”. During operation, the metal electrode at the semiconductor is connected to the ground potential, whereas a variable potential V_G can be applied at the gate electrode to yield a voltage between the two electrodes. The different working modes of such a device can be easily explained in terms of energy band diagrams, here depicted for an inorganic p-type semiconductor (see Figure 3b-e). The application of a voltage and thus an electric field causes a band bending of the electronic bands. As the charge carrier density depends exponentially on the difference between the Fermi level E_F and the energy level of the valence band E_{VB} (for holes) or conduction band E_{CB} (for electrons), the charge carrier density can be modulated by the application of the external voltage. This is called the field effect.

In Figure 3b, the energy band diagram in the case of no applied voltage is shown. For the sake of simplicity, the difference of the work functions of the metal and the semiconductor are assumed to be zero. Furthermore, the insulator is assumed to have an infinite resistance to inhibit charge transport and in this case, the bands are flat which is referred to as the

flat-band condition. For the application of a voltage between the two electrodes, three regimes have to be distinguished (see also Figure 3c-e):

1. Accumulation: By the application of a negative voltage, the bands of the semiconductor bend upwards so that E_F and E_{VB} get closer at the interface to the insulator. As the charge carrier density of the holes depends on this difference $E_F - E_{VB}$, holes accumulate in this region.
2. Depletion: When a positive voltage is applied, the bands bend in the other way so that the density of holes is diminished at the interface to the insulator.
3. Inversion: In this case the applied positive voltage is so large that the intrinsic level E_i crosses the Fermi level E_F. At this point, the density of electrons increases considerably and thus the type of charge carriers at the interface between semiconductor and insulator is inverted compared to the flat-band condition.

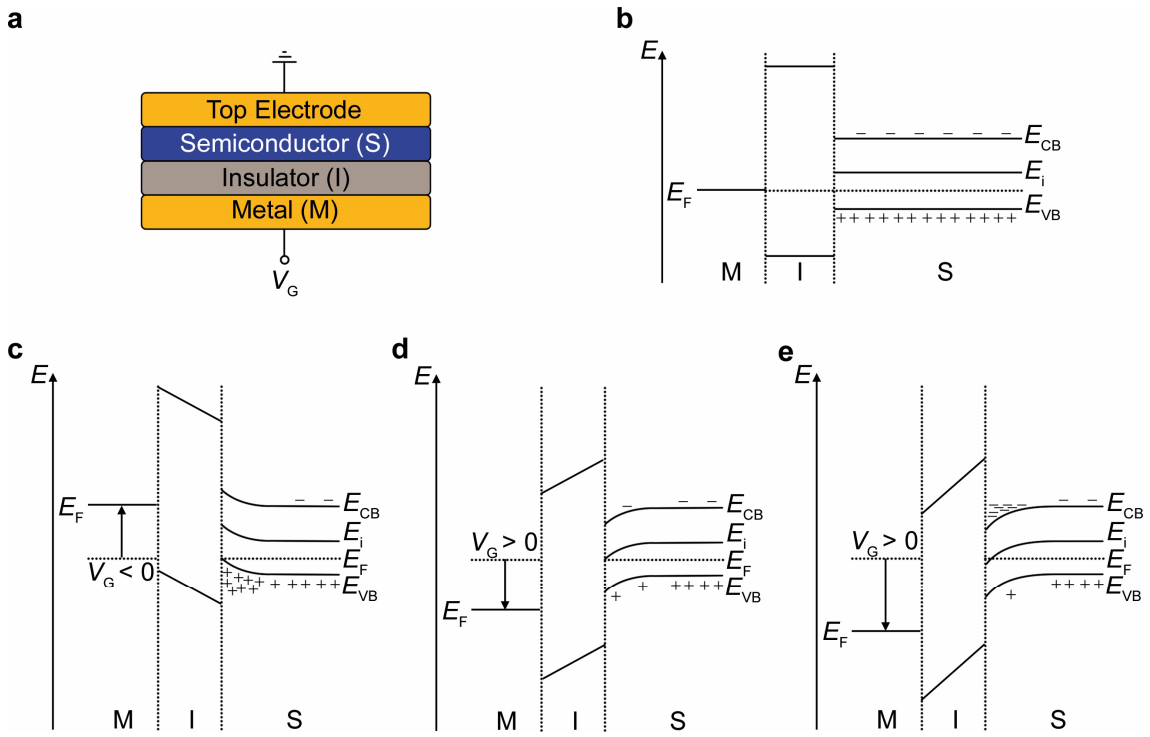

Figure 3. (a) Schematic depiction of a MIS diode; (b-e) Band diagrams and sketched charge carrier densities for different operation regimes, i.e. the flat-band case (b), the accumulation regime (c), the depletion regime (d) and the inversion regime (e).

For inorganic FETs, all three cases can be observed while the widely applied metal-oxide semiconductor FETs (MOSFETs) are operated in the inversion regime. In the case of organic semiconductors, this regime cannot be observed due to a low intrinsic charge carrier density and difficulties in doping organic semiconductors. Thus, such organic MIS

devices and also OFETs are working in the accumulation regime. Here, the MIS diode can be regarded as a capacitor with a constant capacitance. Accordingly, the amount of accumulated charge carriers Q_i per unit area can be calculated with equation (1), where C_i denotes the capacitance of the insulator per unit area, d is the thickness of the insulator and ε_0 and ε_r are the permittivity of vacuum and the relative permittivity, respectively:

$$Q_i = C_i V_G = \varepsilon_0 \varepsilon_r \frac{1}{d} . \quad (1)$$

2.1.2 OFET Architecture

The architecture of an OFET resembles that of a MIS diode, but it consists of one additional electrode. In this regard, an OFET is a three electrode device, with the insulator and organic semiconducting layer in between the three electrodes, which are now called gate (G), source (S) and drain (D) electrodes.

Different architectures can be imagined for the construction of OFETs. Considering the deposition sequence of the layers, these architectures can be distinguished into four different types, namely “bottom-gate, top-contact”, “bottom-gate, bottom-contact”, “top-gate, top-contact” and “top-gate, bottom-contact” (see Figure 4).

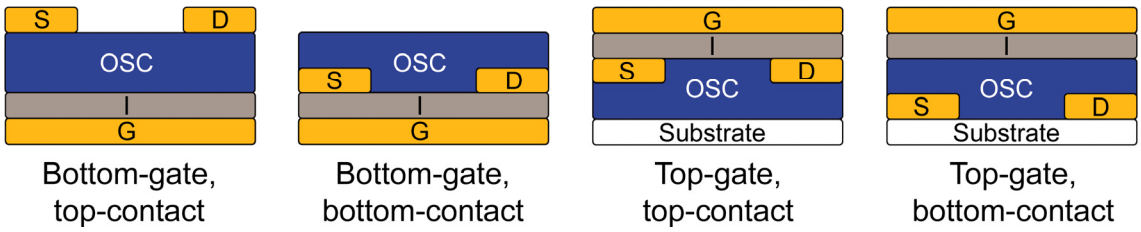

Figure 4. Schematic drawing of different OFET architectures. The layers are denoted as G (gate), I (insulator), OSC (organic semiconductor), S (source) and D (drain).

All these device configurations offer different advantages and disadvantages while the biggest advantage of the bottom-gate structure is that of an easy fabrication as the devices can be processed onto ready-made substrates, e.g. Si/SiO_2 wafers, and no gate structure has to be patterned. Therefore, for a screening of different materials, this configuration gives the most feasible fabrication procedure. For the source and drain contacts, devices in bottom-gate, bottom-contact configuration often show a low performance. This happens because of a disordered molecular arrangement at the interface of the electrodes and the organic semiconductor,[16] which is a result from different surface energies of the insulator as well as the contact electrodes, yielding different growth modes. On the other hand, the

bottom-gate, top-contact structure is disadvantageous regarding the contact resistance as charges have to travel from the electrodes to the conduction channel. However, this drawback is usually not that sincere, since the electric field applied between source and gate electrode is high due to the low thickness of the organic semiconductor (in this thesis, thin films of 30 nm were used). Additionally, with the fabrication of the source and drain electrode (mostly done by vacuum deposition), the metal might penetrate the organic material, thus lowering the contact resistance.[17] Taking these considerations into account, the bottom-gate, top-contact configuration was chosen for the fabrication of the devices in this thesis.

2.1.3 OFET Operation Principle

The operation principle of an OFET is explained in terms of Figure 5 for a transistor with bottom-gate, top-contact configuration.

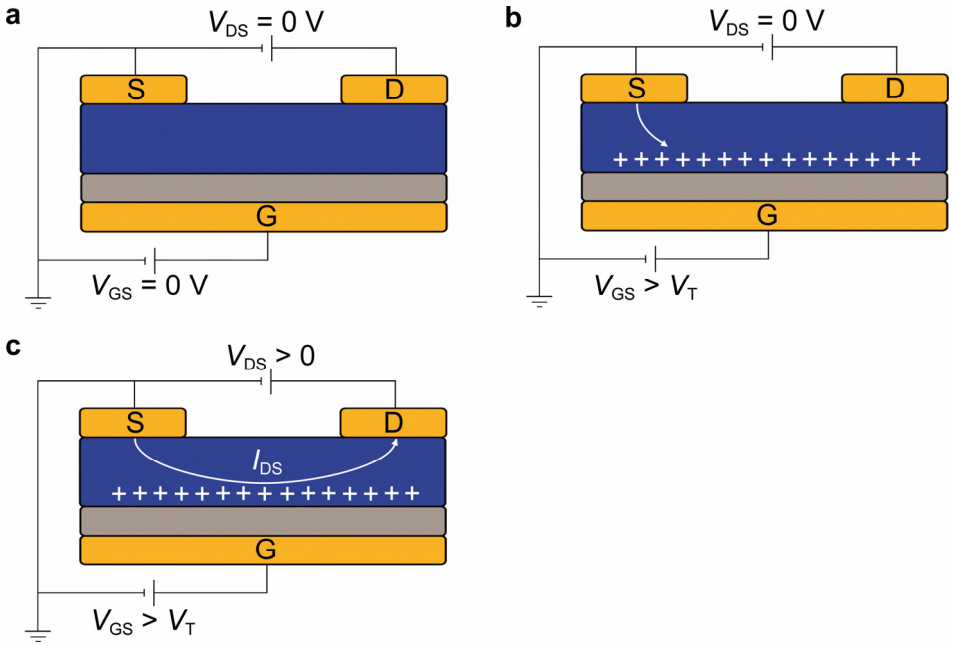

Figure 5. Schematic drawing of the working principle of an OFET with a p-type organic semiconductor material for the following conditions: (a) $V_{GS} = 0$ V, $V_{DS} = 0$ V, no current is flowing; (b) $V_{GS} > V_T$, $V_{DS} = 0$ V, holes accumulate at the semiconductor/dielectric interface; (c) $V_{GS} > V_T$, $V_{DS} > V_{GS}-V_T$, a drain current I_{DS} flows from the source to the drain electrode.

By definition, the source electrode is always connected to the ground potential. The accumulation of charge carriers at the interface of the organic semiconductor and insulator can then be induced by applying a voltage V_{GS} between the gate and source electrode. However, for most organic semiconductors, free charge carriers do not accumulate for any

$V_{GS} \neq 0$ because of various reasons, such as interface dipoles or disorder, leading to deep traps which inhibit charge transport at small V_{GS}. To account for this, the threshold voltage V_T is introduced, which distinguishes the on- from the off-state.[18] For $V_{GS} > V_T$, free charges accumulate at the interface between the insulating dielectric layer and the organic semiconductor while the amount of accumulated charge carriers can be modulated by V_{GS}. Hence, a conducting channel between the source and drain electrodes is formed and by applying a voltage V_{DS} between these two electrodes, a drain current I_{DS} can be measured.

The analysis of transistor devices is done by measuring current-voltage characteristics. Here, the drain current is measured either in dependence on the gate-source voltage, leading to a transfer curve (with constant V_{DS}), or in dependence on the drain-source voltage, which is then called an output curve (with constant V_{GS}). These two characteristics are shown in Figure 6 for a p-type transistor device together with a sketch of the local charge carrier density within the transistor channel, for which three cases are distinguished.

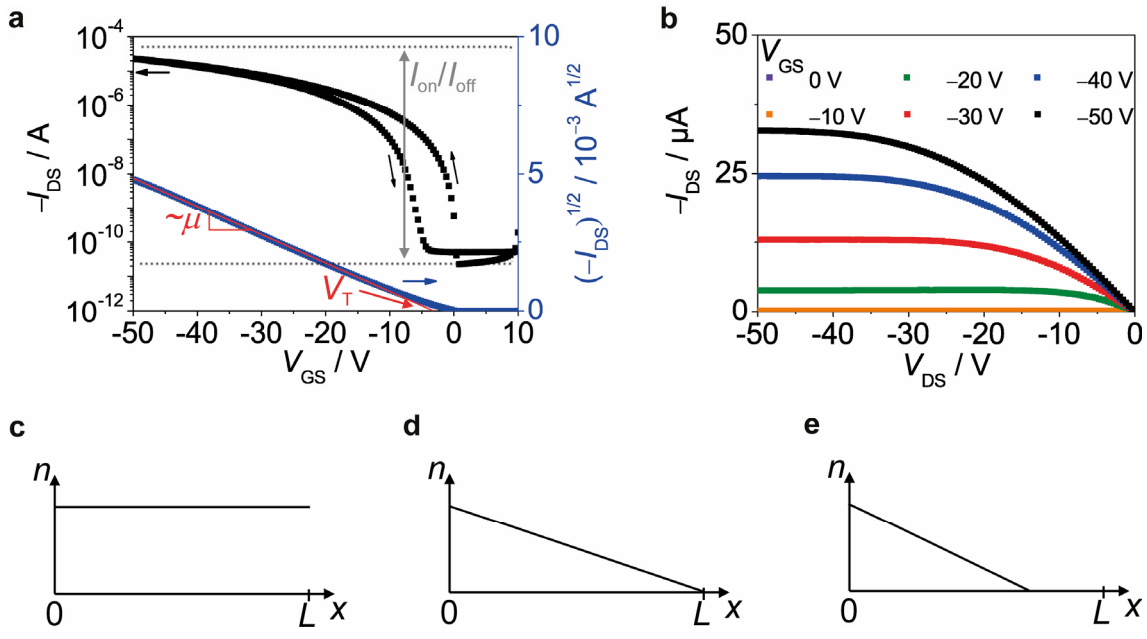

Figure 6. (a) Transfer curve of a p-type OFET with denoted mobility μ, threshold voltage V_T and on/off ratio I_{on}/I_{off}; (b) Output curve of a p-type OFET; (c-e) Charge carrier density n along the channel in x-direction for $V_{DS} << V_{GS} - V_T$ (c), $V_{DS} = V_{GS} - V_T$ (d) and $V_{DS} > V_{GS} - V_T$ (e).

For $V_{DS} << V_{GS} - V_T$, the charge carrier density along the channel is constant since the electric field is also almost constant along the channel due to the applied gate-source voltage. In this case, I_{DS} depends linearly on V_{DS} and V_{GS} and this regime is accordingly

called the linear regime. For $V_{DS} = V_{GS} - V_T$, the charge carrier density in the region of the drain electrode is lowered significantly as there is no driving force for charge carriers to accumulate in this region (due to a similar potential of the drain and the gate electrode). This effect is called pinch-off and at this point, the transition from the linear to the saturation regime occurs, where I_{DS} is not affected by the change of V_{DS}. The saturation regime is then characterized for $V_{DS} > V_{GS} - V_T$ and here, the drain current is fully saturated and depends only on V_{GS}.

A mathematical description of the drain current I_{DS} can be derived from Ohm's law with J_C as current density along the channel (x-direction), σ as conductivity and E_e as the electric field between the source and the drain electrode:

$$J_C = \sigma E_e \, . \tag{2}$$

The measured current I_{DS} is proportional to the current density J_C with the height of the conducting channel d and the width of the channel W. If we assume that the mobility of the charge carriers μ is independent of the voltage and n is the charge carrier density, equation (2) can be rewritten to give equation (3):

$$I_{DS} = d\, W\, n\, \mu \, \frac{\mathrm{d}V(x)}{\mathrm{d}x} \, . \tag{3}$$

Now, under the assumption that the electrical field along the z-direction (height), generated by V_{GS} is much higher than the electrical field along the x-direction generated by V_{DS} (gradual channel approximation), we can state that the electrical field along the z-axis is constant and the charge carrier density n can be written as follows:

$$n = \frac{C_i}{d} \, (V_{GS} - V_T - V(x)) \, . \tag{4}$$

By substituting equation (4) into equation (3), equation (5) is obtained:

$$I_{DS} = W\, C_i\, \mu \, (V_{GS} - V_T - V(x)) \, \frac{\mathrm{d}V(x)}{\mathrm{d}x} \, . \tag{5}$$

Solving this differential equation for the boundary conditions $V(L) = V_{DS}$ and $V(0) = 0$ (with L being the channel length) yields equation (6) which is valid for the linear regime. For the saturation regime, i.e. $V_{DS} \geq V_{GS} - V_T$, I_{DS} depends only on V_{GS} and thus equation (6) can be simplified to equation (7):

$$I_{DS} = \frac{\mu\, W\, C_i}{2L} \, (2\, (V_{GS} - V_T)\, V_{DS} - V_{DS}^2) \, ; \tag{6}$$

$$I_{DS} = \frac{\mu\, W\, C_i}{2L} \, (V_{GS} - V_T)^2 \, . \tag{7}$$

The figures-of-merit for transistor devices calculated in this thesis are the hole charge carrier mobility μ, the threshold voltage V_T and the current on/off ratio I_{on}/I_{off}. Note that mobility values derived in the different regimes can also differ due to a varying charge carrier density, i.e. in the linear regime the charge carrier density is lower than in the saturation regime which might have an effect on the mobility values. In this thesis, all field-effect mobilities were obtained for the saturation regime of the transistor devices to ensure a filling of traps within the semiconducting material. In this regime, the plot of the square-root of I_{DS} against V_{GS} yields a linear dependence according to equation (7). Thus, the mobility can be calculated from the slope of the linear fit of this curve while the threshold voltage is marked by the x-axis intercept of the linear fit. Note that for characterizing the device, I_{DS} is measured for a forward and backward voltage sweep (see small black arrows in Figure 6a). While the hysteresis between these two curves is an indicator of traps within the material, the figures-of-merit were always determined for the forward sweep.

The on/off ratio is determined from the maximum and minimum values of the drain current. Note that for on/off ratios exceeding 10^6, only a value of 10^6 is stated due measurement accuracies of the used instruments, which ensure only a correct measurement of I_{DS} within 10^6 orders of magnitude. The determination of all figures-of-merit together with exemplary transfer and output curves of a p-type OFET is shown in Figure 6.

2.2 Charge Carrier Transport in Organic Materials

In the last section, the working principle of a transistor was discussed and it was shown that the drain current I_{DS} is proportional to the charge carrier mobility μ. In contrast to inorganic semiconductors, where field-effect mobilities of 1000 $cm^2\ V^{-1}\ s^{-1}$ and higher can be measured for doped single crystalline silicon, the mobilities of organic materials are much lower.[6, 11b, 19] Here, crystalline organic semiconductors aim to compete with mobilities of hydrogen-saturated amorphous silicon (a-Si:H), which show in average mobilities in the range of 0.5-1 $cm^2\ V^{-1}\ s^{-1}$.[6a] The reason for these striking differences in mobility values are the diverse bonding characteristics of both classes of materials and the reasons and consequences of this are explained in the following.

For inorganic semiconductors, strong interatomic covalent bonds lead to a quasi-continuous distribution of energetic states due to the Pauli principle to form the valence and conduction bands. In contrast, organic molecules are bound by weak van-der-Waals interactions and thus, only narrow bands are formed from the frontier molecular orbitals – if they are formed at all. When considering band transport which enables high charge carrier mobilities due to the delocalization of the states, only a few reports of organic single crystal devices are found, which show band transport behavior for low temperatures and high material purity.[20] However, for the vast majority of materials, only hopping transport between localized states is observed, especially in polycrystalline or even amorphous thin films, while the threshold between hopping and band transport lies at mobility values of ~1 $cm^2\ V^{-1}\ s^{-1}$.[21] According to Stafström,[22] the important models for charge carrier transport can be classified by comparing the bandwidth, i.e. the strength of molecular or atomic interaction, with the degree of disorder of the molecules in combination with or without coupling of the electrons with the lattice vibrations of the solid, the phonons.

For the simplest approach, which neglects the electron-phonon coupling, comparing the bandwidth B with the degree of disorder D leads to the following two cases:

1. $D < B$: For high bandwidths (strong bond types) and a low degree of disorder (materials with high crystallinity), charge carrier transport is normally explained in terms of band transport along delocalized states. This is the usual case for inorganic semiconductors.

2. $D > B$: For small bandwidths (weak bond types) and a high degree of disorder (e.g. amorphous materials), charge carrier transport is explained by hopping between localized states. The simplest model for this case is the theory by Miller & Abrahams.[23]

2.2.1 Miller-Abrahams Theory

For systems without long-range order, the environment of each molecule differs from that of its neighbor. Thus, in combination with the weak binding forces, there are only energetic states of different values being spatially localized on the molecules themselves. Charge transport is in this case described by a hopping transport with its magnitude described by the charges' hopping frequency ν_{mn} with m and n being two sites with a certain energetic state (schematically depicted in Figure 7).

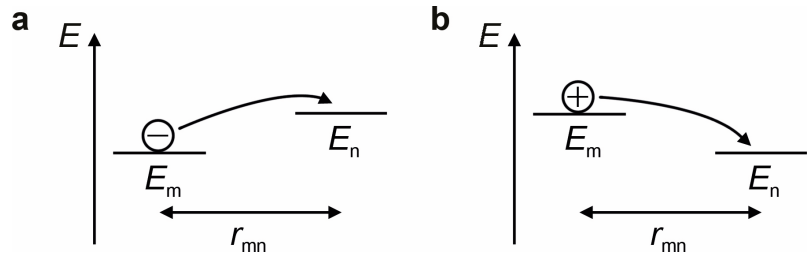

Figure 7. (a) Schematic depiction of an electron jump from the energy level E_m to E_n over the distance r_{mn}; (b) Schematic depiction of a hole jump from the energy level E_m to E_n.

According to Miller & Abrahams, this hopping rate can be described for electrons by equation (8) with contributions of tunneling and thermally activated processes:

$$\nu_{mn} = \begin{cases} \nu_0 \exp(-\xi r_{mn}) \exp\left(-\dfrac{E_n - E_m}{k_B T}\right) \; ; & E_n - E_m > 0; \\ \nu_0 \exp(-\xi r_{mn}) \; ; & E_n - E_m < 0. \end{cases} \tag{8}$$

Here, ν_0 describes the attempt-to-escape frequency, $\exp(-\xi r_{mn})$ the contribution of the tunneling process with ξ being the inverse localization radius, and r_{mn} the distance between sites m and n. The term $\exp\left(-\frac{E_n - E_m}{k_B T}\right)$ is the Boltzmann term of probability of thermally activated hopping across the energy barrier $\Delta E_{mn} = E_n - E_m$ at a temperature T with the Boltzmann constant k_B.

For a downward jump ($\Delta E_{mn} < 0$), the factor of the thermal contribution is replaced by 1 as no activation energy is needed and thus an upward hopping process ($\Delta E_{mn} > 0$) occurs

less likely. For holes, the description follows the same explanation but is inversed, i.e. an upward jump occurs more likely with a thermal contribution factor of 1 than a downward hopping process, as stated in equation (9):

$$\nu_{mn} = \begin{cases} \nu_0 \exp(-\xi r_{mn}) \exp\left(\frac{E_n - E_m}{k_B T}\right) \; ; & E_n - E_m < 0; \\ \nu_0 \exp(-\xi r_{mn}) \; ; & E_n - E_m > 0. \end{cases} \tag{9}$$

2.2.2 Charge Transport in Disordered Materials

In order to estimate the macroscopic charge carrier mobility, it has to be taken into account that for materials showing a hopping transport, the mobility is a function of the charge carrier density *n* which should be explained with the help of Figure 8.

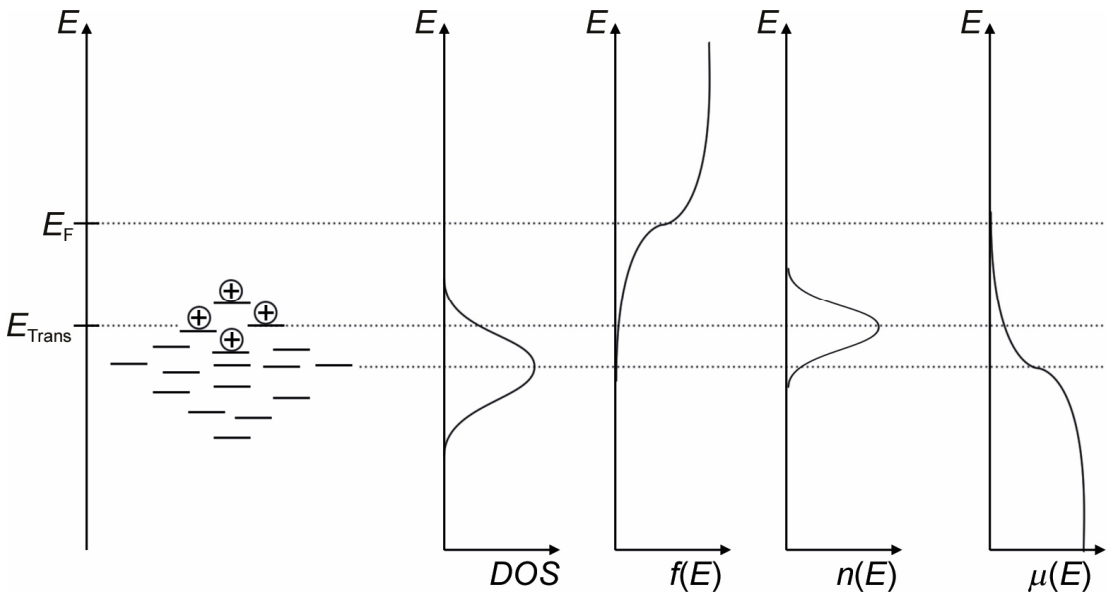

Figure 8. Schematic depiction of energy levels of a disordered material together with the density of states (*DOS*), the Fermi function *f*(*E*), the carrier density *n*(*E*) and the charge carrier mobility μ.

In disordered systems, here depicted for a p-type material, the density of states (DOS) is often approximated by a Gaussian distribution of the HOMO levels due to their random environment in the amorphous solid state.[12a] The charge carrier density of holes then results as a multiplication of the DOS with the fermi function *f*(*E*) which describes the probability that an energetic state is populated. The average of this energy distribution is then called the transport energy E_{Trans}. As a downward jump is less likely than an upward hopping process, the mobility of a hole occupying a state above the transport energy of the Gaussian distribution is lower than for a hole on a level below the transport energy

and the function of the mobility on the energy is schematically depicted in Figure 8. The macroscopic charge carrier mobility is therefore higher for higher charge carrier densities n as well as for narrow Gaussian distributions of the DOS.

2.2.3 Impact of Ground State Dipole Moments on Charge Transport

A disordered arrangement of molecules with permanent ground state dipole moments μ_g enlarges the DOS due to the additional random orientation of μ_g in comparison to a disordered arrangement of unpolar molecules. Accordingly, Bässler and co-workers could demonstrate in the 1990s by calculations, that the charge carrier mobility decreases with increasing ground state dipole moment (see Figure 9). Thus, they concluded that for applications requiring high mobilities, dipolar compounds should not be used.

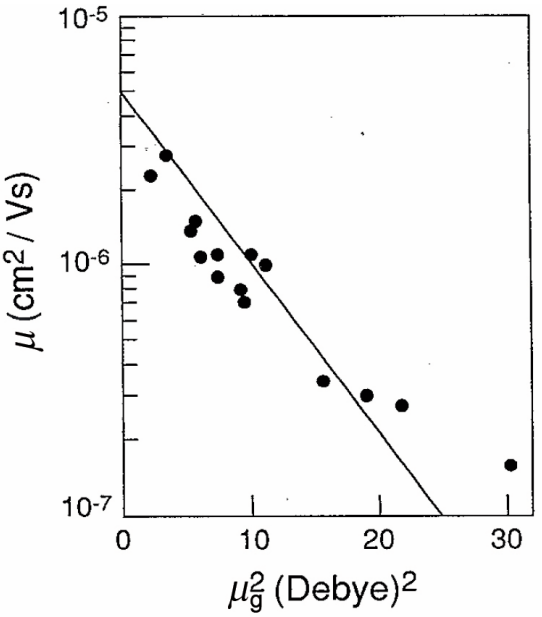

Figure 9. Dependence of the charge carrier mobility μ on the square of the ground state dipole moment μ_g with the black dots being experimental data from ref. [24] and the line being the theoretical prediction from ref. [25]. Reprinted from ref. [25] with the permission of AIP Publishing.

By assuming a hopping transport, non-interacting dipole moments as well as other parameters (e.g. the average distance of organic semiconductor molecules in a polymer matrix), their model describes an exponential decrease of the charge carrier mobility with increasing ground state dipole moment as in $\log \mu \sim -\mu_g^2$.[25] Additionally, experimental data from Sugiuchi and Nishizawa supported these calculations as they could demonstrate the decrease of the hole mobility in molecularly doped polycarbonate (1:1 ratio by weight) by time of flight (TOF) measurements.[24] In this study, molecular reorientation by dipole-

dipole interactions was inhibited by spatial displacement of the dipolar molecules in the polycarbonate matrix. Hence, the measurements indeed showed the predicted $\log \mu \sim -\mu_g^2$ behavior with the exception of the last data point for the most dipolar molecule ($\mu_g \sim 5.5$ D). It was suggested that this deviation could be the result of dipole-dipole interactions, which are stronger for higher ground state dipole moments, but no further studies for more dipolar molecules were carried out.

2.3 Exciton Theory

As described in section 2.2, the arrangement of molecules is of utmost importance regarding solid state applications. In order to analyze this arrangement, several techniques are available, such as X-ray diffraction or electron diffraction. However, in some cases, already the rather simple method of UV-vis absorption can help to deduce certain molecular arrangements. Here, the arrangement of dyes can be described by the simple yet elegant exciton theory developed by Kasha in the 1960s, which is often used for molecules in solution.[26] Influenced by the observation of band splitting for organic single crystals by Davydov,[27] Kasha proposed the exciton theory which explains the change of absorption spectra due to the molecular arrangement, e.g. by aggregation of dyes in solution.

Within the exciton theory, it is assumed that the intermolecular electron overlap is small and thus the exciton theory is a perturbation theory. The molecules are described individually even in the aggregated state and so the Hamiltonian of an aggregated dimer $\hat{H}_{12}$ can be described by equation (10) as the sum of the Hamiltonians of the individual molecules $\hat{H}_1$ and $\hat{H}_2$ as well as a perturbation term $\hat{V}_{12}$:

$$\hat{H}_{12} = \hat{H}_1 + \hat{H}_2 + \hat{V}_{12} \ . \tag{10}$$

The solution of the Schrödinger equation for the ground and the excited state with assuming two identical molecules leads to an optical transition energy E_{12} as difference between ground and excited state as given in equation (11):

$$E_{12} = E_M + \Delta E_{vdW} \pm J \ . \tag{11}$$

Here, E_M is the optical transition energy of an individual monomer, while the two additional terms, namely the stabilization energy ΔE_{vdW} as well as the exciton coupling J are derived as a result of the Schrödinger equation. The stabilization energy ΔE_{vdW} is a consequence of intermolecular van-der-Waals interactions and describes the energy

difference of the ground and excited state of the dimer to those of the monomer, respectively. According to equation (11), the excited state is now split into two energy levels with an energy difference 2*J*. In terms of the classical theory of Kasha and McRae, J can be calculated by equation (12) within the point dipole approximation (PDA) of two interacting transition dipole moments $\boldsymbol{\mu}_{eg}(1)$ and $\boldsymbol{\mu}_{eg}(2)$ within a distance of $\mathbf{r}_{12}$:

$$J = \frac{1}{4\pi\varepsilon_0}\left(\frac{\boldsymbol{\mu}_{eg}(1)\,\boldsymbol{\mu}_{eg}(2)}{|\mathbf{r}_{12}|^3} - \frac{3\left(\boldsymbol{\mu}_{eg}(1)\,\mathbf{r}_{12}\right)\left(\boldsymbol{\mu}_{eg}(2)\,\mathbf{r}_{12}\right)}{|\mathbf{r}_{12}|^5}\right). \tag{12}$$

When assuming the simplest case, i.e. both molecules are equivalent ($\boldsymbol{\mu}_{eg}(1) = \boldsymbol{\mu}_{eg}(2)$) and in coplanar arrangement, equation (12) can be simplified to equation (13), where α and θ describe the rotational and slipping angle between the two transition dipole moments of the individual molecules, respectively, and μ_{eg} is the transition dipole moment (for a sketch, see Figure 10):

$$J = \frac{\mu_{eg}^2}{4\pi\varepsilon_0 r_{12}^3}(\cos\alpha - 3\cos^2\theta)\,. \tag{13}$$

In order to describe the archetype molecular arrangements, some examples are given, first for fixed values of $\alpha = 0°$, $\theta = 90°$ and $\theta = 0°$, then for $\alpha = 0°$ and varying θ, as well as varying α and fixed $\theta = 90°$ and ultimately for the general case without any assumptions.

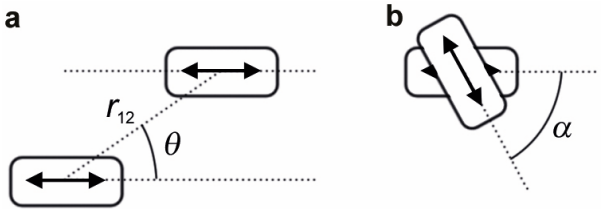

Figure 10. Schematic depiction of two molecules with the intermolecular distance r_{12}, the slip angle θ and the twist angle α. The transition dipole moments are sketched as black arrows.

For $\alpha = 0°$, i.e. no rotational displacement, two limiting cases can be distinguished which are the H- and J-aggregates for $\theta = 90°$ and $\theta = 0°$, respectively (Figure 11). To elucidate which of the transitions from the ground to the split excited state is allowed, the phase relation of the transition dipole moments has to be considered. Here, the transition probability is proportional to the oscillator strength of the whole system, which corresponds to the sum of the individual transition dipole moments. In the case of a dimer, only the transition is allowed, where the transition dipole moments oscillate in-phase,

leading to an oscillator strength of 2*f*, whereas the out-of-phase oscillation always leads to an oscillator strength of zero.

For the H-dimer ($\theta = 90°$), the transition dipole moments are oriented in a parallel fashion. As stated above, only the in-phase oscillation of the transition dipole moments leads to an allowed state, thus yielding a hypsochromic shift of the absorption with respect to the monomer. For the case of the J-dimer ($\theta = 0°$), where the transition dipole moments are oriented in-line, the in-phase arrangement of the transition dipole moments has lower energy and hence results in a bathochromic shift of the absorption while in this case the higher energy state, corresponding to the out-of-phase arrangement, is forbidden.

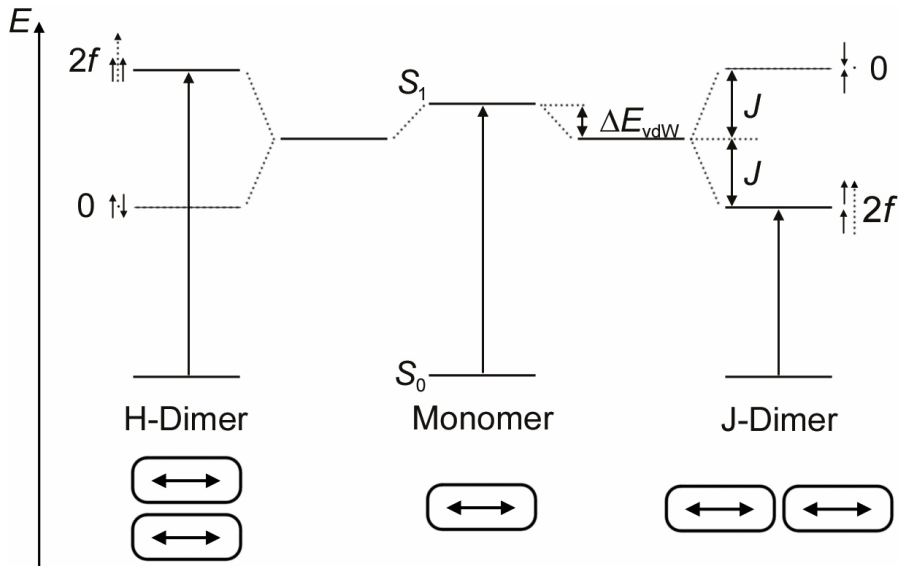

Figure 11. Schematic illustration of the energy levels resulting from exciton coupling from different arrangements of molecules with the transition dipole moments marked as double arrows. Additionally, the phase relation of the transition dipole moments is given in solid arrows and the resulting total oscillator strength as dotted arrow. Adapted from ref. [26b]

While these are the extreme cases, the exciton splitting upon variation of θ for $\alpha = 0°$ is depicted in Figure 12 for a dimer. Here, the splitting decreases for increasing θ in the range of $0° \leq \theta < 54.7°$ and becomes zero for $\theta = 54.7°$ as in this case $\cos\alpha - 3\cos^2\theta = 0$ holds true and degenerate energy levels are obtained, see equations (11) & (13). Afterwards, for increasing θ in the range of $54.7° < \theta \leq 90°$ the exciton splitting increases again. When considering the phase relation of the transition dipole moments, it shows that for $\theta < 54.7°$ only the lower energetic state is allowed, while for $\theta > 54.7°$, only the higher energetic state is allowed. This leads to the common definition of H-aggregates with $\theta > 54.7°$ and J-aggregates with $\theta < 54.7°$.

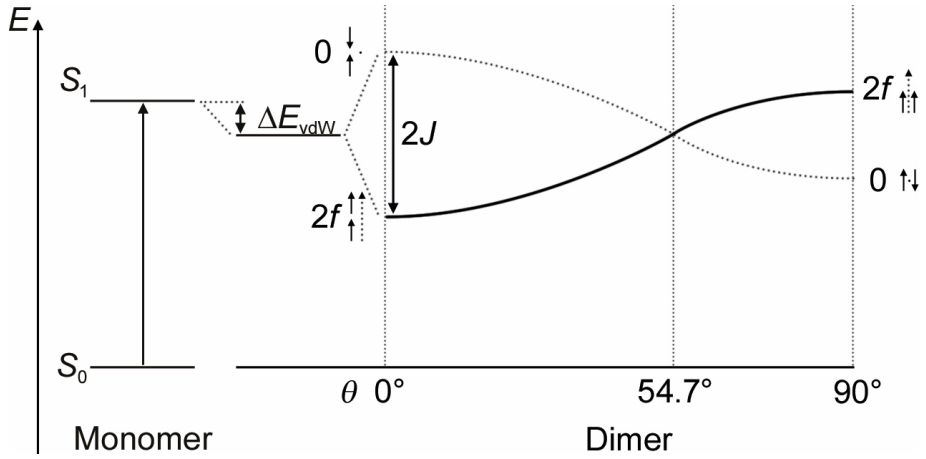

Figure 12. Exciton band diagram for a coupling between two molecules for varying slipping angle θ at fixed r_{12}. The solid black line represents the energy level for an in-phase coupling of the transition dipole moments and thus the allowed energy state for a transition. Adapted from ref. [26b]

The exciton splitting was in the above cases described for a fixed angle α. The exciton splitting energy with varying α is depicted in Figure 13 for $\theta = 90°$. Here, for increasing α, the exciton splitting successively decreases and gets zero for $\alpha = 90°$. Upon increasing α, also the lower energy absorption becomes partially allowed due to the non-vanishing oscillator strength for the out-of-phase arrangement.

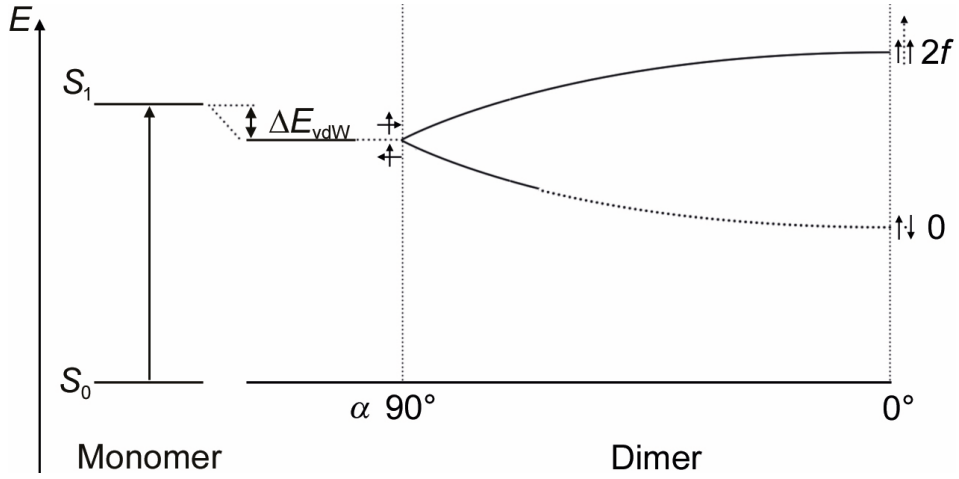

Figure 13. Exciton band diagram for a coupling between two molecules for varying rotational angle α. The system is in an H-type configuration ($\theta = 90°$) for $\alpha = 0°$ and the solid black line represents the allowed energy state for a transition. For $\alpha = 90°$, there is no interaction of the transition dipole moments and hence no energy splitting. Adapted from ref. [26b]

For the general case, an additional consideration has to be made. As α is not fixed to 0°, the term $\cos^2 \theta$ in equation (13) might not be valid if the molecules are not coplanar. An example of such a molecular arrangement is shown in Figure 14 and although both

molecules are identical, the angle between the transition dipole moments and the center-to-center distance $\mathbf{r}_{12}$ are different for both molecules.

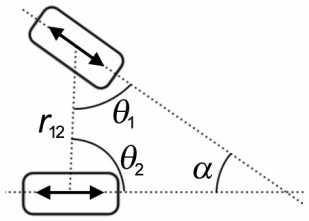

Figure 14. Schematic depiction of molecular arrangement where $\theta_1 \neq \theta_2$.

This leads to equation (14) with θ_1 and θ_2 being the slipping angles of the individual molecules:

$$J = \frac{\mu_{eg}^2}{4\pi\varepsilon_0 r_{12}^3} (\cos\alpha - 3\cos\theta_1 \cos\theta_2) \,. \tag{14}$$

When extending the dimer configuration to aggregates with a size of N coupled molecules, further exciton coupling leads to additional band splitting into N energy levels and alongside, the corresponding bands will get narrower and more intense (Figure 15). Additionally, while the out-of-phase arrangement of transition dipole moments will still be forbidden, transitions with mixed arrangements might be allowed.

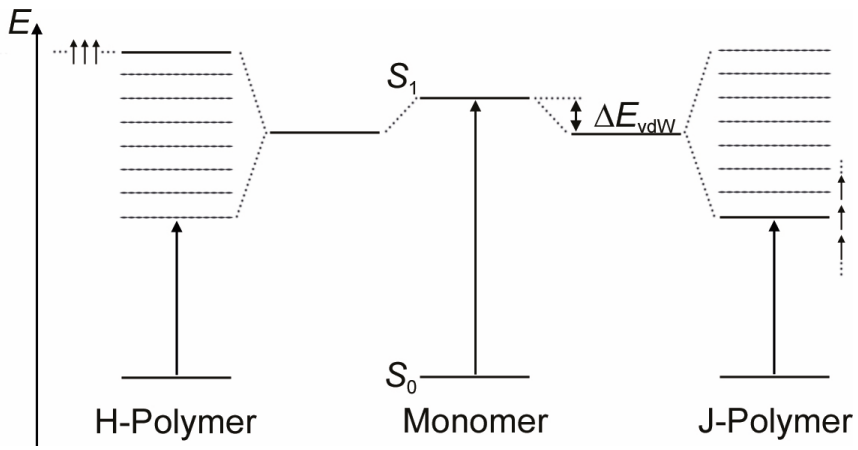

Figure 15. Schematic exciton band diagram for a supramolecular polymer of transition dipole moments arranged in a parallel and in-line fashion. Adapted from ref. [26a]

Considering also supramolecular polymer chains with alternating translational structure ($\alpha \neq 0°$), the two strongest transitions are then the transition of highest energy with out-of-phase coupling and the one of lowest energy, i.e. in-phase coupling (Figure 16).

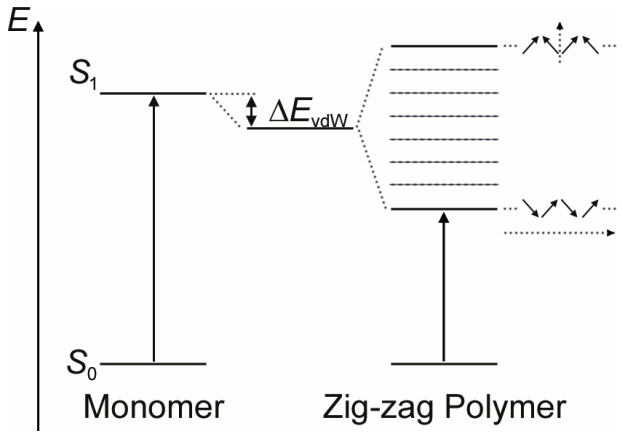

Figure 16. Schematic exciton band diagram for a supramolecular polymer of molecules with transition dipole moments arranged in a zig-zag fashion with indicated phase orientation of highest and lowest energetic transition state. Adapted from ref. [26a]

In order to calculate the exciton coupling energy for such supramolecular polymer chains of the given H- or J-type arrangement, Kasha and McRae proposed that by allowing only next neighbor interactions, the total intermolecular coupling can be calculated as 4*J* if the coupling to both next neighbors is identical.[28]

2.4 Fundamental Properties of Dipolar π-Systems

The dipolarity of π-systems relies on the presence of electron donating and electron withdrawing groups, which exhibit a pronounced inductive or mesomeric effect.[29] Typical dipolar push-pull chromophores, e.g. merocyanine dyes, which are studied in this thesis, consist of a donor (D) and acceptor (A) moiety connected by a polymethine bridge. The fundamental properties of such D−A chromophores will be discussed in this section regarding their electronic structure, their proneness to aggregation and their application in photonics, organic photovoltaics and organic field-effect transistors.

2.4.1 Electronic Structure

The structure of a D−A chromophore can be described by two mesomeric resonance forms being of polyene type (neutral) or betaine type (zwitterionic), which are both depicted in Scheme 1.

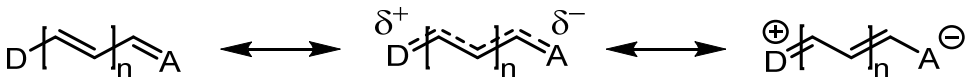

Scheme 1. Polyene type (left), cyanine limit (middle) and betaine type (right) resonance structures of a D−A chromophore.

Depending on the strength of the donor and acceptor moieties as well as the length of the polymethine bridge, the dyes' electronic properties like absorption or ground state dipole moment can be tuned. To quantify the electronic structure of such a dye, two related parameters are discussed, namely the bond length alternation *BLA* as well as the resonance parameter c^2,[30] which are defined by the following two equations (15) and (16):

$$BLA = r(\mathrm{C{-}C}) - r(\mathrm{C{=}C}) \; ; \tag{15}$$

$$c^2 = \frac{1}{2}\left[1 - \frac{\Delta\mu}{\sqrt{4\mu_{eg}^2 + \Delta\mu^2}}\right] . \tag{16}$$

Here, r denotes the bond length of a designated single (C−C) or double (C=C) bond given in the polyene-like structure, $\Delta\mu$ the difference of the dipole moments in ground and excited state ($\Delta\mu = \mu_e - \mu_g$) and μ_{eg} the transition dipole moment.

Regarding the electronic structure, this means that for a polyene-like molecule, $BLA > 0$ and $c^2 < 0.5$ apply as the structure consists of alternating single and double bonds and

there is a significant change of dipole moment upon excitation due to the redistribution of electron density. The design of such molecules can be carried out by using weak donor and acceptor moieties and long polymethine chains. For particularly strong donor and acceptor moieties as well as short polymethine chains, the structure is more betaine-like, yielding parameters of $BLA < 0$ and $c^2 > 0.5$ (as the designated single bonds of the neutral resonance structure now become double bonds in the zwitterionic structure and vice versa, and $\Delta\mu$ becomes negative). The case distinguishing both forms is the so-called cyanine limit where the π-electrons are completely delocalized over the polymethine bridge and all bond lengths are equal $(BLA = 0)$. Additionally, the changes of electron density and geometry upon excitation are small, resulting in a resonance parameter of $c^2 = 0.5$. Experimentally, a dye in the cyanine limit can be easily recognized by its UV-vis absorption band,[31] as shown for a series of merocyanine dyes in Figure 17. Here it can be seen that for increasing donor strength for a given oxopyridone acceptor moiety, the D−A chromophores show a change of the electronic structure from polyene type to the cyanine limit as reflected by the narrow and intense absorption of **5**.

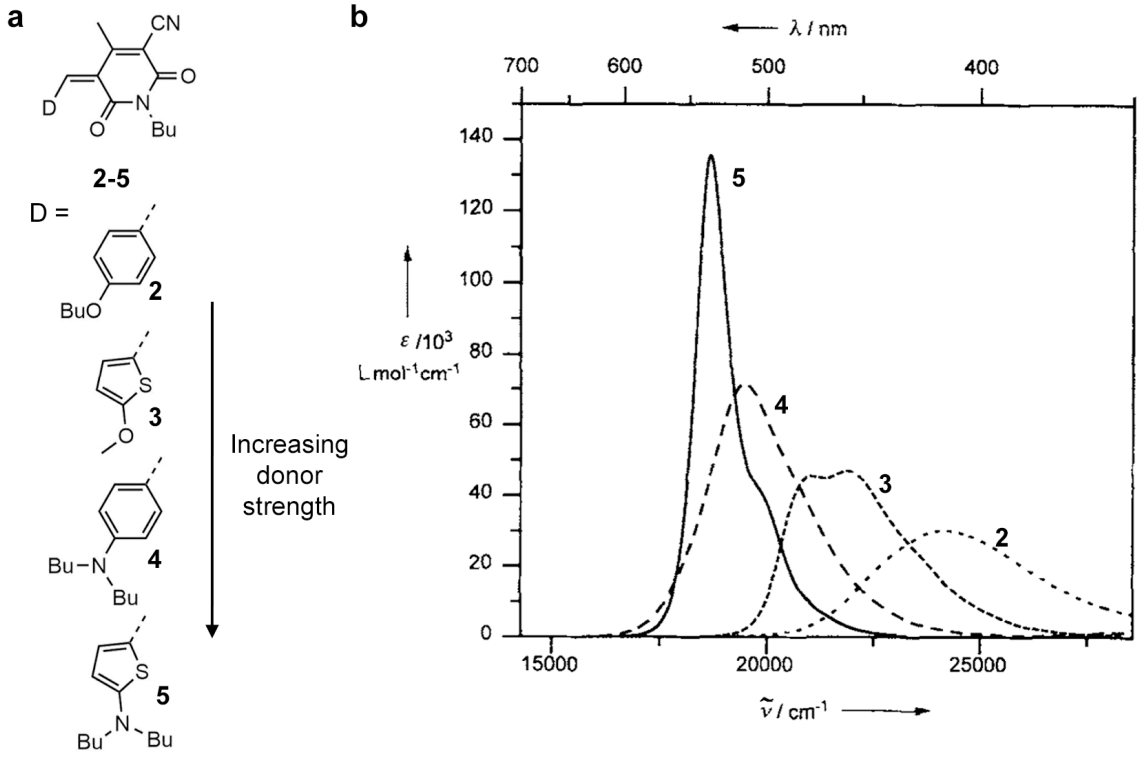

Figure 17. (a) Molecular structures of merocyanine dyes **2**-**5**; (b) UV-vis spectra of merocyanine dyes in 1,4-dioxane, depicting the sharpening and narrowing of the absorption spectrum upon change from polyene type electronic structure (**2**) to the cyanine limit (**5**); Reprinted from ref. [9] with permission from Wiley-VCH Verlag GmbH, Copyright 1997.

2.4.2 Aggregation Properties

The intermolecular forces distinguishing dipolar from other nonpolar molecules is the electrostatic dipole-dipole interaction. Typically, this force is considered too weak to permanently orient molecules in solution and in these cases the interaction energy can be described by the Keesom interaction. Here, the attractive forces between dipolar molecules are averaged over all possible rotational orientations and thus result in only weak interactions.[32]

On the other hand, many merocyanine dyes can easily show high dipolarities in the range of 10-15 D and thus the intermolecular forces are stronger than in the assumption for deriving the Keesom interaction. As the dipolarities afford a directional electrostatic force, it should rather be described within the dipole-dipole interaction by equation (14) as the molecules will not show a random orientation. For the normal case of linear dipolar molecules, close π-π-distances of 3.2-3.5 Å become possible and the antiparallelly stacked conformation is energetically favored over the linearly aligned parallel conformation which would be advantageous for spherically shaped molecules. In 1997, Dalton, Harper and Robinson showed experimental evidence for the failure of promising push-pull chromophores in nonlinear optic (NLO) applications which was explained by the formation of centrosymmetric dimers because of their high ground state dipole moments.[33] Experimental evidence for this thesis was given by Würthner and co-workers who could prove the existence of this centrosymmetric dimer synthons for merocyanine dyes by a combination of UV-vis spectroscopy, NMR spectroscopy and X-ray crystallography.[34]

In this regard, a series of merocyanine dyes ranging from polyene to betaine type was investigated and for all dyes the dimerization process could be described by an equilibrium between monomeric and dimeric species with a binding constant K_D for the dimerization process. The thermodynamic equilibrium can be shifted towards the dimeric species by either increasing the concentration of the molecules, or using solvents with low polarities (schematically depicted in Figure 18 for merocyanine **6** consisting of a pyridine donor and an oxopyridone acceptor moiety). Additionally, this process was monitored by the appearance of a hypsochromically shifted H-band with increasing shift of the equilibrium towards the dimeric species. As merocyanine dyes are polar molecules, monomers are usually well solvated by other polar solvents, which can orient their molecular dipole

moments antiparallel with respect to the ground state dipole moment of the merocyanine dye. For an antiparallel dimer however, both dipole moments cancel each other and thus these unpolar species are well solvated by unpolar solvents.

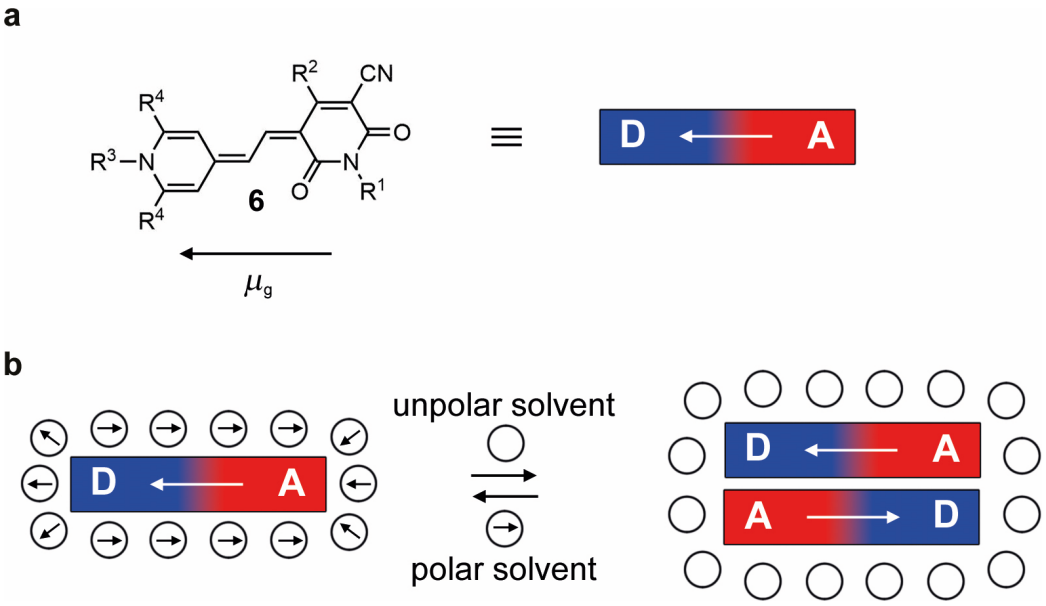

Figure 18. (a) Molecular structure of merocyanine dye **6** investigated in ref. [34] with indicated direction of the ground state dipole moment μ_g and schematic depiction of the molecules; (b) Schematic description of the self-assembly of a D−A chromophore in an unpolar solvent. Adapted from ref.[35]

In Figure 19, the study of the concentration dependent self-assembly of **6** into dimers by UV-vis absorption is shown. It can be seen that with increasing concentration of the dye, the monomer band at 569 nm is diminished and at the same time a hypsochromically shifted band at 492 nm emerges which can be assigned to an increase of amount of dimeric species in the solution. Additionally, the calculated spectra for the pure monomer and dimer, as obtained from the calculated dimerization constant and data at two different concentrations, are given.

In order to prove the self-assembly of the dyes into dimeric structures, 2D ROESY NMR studies in solution as well as X-ray crystallography were performed. By the combination of these techniques, the proposed cofacial antiparallel orientation within the dimeric species could be proven both for solution and for the solid state (see Figure 20). This arrangement of the dyes in the H-dimer is also the reason for the hypsochromic shift seen in Figure 19 which can be explained within Kasha's exciton theory.[26]

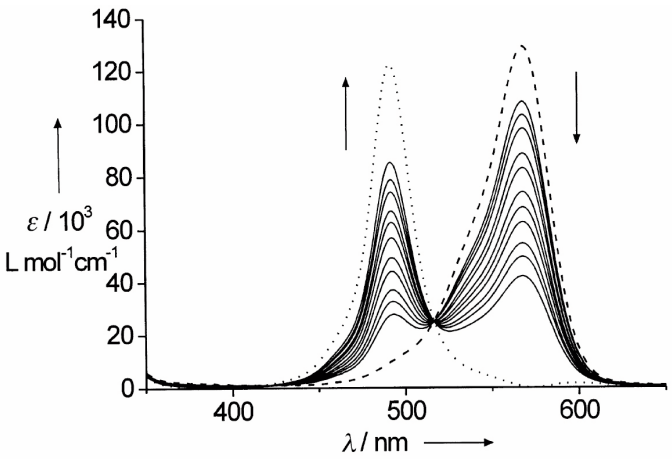

Figure 19. Concentration dependent UV-vis absorption spectra of **6** (R^1 = R^3 = *n*-hexyl, R^2 = methyl, R^4 = H) in 1,4-dioxane at room temperature for a concentration range of $1.5 \cdot 10^{-6}$ M to $3.0 \cdot 10^{-5}$ M (solid lines; the arrows indicate the increasing concentration). Additionally, the absorption spectra of pure monomer (dashed line, λ_{max} = 569 nm) and pure dimer (dotted line, λ_{max} = 492 nm) were calculated with the spectral data from two different concentrations and the calculated dimerization constant. Reprinted from ref. [34a] with permission from Wiley-VCH Verlag GmbH, Copyright 2000.

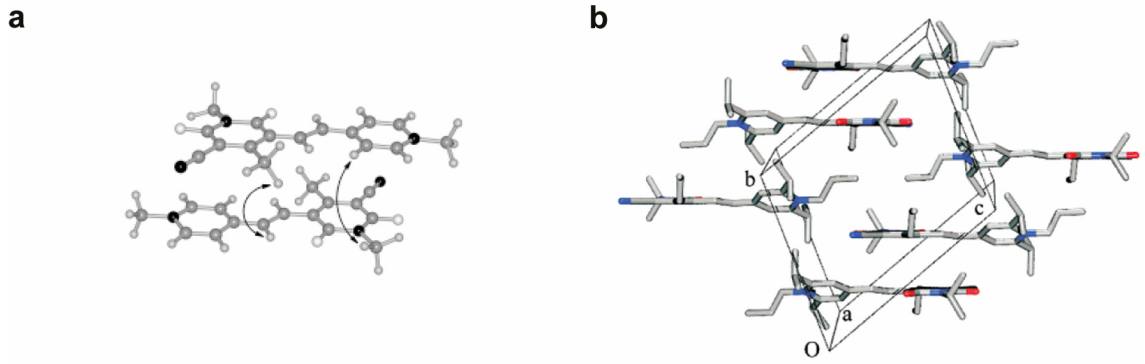

Figure 20. (a) Antiparallel arrangement of the dimeric species of **6** with simplified substituents (all alkyl chains were replaced with methyl groups) in solution based on AM1 calculations as well as 2D ROESY NMR data. Cross coupling of the protons giving ROESY signals are indicated by the black arrows. Reprinted from ref. [34a] with permission from Wiley-VCH Verlag GmbH, Copyright 2000; (b) Crystal structure of **6** (R^1 = R^3 = *i*-propyl, R^2 = R^4 = *n*-propyl) showing the antiparallel arrangement of the dyes in the solid state with close and far dimers. Reprinted from ref. [34b] with permission from the American Chemical Society, Copyright 2002.

Apart from the dimerization, self-assembly into larger H- or J-aggregates are of high interest for these dyes as these structures typically provide optical properties with even larger shifts, narrower bandwidths and in the case of J-aggregates are expected to be highly fluorescent.[36] In the case of the dipolar merocyanines, the case of H-aggregates has been studied extensively by Würthner and co-workers who could demonstrate a plethora of structurally different aggregates by tethering merocyanine dyes to different spacer groups (see Chart 1) in order to form well-defined aggregates.[37]

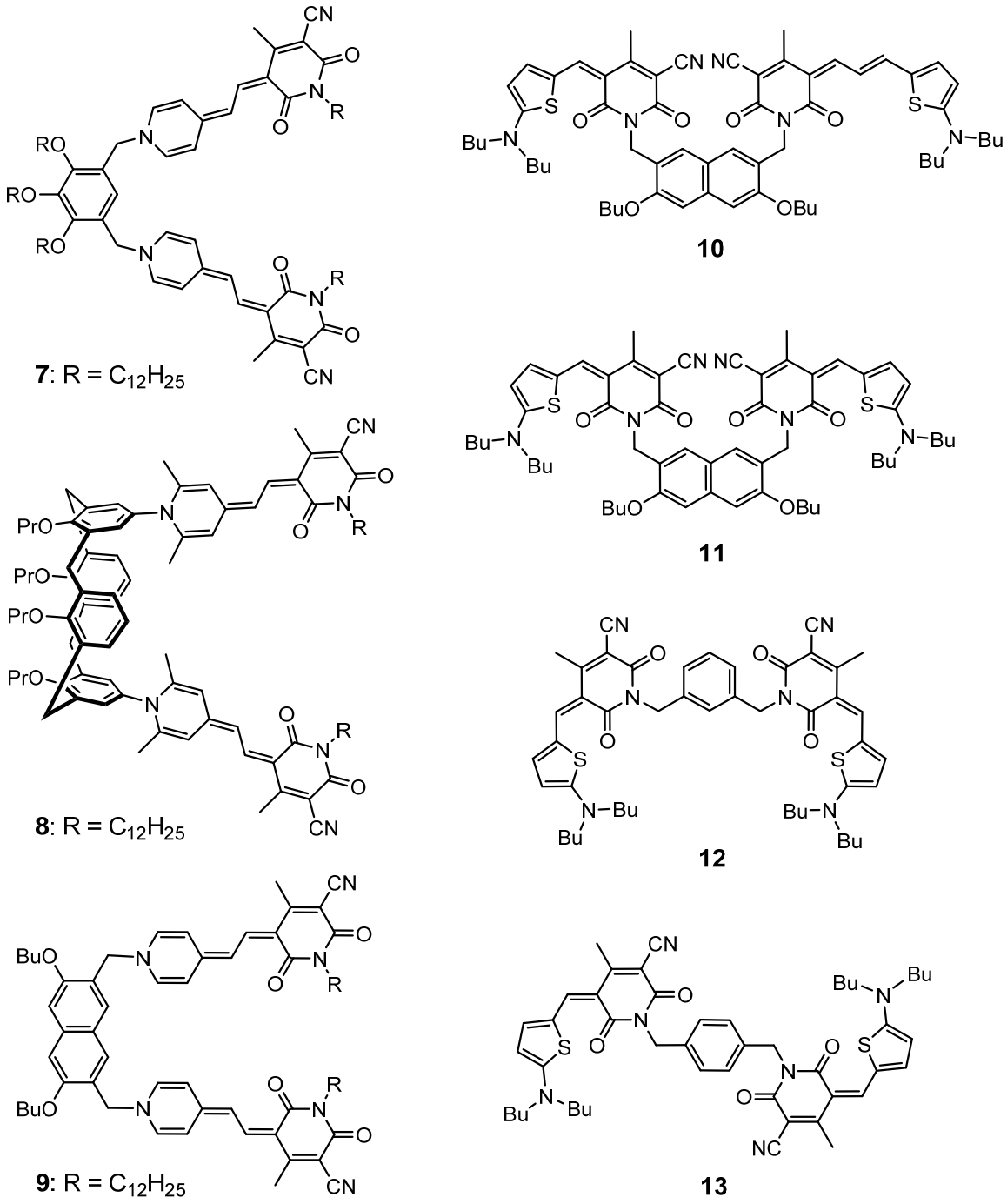

Chart 1. Bis(merocyanines) described in this section.

In this regard, the group could demonstrate the formation of a supramolecular polymer by attaching two merocyanine dyes **6** to a tris(*n*-dodecyloxy)benzyl spacer and this bis(merocyanine) **7** was shown to form oligomers in THF and aggregate even further to fibers and bundles in an unpolar solvent like MCH.[38] Attaching the same dye to a calix[4]arene spacer yielded cyclic trimers of **8** while **9**, with a naphthalene spacer moiety, assembled into discrete stacks of four merocyanine moieties.[39] While these were all

examples for homoaggregates of the same chromophores, the group recently demonstrated the aggregation of **10** into heteroaggregates (in comparison to the homoaggregate of **11**) by linking two different merocyanine dyes to a naphthalene spacer unit (see Figure 21).[40] While Kasha's exciton theory was initially developed for identical chromophores, this study could provide evidence for a strong intermolecular coupling between different dyes as in this case, the couplings for the heteropairs were of larger value than for the homo pair despite the significantly different absorption of the single dyes.

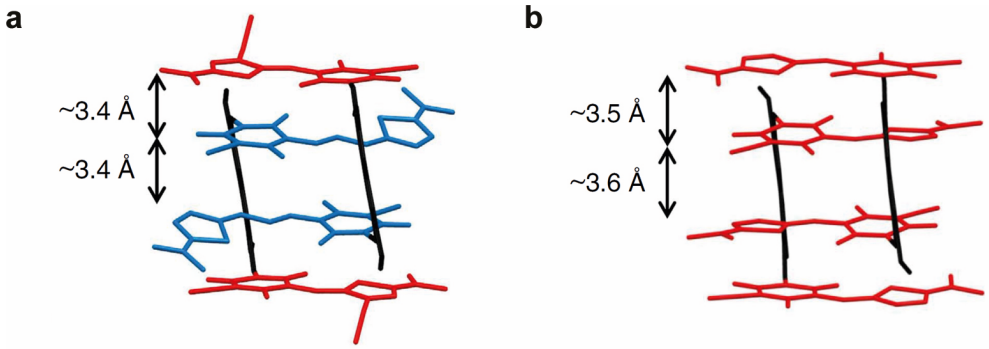

Figure 21. Crystal structures of hetero- (a) and homoaggregate (b) of bis(merocyanines) **10** and **11**. Reprinted from ref. [40] with permission from the authors, Copyright 2016.

In contrast to these supramolecular arrangements providing strong intermolecular coupling between the dyes, the Würthner group could also demonstrate the importance of the spacer unit for the (bis)merocyanines. In this regard, dye **12** assembled into the described quadruple dye stacks with H-type coupling. Due to the change from para- (**12**) to meta-substitution (**13**), dye **13** on the other hand showed an intramolecular folding process also yielding a clear H-type coupling as demonstrated by UV-vis experiments.[41] For J-aggregates, the case is rather different. For the planar merocyanines, the H-type cofacial antiparallel packing is favoured and J-type coupling was only observed under rather special experimental conditions. Indeed, the structural motif giving rise to a J-type coupling is still under discussion. J-aggregates of merocyanine dyes of discrete sizes could be prepared by the Langmuir-Blodgett (LB) technique in the presence of fatty acids.[42] Here, the merocyanines assemble on a water surface and form aggregates which exhibit a pronounced bathochromic shift of the absorption. For such aggregates of dye **14**, a brickstone molecular arrangement with a slipping angle of 30° was proposed based on the extended dipole model by the group of Kuhn in the 1970s (see Figure 22).[42c, 43]

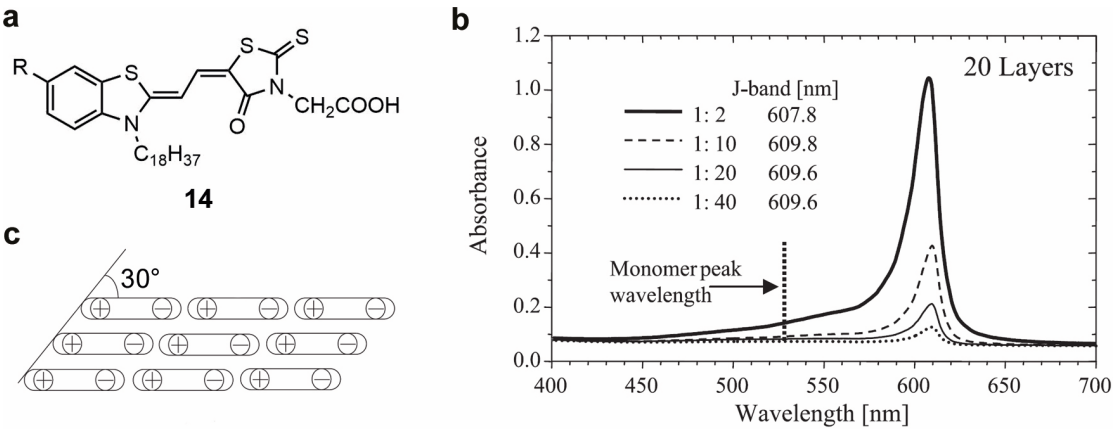

Figure 22. (a) Chemical structure of **14**; (b) Absorption spectra of a LB film of 20 layers of a mixture of merocyanine dye **14** (R = methyl) with arachidic acid from 1:2 to 1:40. Reproduced from ref. [42c] with permission from Elsevier; (c) Proposed packing model of merocyanine dyes (depicted by rods with positive and negative charge) in the LB film with a slipping angle of the rows of 30°. Reproduced from ref. [42c] with permission from Elsevier.

Another study on the J-type coupling of **14** (R = H) was presented by Ueda and Nitta, who demonstrated the appearance of a narrow J-band upon exposing a vacuum deposited thin film of **14** to dimethylamine vapour.[44] However, when annealing above 50 °C, the intensity of the J-band decreased while the intensities of monomer and dimer bands increased to give the as-deposited spectra. The J-band was then explained by a modelled arrangement of the dyes into antiparallel packing structures with large lateral slips.

Yagai and co-workers could demonstrate another J-type coupling arrangement by complexation of merocyanine dye **15** with bismelamine receptors **18**.[45] Depending on the receptor, the coupling could be controlled between H-type in a supramolecular polymer of **15** with **16** or J-type in a closed oligomer of **15** with **18** (see Figure 23).

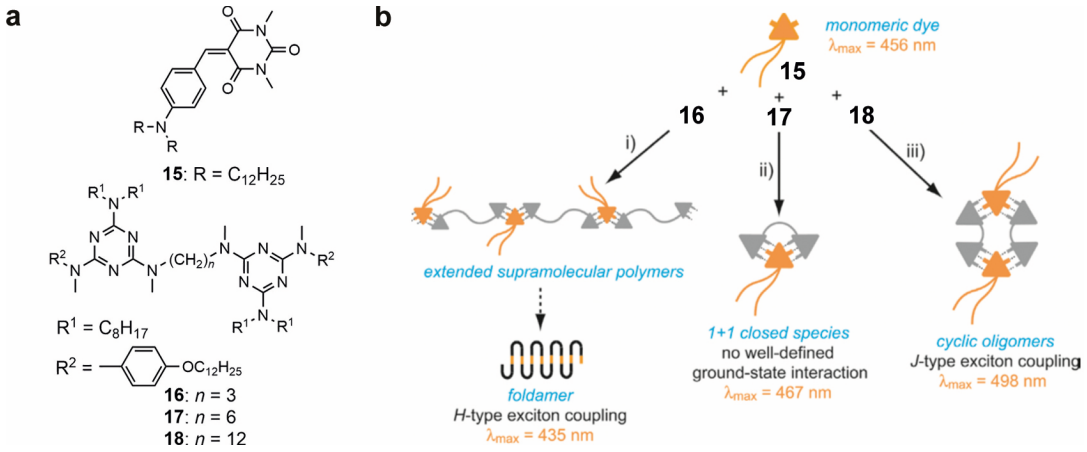

Figure 23. (a) Chemical structures of **15**-**18**; (b) Schematic depiction of complexation of **15** with **16** (i), **17** (ii) or **18** (iii) into structural motifs with different exciton coupling. Reproduced from ref. [45] with permission from The Royal Society of Chemistry.

In addition, by choosing a combination of a diarylethene receptor together with a bismelamine receptor, the coupling could be reversibly switched by irradiation from H- to J-type.[46]

2.4.3 Application in Photonics, Photovoltaics and Electronics

With advantageous properties, such as high and easily tunable absorption as well as easy accessibility, merocyanine dyes are promising candidates for various (opto-)electronic devices. In this section, the application of dipolar dyes for the fields of photonics (Chart 2), especially nonlinear optics and photorefractivity (PR), photovoltaics (Chart 3) and transistors (Chart 4) will be outlined.

Nonlinear Optics and Photorefractivity

Until the 1960s, it was strictly believed that all optical media behave linearly, i.e. the refractive index and absorption coefficient are constant, light does not change its frequency when passing through media and two beams of light in the same region of a medium do not interfere with each other. However, with the uprise of lasers, light of high intensity became accessible and thus in 1961 Franken *et al.* could demonstrate for the first time second harmonic generation (SHG) with a ruby laser.[47] This effect is today used for the SHG of a Nd:YAG Laser, which emits at 1064 nm, but the observed wavelength is modulated to 532 nm, i.e. green light.

The explanation of this effect relies on the molecular polarization p of a material as a response to an applied electromagnetic field and is described in terms of a Taylor series in equation (17). Here, p_0 is the equilibrium polarization of a molecule, E_j the vector component of the applied electric field and α_{ij} the linear polarizability. For low intensities, the description of the polarization is limited to the linear term, but for high intensities, the first and second nonlinear hyperpolarizabilities β_{ijk} and γ_{ijkl} have to be considered as well:

$$p = p_0 + \alpha_{ij}E_j + \beta_{ijk}E_jE_k + \gamma_{ijkl}E_jE_kE_l + \ldots \quad . \tag{17}$$

For molecules to show large first hyperpolarizabilities, they have to be non-centrosymmetric. Additionally, the change of dipole moment upon excitation should be high as described in equation (18) by the two-state model by Oudar and Chemla with μ_{eg} being the transition dipole moment for the optical transition from ground to excited state,

$\Delta\mu$ the change of dipole moment from ground to excited state and E_{eg} the transition energy:[48]

$$\beta \sim \frac{\mu_{eg}^2 \Delta\mu}{E_{eg}^2} \quad . \tag{18}$$

By these nonlinear interactions with an electric field, the optical properties of the material like the refractive index can be modulated by incident light. The response of such a bulk material to an applied electric field is then described by the electro-optic coefficient, which is proportional to β. Thus, in order to optimize the first hyperpolarizability, the first molecules were designed with aromatic π-systems and electron donating and withdrawing groups to induce the push-pull character, e.g. 4-(*N*,*N*-dimethylamino)-4'-nitrostilbene (**19**) and disperse red (**20**) derivatives. In the early 1990s, Marder and co-workers proposed a model on how to design good push-pull chromophores by an investigation of hyperpolarizabilities in solvents of different polarities in combination with theoretical calculations. With the solvent polarity changing the electronic distribution and molecular geometry for several merocyanines, the bond length alternation could be tuned and it was shown that for a *BLA* of around 0.04, β shows an optimum value in calculations. Thus, by the choice of the right donor and acceptor moieties, chromophores with suitable *BLA* values were designed and consequently showed large β values of around $7.42 \cdot 10^{-48}$ C^3 m^3 J^{-2}, which were obtained by electric field induced second harmonic generation measurements for acceptors of 3-phenyl-5-isoxazolone and thiobarbituric acid derivatives (e.g. **21**, **22** and **23**).[49] Unfortunately, in most of the cases, the large molecular hyperpolarizabilities were not reflected in high responses of bulk materials. Here, also a non-centrosymmetric ordering of the molecules is essential and to realize this, the push-pull chromophores were typically diluted in polymers and aligned by an electric field to give so-called "poled polymers". Unluckily, the electro-optic coefficient for materials obtained by this technique was not as high as expected for high densities of loaded chromophores in the polymer (see Figure 24). Essentially, this was caused by dipole-dipole interactions which aligned the chromophores and yielded centrosymmetric bulk materials, thus showing much smaller nonlinear effects than expected and demonstrating that the electro-optic coefficient is not only dependent on β, but also on the chromophore density and their ordering.[33]

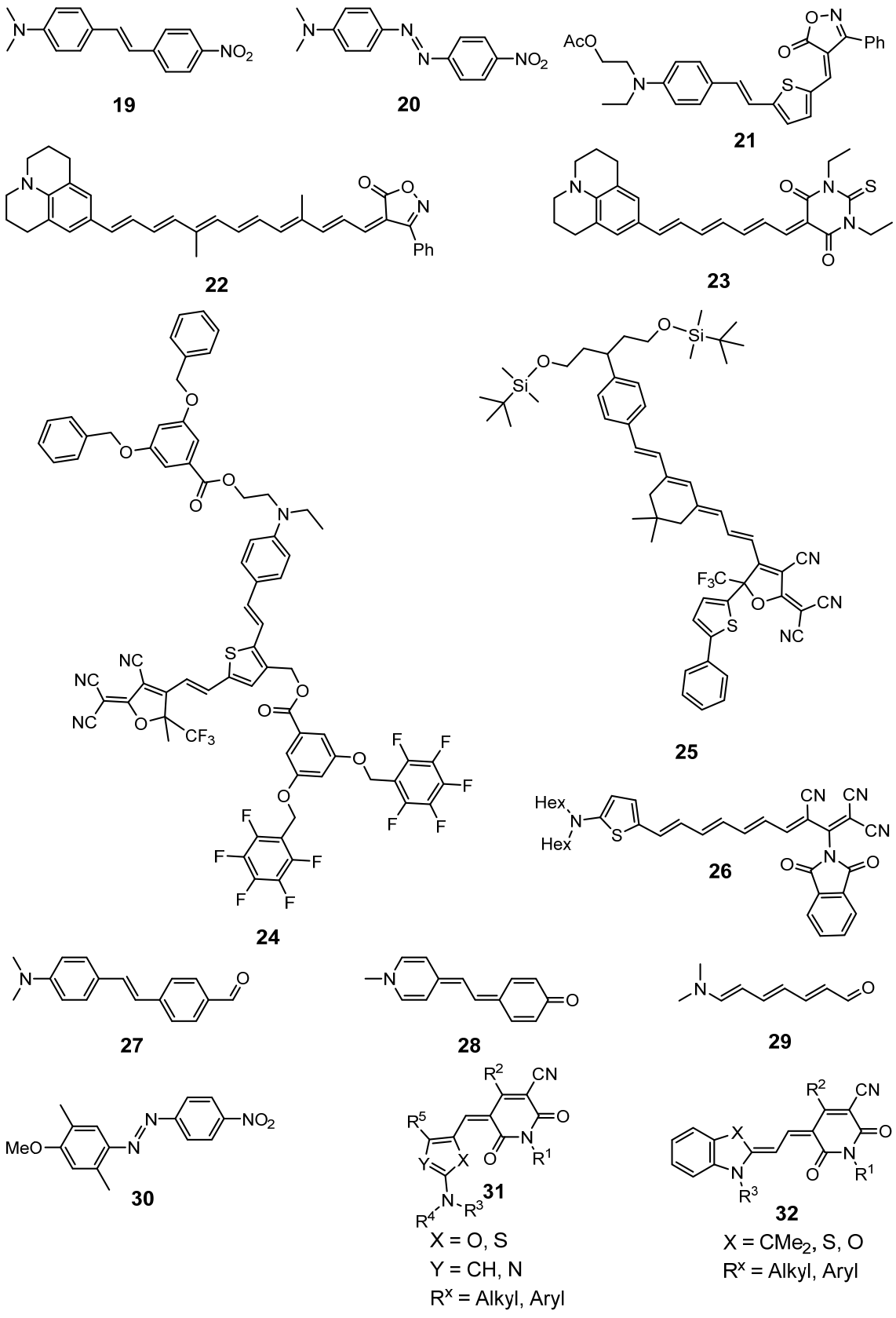

Chart 2. Molecules described in the section on NLO and PR chromophores.

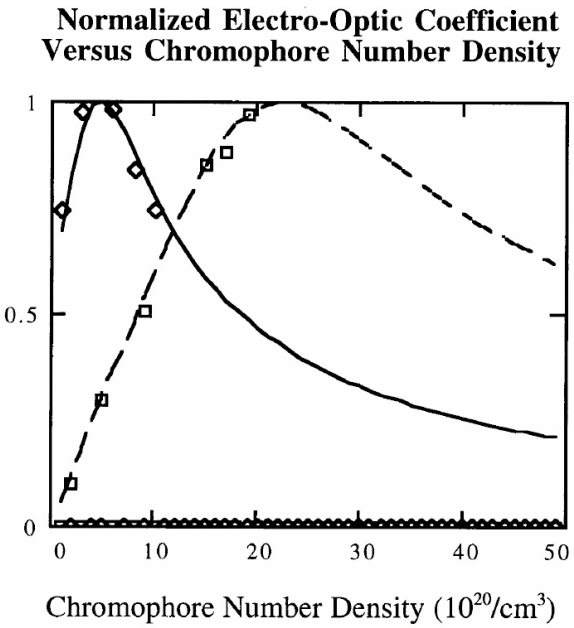

Figure 24. Normalized electro-optic coefficient as a function of the chromophore number density for experimental values of chromophores **20** (diamonds) and **21** (squares) as well as theoretical calculations (solid and dashed lines). Reprinted from ref. [33] with permission from the National Academy of Sciences, Copyright 1997.

Consequently, the groups of Jen, Dalton and Robinson started to synthesize dendronized chromophores which are less prone to aggregation due to their sterics. With this approach, these groups could demonstrate macroscopic electro-optic coefficients of up to 327 pm V^{-1} for a blend of their chromophores **24** and **25** which is much larger than for the inorganic reference material $LiNbO_3$ of 30 pm V^{-1}.[50] An alternative idea came by the groups of Marks and Ratner, who could show in 1998 that by twisting the donor and acceptor moieties with respect to each other, high quadratic hyperpolarizabilities of up to $8.91 \cdot 10^{-48}$ C^3 m^3 J^{-2} can be obtained as demonstrated by a series of intermolecularly twisted merocyanines and quinopyrans.[51]

Quite recently, also the *BLA* paradigm was questioned, when the groups of Blanchard-Desce, Das and Würthner could measure large hyperpolarizabilities up to $3.49 \cdot 10^{-47}$ C^3 m^3 J^{-2} by hyper Rayleigh scattering measurements for a series of merocyanine dyes with structures close to the cyanine limit (with the best performing dye **26**).[52] With this and recent results demonstrating nonlinear optical phenomena of even single molecules,[53] several new possibilities are expected to be explored within the next years.

Turning the focus onto photorefractive applications, the materials not only need to show an electro-optic response, but also photoconductivity. Here, the intersection of two

coherent laser beams causes an interference pattern within a material, leading to a non-uniform intensity distribution. Consequently, free excess charges are generated in high intensity regions which then redistribute to regions with no charges and thus generate a non-uniform space charge field within the material. This causes an electro-optic effect in the material and ultimately leads to a modulation of the refractive index, which contains the information on the interference pattern of the laser. Here, also poled polymers as described above are typically used and hence it was believed that the design criteria derived above apply again as the hyperpolarizability should be the important parameter. However, for some polymers, i.e. with glass temperatures close to room temperature, the dispersed dipolar molecules can reorient and yield an additional contribution to the refractive index modulation.[54] For this case, also the anisotropy of the linear polarizability $\delta\alpha_{ij}$ should be taken into account which is defined as difference of the polarizability along the long axis to the short axes while the important parameter is a product of the square of the ground state dipole moment and the anisotropy of the linear polarizability $\mu_g^2\delta\alpha_{ij}$. Unluckily, α_{ij} and β_{ijk} cannot be optimized simultaneously as α_{ij} is maximized for high transition dipole moments which usually occur for molecules in the cyanine limit ($c^2 = 0.5$), where β_{ijk} is zero as shown by calculations of Gorman and Marder for merocyanine dyes **27**, **28** and **29** (see Figure 25).[49a]

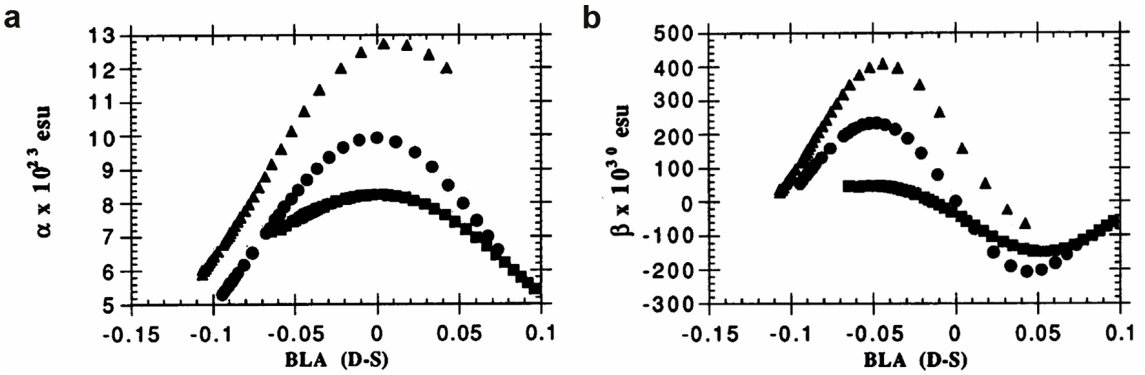

Figure 25. Calculated linear polarizability defined as $\alpha = (\alpha_{xx} + \alpha_{yy} + \alpha_{zz})/3$ (a) and first hyperpolarizability β_{xxx} along the long molecular axis (b) as function of the *BLA* for **27** (squares), **28** (circles) and **29** (triangles). Reproduced from ref. [49a] with permission from the National Academy of Sciences, Copyright 1993.

Until this was realized, materials with high β values were used for PR applications, such as 2,5-dimethyl-4-(*p*-nitrophenylazo)anisole **30**, which was successfully applied in a blend with a carbazole photoconductor and a 2,4,7-trinitro-9-fluorenone sensitizer.[54b] However, Würthner *et al.* could show that the contribution of $\delta\alpha_{ij}$ seemed to be much

larger and thus high performing molecules were expected to be at the cyanine limit, while the best NLO chromophores were of polyene type.[9] Accordingly, it was found for a series of merocyanine dyes, that materials have to be designed specifically for low glass transition temperatures as the linear polarizability and first hyperpolarizability could not both be optimized at the same time.[55] Also, high dye loadings of the polymers were needed for a good photorefractive effect and in this regard, molecules with an oxopyridone acceptor in combination with either an aminothiophene (**31**) or an indoline moiety (**32**) showed promising properties due to higher solubilities without aggregation tendency.[56] While the research focus was on the molecular properties, the influence of the surrounding on the photorefractive properties was neglected. Thus, in 2006 the groups of Abbotto and Wortmann published a study on how the surrounding polarity affects the molecular properties and could demonstrate that the polarity can change the photorefractive response by up to two orders of magnitude.[57] These results lead to the conclusion that by a proper choice of the host polymer, the photorefractive response can be influenced significantly.

Photovoltaics

As the sunlight is the energy source with the largest energy capacity, the idea of turning sunlight into electrical power energy dates back to the discovery of the photovoltaic effect by Becquerel in 1839.[58] Within this approach, the figure-of-merit of solar cells is the power conversion efficiency *PCE* which is defined by the ratio of the maximum producible electrical power P_{max} to the incident light power P_{light} as described in equation (19). Here, the generated maximum electrical energy can be described as the product of three factors: The open circuit voltage V_{OC}, at which no current is flowing, the short-circuit current density J_{SC} for a voltage of $V = 0$ and the fill factor *FF*, which describes the ratio between the maximum generated power of the solar cell and the product of V_{OC} and J_{SC}:

$$PCE = \frac{P_{max}}{P_{light}} = \frac{V_{OC}\, J_{SC}\, FF}{P_{light}} \,. \qquad (19)$$

For organic solar cells, dipolar merocyanine dyes were among the first candidates to be tested for application due to their high molar extinction coefficients. In 1978, a Schottky diode with a layer of dye **33** between Al|Al_2O_3 and Ag electrodes was reported by Morel *et al.* and reached *PCE*s up to 0.70 %.[10c] In the later years, also solar cells based on merocyanine **34** could be fabricated with similar power conversion efficiencies, e.g. by Kudo and Moriizumi.[10a] However, these devices were either only one component solar

cells or in a planar heterojunction geometry, meaning that there was no effective exciton dissociation due to a low external driving force. Thus, the *PCE*s remained low although being remarkable for such device structures at that time. The real breakthroughs of organic photovoltaics occurred in 1986 with the first planar heterojunction (PHJ) device by Tang[59] and in 1995 with the introduction of the bulk heterojunction (BHJ) concept by the group of Heeger.[60] Regarding the usage of merocyanine dyes, the Gaussian disorder model described in section 2.2, which states that molecules with high ground state dipole moments should not be suitable for high mobility applications, had the consequence that dipolar compounds were neglected for small molecule photovoltaics in the following years. However, taking into consideration the previously described tendency of dipolar dyes to form centrosymmetric dimers,[15] merocyanines and other dipolar D−A compounds were again considered for organic photovoltaics.

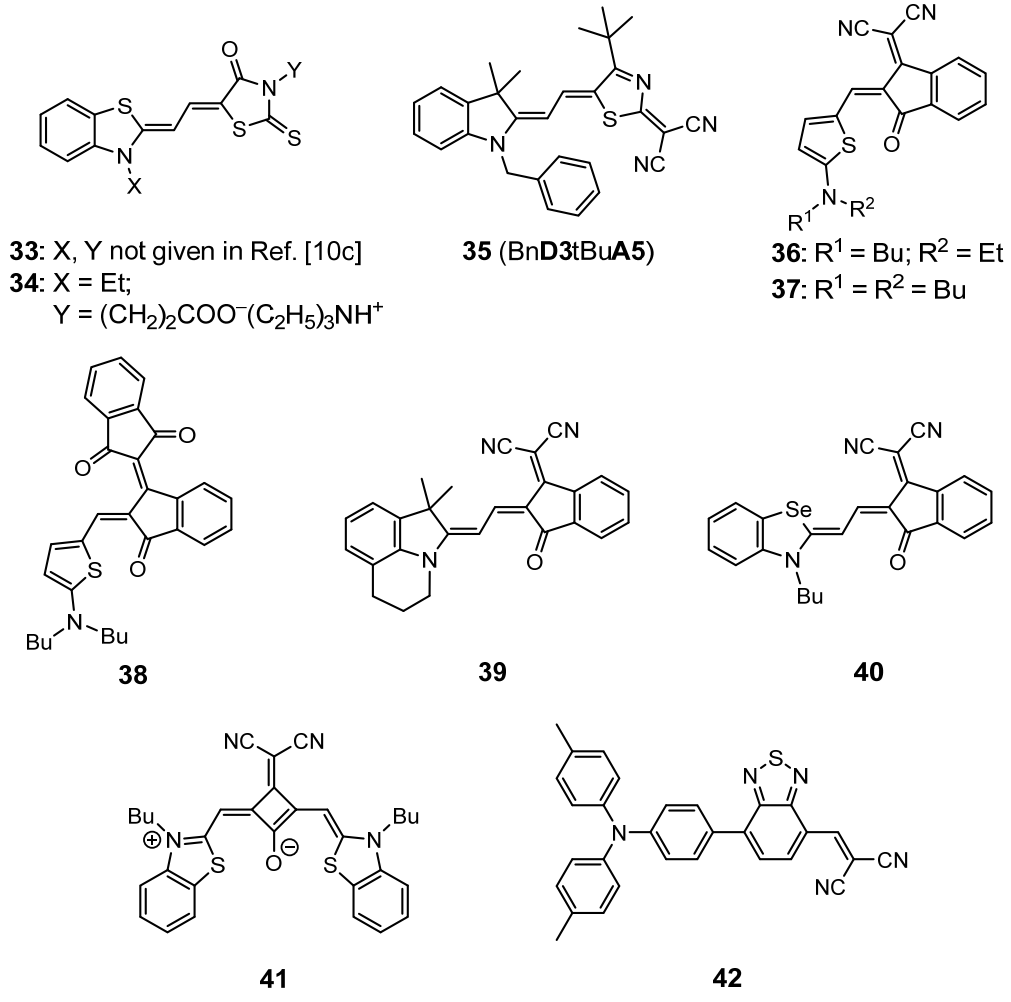

Chart 3. Molecules described in the section on organic solar cells.

In 2008, two series of merocyanine-based solution processed BHJ solar cells with $PC_{61}BM$ as acceptor material were published by the groups of Würthner and Meerholz. With a maximum *PCE* of 1.7 % for solar cells with dye **35** as donor material, this was the highest reported *PCE* for solution processed BHJ solar cell based on small molecules at that time (device architecture: ITO|PEDOT:PSS|**35**:$PC_{61}BM$|Al, with ITO being indium tin oxide and PEDOT:PSS being Poly(3,4-ethylenedioxythiophene):polystyrene sulfonate; note that for a consequent numeration of the dyes, dye **35** will in the following chapters be referred to as Bn**D3**tBu**A5**).[13] Moreover, in 2011, the groups could publish an extended series of dyes bearing an aminothiophene donor unit combined with seven different acceptor moieties.[61] It could be shown that an increasing acceptor strength yields a shift of the absorption towards the NIR region and also a downward shift of the LUMO level. Hence, by successful modification of these parameters by molecular structure, the indandione-malononitrile acceptor unit yielded the best *PCE* of this series (3.0 %) in solution processed BHJ cells for dye **36** (ITO|PEDOT:PSS|**36**:$PC_{61}BM$|Al). Additionally, this value could be further increased up to 4.5 % with an optimized device structure of ITO|MoO_3|**36**:$PC_{71}BM$|Ba|Ag.[61] By the examination of single crystal structures of a well performing dye **37** (*PCE* = 2.3 %) and bad performing dye **38** (*PCE* = 1.0 %) in same device architectures as for **36**, the authors could demonstrate the importance of a close solid state packing of the dyes (see Figure 26). While for both dyes, an antiparallel arrangement with two unequal neighbors is revealed in the respective single crystal structure, only dye **37** showed close packing to both neighbors while for dye **38** this is prohibited by the sterics of the bis-indandione acceptor.

In the same year, these groups could demonstrate an impressive *PCE* of 5.8 % for vacuum processed solar cells containing merocyanine dye **39** with indandione-malononitrile acceptor in combination with an indolenine donor unit (ITO|MoO_3|**39**:C_{60}|BPhen|Ag; BPhen stands for Bathophenanthroline).[62] Compared to an earlier study on the molecule,[63] a change of the device architecture from PEDOT:PSS to MoO_3 as hole transport layer yielded an increase of the average *PCE* from 4.9 % up to 5.8 % with a maximum of one cell at 6.1 %. Moreover, in light intensity dependent measurements, the performance remained stable for intensities down to 10 mW cm^{-2} with *PCE* values around 6.0 %. Lately, the effect of implementation of selenium as heteroatom into another indolenine donor unit derivative was studied and *PCE*s of up to 6.2 % could be achieved for vacuum processed solar cells with merocyanine dye **40**

(ITO|MoO_3|**40**|**40**:C_{60}|C_{60}|BPhen|Ag). In these cells, the bulk heterojunction layer was sandwiched between the neat films of the donor and acceptor components (typically called planar mixed heterojunction, PMHJ).[64]

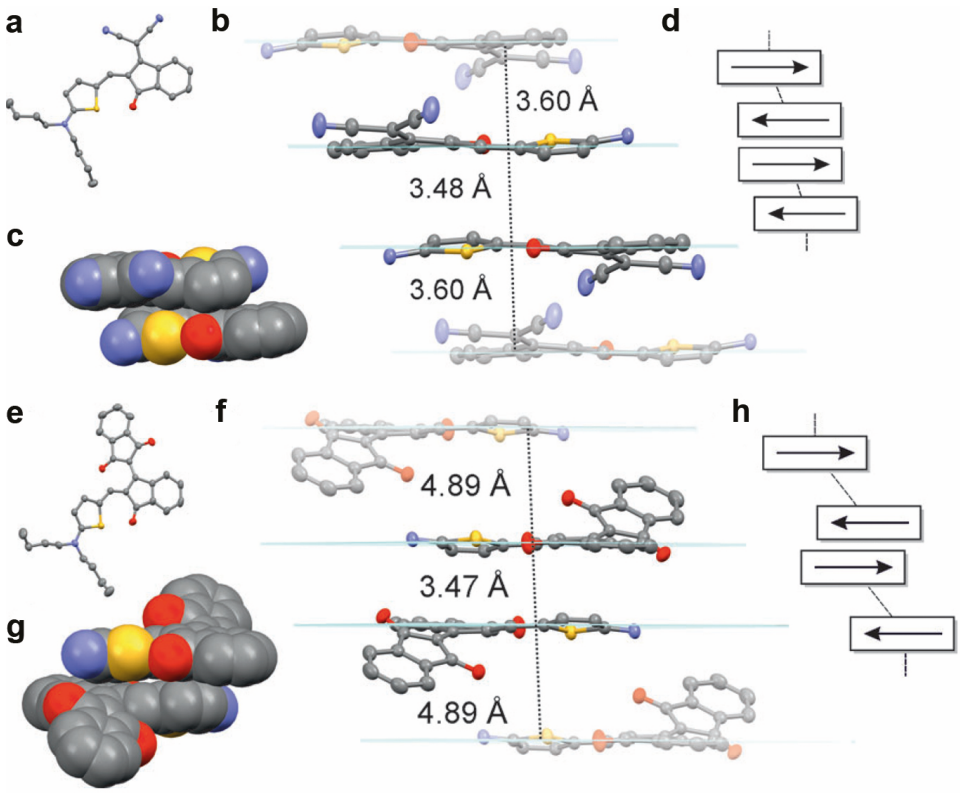

Figure 26. Packing of merocyanine dyes **37** (a-d) and **38** (e-h) in the single crystal structure with molecular structure (a,e), closely cofacially stacked dimers (b,f), spacefill representation of the closest dimer (c,g) and a schematic of the packing (d,h). Reprinted from ref. [61] with permission from Wiley-VCH Verlag GmbH & Co. KGaA, Copyright 2011.

As merocyanine dyes showed promising *PCE*s for photovoltaic applications, other dipolar D−A compounds have been studied as well, such as dyes based on triphenylamine or squaraines with *PCE*s mostly ranging from 2-5 %.[65] For these dyes, the efficiencies remained modest compared to the current best performing small molecule solar cells, but the propensity for organic solar cells was demonstrated by remarkable open circuit voltages V_{OC} above 1 V and, in the case of the squaraines, also high short circuit currents up to 12 mA cm^{-2} for compound **41**.[66] In 2012, the groups of Wong and Darling could demonstrate *PCE*s of 6.8 % for compound **42** in a PMHJ device architecture ITO|MoO_3|**42**|**42**:C_{70}|C_{70}|Bathocuproine|Ag.[67] By carefully designing the triaryl donor moiety in combination with their previously used 2,13-benzothiadiazole and dicyanovinylene group in a D–A–A type structure,[68] the group was able to find a fine balance between devices with high J_{SC} and high V_{OC}, finally yielding a device with the at

that time highest reported *PCE* for dipolar compounds. By further optimization, the groups of Thompson, Green and Forrest could show average *PCE*s of 9.6 % for compound **42** in a device architecture ITO|MoO_3|**42**:C_{70}|BPhen:C_{60}|BPhen|Ag in 2015.[69]

Thin Film Transistors

Owing to the remarkable efficiencies of merocyanine single component solar cells in the 1970s and 80s, Kudo & co-workers started to investigate the propensity of merocyanines for application in OTFTs. They could show in a study with three merocyanine dyes in 1984 that these dyes showed hole transport in a transistor device on Si/SiO_2 substrates. However, only poor mobilities with a maximum of $1.5 \cdot 10^{-5}$ cm^2 V^{-1} s^{-1} for **43** could be obtained which was attributed to the formation of deep traps in the devices.[10b] As in the case of solar cells, D−A type molecules were overlooked during the rapid development of new organic semiconductors in the 1990s and 2000s with mobilities approaching and finally exceeding the benchmark of 1 cm^2 V^{-1} s^{-1} of amorphous silicon.[6b]

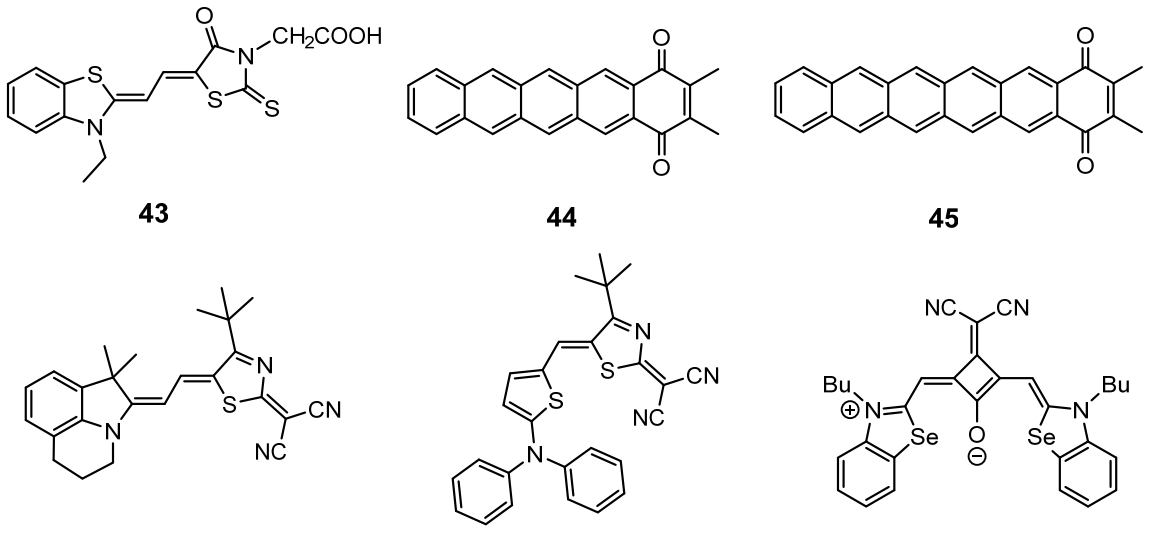

43 **44** **45**

46 (bPr**D3**tBu**A5**) **47** (Ph**D5**tBu**A5**) **48**

Chart 4. Molecules described in the section for OTFT applications.

In 2005, the group of Nuckolls in cooperation with Bell Laboratories fabricated OTFTs of pentacene and hexacene both end-functionalized with a 1,4-quinone moiety (**44** and **45**).[70] By this modification, they could demonstrate for the first time a stable hexacene derivative with a field-effect mobility of 0.05 cm^2 V^{-1} s^{-1}. Close interplanar distances of 3.25 Å in single crystals were attributed to the attractive electrostatic forces due to the molecules' dipolar character. Next, in 2012 a new improvement in terms of mobility

values could be demonstrated when Würthner and co-workers could show the application of a merocyanine dye **46** in OTFTs with reasonable hole mobilities of 0.18 $cm^2\ V^{-1}\ s^{-1}$ on $Si/SiO_2/AlO_x$/*n*-tetradecylphosphonic acid (TPA) substrates (like in the case of dye **35**, dye **46** is in the next chapters referred to as bPr**D5**tBu**A5**).[14] Similar to the results of Kudo and co-workers, devices on Si/SiO_2 showed only low mobility values which could be ascribed to the formation of amorphous thin films which were in contrast to the highly crystalline films of the devices on $Si/SiO_2/AlO_x$/TPA substrates (see Figure 27).

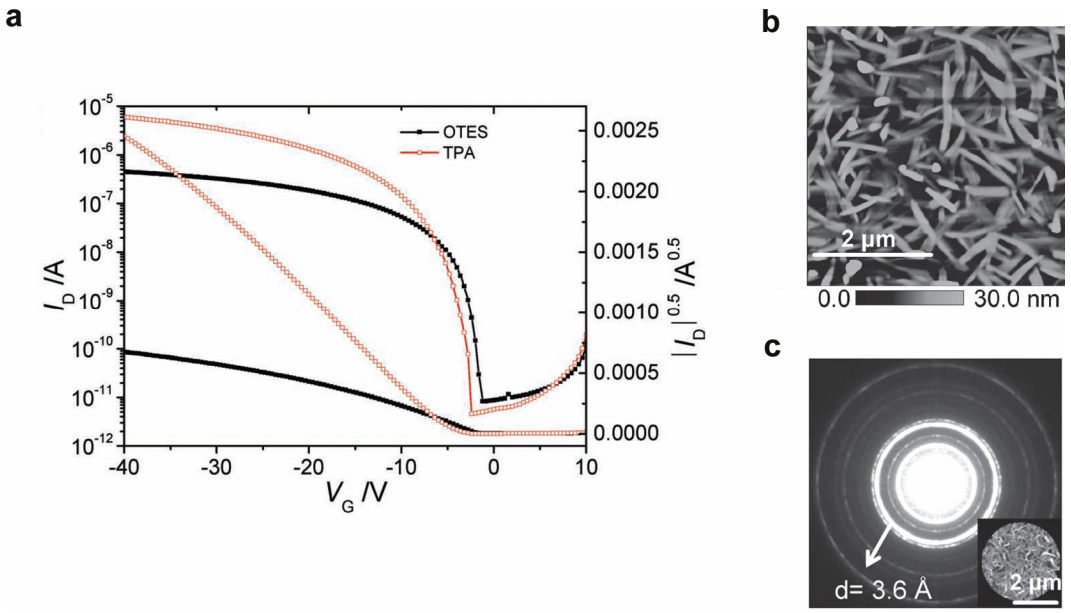

Figure 27. (a) Transfer curves of OTFTs of dye **46** on octadecyltriethoxysilane modified Si/SiO_2 substrate as well as on TPA modified Si/SiO_2 substrate; (b) AFM image of 30 nm thin film of **46** on TPA modified Si/SiO_2 substrate; (c) SAED measurement of 30 nm thin film of **46**. Reproduced from ref. [14] with permission from WILEY-VCH Verlag GmbH & Co. KGaA, Copyright 2012.

In 2015, an even higher value of 0.64 $cm^2\ V^{-1}\ s^{-1}$ could be demonstrated by Würthner and co-workers for OTFTs of merocyanine dye **47** in the same device architecture $Si/SiO_2/AlO_x$/TPA (dye **47** is in the next chapters referred to as Ph**D5**tBu**A5**).[71] It is also noteworthy that for the dipolar unsymmetrical squaraine dye **48**, Würthner and co-workers could achieve a hole mobility value of 1.3 $cm^2\ V^{-1}\ s^{-1}$ on TPA modified substrates.[72]

Conclusion

As described in this chapter, merocyanine dyes already proved to be useful organic materials for many solid state applications, including OTFTs, despite their high ground state dipole moments. In the field of organic transistors, there was no comprehensive study available on how the packing structure influences the device properties as no crystal structure for the described transistor devices was available. Instead, only a proposed arrangement based on thin film UV-vis absorption exhibiting a spectral shift and diffraction measurements of thin films was suggested by Würthner and co-workers in 2012.[14] Furthermore, it also remained unclear if mobilities beyond the benchmark of 1 $cm^2 V^{-1} s^{-1}$ are achievable for this class of dyes. Additionally, the assembly of such molecules into J-type structures has only been demonstrated for rather special experimental conditions and no guideline in terms of a crystal engineering approach to generate such structures was available. These issues are addressed in the following chapter of this thesis.

Chapter 3

-

Results and Discussion

3.1 Charge Transport Properties of Dipolar Merocyanine Dyes in OTFTs*

In this chapter, the charge transport properties of merocyanine dyes are investigated by application in OTFTs. It is shown that the potential of merocyanines to act as hole semiconductors in thin films strongly depends on the crystal structure. The results are explained by an investigation on twenty molecules with various donor (**D1-D4**) and acceptor heterocycles (**A1-A5**, see Chart 5 and list of substances at the end of the thesis). First, the molecular properties of the dyes are given by means of investigations of UV-vis absorption, electro-optical absorption measurements (EOAM) and cyclic voltammetry (CV). Afterwards, the results on OTFT devices are outlined where the dyes are shown to separate into two groups, showing either bad ($\mu < 10^{-3}$ cm^2 V^{-1} s^{-1}) or good performance ($\mu > 10^{-3}$ cm^2 V^{-1} s^{-1}) under ambient conditions. These differences are then explained to result from different single crystal structures as well as thin film morphologies, measured by atomic force microscopy (AFM), X-ray diffraction (XRD) as well as selected area electron diffraction (SAED). Lastly, a comparison to the disorder charge transport theory is given and a growth mode of the dyes could be established by density functional theory (DFT) calculations.

* This chapter has been published in A. Liess, L. Huang, A. Arjona-Esteban, A. Lv, M. Gsänger, V. Stepanenko, M. Stolte, F. Würthner, *Adv. Funct. Mater.* **2015**, *25*, 44-57. Reproduced with permission from WILEY-VCH Verlag GmbH & Co. KGaA, Copyright 2014.
Synthesis and characterization of molecular properties were done by Dr. Alhama Arjona Esteban, Dr. Hannah Bürckstümmer and Dr. Elena Tulyakova. OTFTs were fabricated in a joint project with Dr. Lizhen Huang and Dr. Aifeng Lv. Single crystal X-ray and XRD measurements were performed by Dr. Marcel Gsänger, Dr. Lizhen Huang as well as Dr. Ebru Duman and Dr. Christian Lehmann (Max-Planck-Institut für Kohlenforschung, Mühlheim). AFM, TEM and SAED measurements were performed by Dr. Lizhen Huang and Dr. Vladimir Stepanenko and electro-optical measurements were done by Dr. Matthias Stolte. The calculation of electrostatic potentials was performed by Dr. Alhama Arjona Esteban.

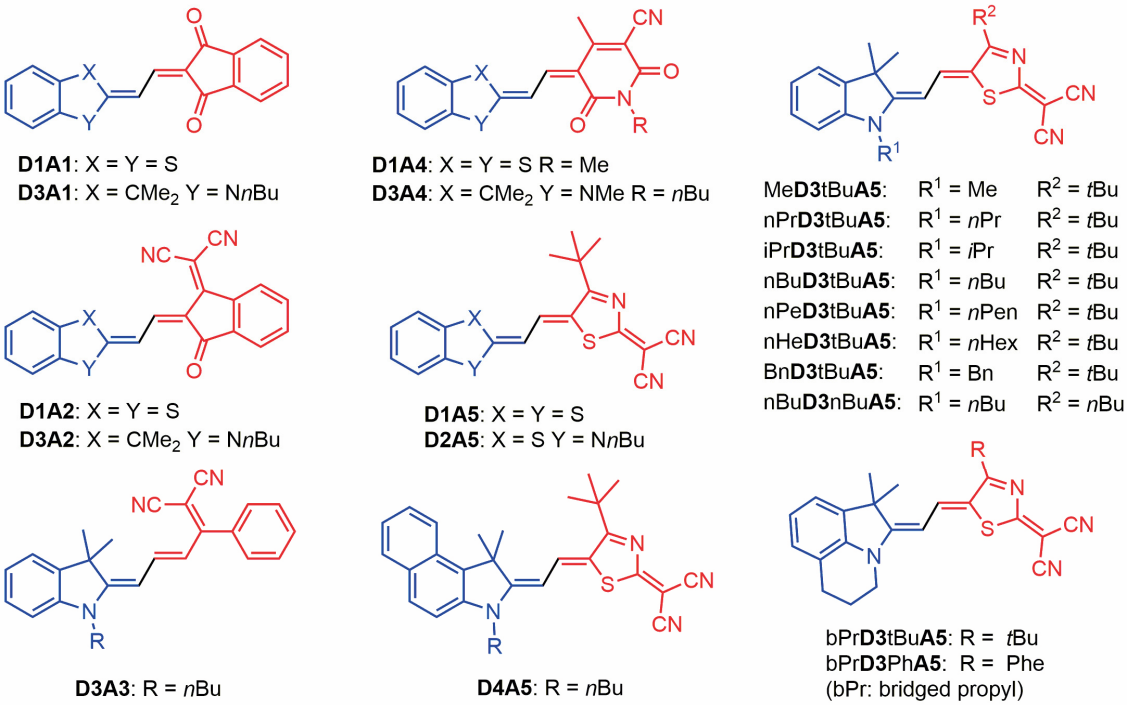

Chart 5. Chemical structures of merocyanine dyes investigated in this chapter with the donor part colored in blue and the acceptor part colored in red.

3.1.1 Molecular Properties

The molecular properties that are of interest for applications of these dyes in organic electronics are collected in Table 1. These properties include the absorption maxima λ_{max} and absorption coefficients ε_{max} that were derived from UV-vis spectroscopy as well as the oxidation and reduction potentials $E_{1/2}$ that were obtained from CV.

In general, all of these D−A dyes show intense absorption bands (ε_{max} > 50000 L mol^{-1} cm^{-1}) in the visible range of light (Figure 28). The comparison of the various acceptors reveals that the 2-(4-alkylthiazol-2(3H)-ylidene)malononitrile acceptor (dyes with acceptor **A5**) leads to the most bathochromically shifted absorption bands (λ_{max} > 600 nm), followed by 2-(3-oxo-2,3-dihydro-1H-inden-1-ylidene)malononitrile (**D1A2**, **D3A2**), 1,4-dialkyl-3-cyano-6-hydroxy-2-pyridone (**D1A4**, **D3A4**), 2-benzylidenemalononitrile (**D3A3**) and 1,3-indandione (**D1A1**, **D3A1**). Accordingly, there is a quite good correlation between the optical band gap (inversely correlated to λ_{max}) and the number of methine units between the nitrogen or sulfur donor atoms and the carbonyl or cyano acceptor groups which range from four (**D1A1**, **D3A1**) to eight (dyes with acceptor **A5**).

Table 1. (Electro-)optical and electrochemical properties of merocyanine dyes[a] determined by UV-vis[b] and electro-optical absorption spectroscopy[c] as well as cyclic voltammetry[d].

	λ_{max}[b] / nm	ε_{max}[b] / L mol^{-1} cm^{-1}	μ_g[c] / D	$\Delta\mu$[c] / D	c^2 / 1	$E_{1/2,Ox}$[d] / V	$E_{1/2,Red}$[d] / V
D1A1	517	62200	2.8	9.2	0.27	0.79[e]	–1.51
D3A1	496[73]	114600[73]	3.8[73]	3.8	0.40	0.61[e],[73]	–1.94[73]
D1A2	595	61900	3.9	8.9	0.26	0.84[e]	–1.19[e]
D3A2	576[74]	66400[74]	6.2	4.2	0.40	0.65[74]	–1.52[74]
D3A3	533	99700	9.4	7.9	0.32	0.42[e]	–1.76
D1A4	572	67400	10.0	8.2	0.30	0.82[e]	–1.23[e]
D3A4	520[9]	118000[9]	12.8[9]	1.9[9]	0.45[75]	0.68	–1.71[e]
D1A5	609 663[f]	57000 34100[f]	11.7	10.3	0.27	0.58	–1.08[e]
D2A5	631	120000	15.0	–0.3	0.51	0.39[e]	–1.45[e]
Me**D3**tBu**A5**	622	124700	-	-	-	0.40	–1.42
nPr**D3**tBu**A5**	624	131200	-	-	-	0.42	–1.43
iPr**D3**tBu**A5**	624	131000	-	-	-	0.43	–1.43
nBu**D3**tBu**A5**	624[73]	128500	13.3[73]	1.8	0.46	0.43[73]	–1.42[73]
nPe**D3**tBu**A5**	624	131800	-	-	-	0.43	–1.42
nHe**D3**tBu**A5**	624[76]	132500[76]	13.0[76]	1.8[76]	0.46[76]	0.44[76]	–1.43[76]
Bn**D3**tBu**A5**	625	112500	12.5	2.7	0.44	0.46	–1.40
nBu**D3**nBu**A5**	618[77]	137100[77]	-	-	-	0.47	–1.47[e]
bPr**D3**tBu**A5**	627[14]	146100[14]	13.6[14]	1.2[14]	0.47	0.38[14]	–1.46[14]
bPr**D3**Ph**A5**	635	123200	-	-	-	0.42	–1.38[e]
D4A5	640	65600	13.7	1.8	0.44	0.41	–1.41

[a] Due to similar optical as well as electrochemical properties of dyes **D3A5**, EOAM were not performed for dyes Me**D3**tBu**A5**, nPr**D3**tBu**A5**, iPr**D3**tBu**A5**, nPe**D3**tBu**A5**, nBu**D3**nBu**A5** and bPr**D3**Ph**A5**; [b] UV-vis: CH_2Cl_2, ~10^{-5} M, 298 K; [c] EOAM: 1,4-dioxane, ~10^{-6} M, 298 K, corrected to give "gas phase" dipole moments by Onsager cavity field correction;[78] [d] CV: CH_2Cl_2, ~10^{-4} M, 298 K, TBAHFP as electrolyte and with reference Fc/Fc^+; [e] Peak potential of irreversible redox process; [f] Values obtained for the long-wave shoulder of the spectrum (see Figure 28) by fitting the spectrum with Gaussians.

In contrast to these pronounced effects by the acceptor units, the influence of the donor methylene base on the absorption properties is more subtle. In general, the λ_{max} values show smaller variations, e.g. 631 nm, 625 nm and 609 nm for **D2A5**, **D3A5**, and **D1A5**, respectively, whilst the band shapes are different (Figure 28), leading to pronounced

variations in the ε_{max} values which accordingly do not reflect the tinctorial strength of the dyes but the broadness of the absorption band.

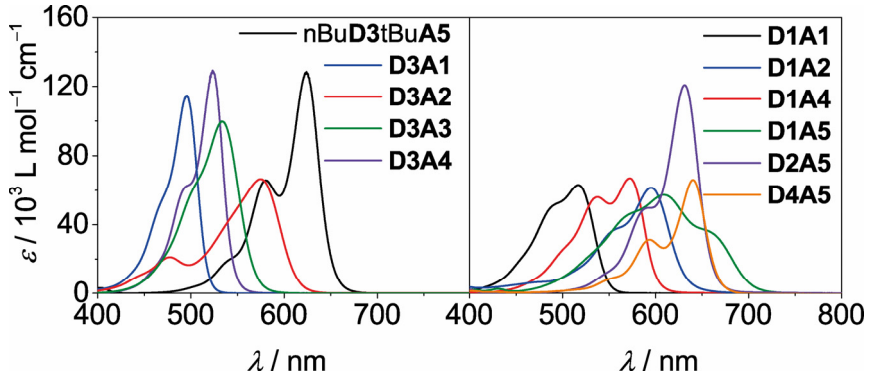

Figure 28. UV-vis spectra of investigated D−A dyes in CH_2Cl_2 (~10^{-5} M, 298 K). As the dyes of the **D3A5** family show very similar absorption spectra, only the spectrum of nBu**D3**tBu**A5** is included.

These changes in band shape can be related to the electron-donor strength of the respective methylene bases and the concomitant polarization of the π-scaffold from more polyene-like dyes (broad bands with lower ε_{max}) to more cyanine-like (sharp band with higher ε_{max}) which will be discussed later (EOAM). With cyclic voltammetry at least one oxidative and one reductive wave could be determined for all D−A dyes of this study, albeit the respective redox processes were not always reversible. A comparison between the optical gap (determined from the absorption maxima, i.e. hc_0/λ_{max}) and the electrical gap (determined from the oxidation and reduction potentials, i.e. $E_{1/2,Ox} - E_{1/2,Red}$) yielded a deviation of about 0.1-0.2 eV, corroborating that the $S_0 \rightarrow S_1$ transition is governed by an electronic excitation from the HOMO to the LUMO level. Considering that the ferrocene/ferrocenium reference applied in the cyclic voltammetry experiments is located at −5.15 eV vs. vacuum level,[79] all investigated D−A dyes are expected to act as electron donors in combination with fullerene acceptors in solar cells or as hole conductors in combination with gold electrodes in OTFTs. Because the electron donor properties are related to the HOMO frontier orbital, it is noteworthy that the HOMO level is located at around −5.6 eV for the majority of the investigated dyes (in particular for almost all members of the extended series of the **A5** acceptor family) and range up to −6.0 eV for 1,3-benzodithiole-2-ylidene dyes **D1A2** and **D1A4**. These results indeed suggest that this methylene base has a lower electron donating power compared to the other two which is

surprising due to the wide application of such dithiole donors in tetrathiafulvalenes and related molecules.[80]

For this study, the most important molecular property of all dyes given is the ground state dipole moment μ_g that is obtained from electro-optical absorption measurements in 1,4-dioxane and corrected by Onsager cavity field correction to give "gas phase" dipole moments of the respective molecules.[78] The majority of these dyes have indeed very large dipole moments above 10.0 D and up to 15.0 D (**D2A5**) which complies with significant transfer of electron density from the donor to the acceptor heterocycles via the conjugated bridge in the ground state. Only for dyes **D1A1**, **D3A1**, **D1A2**, and **D3A2** the dipole moments remain smaller (2.8-6.2 D), which is explained by the fact that the π-conjugated path reverses its direction in the respective acceptor units, i.e. the carbonyl groups are oriented backwards toward the donor heterocycles. In addition to the ground state dipole moments the EOAM method also provides the change of the dipole moment upon optical excitation of the molecules into the excited singlet state $\Delta\mu$ and – under the assumption that both ground and excited state are composed of complementary contributions of an unpolar and a zwitterionic valence structure (see Scheme 1) – the c^2 value according to Wortmann.[30b, 55, 81] For the given series of D−A dyes, c^2 values between 0.26 (**D1A2**) and 0.51 (**D2A5**) were derived by EOAM (Table 1). The fact that the open-chain polymethine dye **D3A3** exhibits a polyene-like electronic structure ($c^2 = 0.32$, i.e. dominating unpolar structure in the ground state and strong bond length alternation) and that the analogous heterocyclic polymethine dye **D3A2** is significantly closer to the cyanine limit ($c^2 = 0.40$) complies with earlier studies that demonstrated how quinoid acceptor heterocycles can be used to polarize D−A dyes towards more zwitterionic structures.[50b, 55, 81-82] The fact that polyene-like electronic structures are also shown by the dyes with 1,3-benzodithiole-2-ylidene donor (**D1A1**, **D1A2**, **D1A4**, **D1A5**) reveals a distinct difference between 1,3-benzodithiole-2-ylidene on the one hand and 3-alkyl-2,3-dihydrobenzothiazol-2-ylidene and 1-alkyl-3,3-dimethylindolin-2-ylidene on the other hand. Dyes based on the latter donor units in combination with acceptor heterocycles exhibit always an electronic structure close to or perfectly at the cyanine limit ($c^2 > 0.40$), concomitant with narrow and high intensity absorption bands.

3.1.2 Transistor Devices

In order to investigate the suitability of these merocyanine dyes as semiconductors in transistor devices, vacuum processed OTFTs were fabricated in a bottom-gate, top-contact configuration on Si/SiO_2 as well as *n*-tetradecylphosphonic acid (TPA) modified substrates, which typically improve the thin film crystallinity and yield better results compared to Si/SiO_2. Results on solution processed OTFTs are not reported here as devices of the twenty D–A dyes could rarely be obtained due to solubility problems as well as inhomogeneous film formation on non-functionalized substrates like Si/SiO_2. Thus, if at all, only poor performance of the mobility the range of 10^{-4}-10^{-7} $cm^2\ V^{-1}\ s^{-1}$ in air was obtained. With the exception of dye **D4A5**, which decomposed at the required temperature for sublimation, all other dyes could be deposited by vacuum processing. To optimize the device performance, the dyes were deposited onto heated substrates in the range of 50-120 °C to enable a more crystalline film formation (for the influence of the substrate temperature T_S on the device's performance, see Table 2).

Table 2. Mobility (μ), threshold voltage (V_T) and current on/off ratio (I_{on}/I_{off}) of transistors of dyes nBu**D3**tBu**A5** and bPr**D3**tBu**A5** on TPA modified substrates with variation of the substrate temperature T_S.[a)]

	T_S / °C	T_{Subl}[a)] / °C	μ[b)] / $cm^2\ V^{-1}\ s^{-1}$	V_T[b)] / V	I_{on}/I_{off}[b)] / 1
nBu**D3**tBu**A5**	80	141	0.06	–8	10^6
	100		0.07	–6	10^5
	110		0.21	–4	10^6
	120		0.13	–5	10^6
bPr**D3**tBu**A5**	80[14]	144	0.09[14]	–5[14]	10^6[14]
	100[14]		0.17[14]	–5[14]	10^5[14]
	110		0.13	–6	10^5
	120[14]		0.18[14]	–5[14]	10^6[14]
	125		0.08	–6	10^5

[a)] During the sublimation, the deposition rate was gradually increased up to 1 nm min^{-1}, starting with a rate of 0.2 nm min^{-1} at the sublimation temperature T_{Subl} for the first 10 nm of the thin film. The substrates were heated to the given substrate temperature T_S; [b)] Average value of five transistors. The parameters showed a variation of less than 10 %.

Transfer characteristics were measured at ambient conditions in the saturation regime with a source-drain voltage of $V_{DS} = -50$ V. The effective hole mobilities μ and threshold voltages V_T were determined in the saturation regime according to equation (7). For every merocyanine, the electrical parameters were averaged over at least five OTFTs and showed a variation of less than 10 %. For the working devices, all OTFTs showed hole transport behavior, while the performance varied strongly with the substrate.

Table 3 shows the determined mobilities, threshold voltages and current on/off ratios for the devices on Si/SiO_2 substrates. Out of the twenty investigated dyes, the devices of five dyes (**D3A1**, **D1A2**, **D3A3**, **D1A4**, nHe**D3**tBu**A5**) showed no field effect at all. Notably, two of them (**D1A2**, **D1A4**) exhibit the 1,3-benzodithiole-2-ylidene donor which may be taken as an indication that a lack of alkyl side chains prohibits the formation of closed thin films.

The devices of the other fourteen dyes exhibited threshold voltages ranging from −17 up to +1 V, while the hole mobilities and current on/off ratios are in the range of 10^{-4}-10^{-6} $cm^2\ V^{-1}\ s^{-1}$ and 10^2-10^3, respectively. These low mobilities are related to the presence of amorphous thin films according to our AFM studies (see below). It appears that there is no clear-cut correlation between the electrical properties of the devices on Si/SiO_2 substrates and the molecular structure of the particular dyes, albeit the lowest value given for 1,3-benzodithiole-2-ylidene dye **D1A1** again supports the idea that the absence of alkyl side chains has a negative effect on the device performance. Accordingly, the only good performing dye **D1A5** of the 1,3-benzodithiole-2-ylidene series (**D1A1**, **D1A2**, **D1A4**, **D1A5**) is the only one that is equipped with a *tert*-butyl group (at the acceptor heterocycle). With regard to the impact of dipolarity on the charge transport properties, it is interesting to see that the hole mobilities slightly increase with increasing dipole moment which is indeed at odds with the common hopping transport model of Bässler[12b, 25] and discussed later (see section 3.1.6).

Whilst the consistently amorphous thin films on Si/SiO_2 substrates showed only small variations of the transistor performance for the whole series of dyes, there was a larger differentiation of the electrical properties of the devices on the TPA modified substrates for the various dyes (Table 4). On this self-assembled monolayer seven dyes (**D3A1**, **D3A2**, **D3A3**, **D1A4**, **D3A4**, **D1A5**, Bn**D3**tBu**A5**) showed no transistor performance at all, two dyes (**D1A1**, **D1A2**) remained on a low level ($\mu \sim 10^{-5}$-10^{-6} $cm^2\ V^{-1}\ s^{-1}$) as observed on Si/SiO_2, but for the other ten dyes (**D2A5**, Me**D3**tBu**A5**, nPr**D3**tBu**A5**,

iPr**D3**tBu**A5**, nBu**D3**tBu**A5**, nPe**D3**tBu**A5**, nHe**D3**tBu**A5**, nBu**D3**nBu**A5**, bPr**D3**tBu**A5**, bPr**D3**Ph**A5**), a significant improvement was observed.

The transfer characteristics of the OTFTs of dyes **D2A5**, nBu**D3**tBu**A5** and bPr**D3**tBu**A5** are depicted in Figure 29. Note, that the transfer characteristics of all OTFTs on the TPA modified substrates showed a mediocre hysteresis of the drain current for the forward and backward measurement cycle, which is investigated in the next chapter 3.2.

Table 3. Mobility (μ), threshold voltage (V_T) and current on/off ratio (I_{on}/I_{off}) of the series of merocyanine dye based transistors on Si/SiO_2 modified substrates.[a)]

	T_S / °C	T_{Subl}[a)] / °C	μ[b)] / $cm^2\ V^{-1}\ s^{-1}$	V_T[b)] / V	I_{on}/I_{off}[b)] / 1
D1A1	65	105	$2.4\cdot10^{-6}$	–3	10^3
D3A1	80	113		No field effect	
D1A2	80	179		No field effect	
D3A2	50	103	$1.3\cdot10^{-5}$	–10	10^2
D3A3	50	96		No field effect	
D1A4	80	140		No field effect	
D3A4	50	113	$3.6\cdot10^{-6}$	–11	10^2
D1A5	80	117	$1.1\cdot10^{-5}$	–17	10^3
D2A5	120	151	$2.2\cdot10^{-5}$	0	10^2
Me**D3**tBu**A5**	110	155	$7.8\cdot10^{-6}$	–12	10^2
nPr**D3**tBu**A5**	120	138	$4.7\cdot10^{-5}$	–2	10^2
iPr**D3**tBu**A5**	110	131	$2.6\cdot10^{-5}$	–5	10^2
nBu**D3**tBu**A5**	110	141	$3.7\cdot10^{-5}$	–5	10^2
nPe**D3**tBu**A5**	100	130	$7.7\cdot10^{-5}$	0	10^2
nHe**D3**tBu**A5**	95	127		No field effect	
Bn**D3**tBu**A5**	60	128	$5.3\cdot10^{-6}$	–6	10^2
nBu**D3**nBu**A5**	90	130	$3.2\cdot10^{-5}$	+1	10^2
bPr**D3**tBu**A5**[14]	120	144	$1.6\cdot10^{-4}$	–2	10^2
bPr**D3**Ph**A5**	100	170	$5.8\cdot10^{-6}$	–14	10^2
D4A5	Decomposition			n/a	

[a)] During the sublimation, the deposition rate was gradually increased up to 1 nm min^{-1}, starting with a rate of 0.2 nm min^{-1} at the sublimation temperature T_{Subl} for the first 10 nm of the thin film. The substrates were heated to the given substrate temperature T_S; [b)] Average value of five transistors. The parameters showed a variation of less than 10 %.

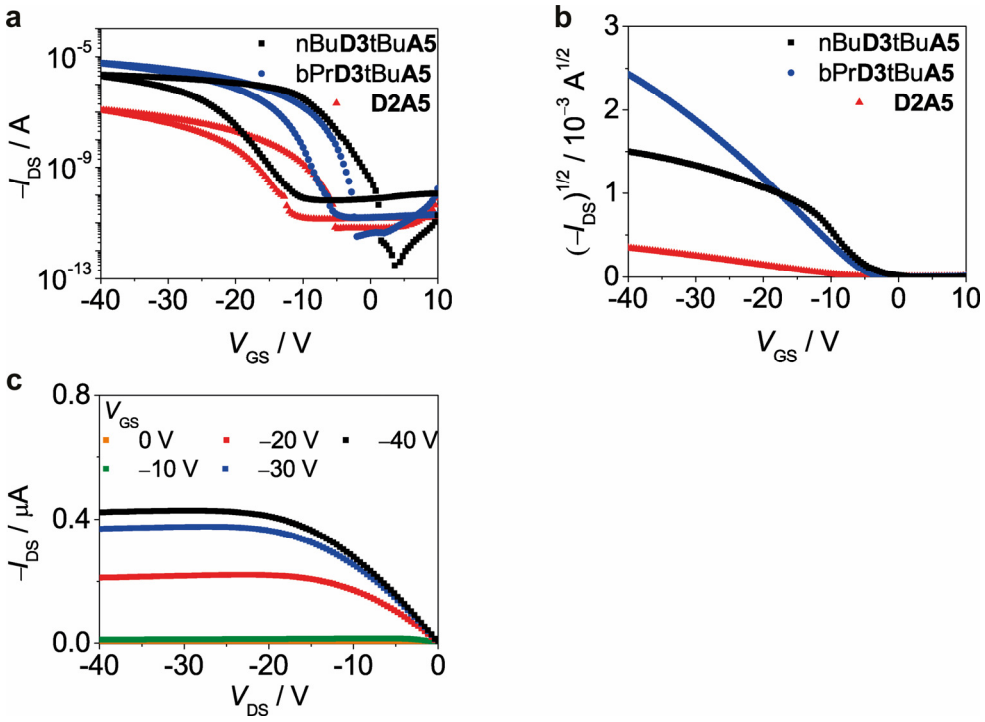

Figure 29. (a) Transfer curves of merocyanine **D2A5** (red triangles), bPr**D3**tBu**A5** (blue circles) and nBu**D3**tBu**A5** (black squares) based transistors on the TPA modified substrates with $V_{DS} = -50$ V; (b) Square root of the drain current of the devices of dyes **D2A5** (red triangles), bPr**D3**tBu**A5** (blue circles) and nBu**D3**tBu**A5** (black squares) on the TPA modified substrates with $V_{DS} = -50$ V; (c) Output curve of merocyanine nBu**D3**tBu**A5** based transistor on the TPA modified substrates.

Comparing the electrical properties, the values of the hole mobilities and current on/off ratios on the TPA modified substrates are spread over a much wider range as for the devices on Si/SiO_2, peaking at values of $\mu = 0.21$ cm^2 V^{-1} s^{-1} and $I_{on}/I_{off} = 10^6$ for dye nBu**D3**tBu**A5** on the TPA modified substrate.[14] Taking into account the various acceptors, it becomes clear, that the best devices were obtained for dyes with the 2-(4-alkylthiazol-2(3H)-ylidene)malononitrile acceptor (**A5** in Chart 5). All of these dyes belong to the same family bearing 1-alkyl-3,3-dimethylindolin-2-ylidene ("Fischer base") **D3**/**D4** donors (in one case a 3-alkyl-2,3-dihydrobenzothiazol-2-ylidene **D2**) and 2-(4-alkylthiazol-2(3H)-ylidene)malononitrile **A5** acceptors. The consistently good performance observed for the majority of these dyes corroborates their inherent proneness for the formation of crystalline thin films for quite different side chains (e.g. *tert*-butyl, *n*-butyl or phenyl at the acceptor heterocycle). Out of the investigated thirteen molecules, the devices of only two dyes (**D1A5**, Bn**D3**tBu**A5**) did not work (again, dye **D4A5** decomposed during the sublimation). The mobilities of the working devices are all larger than 10^{-3} cm^2 V^{-1} s^{-1} and the current on/off ratios are all well above 10^4.

Table 4. Mobility (μ), threshold voltage (V_T) and current on/off ratio (I_{on}/I_{off}) of the series of merocyanine dye based transistors on TPA modified substrates.[a)]

	T_S / °C	T_{Subl}[a)] / °C	μ[b)] / cm^2 V^{-1} s^{-1}	V_T[b)] / V	I_{on}/I_{off}[b)] / 1
D1A1	65	105	$4.3\cdot10^{-5}$	0	10^2
D3A1	80	113		No field effect	
D1A2	80	179	$3.9\cdot10^{-6}$	–3	10^2
D3A2	50	103		No field effect	
D3A3	50	96		No field effect	
D1A4	80	140		No field effect	
D3A4	50	113		No field effect	
D1A5	80	117		No field effect	
D2A5	120	151	0.0043	–11	10^4
Me**D3**tBu**A5**	110	155	0.018	–13	10^5
nPr**D3**tBu**A5**	120	138	0.076	–8	10^6
iPr**D3**tBu**A5**	110	131	0.12	–5	10^6
nBu**D3**tBu**A5**	110	141	0.21	–4	10^6
nPe**D3**tBu**A5**	100	130	0.011	–9	10^5
nHe**D3**tBu**A5**	95	127	0.050	–9	10^6
Bn**D3**tBu**A5**	60	128		No field effect	
nBu**D3**nBu**A5**	90	130	0.026	–12	10^5
bPr**D3**tBu**A5**[14]	120	144	0.18	–5	10^6
bPr**D3**Ph**A5**	100	170	0.010	–8	10^5
D4A5	Decomposition			n/a	

[a)] During the sublimation, the deposition rate was gradually increased up to 1 nm min^{-1}, starting with a rate of 0.2 nm min^{-1} at the sublimation temperature T_{Subl} for the first 10 nm of the thin film. The substrates were heated to the given substrate temperature T_S; [b)] Average value of five transistors. The parameters showed a variation of less than 10 %.

In contrast, OTFTs of dyes with 1,3-indandione **A1** (**D1A1**, **D3A1**), 2-(3-oxo-2,3-dihydro-1H-inden-1-ylidene)malononitrile **A2** (**D1A2**, **D3A2**), 2-benzylidenemalononitrile **A3** (**D3A3**) and 1,4-dialkyl-3-cyano-6-hydroxy-2-pyridone **A4** (**D1A4**, **D3A4**) as acceptor moiety either showed no field effect at all or exhibited only low charge carrier mobilities. Out of these seven molecules, the devices of only two dyes (**D1A1**, **D1A2**) showed p-channel behavior, yielding mobilities in the range of 10^{-5}-10^{-6} cm^2 V^{-1} s^{-1} as well as

current on/off ratios of the order of 10^2. These values are comparable to those of their thin films on Si/SiO_2 substrates (see Table 3).

Comparing the different donors of the dyes bearing the 2-(4-alkylthiazol-2(3H)-ylidene)malononitrile **A5** acceptor, it can be seen that the 1,3-benzodithiole-2-ylidene donor (**D1A5**) yields devices with no field effect. For the 3-alkyl-2,3-dihydrobenzothiazol-2-ylidene donor (**D2A5**), the mobility of the devices is of the order of 10^{-3} cm^2 V^{-1} s^{-1} and rises above 10^{-2} cm^2 V^{-1} s^{-1} for devices with molecules containing 1-alkyl-3,3-dimethylindolin-2-ylidene ("Fischer base") as donor unit (**D3A5** family). Concurrently, the current on/off ratio rises one order of magnitude when replacing 3-alkyl-2,3-dihydrobenzothiazol-2-ylidene **D2** by 1-alkyl-3,3-dimethylindolin-2-ylidene ("Fischer base") **D3** donors. For the threshold voltage, no such correlation can be obtained. However, there is a loose connection between the values of the threshold voltage and the mobility, as devices with a high mobility tend to have a smaller threshold voltage than devices with a lower mobility.

Taking a closer look on the performance of the series of the best dyes **D3A5**, an influence of the variation of the alkyl chain substituent can be established. For a linear alkyl chain, the mobility rises with increasing chain length from the methyl substituent (Me**D3**tBu**A5**) over *n*-propyl (nPr**D3**tBu**A5**) to *n*-butyl (nBu**D3**tBu**A5**) with a peak mobility of $\mu = 0.21$ cm^2 V^{-1} s^{-1}. Further elongation of the alkyl chain to *n*-pentyl (nPe**D3**tBu**A5**) and *n*-hexyl (nHe**D3**tBu**A5**) results in a decline of the mobility. When substituting the alkyl chain with a benzyl group (Bn**D3**tBu**A5**), the devices exhibit no field effect at all. For the different configurations of the attached propyl group (dyes nPr**D3**tBu**A5**, iPr**D3**tBu**A5** and bPr**D3**tBu**A5**), the devices show an improvement from *n*-propyl (nPr**D3**tBu**A5**) over *i*-propyl (iPr**D3**tBu**A5**) to the bridged propyl (bPr**D3**tBu**A5**) configuration with the best mobility within this series of $\mu = 0.18$ cm^2 V^{-1} s^{-1} for dye bPr**D3**tBu**A5**.

3.1.3 Thin Film Morphology and Microstructure

The previous results indicate that the devices fall into two classes, i.e. devices with $\mu > 10^{-3}$ cm^2 V^{-1} s^{-1} can be attributed to crystalline thin films and those devices with $\mu < 10^{-4}$ cm^2 V^{-1} s^{-1} can be attributed to amorphous thin films. In order to obtain confirmation for these conclusions, the molecular films with a nominal thickness of 30 nm were analyzed by AFM and representative results are shown in Figure 30.

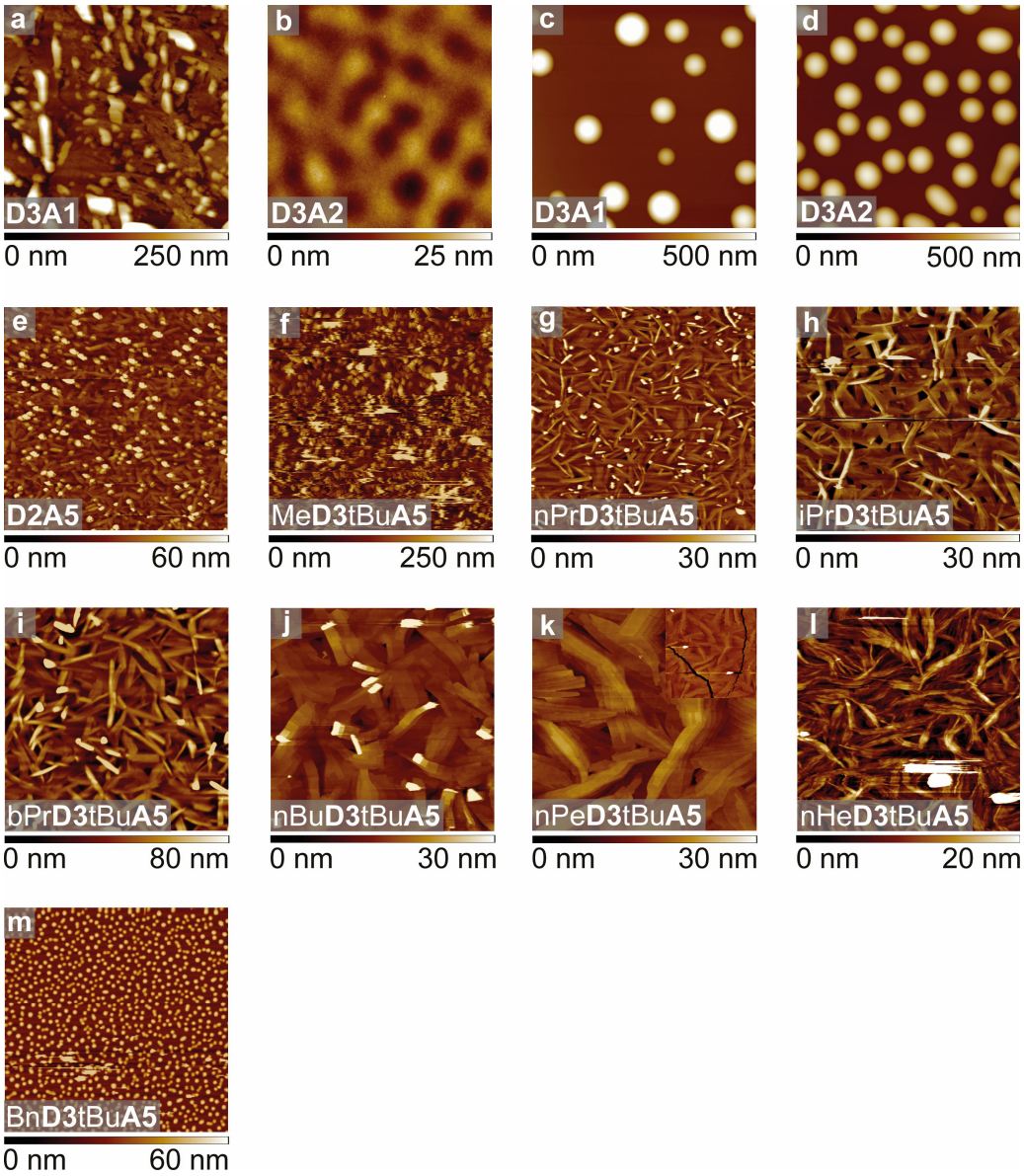

Figure 30. AFM height images of 30 nm vacuum deposited thin films (nominal thickness) of **D3A1** (a), **D3A2** (b) on Si/SiO_2, as well as **D3A1** (c), **D3A2** (d), **D2A5** (e), Me**D3**tBu**A5** (f), nPr**D3**tBu**A5** (g), iPr**D3**tBu**A5** (h), bPr**D3**tBu**A5** (i), nBu**D3**tBu**A5** (j), nPe**D3**tBu**A5** (k), nHe**D3**tBu**A5** (l) and Bn**D3**tBu**A5** (m) on the TPA modified substrates. Each image scales to 5×5 μm^2; the inset in (k) scales to 10×10 μm^2.

In the case of dye **D3A1** on Si/SiO_2, no continuous film but rather unconnected domains were formed during the deposition process, hence providing no percolation pathways for charge carriers. This explains quite reasonably, why devices of some dyes did not show any semiconducting behavior. AFM images of smooth thin films with no structural features were obtained for dye **D3A2** on Si/SiO_2 which is typical for thin films of the investigated dyes on Si/SiO_2 exhibiting poor OTFT performance (Table 3). The very similar, yet low mobility values (10^{-4}-10^{-6} cm^2 V^{-1} s^{-1}) of OTFT devices on Si/SiO_2

suggest that they are mainly governed by the amorphous thin films morphology despite their different molecular properties or packing.

On the TPA modified substrate, the thin films of dyes **D3A1** and **D3A2** show a dewetting of the substrate, forming droplet-like grains which again are not interconnected. Therefore, those devices did not show any field effect. However, for the other devices with $\mu > 10^{-3}$ cm^2 V^{-1} s^{-1}, the AFM images clearly show a structured surface. Thin films of dyes **D2A5** and Me**D3**tBu**A5** exhibit small needle-like domains with grain lengths of up to 0.5 µm. Imaging the surface of the thin film of dye Me**D3**tBu**A5** was challenging due to upright standing needles and its resulting high roughness (*RMS* ~ 45-85 nm). Both features explain well the fact that mobilities of the corresponding OTFTs were among the lowest values in this series of **D3A5** dyes. On the other hand, the thin films of almost all other **D3A5** dyes clearly show larger sized grains and layered structures which explain well the higher charge carrier mobilities of their devices. For dye nBu**D3**tBu**A5**, a clear terrace-like morphology with grain sizes up to 2 µm and a step height of 1.1 ± 0.2 nm can be observed. For dye bPr**D3**tBu**A5**, the morphology of the thin films is similar to that of the film of dye nBu**D3**tBu**A5** although showing slightly smaller rod-like grains and not so well-defined terrace-like structures. This corresponds with the fact that the OTFT of dye nBu**D3**tBu**A5** shows a slightly higher mobility as that of dye bPr**D3**tBu**A5** and demonstrates that the film morphology gives good explanations for the different mobility values.

For the family of dyes **D3A5**, the substituent at the donor moiety has a significant influence on the thin film morphology. For an attached methyl group (dye Me**D3**tBu**A5**), the surface of the thin film shows small crystalline regions and is very rough. However, when elongating the alkyl chain, the surfaces become smoother and the grain sizes rise with increasing length of the alkyl chain from methyl (Me**D3**tBu**A5**) to *n*-pentyl (nPe**D3**tBu**A5**). Further elongation of the alkyl chain to *n*-hexyl (nHe**D3**tBu**A5**) leads to frayed islands while a substitution of the alkyl chain with a benzyl group (Bn**D3**tBu**A5**) induces a dewetting of the substrate. Note that for the thin film of dye nPe**D3**tBu**A5**, the grain size of the islands is the biggest of all investigated thin films. However, as the inset in Figure 30k shows, there are cracks in the thin film, surely affecting the percolation pathways.

3.1.4 Single Crystal X-Ray Analysis

In order to further investigate the diversified device performance, single crystal structures of compounds **D3A1**, **D3A2**, **D3A4**, Me**D3**tBu**A5**, nBu**D3**tBu**A5**, nHe**D3**tBu**A5** and bPr**D3**tBu**A5** were determined. All crystals were grown from solution by either slow evaporation of the respective solvent or slow diffusion of a bad solvent into the solution of the respective dye. Dyes **D3A1** and **D3A4** have been crystallized from $CHCl_3$/*n*-hexane, dye **D3A2** from CD_2Cl_2. The crystals of the four dyes of the **D3A5** family were grown from CH_2Cl_2.

From the X-ray structures of these seven molecules, the *BLA* values for the three C–C bonds between donor and acceptor heterocycles are calculated and correlated to the "gas phase" c^2 values determined for the molecules in solution (for the assignment of the bonds, see Figure 31). However, no quantification, i.e. calculation of c^2 values from *BLA* values to quantify the offset from the cyanine limit, can be done.

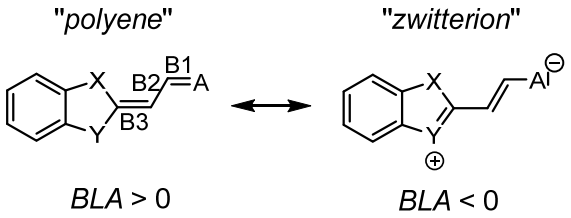

Figure 31. Assignment of the bonds B1-B3 of the methine bridge of the D–A dyes for calculating the bond length alternation *BLA* in the crystal structure.

The obtained *BLA* values are given along with the measured bond lengths in Table 5 and it can be seen that dyes **D3A1** and **D3A2** exhibit the smallest bond length alternation with a value close to zero of *BLA* = −0.001 Å and *BLA* = −0.005 Å, respectively. Dye **D3A4** as well as the four dyes of the **D3A5** family show larger negative *BLA* values between *BLA* = −0.015 Å and *BLA* = −0.025 Å. Comparing the *BLA* values to the "gas phase" c^2 values (Table 1), one notices that the structure of all dyes in the solid state is shifted towards the more zwitterionic resonance structure as indicated by the negative *BLA* values. Owing to the more polarizing solid state environment, the dyes **D3A1** and **D3A2** with the lowest c^2 values of 0.40 are now the ones closest to the cyanine limit (corresponding to $c^2 = 0.5$) in the crystalline state.

Table 5. Bond lengths of the methine bridge of the dyes in the crystal structure and calculated bond length alternation *BLA* as averaged over both possible bond length alternations *BLA*(B2−B1) and *BLA*(B2−B3). As comparison, the c^2 values of the dyes in solution from Table 1 are given.

	B1 / Å	B2 / Å	B3 / Å	*BLA* / Å	c^2 / 1
D3A1	1.382	1.385	1.390	−0.001	0.40
D3A2	1.392	1.385	1.387	−0.005	0.40
D3A4	1.410	1.384	1.406	−0.024	0.45[75]
Me**D3**tBu**A5**	1.401	1.375	1.398	−0.025	-
nBu**D3**tBu**A5**	1.395	1.378	1.398	−0.019	0.46
nHe**D3**tBu**A5**	1.396	1.377	1.388	−0.015	0.46[76]
bPr**D3**tBu**A5**	1.398	1.382	1.397	−0.016	0.47

The packing of dyes **D3A1**, **D3A2**, **D3A4**, Me**D3**tBu**A5**, nBu**D3**tBu**A5,** nHe**D3**tBu**A5** and bPr**D3**tBu**A5** are depicted in Figure 32 and Figure 33 with the acceptor part of the molecule colored red, the donor moiety colored blue and their alkyl chain in grey. Note that due to a slight twisting of some molecules along the polymethine bridge and concomitant lack of overall planarity, the given π-π-distances are calculated for the spacing between parallel acceptor moieties. One common feature which can be found in all of the obtained crystal structures is the antiparallel alignment of neighboring molecules, indicating that the ground state dipole moment has a major impact on the packing of the dyes. Accordingly, as suggested in a previous concept article,[15] this antiparallel dimer motif may be regarded as a "supramolecular synthon"[83] albeit the arrangement of the molecules is not as precisely defined by the dipole moments of molecules as for instance for hydrogen bonds.[83] Thus, at a closer look, two distinct packing motifs can be distinguished: The acceptor moiety of one molecule lies either on top of a donor moiety (**D3A1**, **D3A2**, **D3A4**) or on top of another acceptor moiety (**D3A5** series) of the closest neighboring molecule. Additionally, the π-π-distances of the two adjacent molecules are either different (**D3A1**, **D3A2, D3A4**) or (almost) equal (**D3A5** series).

The first case − one next neighbor is located at a significantly closer distance and the acceptor lies on top of the neighbor's donor moiety − may be regarded as a situation, where the dipolar interaction energy between two dyes has been optimized at the expense of the other now more distant surrounding molecules. Despite larger intermolecular distances and a more pronounced slipping of the further neighbor, a continuous one-dimensional π-stack of the dimer units for dyes **D3A2** and **D3A4** can still be

recognized. In contrast, for dye **D3A1**, the packing motif consists only of an isolated antiparallelly stacked dimer unit with a π-π-distance of 3.989 Å, whereas the molecules of this dimer unit have no overlap with the π-surfaces of the other neighboring molecules.

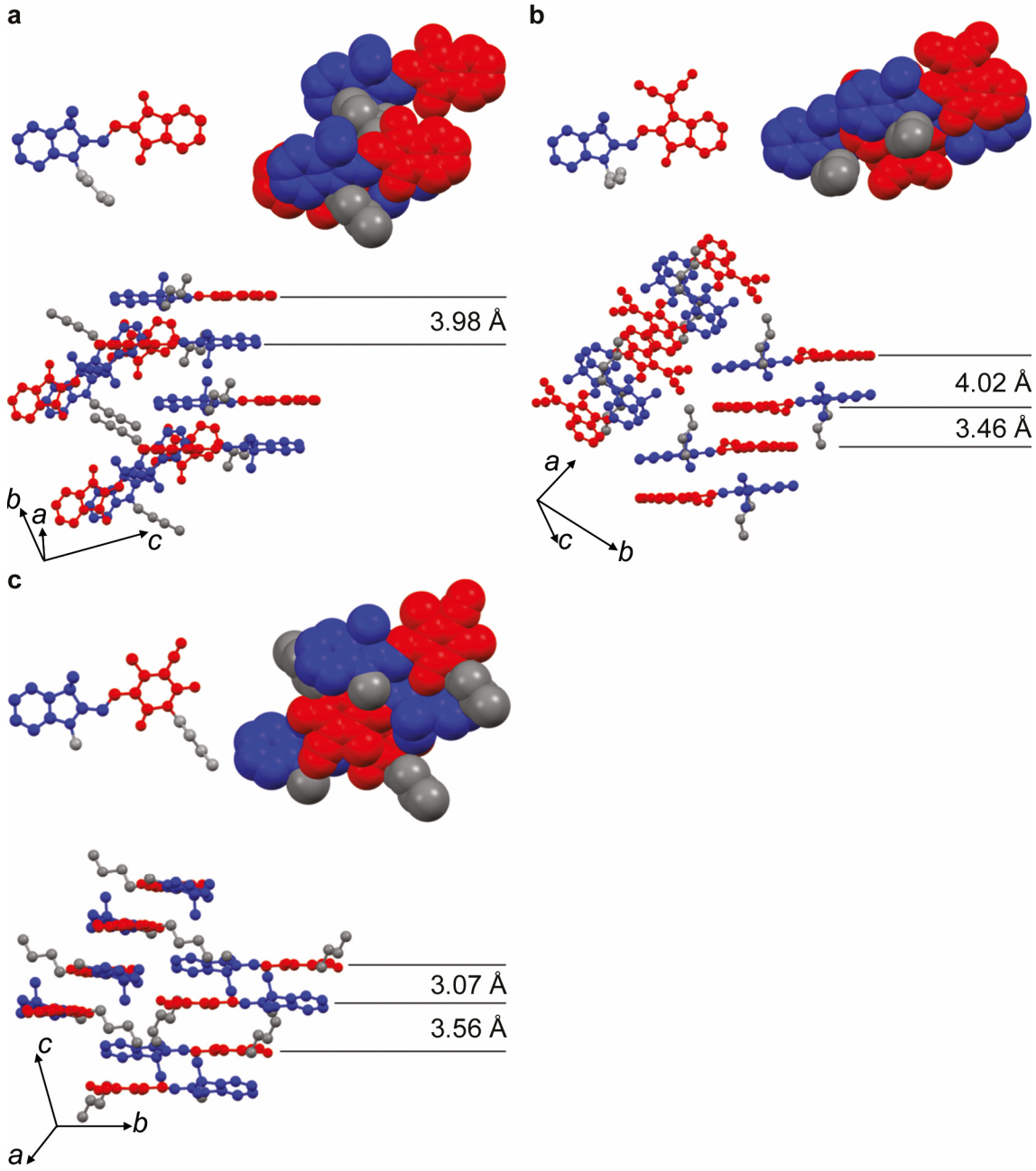

Figure 32. Crystal packing of **D3A1** (a), **D3A2** (b) and **D3A4** (c) with the acceptor part of the molecule colored red, the donor moiety colored blue and the alkyl chain at the acceptor/donor colored grey. Shown is the molecular structure with packing of the respective closest dimers as well as side views to reveal the corresponding π-π-stacking distances of the molecules to their closest neighbors (calculated for the acceptor moieties). Hydrogens are omitted for clarity.

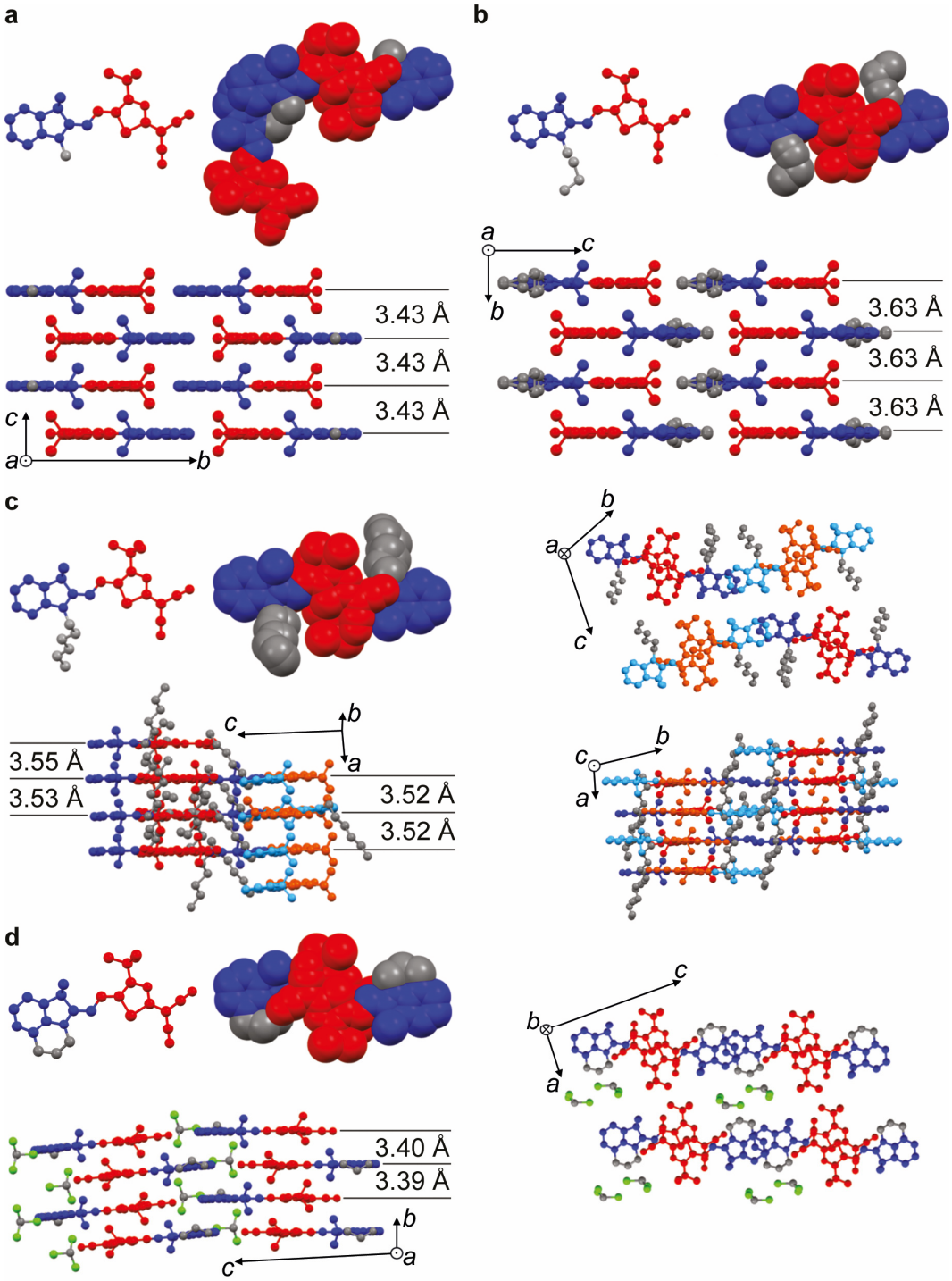

Figure 33. Crystal packing of Me**D3**tBu**A5** (a), nBu**D3**tBu**A5** (b), nHe**D3**tBu**A5** (c) and bPr**D3**tBu**A5** (d) with the acceptor part of the molecule colored red (orange), the donor moiety colored blue and the linear alkyl chain at the donor colored grey. Shown is the molecular structure with the packing of the respective closest dimers as well as side views to reveal the corresponding π-π-distances of the molecules to their closest neighbors (calculated for the acceptor moieties). For dye bPr**D3**tBu**A5** (c), $CHCl_3$ was incorporated into the crystal. Additionally, a top view is presented for a better understanding of the crystal structure. In the crystal structure of dye nHe**D3**tBu**A5** (d), there are two nonequivalent molecules with different intramolecular twist which is depicted by the differently colored molecules. Again, a top view and another side view of the packing are presented for better understanding of the crystal structure. Hydrogens are omitted for clarity.

The second case, found for all dyes of the **D3A5** family, shows a brickwork-type packing pattern with four next neighbors located at almost the same π-π-distance. This packing resembles a more balanced allocation of the dipolar interaction energy between all neighboring dyes with π-π-overlap in the crystal, but requires a significant slipping between the molecular centers, which is supported by the bulky *tert*-butyl and $C(Me)_2$ subunits of these molecules. Because of the antiparallel orientation of neighboring D−A molecules this packing motif affords acceptor-acceptor and donor-donor contacts between the π-stacked molecules. Further analysis of the molecular long-range packing shows that there are again two distinguished arrangements, one showing stacks of dimers which are tilted and twisted against each other (**D3A1**, **D3A2**, **D3A4**), the other showing a two-dimensional layer-like structure (**D3A5** series).

In this layered packing motif (**D3A5** series), isolated dimers cannot be distinguished as each next neighboring molecule has (almost) the same π-π-distance. These π-π-distances are 3.43 Å for dye Me**D3**tBu**A5** and 3.63 Å for dye nBu**D3**tBu**A5**. In both cases, the molecules have a perfectly planar backbone and the acceptor parts overlap, while for dye Me**D3**tBu**A5** the donor parts overlap additionally. For dye nHe**D3**tBu**A5**, the analysis is not that simple, as there are two different conformations of the molecule present in the crystal (see Figure 33), one showing only a small twist between the donor and the acceptor part of 2.8°, the other showing a larger twist of 8.9°. Furthermore, the π-π-distance is not identical for both conformations and varies slightly. However, the layer-like packing is still present. The analysis of the crystal structure of bPr**D3**tBu**A5** indicates a layered structure as well, although the crystal incorporated the solvent $CHCl_3$ from which the crystal was grown, therefore not showing perfectly aligned planes with a distance of about 3.39-3.40 Å.

It is quite remarkable that all merocyanine dyes with high performance in OTFTs ($\mu > 10^{-3}$ cm^2 V^{-1} s^{-1}) show the second type of 2D packing motif. When comparing these results to the OTFT performances of the devices and the AFM results, it becomes clear that the thin film of those dyes, which show a packing motif with tilted stacks or isolated dimers, also show no field effect on the TPA modified substrate due to a dewetting of the substrate. However, the thin films of **D3A5** dyes with the layered single crystalline structure show all decent field-effect mobilities of $\mu > 0.01$ cm^2 V^{-1} s^{-1}.

3.1.5 XRD and SAED Studies

With regard to the issues of molecular packing in the thin films as well as their molecular orientation on the substrate, out-of-plane X-ray diffraction (XRD) and selected area electron diffraction (SAED) measurements were performed and correlated to the single crystal structures. The two techniques can be regarded as complementary as XRD gives information about planes which are oriented parallel to the substrate while SAED shows diffraction for planes which are standing upright on the substrate. Because crystalline films with good transistor performance could only be obtained for dyes of the **D3A5** family, the further studies were focused on members of this class of compounds. Please note that the result of the SAED analysis given here for dye bPr**D3**tBu**A5** is slightly different to the one given in reference [14]. This is due to a more refined measurement of a sample with only 5 nm thin film to investigate the first few monolayers.

Figure 34 shows the XRD patterns of the thin films of compounds Me**D3**tBu**A5**, nBu**D3**tBu**A5** and bPr**D3**tBu**A5** on TPA modified substrates including the corresponding simulated powder spectra for Me**D3**tBu**A5** and nBu**D3**tBu**A5**, which were derived from the single crystal structure using the software *Mercury*.[84] The XRD pattern of the dye Me**D3**tBu**A5** shows only one clear peak at 7.3°, which correlates well with the rough surface and poor crystallinity of the thin film and can be assigned to the (020) peak of the simulated powder spectrum. When analyzing the XRD pattern of the thin film of dye nBu**D3**tBu**A5**, there are three clear diffraction peaks at 8.0°, 16.0° and 24.1°, corresponding to the crystalline (10−1), (20−2) and (30−3) planes. The number of peaks as well as their intensity and line width indicate a much higher degree of crystallinity in the film than for Me**D3**tBu**A5** which is further supported by the fact that the thin film of dye nBu**D3**tBu**A5** also showed the largest grains in the AFM images. The thin film of dye bPr**D3**tBu**A5** shows two distinct peaks at 9.1° and 9.6°. Such close lying peaks could mean that two orientations of crystallites with equal contributions to the thin film phase exist in the thin film. Because a solvent-free single crystal for this dye could not be grown, a more in-depth analysis is not possible for this material.

Complementary to the above stated results of the XRD analyses, SAED measurements give insights into the arrangement of planes perpendicular to the surface. Strong diffraction cycles were observed for all three thin films and indicate the polycrystalline nature of these, which is supported by the AFM results (Figure 30) as well as the morphology of the regions which were used for SAED (inset in Figure 34b,d,f).

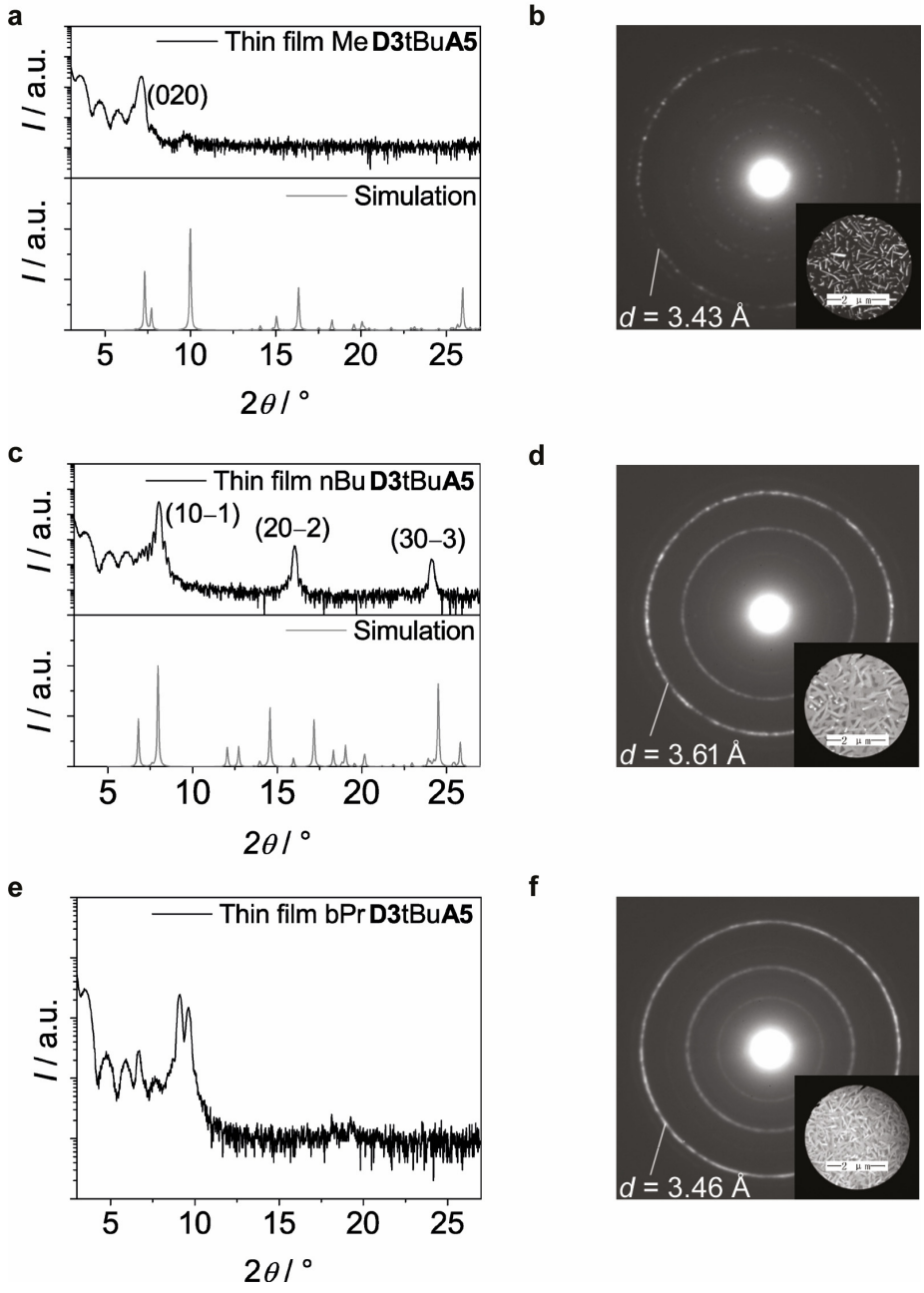

Figure 34. XRD patterns (black lines) for 30 nm thin films on TPA modified substrates with corresponding powder spectra (grey lines) simulated from single crystal structures (a, c, e) as well as corresponding SAED diffraction patterns for 5 nm thin films on TPA modified substrates with calculated interplanar distances *d* (b, d, f) of dyes Me**D3**tBu**A5** (a,b), nBu**D3**tBu**A5** (c,d) and bPr**D3**tBu**A5** (e,f). The insets in b), d) and f) show the region of the thin films from TEM measurements for which SAED experiments were performed.

This is reasonable, as the vacuum deposition is a nondirectional deposition technique. From the distance of the diffraction cycles to the center spot, the corresponding interplanar distances were calculated and showed to be in good agreement with the π-π-distances from the single crystal structures (Figure 32, Figure 33). In this regard, the diffraction pattern of dye nBu**D3**tBu**A5** indicates a lattice spacing of 3.61 Å, whereas compounds

Me**D3**tBu**A5** and bPr**D3**tBu**A5** give smaller lattice spacings of 3.43 Å and 3.46 Å, respectively. All three values are in excellent agreement with the π-π-distances found in single crystals which are 3.63 Å for nBu**D3**tBu**A5**, 3.43 Å for Me**D3**tBu**A5** and 3.40 Å for bPr**D3**tBu**A5**. The shorter π-π-distances for Me**D3**tBu**A5** and bPr**D3**tBu**A5** are reasonable as the long butyl chain of nBu**D3**tBu**A5** possesses more flexibility and gives rise to a larger steric effect compared to the bridged propyl and methyl group. This might also be the reason why the devices of compound bPr**D3**tBu**A5** still could achieve high mobilities although the thin film morphology appears not as good as the one of compound nBu**D3**tBu**A5**.

From the XRD, SAED and single crystal results, the orientations of the molecules Me**D3**tBu**A5** and nBu**D3**tBu**A5** on the TPA modified substrates can be deduced and are depicted in Figure 35. The diffraction planes observed in the XRD experiments are hereby oriented almost parallel to the substrate ((020) for dye Me**D3**tBu**A5** and (10−1) for dye nBu**D3**tBu**A5**) whereas the diffraction planes from the SAED measurements, arising from the planes where the π-π-stacking occurs, are almost perpendicular to the substrate.

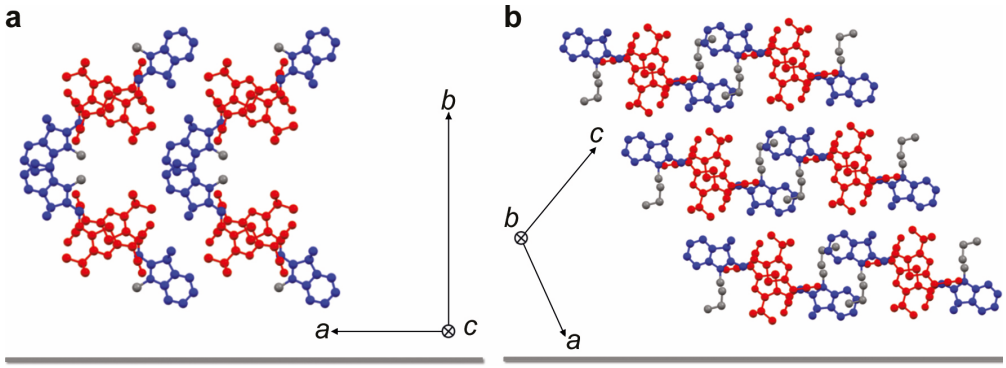

Figure 35. Orientation of the molecules within the thin film of dyes Me**D3**tBu**A5** (a) and nBu**D3**tBu**A5** (b) on TPA modified substrates based on the XRD, SAED and single crystal results. Additionally, the respective axes of the single crystalline structures are given.

The single crystal results show that the π-π-stacking lies in the direction of the *c*-axis for dye Me**D3**tBu**A5** whereas for dye nBu**D3**tBu**A5**, it lies in the direction of the *b*-axis. From these results it can be concluded that both molecules adopt an edge-on orientation on the TPA modified surface within the crystalline domains of the thin films and show a close π-π-stacking along the direction of the transistor channel which enables efficient charge carrier transport.

3.1.6 Impact of Molecule-Substrate and Dipolar Molecule-Molecule Interactions

While these results show that molecules with high ground state dipole moments can exhibit good charge carrier mobilities, a comparison to the model by Bässler and co-workers (see section 2.2.3) should be done. As they used time of flight (TOF) measurements for the determination of the charge carrier mobility of the molecularly doped polycarbonate, their data are not directly comparable to these results obtained from OTFT measurements, which include device parameters and not only parameters of the material itself. In addition, bulk materials were investigated in this thesis where direct contacts between our dipolar dyes are unavoidable. However, a similar plot of the mobility μ in dependence on the ground state dipole moment μ_g is depicted in Figure 36. While Sugiuchi and Nishizawa investigated only molecules with small dipole moments (μ_g up to 5.56 D; grey triangles in Figure 36), this situation is now entirely different for the series of merocyanine dyes whose ground state dipole moments cover a much larger range up to μ_g = 15.0 D. The OTFT data show that the mobilities of the devices of the merocyanine dyes on the Si/SiO_2 substrates are not influenced by the dipole moment and vary in a random manner between 10^{-4}-10^{-6} $cm^2\ V^{-1}\ s^{-1}$ (black squares in Figure 36). In order to rationalize these results with the previously described model, it must be addressed if the dipole moments in the thin films are non-interacting with respect to the thin film morphology. As merocyanine dyes are highly dipolar (μ_g up to 15.0 D, Table 1) and the films only consist of organic semiconductor molecules without any polymer matrix, the molecules will surely interact. However, for the OTFT architecture, where charge transport takes place in the first layers of the interface, the interaction between substrate and semiconducting molecules has to be taken into account as well. As the mobilities of the OTFTs of our dyes on the Si/SiO_2 substrate show no clear dependence on the dipole moment (see Figure 36) and the AFM results indicate an amorphous morphology, the interaction between the molecules and the substrate probably superimposes the dipole-dipole interaction. Hence, the lack of influence on the packing from dipole-dipole interaction is ensured by the higher interaction between the substrate and the respective dye. The fact that the investigated merocyanines do not form ordered monolayers has recently also been confirmed for thin films on a Au(111) surface.[73]

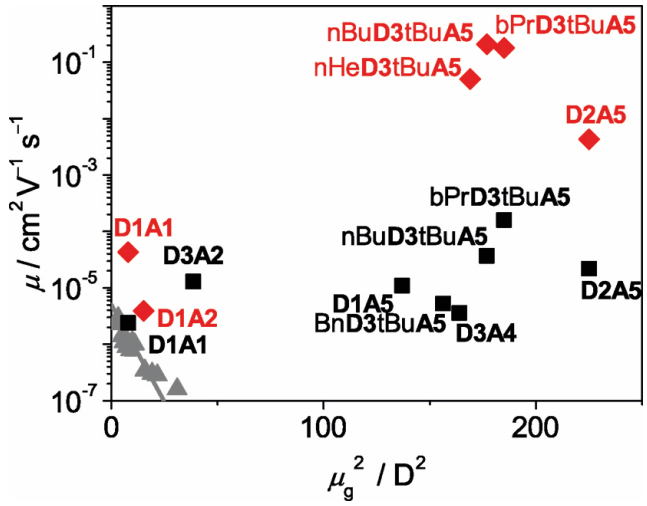

Figure 36. Dependence of the OTFT hole mobilities on the square of the ground state dipole moments of the D−A dyes. The values are given for the thin films on the untreated Si/SiO_2 (black squares) as well as on the TPA modified substrates (red diamonds). Additionally, the mobilities from ref. [24] (grey triangles) with their linear fit from ref. [25] (grey line) are shown. For clarity, not all members of the **D3A5** family are depicted.

Notably, although being a device parameter, the mobility of the OTFTs with the least dipolar dye **D1A1** as organic semiconductor seems to loosely fit into the range of the mobility values which are predicted by Dieckmann, Bässler and Borsenberger.[25] In contrast, looking at the mobility values for the more dipolar dyes on Si/SiO_2, these do not show a log $\mu \sim -\mu_g^2$ behavior over the investigated range of dipole moments. This can be explained by the growing dipole-dipole interaction with higher dipolarity of the molecules as the electrostatic energy between two dipoles correlates quadratically with the dipole moment. Thus, the dipole-dipole interaction becomes more important regarding film formation although still not being the morphology determining factor. As Dieckmann, Bässler and Borsenberger already mentioned in their study, deviations from the model for higher dipole moments ($\mu_g > 5$ D) clearly show the importance of dipole-dipole interactions which tend to align in an antiparallel manner in unpolar environment. Accordingly, this study corroborates that antiparallel aligned dimers are formed, which can be regarded as an unpolar moiety and will therefore not broaden the density of states as expected from a random orientation of dipole moments.

For the TPA modified surface, the case is different. As the surface energy is significantly reduced in comparison to the untreated Si/SiO_2,[85] it can be expected that there is a lower degree of interaction between organic molecules and the TPA functionalized surface than with the Si/SiO_2 surface. This has already been stated for thin films of pentacene on TPA as well as on other functionalized surfaces.[85-86] Consequently, the intermolecular forces

now dominate the film formation which is supported by the AFM results showing clear structural features rather than unstructured amorphous surfaces of the thin films on the TPA modified substrates (Figure 30). Therefore, the relationship between charge carrier mobility and dipole moment will be completely different from the $\log \mu \sim -\mu_g^2$ behavior predicted for randomly disordered molecules. This study shows that in the case of low dipole moments of ~3-6 D the reduced interaction between the surface and the molecule leads to a dewetting of the surface (Figure 30c,d) or to the formation of amorphous structures, which are not favorable for providing high charge carrier mobilities. Therefore, for the dyes with low dipole moments, the corresponding mobilities fall into the same range as for the devices on Si/SiO_2. This corresponds well with the single crystal structures of these dyes which show only a low dimensional ordering of the molecules. On the other hand, for dyes bearing a larger dipole moment of 13-15 D, the high dipole-dipole interaction directs a highly ordered layer-like packing motif (Figure 33) and the mobility even increases significantly by up to four orders of magnitude to yield a maximum of 0.21 $cm^2\ V^{-1}\ s^{-1}$ (red diamonds in Figure 36).

3.1.7 Electrostatic Surface Potentials for Dye Monomers and Dimers

To elucidate why packing arrangements with different dimensional ordering (isolated dimers/tilted stacks in contrast to equidistant layers; Figure 32 vs. Figure 33) are formed for the given series of molecules, DFT calculations were performed to visualize the electrostatic potential on the van-der-Waals surface of appropriate dimers taken from the crystal structures of dyes **D3A1**, **D3A2**, Me**D3**tBu**A5** and nBu**D3**tBu**A5**. For comparison, the electrostatic potentials of the respective monomers were calculated as well and are shown together with those of the dimers in Figure 37. The monomers of all dyes clearly show the dipolar character of the molecules as well-defined centers of electron density can be seen. However, as expected based on our experimental data (Table 1), the dipolar nature of dye nBu**D3**tBu**A5** is also most pronounced in the calculation.

Going from the monomer to the dimer, the electrostatic potential for dye **D3A1** becomes quite homogeneous throughout the molecular backbone, therefore illustrating the approach of the "supramolecular synthon". The centrosymmetric dimer can thus be regarded as an unpolar moiety. For dye nBu**D3**tBu**A5**, the dimer is again less polar than the monomer, but a slight dipolar character for both molecules is still retained as the molecules are slipped against each other and mainly overlap with their acceptor parts.

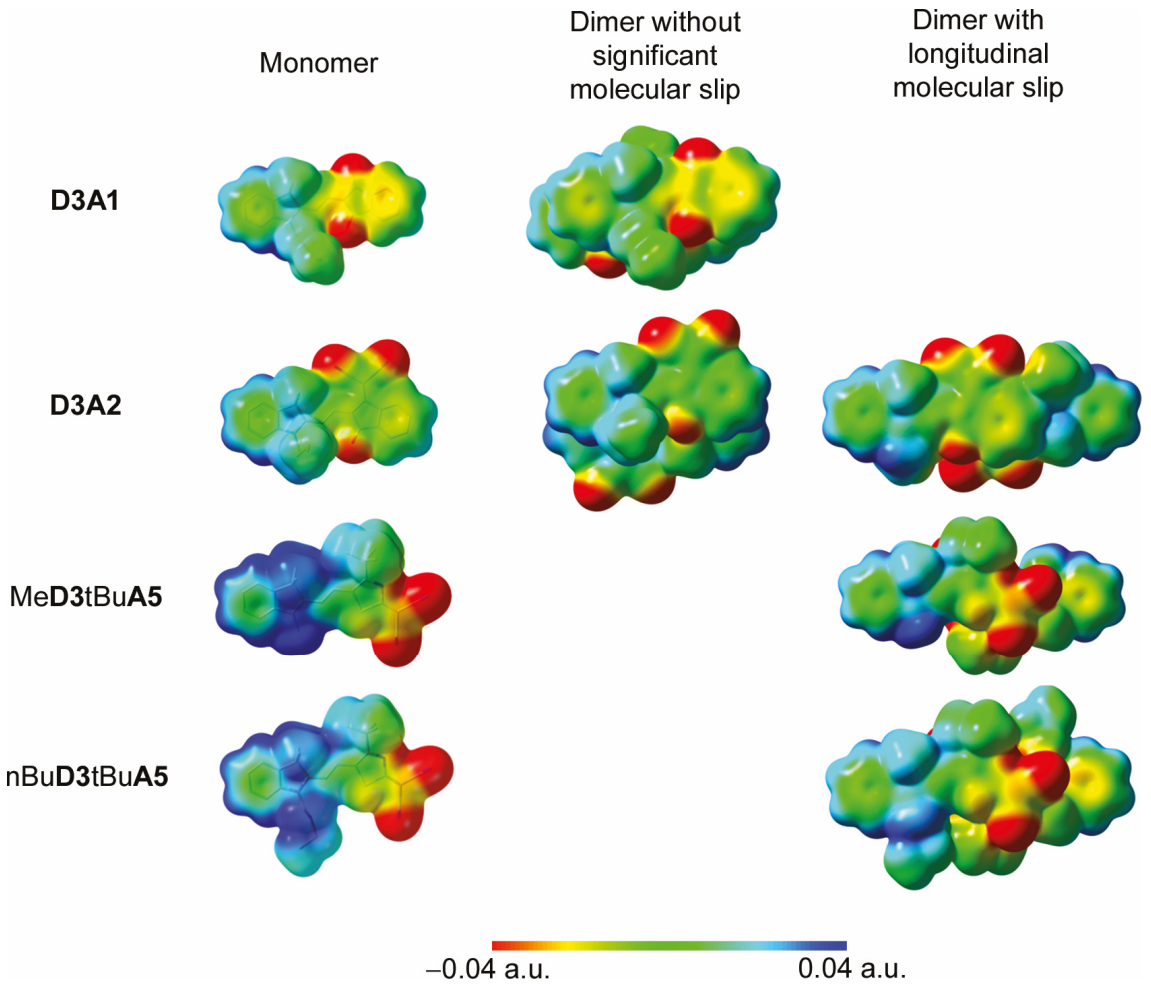

Figure 37. Electrostatic potential on the van-der-Waals surface of monomers and dimers of dyes **D3A1**, **D3A2**, Me**D3**tBu**A5** and nBu**D3**tBu**A5** (obtained for an isovalue of 0.001). The geometries of the monomers and dimers were taken from the crystal structures.

This slip arises from the sterical demand of the bulky *tert*-butyl group attached to the acceptor and the $C(Me)_2$ group at the donor part. In this case, the polar surfaces are not fully covered and can induce an ordered alignment of other neighboring molecules. Dye **D3A2** seems to fall just in between these two cases as two non-equivalent dimers can be found in the crystal structure, one with a longitudinal molecular slip due to the $C(Me)_2$ group as well as the *n*-butyl chain and one without. The electrostatic potential of the dimer with a molecular slip again shows a slight dipolar character of both molecules whereas the result of the dimer with almost no molecular slip exhibits a more homogeneous electrostatic potential throughout the molecular backbone without fully annihilating the dipolar character. Still, this indicates a higher compensation of the molecular dipoles than for the dimer with the slipped arrangement and can be compared to the case of dye **D3A1**.

3.1.8 Rationalization of the Two Types of Packing

The two types of packing arrangements of the dyes (layers vs. isolated dimers/tilted stacks) on the TPA modified substrate can be explained as follows: Due to the dipole-dipole interaction, which acts over a long range, all dyes assemble with next neighbors in an antiparallel fashion. For the dimers of dye **D3A1**, the molecules are well-stacked on top of each other (donor on top of acceptor), hence yielding a compensation of the electrostatic potential and cancelling out the dipole moments. However, dispersion interactions (e.g. van-der-Waals interactions), determined mainly by the sterics of the molecules' substituents, are relevant as well and can lead to slipped arrangements where the acceptor parts of neighboring molecules overlap with each other. Hence, for dye **D3A2** a dimer with this longitudinal slip can be found in the crystal structure. However, when such a dimer is formed, the next molecule − like for dye **D3A1** − can only pack in such a way as to align antiparallel exactly on top of one molecule of the slipped dimer. If such a well-aligned dimer without or with only small molecular displacement is formed during the growth of a crystal, there is no further driving force to induce a highly ordered packing (especially for dyes with a low dipole moment) which ultimately results in isolated dimers (**D3A1**, Figure 32a) or tilted or twisted stacks of dimers (**D3A2**, Figure 32b).

The impact of sterics on the molecular packing can also be observed in the case of dye **D3A4**. Due to the high dipole moment of 12.8 D the tendency to pack in a layer-like motif can be clearly seen (Figure 32c). However, the sterical hindrance by the *n*-butyl chain at the acceptor and the two methyl groups at the donor part is too big. When a slipped dimer with overlapping acceptor parts is formed, the next molecule can only be located in such a way as to have a small overlap with the π-system of the dimer molecules. Therefore, only stacks which are twisted against each other can be formed. Presumably, if there was less sterical hindrance, the dyes would again form stacks of dimers with significant π-overlap which has already been shown for similar dyes in crystal structures as well as by the formation of dimer aggregates in solution for highly dipolar molecules even with no sterical hindrance.[34b, 61] For the dyes of the **D3A5** family, dipolarity and sterics are balanced just right to direct the desired two-dimensional layer arrangement on the transistor dielectric. The two methyl groups at the donor part and the *tert*-butyl group at the acceptor moiety lead to a slip of the molecules (Figure 33), hence sustaining the polar

character of the molecules in a centrosymmetric dimer unit. Therefore, the large dipole moment can give rise to the growth of a 2D brickwork-type crystal structure.
Rephrasing, for merocyanines and presumably also for any D−A push-pull dye scaffold, the dipole moment together with well-designed sterics of the molecule actually play the key roles in the formation of well-ordered packing motifs as it induces highly ordered 2D layer-like crystal structures, which enable decent device performance. This is in contrast to former belief that molecules with high dipole moments should not be used for applications where a high charge carrier mobility is needed. In fact, these results even suggest that if molecules with dipole moments are used as semiconductors in OTFTs, the dipole moment has to be sufficiently high to induce an advantageous intimate packing of the dyes which will ultimately result in good charge carrier mobility values of the device. It might even be speculated that the strong Coulomb interaction between appropriately packed dipolar dyes might enable closer π-π-contacts below typical van-der-Waals distances and concomitantly larger transfer integrals (which depend by e^{-r} on distance).

3.1.9 Conclusion

Twenty merocyanine dyes composed of various donor and acceptor moieties were systematically investigated with respect to their charge transport properties by application as p-type semiconductors in organic thin film transistors on two different substrates. The studies show that the vast majority of the thin films formed by these dipolar D–A dyes are amorphous, even after tedious variation of substrate temperature and deposition rate. Thus, if at all, only low hole charge carrier mobilities around 10^{-4}-10^{-6} $cm^2\ V^{-1}\ s^{-1}$ were determined for these OTFTs on Si/SiO_2 under ambient conditions. As an exception, among the most dipolar subseries ($\mu_g \sim 13$ D), several dyes of the **D3A5** family could be identified that showed remarkably improved performance with mobilities of up to 0.21 $cm^2\ V^{-1}\ s^{-1}$ on substrates modified with a self-assembled monolayer of TPA. Comparison of the obtained mobility values to Bässler's disorder charge transport theory shows that the mobility values do not match the predicted $\log \mu \sim -\mu_g^2$ behavior but even increase with increasing dipole moments, indicating the formation of highly crystalline films for the **D3A5** family. Whereas all thin films of merocyanines are built up from antiparallel aligned dimers, the outstanding feature of these **D3A5** dyes is that they all crystallize in a two-dimensional layer-like structure with slipped π-stacking arrangements, which could be confirmed by SAED, XRD and single crystal structure analysis. From the

calculated electrostatic surface potentials, it seems reasonable that these two-dimensional brickwork-type patterns are formed due to the well-balanced sterics as well as the high dipolarity of the respective dyes. In this regard, properly positioned bulky substituents prohibit the dyes from forming isolated dimers with no overall dipole moment and yield a longitudinally slipped dimer unit in which the dipolar character of the molecules is retained.

3.2 SCFETs of a Dipolar Merocyanine Dye[†]

The last section focused on the charge transport properties of merocyanine dyes by application in OTFTs. Here it was shown that despite promising hole mobility values of up to 0.21 $cm^2 V^{-1} s^{-1}$, the real difficulty was the fabrication of highly crystalline layers. Futhermore, charge transport in thin films is always hampered by grain boundaries. In this section, by application of the best dye nBu**D3**tBu**A5** in single crystal field-effect transistors (SCFETs), the intrinsic charge transport properties as well as predominant charge transport directions are adressed. Furthermore, the potential of merocyanine dyes for high mobility application is explored.

3.2.1 XRD and SAED Studies

Nanocrystals of nBu**D3**tBu**A5** were grown from a $CHCl_3$/MeOH solution on TPA modified substrates (see experimental part). These nanocrystals exhibited needle-like shapes with varying lengths from several micrometers up to hundreds of micrometers (see appendix). As shown in the previous section, this dye crystallizes in a brickwork-type pattern where the molecules are aligned antiparallel, mainly driven by their ground state dipole moment of 13.3 D (see Figure 33).

To verify the crystalline structure of the single crystals on the substrate, out-of-plane XRD experiments were carried out. In the obtained diffraction pattern, five diffraction peaks at $2\theta = 6.9°$, 8.1°, 13.7°, 16.1° and 24.1° could be observed (see Figure 38). Compared to a powder spectrum, which was simulated based on the single crystal structure with the program *Mercury*,[84] these peaks could be identified as resulting from two sets of lattice planes: (001) and (002), as well as (10−1), (20−2) and (30−3). Hence, with this fabrication, two different orientations of single crystals are obtained on the TPA modified wafers which might have an impact on the transistor behavior as the charge injection from two differently aligned metal/organic interfaces could vary as it is discussed later.[87] To ensure crystallinity, SAED measurements were performed additionally (Figure 38). In these experiments, a clear diffraction pattern was observed which confirms that these needles are indeed single crystals. The diffraction pattern along the elongation direction of the

[†] This chapter has been published in A. Liess, M. Stolte, T. He, F. Würthner, *Mater. Horiz.* **2016**, *3*, 72-77. Reproduced in parts with permission from The Royal Society of Chemistry, Copyright 2016.
XRD measurements were performed Dr. David Schmidt. SEM, TEM and SAED measurements were performed by Dr. Vladimir Stepanenko.

needle gives a lattice spacing of 7.3 Å which coincides well with the single crystal lattice parameter b = 7.2565 Å and thus demonstrates that the needles are elongated along the b-axis which is also the π-π-stacking direction.

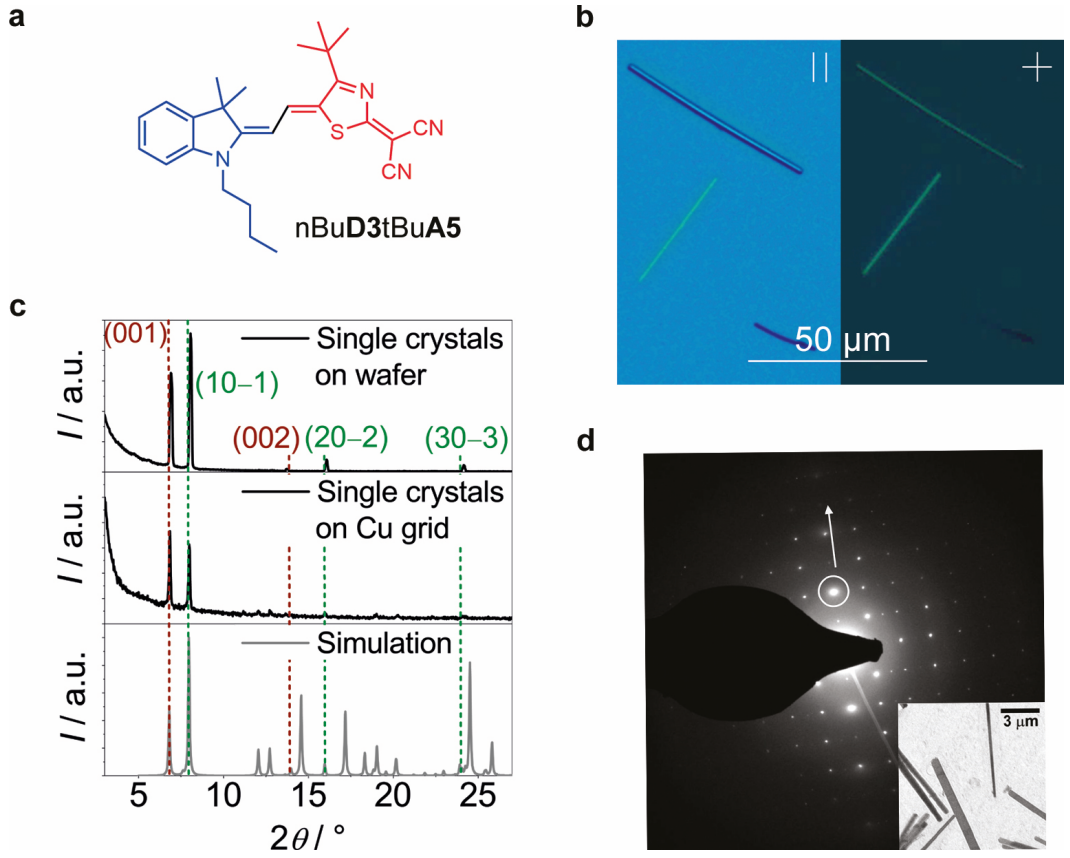

Figure 38. (a) Molecular structure of investigated dye nBu**D3**tBu**A5**; (b) Bright-field microscopy image and cross-polarized microscopy image of single crystals of merocyanine dye nBu**D3**tBu**A5** on a TPA modified substrate; (c) XRD patterns (black lines) of single crystals of merocyanine dye nBu**D3**tBu**A5** on a TPA modified substrate in comparison with that of single crystals of merocyanine dye nBu**D3**tBu**A5** on a copper grid used for SAED measurements and the powder pattern simulated from the single crystal structure[84] (grey line) as well as indexed reflexes arising from two sets of lattice planes (red and green lines); (d) SAED pattern of a single crystal of merocyanine dye nBu**D3**tBu**A5** with indicated direction of crystal elongation as white arrow (inset: TEM image of single crystals of dye nBu**D3**tBu**A5** used for SAED experiments).

3.2.2 Transistor Devices

Next, homogeneous crystals with thicknesses d smaller than 1.0 µm were selected and 100 nm thick gold source and drain electrodes were deposited in vacuum according to the gold wire shadow mask technique (see experimental part).[88] Finally, the transfer and output characteristics of the devices were measured under ambient conditions with a drain-source voltage of V_{DS} = −50 V in the saturation regime according to equation (7).

In total, 22 SCFETs were fabricated, out of which only one device did not work. Their device dimensions and SCFET parameters are provided in Figure 39 and Table 6, while a graphic illustration of the mobility distribution of all SCFETs is shown in Figure 40. The transfer curve as well as a secondary electron microscope (SEM) image of a representative device are depicted in Figure 40b,c (for all other transfer curves, see appendix). Note, that the plot of $(-I_{DS})^{1/2}$ vs. V_{GS} shows a nonlinear behavior giving rise to only a narrow V_{GS} region where optimal performance is given. This non-ideality cannot be attributed to contact resistance as no S-shape in the linear regime as well as no drop of I_{DS} in the saturation regime can be observed in the output curve (Figure 40d). Despite this obvious drawback, which might originate from fabrication and characterization in ambient media, all mobilities were deduced in this region of optimal operation to demonstrate the potential of merocyanine dyes in SCFETs.

All devices showed p-type field-effect mobilities ranging from 0.11 $cm^2 V^{-1} s^{-1}$ up to 2.34 $cm^2 V^{-1} s^{-1}$, yielding an average device mobility of 0.87 $cm^2 V^{-1} s^{-1}$, while the threshold voltages of the devices varied from –13 V to 0 V and the current on/off ratios were determined to be in the range of 10^3-10^5. As it is known that the thickness of single crystals in bottom-gate, top-contact transistor devices can play a crucial role in terms of device performance − an increasing crystal thickness will lead to a limited drain current due to an increasing contact resistance[89] − the thicknesses of the nanocrystals have been investigated by AFM and show a wide variety with values from 49 nm to 930 nm. For devices with thicknesses $d < 500$ nm, the average mobility rises to 1.05 $cm^2 V^{-1} s^{-1}$ while the range of the threshold voltage and the current on/off ratio does not change compared to the crystals with higher thicknesses.

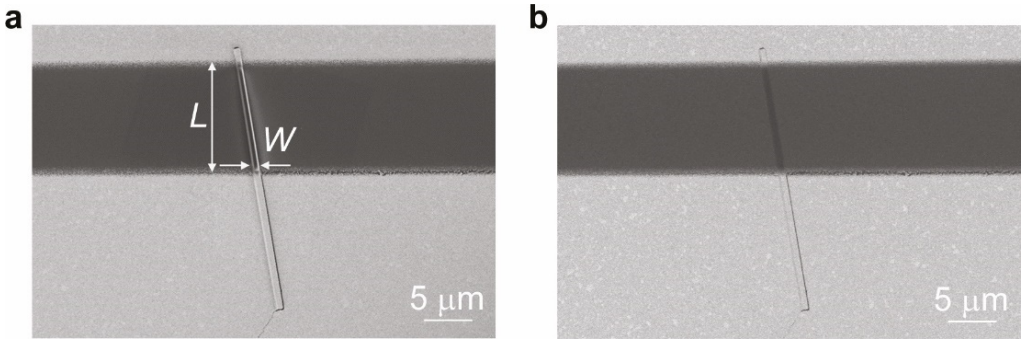

Figure 39. SEM images of representative device obtained with secondary electron detector (a) and energy selective backscattered electron detector (b) for conservative determination of the device dimensions.

Table 6. Channel length (L), channel width (W), crystal thickness (d), charge carrier mobility (μ), threshold voltage (V_T) and current on/off ratio (I_{on}/I_{off}) of all fabricated SCFETs of merocyanine dye nBu**D3**tBu**A5**. The list is sorted with decreasing mobility.

#	L / μm	W / μm	d / nm	μ / $cm^2\ V^{-1}\ s^{-1}$	V_T / V	I_{on}/I_{off} / 1
1	10.5	0.4	128	2.34	–3	$4{\cdot}10^5$
2	11.2	0.4	104	1.74	–2	$2{\cdot}10^5$
3	10.3	0.3	77	1.72	–2	$3{\cdot}10^5$
4	13.0	1.0	313	1.47	–3	$3{\cdot}10^5$
5	9.0	0.4	103	1.45	–2	$2{\cdot}10^4$
6	23.4	1.7	195	1.38	0	$2{\cdot}10^5$
7	23.2	1.9	75	1.03	0	$2{\cdot}10^4$
8	3.8	0.3	87	0.95	0	$2{\cdot}10^4$
9	13.4	0.6	169	0.84	0	$5{\cdot}10^4$
10	12.0	0.6	319	0.83	–13	$2{\cdot}10^5$
11	11.0	0.8	394	0.82	–4	$9{\cdot}10^4$
12	10.2	0.5	203	0.69	–9	$1{\cdot}10^4$
13	12.4	2.0	170	0.56	–1	$5{\cdot}10^4$
14	10.5	0.2	64	0.42	–6	$6{\cdot}10^3$
15	11.1	1.7	742	0.41	–3	$4{\cdot}10^4$
16	9.6	1.0	145	0.37	–6	$3{\cdot}10^4$
17	9.6	1.6	930	0.33	–1	$8{\cdot}10^3$
18	7.4	1.1	658	0.26	–2	$1{\cdot}10^4$
19	12.9	1.1	730	0.26	–5	$2{\cdot}10^4$
20	25.1	0.2	49	0.22	–3	$2{\cdot}10^3$
21	8.1	1.4	637	0.11	–3	$3{\cdot}10^4$
22	11.9	1.1	818	No field effect		

Investigations on the device stability were performed on the best SCFET with a mobility of 2.34 $cm^2\ V^{-1}\ s^{-1}$, a threshold voltage of −3 V and an on/off ratio of $4{\cdot}10^5$. Keeping the device in air for 45 d showed a decrease of the mobility to below 10% of its initial value after 20 d while then staying constant (Figure 40e). After 45 d, the device showed no transistor behavior anymore and a recovery of device performance by annealing in vacuum was not possible (Figure 41). As the on-current decreases in almost the same

manner as the mobility, the decrease of the mobility can be explained by a reduction of the on-current (Figure 40e). In terms of threshold voltage and on/off ratio, the device shows a good stability. Over 30 d, the threshold voltage shows only a small shift from −3 V to −6 V while the on/off ratio remains almost constant and drops only from $4 \cdot 10^5$ to $9 \cdot 10^4$ (see Figure 40f). Storage of the devices in different environments, i.e. argon, ambient, dry and humid air (100 % relative humidity), showed no improvement of their stability (see appendix). The device degradation is thus attributed to the fabrication and the characterization under ambient conditions.

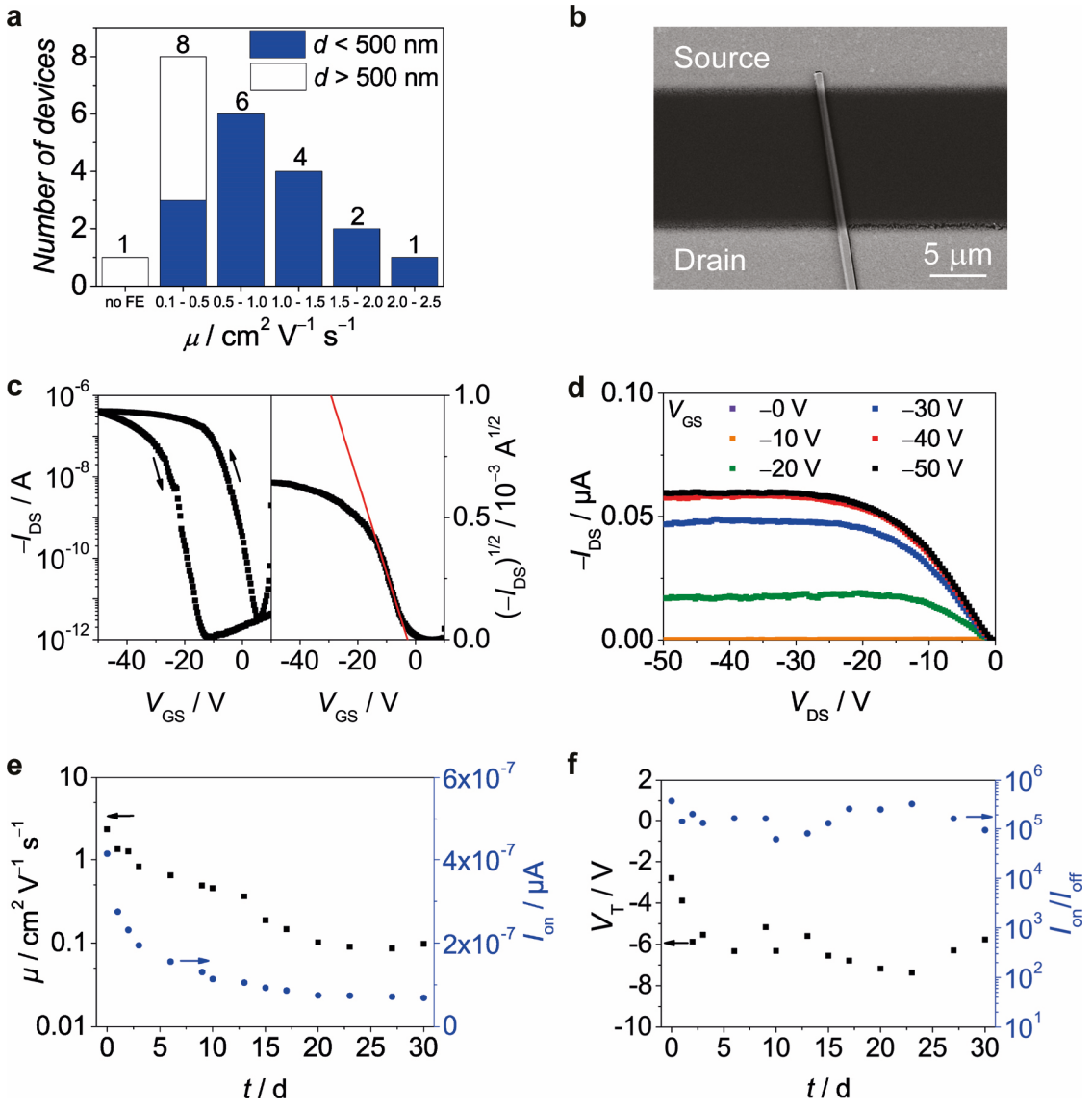

Figure 40. (a) Distribution of the mobility values of all 22 devices; (b-d) SEM picture (b), transfer curve (c, left) with plot of the square root of the drain current (c, right) and corresponding linear fit (c, red line) as well as output curve (d) of representative device; (e-f) Development of the mobility (e, black squares), on-current I_{on} (e, blue circles), threshold voltage (f, black squares) and on/off ratio (f, blue circles) of representative device over 30 d when kept in air.

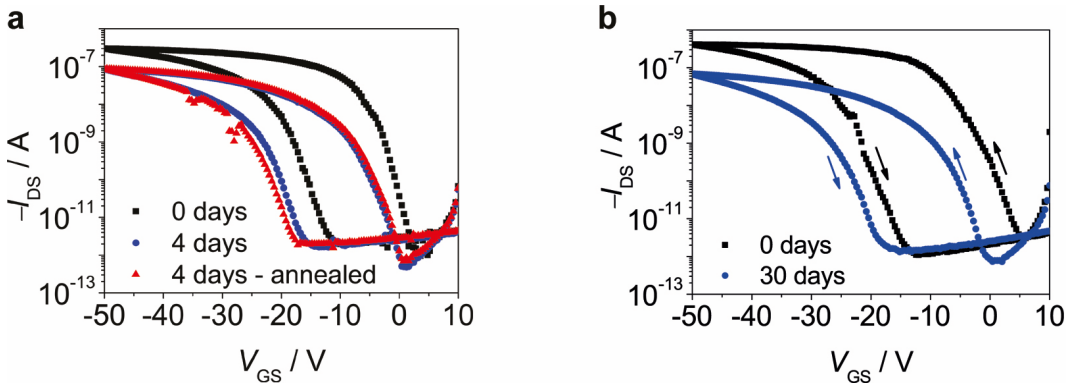

Figure 41. (a) Transfer characteristics of device #3 as measured after fabrication (0 d), after 4 d in air as well as after 4 d in air and vacuum annealing for 2 h at 100 °C; (b) Transfer characteristics of device #1 as measured directly after fabrication and after keeping the device for 30 d in air.

It should be noted that the transfer curves of the devices show a hysteresis for which the drain current is higher for the forward than for the backward measurement cycle. The hysteresis broadens for measurements at higher temperatures and for measurements with a lower sweep rate (see appendix and Figure 42).

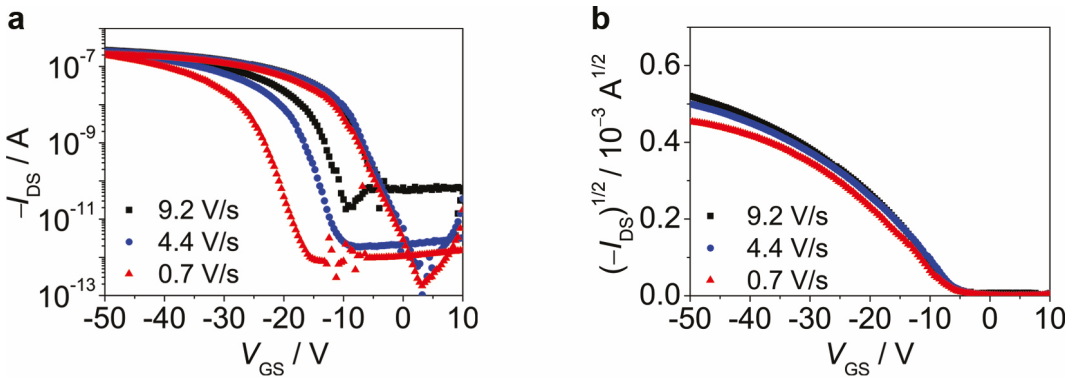

Figure 42. (a) Transfer characteristics of device #3 measured for different sweep rates; (b) Corresponding plot of the square root of the drain current of device #3 for different sweep rates.

This behavior suggests a slow response of mobile charge carriers to the applied electrical field,[90] for which a polaronic/bipolaronic mechanism is proposed in the field of conjugated polymers.[90-91] Whether this mechanism applies for the devices of nBu**D3**tBu**A5** in air is however beyond the scope of this thesis. Either way, the hysteresis can be significantly reduced if the gate-source voltage is swept only up to –30 V (see Figure 43) which shows that the devices suffer from electrical stress when the gate-source voltage is swept up to –50 V.

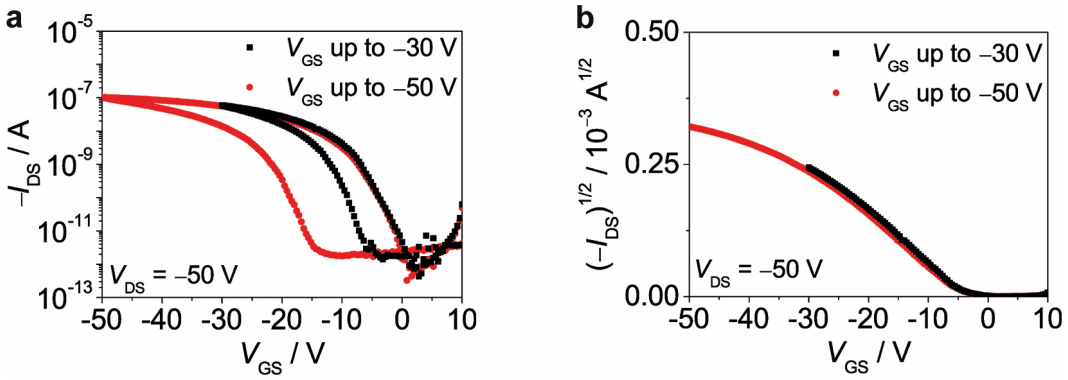

Figure 43. Transfer characteristics (a) as well as corresponding plot of the square root of the drain current (b) of representative device measured at a drain-source voltage of V_{DS} = −50 V from V_{GS} = 10 V up to V_{GS} = −30 V (black squares) and V_{GS} = −50 V (red circles).

3.2.3 Charge Transport Directions

To gain insight into the intrinsic charge carrier transport properties, the transfer integrals *t* for next neighbors of a molecule were calculated by DFT. These calculations showed that hole transport is in fact possible in three directions, namely the [010] (*b*-axis), the [101] and the [100] directions (see Table 7 as well as Figure 44 and Figure 45).

Table 7. Calculated transfer integrals *t* of a central molecule with next neighboring molecule.

Next neighbor	1/1’	2/2’	3/3’	4	5	6	7	8	9	10
|*t*| / meV	0	8	9	15	0	0	0	0	0	0

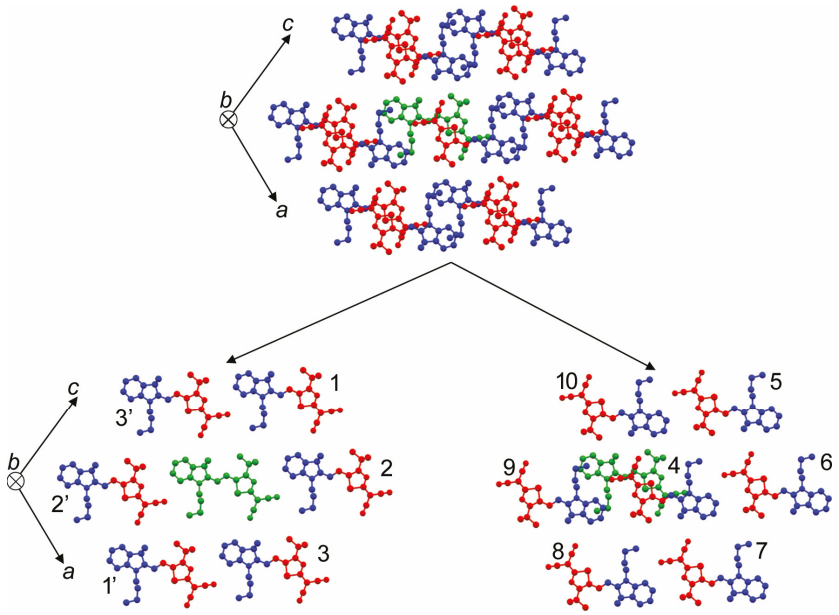

Figure 44. Numeration of the next neighboring molecules around a central molecule (green).

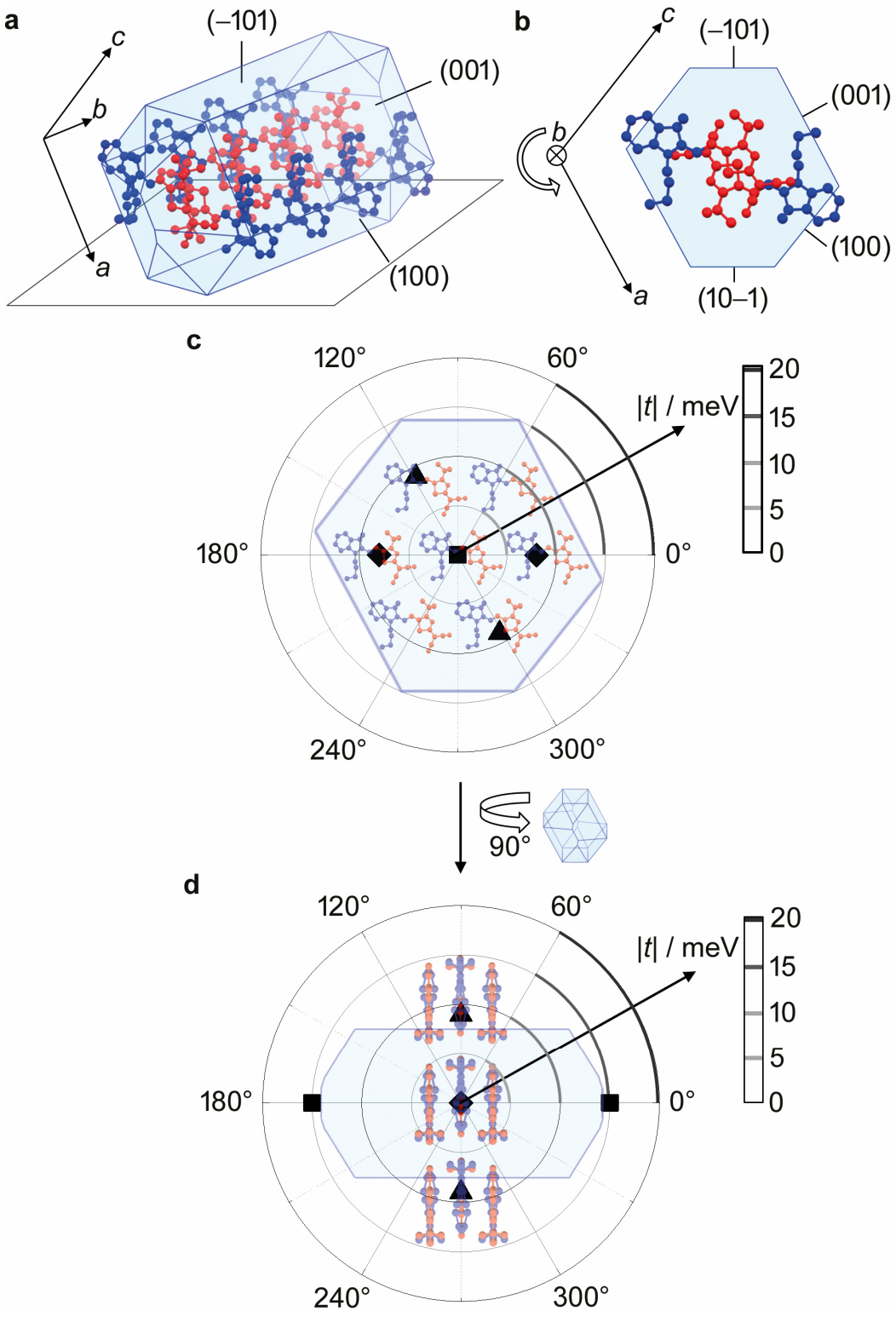

Figure 45. (a) BFDH morphology of a single crystal of dye nBu**D3**tBu**A5** on the substrate with crystallographic directions and indexed relevant lattice planes; (b) View on the (010) plane of the BFDH morphology with indexed relevant lattice planes as well as possible rotation direction around the *b*-axis of the elongated crystals; (c-d) Calculated transfer integrals *t* for next neighboring molecules with view on the (010) plane (c) as well as for next neighboring molecules with view along the [101] direction (d) with values of *t* denoted as filled symbols.

The calculations elucidate that for all of these three directions, the transfer integral has similar values of 8 meV (direction [101]), 9 meV (direction [100]) and 15 meV (direction [010]), while for next neighbors in other directions the calculations of the transfer integrals result in a value of zero.

To demonstrate the charge transport directions, also the Bravais-Friedel-Donnay-Harker (BFDH) morphology of the crystals was calculated from the single crystal structure with the program *Mercury*[84]. The calculation yields a needle-like morphology in accordance to the experimental observation with an elongation along the *b*-axis which is equal to the π-π-stacking direction of the molecules. Furthermore, it can be easily rationalized why two different orientations (001) and (10−1) of the crystal planes can be observed by XRD experiments (see Figure 38c), as they result from a simple rotation around the *b*-axis of the elongated crystals (see Figure 45). This lack of preferential out-of-plane orientation corresponds to the fact that the TPA modified surface has a low surface energy[85] which might result in a low interaction of the surface with the organic molecules.

These results suggest that for an applied electrical field in the [010] direction, i.e. along the drain-source channel of the SCFETs, the charge carriers will be transported mainly along the π-π-stacking direction (Figure 45d). The injection of the charge carriers, however, should mainly take place within the (010) plane as this stands upright on the surface. As a two dimensional charge transport within this plane is possible with almost equal transfer integrals for two directions [101] and [100], the orientation of the crystal on the substrate actually makes no difference for charge injection. Furthermore, these results with similar transfer integrals in three linearly independent directions show that even with traps or defects present in the channel region, a charge carrier can easily circumvent these and be transported within the brickwork-type packing arrangement of the dyes.

3.2.4 Conclusion

In order to explore the intrinsic charge carrier mobility values without contributions of grain boundaries, SCFETs were fabricated of dye nBu**D3**tBu**A5** on TPA modified substrates. These devices showed an average mobility of 1.05 $cm^2\ V^{-1}\ s^{-1}$ for nanocrystal thicknesses $d < 500$ nm with the best device reaching a value of 2.34 $cm^2\ V^{-1}\ s^{-1}$ measured in air. This is the first time that high mobility values >1.00 $cm^2\ V^{-1}\ s^{-1}$ are demonstrated for organic field-effect transistor devices consisting of a highly dipolar compound (dipole moment of 13.3 D) as organic semiconductor. Furthermore, it could be

demonstrated by DFT calculations that holes are primarily transported along the π-π-stacking direction as expected from the π-overlap of the molecules. Other directions are however also possible with similar transfer integrals in three linearly independent directions, thus demonstrating the charges' ability to easily circumvent traps and defects. This points to an isotropic charge transport within the merocyanine dyes which is a most desirable property regarding materials for high mobility applications.[92]

3.3 Optical Properties of Dipolar Merocyanines Dyes‡

In the last section, the potential of merocyanine dyes for application in OFETs was described. In 2015, Lv *et al.* could show that by using an aminothiophene donor **D5** in combination with a thiazole acceptor **A5**, OTFTs with hole mobilities of up to 0.64 $cm^2\ V^{-1}\ s^{-1}$ could be achieved.[71] Furthermore, this compound showed intriguing UV-vis absorption properties in the thin film, i.e. a red-shifted J-band, and thus, the **D5A5** series (see Chart 6 and list of substances at the end of this thesis) was synthesized. As the hole transport properties of these dyes were not outstanding and only of the order of $10^{-2}\ cm^2\ V^{-1}\ s^{-1}$, this chapter focuses solely on their optical properties in the solid state.

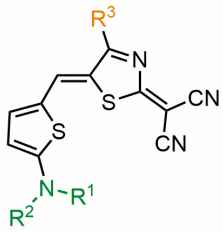

EtD5tBuA5: $R^1 = R^2 = Et$ $R^3 = t\text{Bu}$
EtBuD3tBuA5: $R^1 = Et$ $R^2 = n\text{Bu}$ $R^3 = t\text{Bu}$
nPrD5tBuA5: $R^1 = R^2 = n\text{Pr}$ $R^3 = t\text{Bu}$
nBuD5tBuA5: $R^1 = R^2 = n\text{Bu}$ $R^3 = t\text{Bu}$
nHeD5tBuA5: $R^1 = R^2 = n\text{Hex}$ $R^3 = t\text{Bu}$
nBuD5nBuA5: $R^1 = R^2 = n\text{Bu}$ $R^3 = n\text{Bu}$

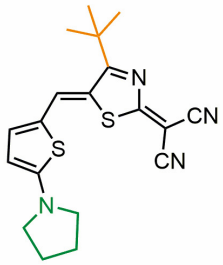

PyrlD5tBuA5

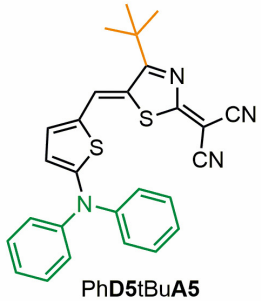

PhD5tBuA5

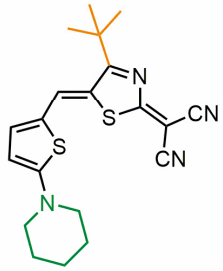

PipD5tBuA5

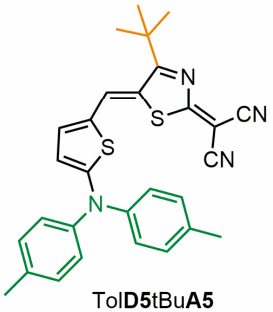

TolD5tBuA5

Chart 6. Chemical structures of merocyanine dyes investigated in this chapter with the varying substituent at the donor colored in green and the varying substituent at the acceptor colored in orange.

First, the molecular properties of all dyes were investigated by means of UV-vis absorption, EOAM and CV. As expected based on an identical π-scaffold, only very minor

‡ Parts of this chapter (results for dyes PyrlD5tBuA5, nPrD5tBuA5, nBuD5nBuA5) have been published in A. Liess, A. Lv, A. Arjona-Esteban, D. Bialas, A.-M. Krause, V. Stepanenko, M. Stolte, F. Würthner, *Nano Lett.* **2017**, *17*, 1719-1726. Reproduced with permission from the American Chemical Society, Copyright 2017.
Synthesis and characterization of molecular properties was done by Dr. Alhama Arjona Esteban, Dr. Hannah Bürckstümmer, Thorsten Günder and Fabian Holzmeier. Single crystal X-ray and XRD measurements were carried out by Ana-Maria Krause and Dr. David Schmidt. TEM & SAED measurements were performed by Dr. Vladimir Stepanenko and electro-optical measurements were done by Dr. Matthias Stolte.

differences are observed for the derived molecular properties λ_{max}, ε_{max}, $E_{1/2,Ox}$, μ_g and μ_{eg}. Then, the thin film optical properties of all dyes were measured, which show distinct H- or J-type absorption bands, respectively, as well as a weak fluorescence. The absorption bands are explained by combination of single crystal X-ray analysis with XRD, SAED and AFM of the thin films. To elucidate, which structural segment provides the observed spectral signatures, the polarized absorption of nanocrystals is discussed and the observed spectral shifts are verified to result from the identified signatures by time-dependent density functional theory (TD-DFT) calculations. Lastly, by mixing dyes which show either H- or J-type coupling, respectively, the incorporation of a J-type coupling dye into the H-type packing motif is demonstrated.

3.3.1 Molecular Properties

The molecular properties of the merocyanine dyes of the **D5A5** group were investigated by UV-vis absorption, EOAM and CV and are shown in Table 8.

For the dyes with aliphatic substituents, the UV-vis absorption spectra in chloroform solution show alike charge transfer absorption bands with absorption maxima (λ_{max}) at 648-654 nm, full widths at half maximum (*FWHM*) of around 700 cm^{-1} and high extinction coefficients in the range of 111000-147000 L mol^{-1} cm^{-1} (Figure 46, Table 8). Additionally, the transition dipole moments are similar with values of 9.6-10.3 D. The ground state dipole moments μ_g of the dyes were measured by EOAM in 1,4-dioxane and showed to be as large as 13-14 D while the change of the dipolarity upon optical excitation ($S_0 \rightarrow S_1$) is low with a dipole difference of only +2 D. This implies that there is already in the ground state a significant charge transfer from the donor to the acceptor moiety as reflected by the large ground state dipole moments. Accordingly, the resonance parameter c^2 is about 0.45 for all these dyes, meaning that the molecules are close to the cyanine limit of $c^2 = 0.5$ with an almost equal contribution of both resonance structures. By CV, one reversible oxidation as well as one irreversible reduction wave could be determined for all dyes at similar potentials (Table 8). The electrochemical bandgap measured by CV as the difference between the oxidation and reduction potentials as well as the optical bandgap determined from the absorption maximum (hc_0/λ_{max}) correlate well and differ only by 0.2 eV, implying that the $S_0 \rightarrow S_1$ transition mainly arises from a charge transfer excitation from the HOMO to the LUMO level.

Table 8. (Electro-)optical and electrochemical properties of merocyanine dyes[a] determined by UV-vis[b], electro-optical absorption spectroscopy[c] as well as cyclic voltammetry[d].

	λ_{max}[b] / nm	ε_{max}[b] / L mol^{-1} cm^{-1}	μ_{eg}[b] / D	*FWHM*[b),e] / cm^{-1}	μ_g[c] / D	$\Delta\mu$[c] / D	c^2 / 1	$E_{1/2,Ox}$[d] / V	$E_{p,Red}$[d),f] / V
Pyrl**D5**tBu**A5**	651	124000	10.1	690	13.9	2.1	0.45	0.34	−1.39
Pip**D5**tBu**A5**	651	128800	10.2	710	-	-	-	-	-
Et**D5**tBu**A5**	649	124000	9.7	700	-	-	-	-	-
EtBu**D5**tBu**A5**	650	129900	9.9	720	-	-	-	-	-
nPr**D5**tBu**A5**	651	126100	9.7	690	13.6	2.4	0.44	0.36	−1.36
nBu**D5**tBu**A5**	654	111400	9.6	640	13.1	2.5	0.44	0.37	−1.39
nHe**D5**tBu**A5**	652	146300	10.3	690	-	-	-	-	-
nBu**D5**nBu**A5**	648	127900	10.1	700	13.2	2.0	0.45	0.37	−1.35
Ph**D5**tBu**A5**	658	69500	10.0	1260	10.4	9.1	0.29	0.49	−1.20
Tol**D5**tBu**A5**	664	76300	10.2	1340	-	-	-	-	-

[a] Due to similar optical and electrochemical properties of dyes **D5A5**, EOAM and CV were not performed for dyes Pip**D5**tBu**A5**, Et**D5**tBu**A5**, EtBu**D5**tBu**A5**, nHe**D5**tBu**A5** and Tol**D5**tBu**A5**; [b] UV-vis: $CHCl_3$, ~10^{-5} M, 298 K; [c] EOAM: 1,4-dioxane, ~10^{-6} M, 298 K, corrected to give "gas phase" dipole moments by Onsager cavity field correction;[78] [d] CV: CH_2Cl_2, ~10^{-4} M, 298 K, TBAHFP as electrolyte and with reference Fc/Fc^+; [e] *FWHM* was derived as twice the distance between the absorption maximum to the closest edge at half maximum of the unsymmetrically shaped absorption bands to prevent falsification by overlapping transitions; [f] Peak potential of irreversible redox process.

For the two dyes with aryl substituents, the situation is slightly different. Again, these dyes show charge transfer bands in chloroform solution with absorption maxima at 658-664 nm but much lower extinction coefficients in the range of 70000 L mol^{-1} cm^{-1} and *FWHM* of around 1300 cm^{-1}. Compared to the dyes with aliphatic substituents, these two molecules exhibit similar transition dipole moments of 10.0-10.2 D. Concerning the electrooptical properties, dye Ph**D5**tBu**A5** shows a lower ground state dipole moment of 10.4 D with a much higher change of the dipolarity upon optical excitation of 9.1 D. This corresponds also with the lower c^2 value of 0.29, which means that this dye is more polyene-like. The electrochemical redox potentials show a shift towards more positive values compared to the dyes with aliphatic substituents, but again a reversible oxidation and an irreversible reduction wave could be determined, yielding a difference of 0.2 eV for the electrochemical and optical bandgap.

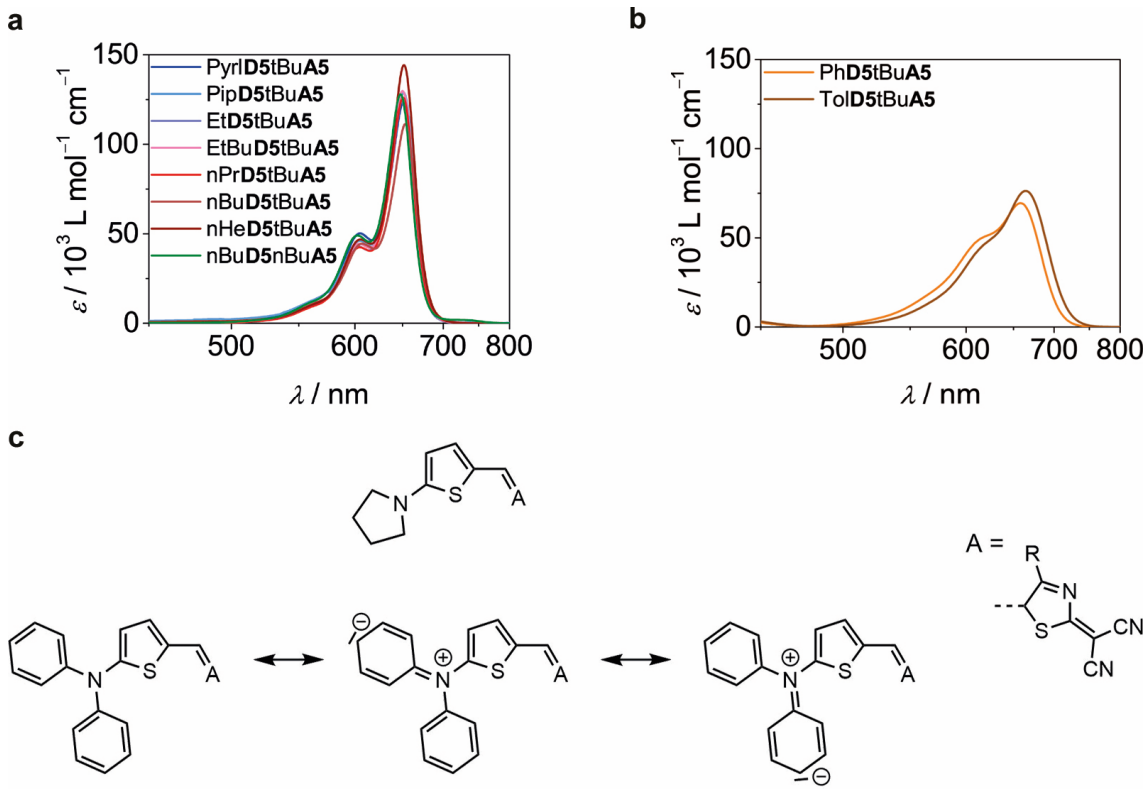

Figure 46. (a,b) UV-vis absorption spectra of dyes **D5A5** with aliphatic (a) and aryl (b) donor substituents in chloroform solution (10^{-5} M, 298 K); (c) Mesomeric resonance structures of neutral structure of dyes Pyrl**D5**tBu**A5** (top) and Ph**D5**tBu**A5** (bottom).

As all presented dyes are composed of the same chromophore backbone, it seems reasonable that the optical and electronic molecular properties investigated by UV-vis absorption, EOAM and CV are almost identical for dyes with aliphatic substituents. The deviations for dyes Ph**D5**tBu**A5** and Tol**D5**tBu**A5** can be explained as follows: While their absorption is significantly broadened compared to the dyes with aliphatic substituents, the transition dipole moments of all dyes are similar. Hence, the differences are explained by a conformational effect due to the attached phenyl or tolyl substituents, which have a clear effect on the π-system as depicted in Figure 46c. The corresponding neutral structure of the molecules can be described by several mesomeric resonance structures in contrast to the dyes with aliphatic substituents, yielding broader absorption spectra. Note that for all dyes, no fluorescence was observed, which is the most common case for dipolar merocyanine dyes in solution as these typically undergo a fast nonradiative relaxation by a bond-twisting mechanism.[93]

3.3.2 Optical Properties of Thin Films

While the molecular properties of the dyes of the **D5A5** family with aliphatic substituents are quite similar and also the dyes with aryl substituents show comparable absorption maxima, the variation of the donor substituents should significantly influence the solid state packing and therefore the optical properties of the dyes in the solid state should vary.[94]

Accordingly, thin films with nominal thicknesses of 10 ± 3 nm were prepared by spin coating from a chloroform solution onto quartz substrates and absorption spectra were measured in transmission mode. Note that all thin films except that of nBu**D5**nBu**A5** were annealed at 130 °C for 5 min after fabrication to induce higher crystallinity as indicated by the more pronounced features in the thin film absorption spectra (see Figure 47 and Table 9; the details of the annealing process are described in section 3.3.3) and by diffraction results (see section 3.3.5). The thin film of nBu**D5**nBu**A5** was measured as prepared, as it showed a decrease in crystallinity upon heating. Although the molecular properties in solution are equal (for dyes with aliphatic substituents) or at least comparable (for dyes with aryl substituents), the thin film absorption spectra differ significantly and show intriguing absorption bands, such as a dimer-like broad absorption (nBu**D5**nBu**A5**) or narrow and strongly shifted H- and/or J-type absorption bands (all other dyes).

In this regard, the broad absorption spectrum for the thin film of nBu**D5**nBu**A5** exhibits two maxima located at 606 nm and 664 nm. While thin film spectra − compared to solution spectra − usually show a broadening and red-shift of the absorption even in the amorphous state, the appearance of a blue-shifted maximum is indicative of the formation of dimers with H-type coupling. Indeed, such dimer formation could also be observed in concentration-dependent UV-vis absorption studies in 1,4-dioxane with a maximum of the dimeric species at $\lambda = 588$ nm (Figure 48a, dimerization constant[34b] $K_D = 600\ M^{-1}$), which matches well the thin film absorption at 606 nm. Thus, it can be hypothesized that the thin film is composed of dimeric species and amorphous material of nBu**D5**nBu**A5**, which is indeed later supported by the diffraction results.

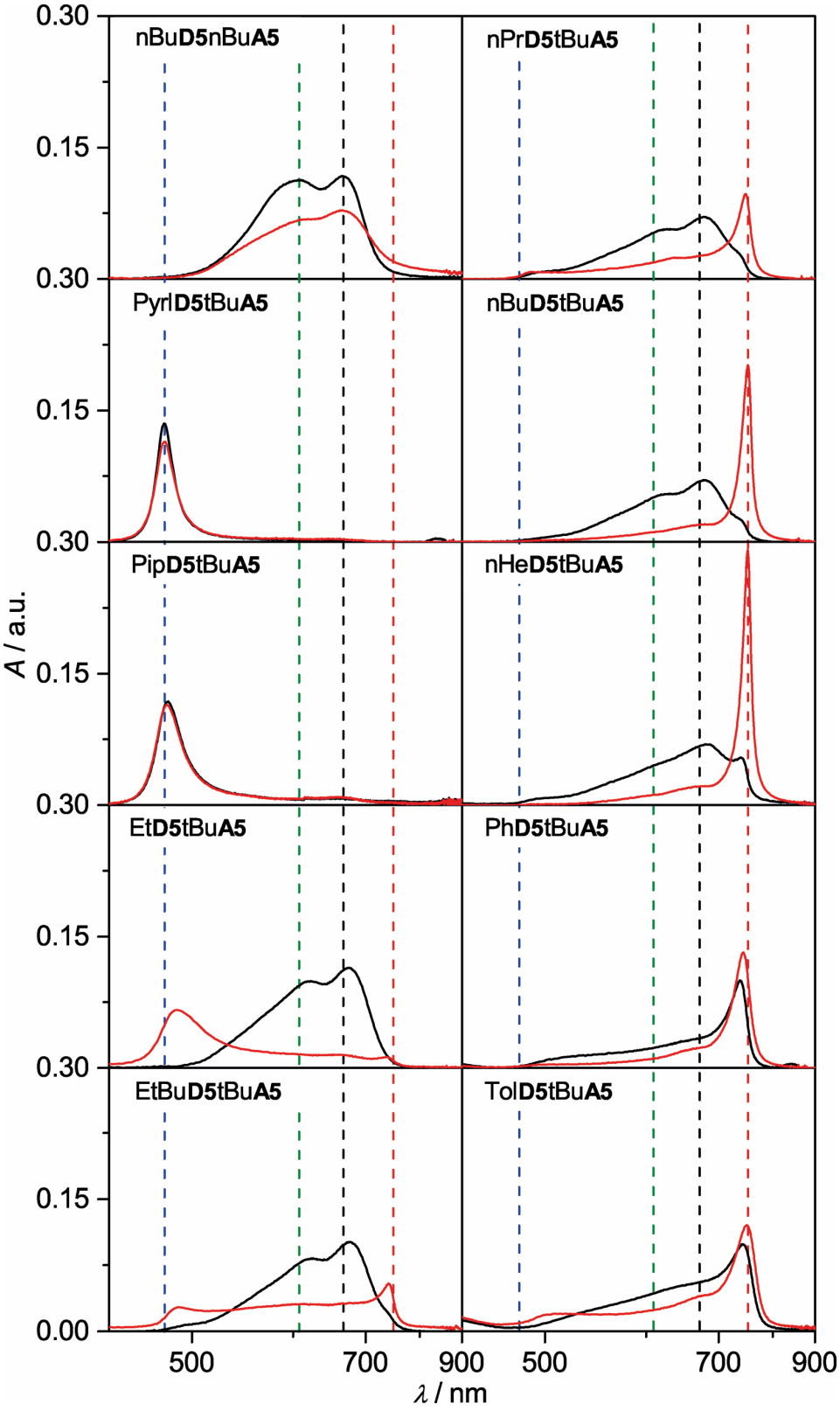

Figure 47. UV-vis absorption spectra of thin films of dyes **D5A5** measured directly after fabrication (black solid lines) and after annealing at 130 °C for 5 min (red solid lines). As a guide to the eye, the dashed lines mark the position of the H-band of PyrlD5tBu**A5** at 479 nm (blue), of the dimer and monomer band of nBu**D5**nBu**A5** at 606 nm (green) and 664 nm (black), respectively, as well as the J-band of nHe**D5**tBu**A5** at 750 nm (red).

Table 9. Optical properties of thin films of dyes of the **D5A5** group on quartz substrates after fabrication as well as after annealing at 130 °C for 5 min.

Dye	Thin film as fabricated[a)]		Thin film annealed[b)]		Nanocrystals[c)]		Calculation[d)]
	λ_{max} / nm	*FWHM*[e)] / cm^{-1}	λ_{max} / nm	*FWHM*[e)] / cm^{-1}	λ_{max} / nm	*FWHM*[e)] / cm^{-1}	λ_{max} / nm
Pyrl**D5**tBu**A5**	478	580	479	750	475	1660	521
Pip**D5**tBu**A5**	482	880	480	840	-	-	-
Et**D5**tBu**A5**	673	1550	487	1130	-	-	-
EtBu**D5**tBu**A5**	676	1500	489	900	-	-	-
nPr**D5**tBu**A5**	678	1870	746	420	488 741	596 580	622 755
nBu**D5**tBu**A5**	678	1640	751	280	-	-	-
nHe**D5**tBu**A5**	680	n/a	750	280	-	-	-
nBu**D5**nBu**A5**	606	3290	664	2150	-	-	618
Ph**D5**tBu**A5**	737	490	742	530	-	-	-
Tol**D5**tBu**A5**	741	710	749	630	-	-	-

[a)] Thin film deposited by spin coating on quartz; [b)] Thin film deposited by spin coating on quartz after annealing at 130 °C for 5 min; [c)] Nanocrystals grown from solution on quartz substrates (see section 3.3.6); [d)] TD-DFT (ωB97/def2-SVP), absorption maxima of a stack of eight molecules (Pyrl**D5**tBu**A5**), a strand of eight molecules (nPr**D5**tBu**A5**) as well as a dimer moiety (nBu**D5**nBu**A5**, see section 3.3.7). The wavelengths were shifted by 5400 cm^{-1} towards lower energies to adjust for the difference given for the calculated and experimental monomer absorption band (see ref. [40]); [e)] *FWHM* was derived as twice the distance between the absorption maximum to the closest edge at half maximum of the unsymmetrically shaped absorption bands to prevent falsification by overlapping transitions.

For the dyes with a *tert*-butyl group at the acceptor, the situation is different. All dyes with alkyl chains at the donor show a broad spectrum after fabrication, resembling the spectrum of the annealed thin film of nBu**D5**nBu**A5** caused by a disordered arrangement in amorphous state. However, annealing of the thin films always yields a hypsochromically and/or bathochromically shifted absorption band with absorption maxima at 480-490 nm and 735-750 nm, respectively, as well as for the most prominent J-bands of nBu**D5**tBu**A5** and nHe**D5**tBu**A5**, a remarkably reduced *FWHM* of 280 cm^{-1}. This implies a strong H- or J-type exciton coupling and it seems that the alkyl chain length plays a crucial role in determining which of the H- or J-band is most prominent. For Et**D5**tBu**A5**, bearing ethyl chains, the H-band is clearly the most prominent, while for longer chain lengths (*n*-propyl, *n*-butyl, *n*-hexyl) the J-band is more dominant. For dye Et**D5**tBu**A5** with one ethyl and one *n*-butyl chain, i.e. an intermediate case, the annealing procedure yields H- and J-bands of similar intensity. Thus, the intensity of the H-band decreases with increasing chain

length while the intensity of the J-band increases with increasing chain length. Upon rigidifying the donor substituents (Pyrl**D5**tBu**A5** and Pip**D5**tBu**A5**), the hypsochromically shifted band appears already after spin coating and the annealing process just slightly changes the intensity of the band. On the other hand, when introducing bulky phenyl or tolyl substituents, the J-band appears already after spin coating and the intensity can be slightly raised by annealing of the thin films. For the dyes with the *tert*-butyl acceptor, similar aggregation studies in solution as for nBu**D5**nBu**A5** were unfortunately not possible due to the low solubility, but show for Pyrl**D5**tBu**A5** an indication of an H-band shortly before precipitation (Figure 48b).

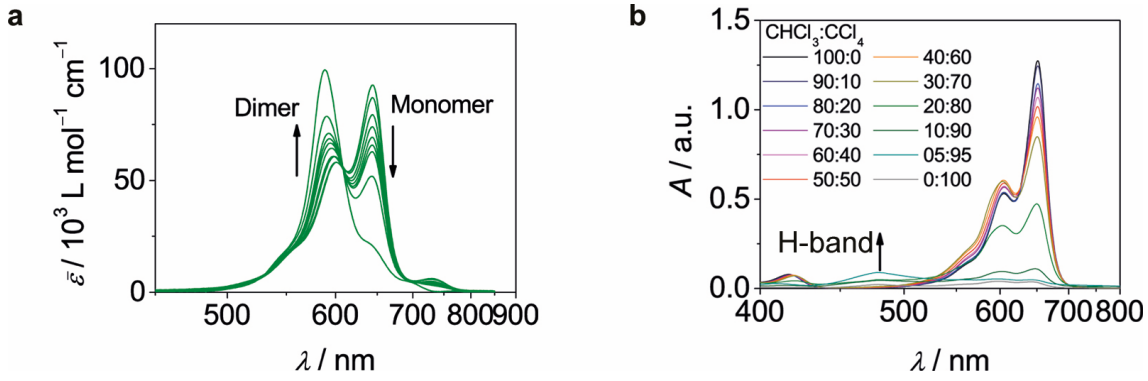

Figure 48. (a) Concentration-dependent UV-vis absorption spectra of nBu**D5**nBu**A5** in 1,4-dioxane (293 K) with the arrows indicating changes upon increasing concentration from 10^{-6} M to 10^{-3} M; (b) UV-vis absorption aggregation study of dye Pyrl**D5**tBu**A5** in $CHCl_3$:CCl_4 mixtures (10^{-4} M, 293 K). At $CHCl_3$ quantities of ≤ 20 %, precipitation occurred and a small H-band at 479 nm was observed which is exactly the same position as the H-band of the thin film of dye Pyrl**D5**tBu**A5**.

By equation (20), the exciton coherence length N_C, which is the number of molecules over which the exciton wavefunction is delocalized and thus the lower limit of the aggregate size,[95] can be estimated for J-coupled dyes from the linewidth of the spectra of the monomer and the aggregated state in solution.[96] Here, this equation is applied to the thin film spectra to assess the coherence length in the solid state as it has been demonstrated before.[96a] To prevent falsification from overlapping transition, the linewidths of the spectra at two thirds of the maximum has been used for both the monomer ($\tilde{\nu}_{2/3}$(M)) and the J-coupled dyes ($\tilde{\nu}_{2/3}$(J)):

$$\sqrt{N_C} = \frac{\tilde{\nu}_{2/3}(\mathrm{M})}{\tilde{\nu}_{2/3}(\mathrm{J})} . \qquad (20)$$

Calculating the coherence lengths for thin films of dyes showing J-type coupling results in values of 3 ± 2 (nPr**D5**tBu**A5**) to 7 ± 2 (nHe**D5**tBu**A5**). These are of the same size as

those obtained for J-aggregates of merocyanine dyes in Langmuir-Blodgett films and of J-aggregates of thiacarbocyanine dyes in thin films,[96a, 97] yet smaller than for some J-aggregates of cyanine dyes in solution, which show coherence lengths up to 10-20.[98] Note, that the values are calculated from the linewidth of the monomer in solution ($\tilde{\nu}_{2/3}$(M) = 510 cm^{-1}), which is significantly smaller than that of the amorphous thin film spectrum. Using the linewidth of the monomer band at 664 nm of the thin film spectrum of nBu**D5**tBu**A5** ($\tilde{\nu}_{2/3}$(M) = 1260 cm^{-1}), a coherence length of 42 ± 7 is obtained for thin films of nHe**D5**tBu**A5**, which is considerably higher than the values discussed above.

Furthermore, the emission properties of thin films of Pyrl**D5**tBu**A5**, nPr**D5**tBu**A5** and nHe**D5**tBu**A5** with an optical density (OD) of 0.1-0.3 were investigated in a front face geometry setup (22.5°). Only a very weak emission with maxima in the same range of 749-764 nm was observed for an excitation at 480 nm, although large emission and excitation bandwidths of 12 nm were applied. This yields a small Stokes shift of 50 cm^{-1} for nPr**D5**tBu**A5** and nHe**D5**tBu**A5** (Figure 49, Table 10), together with small *FWHM* of 480 cm^{-1} and 330 cm^{-1}, respectively, confirming the J-type coupling although higher emission intensities are usually expected for J-aggregates.[99] In contrast to aggregates in solution, coupled dyes in the solid state suffer from additional deactivation pathways (e.g. grain boundaries, quenching sites),[100] further rationalizing the low fluorescence intensity.

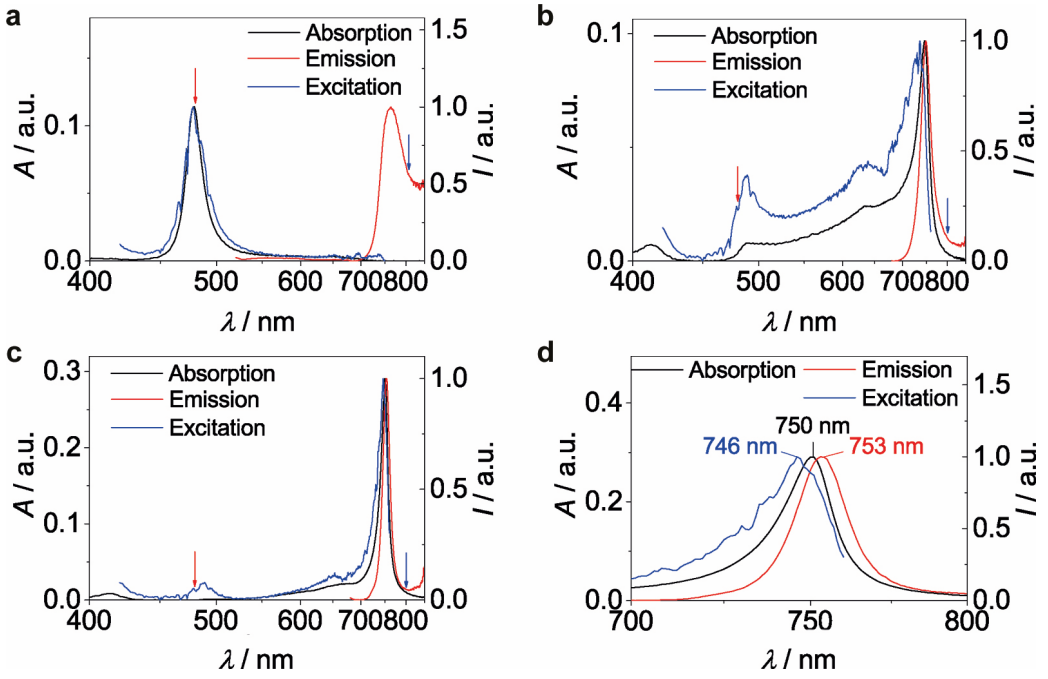

Figure 49. Absorption (black), emission (red) and excitation (blue) spectra of thin films of Pyrl**D5**tBu**A5** (a), nPr**D5**tBu**A5** (b) and nHe**D5**tBu**A5** (c,d); In (a-c), the arrows indicate the wavelengths at which the excitation (blue) and emission (red) spectra were recorded, respectively.

Table 10. Properties of absorption, excitation and emission spectra of spin-coated thin films of Pyrl**D5**tBu**A5**, nPr**D5**tBu**A5** and nHe**D5**tBu**A5** on quartz substrates after annealing at 130 °C for 5 min.

Dye	Absorption	Emission[a),b)]		Excitation[a),c)]	Stokes shift / cm^{-1}
	λ_{max} / nm ($\tilde{\nu}_{max}$ / cm^{-1})	λ_{max} / nm ($\tilde{\nu}_{max}$ / cm^{-1})	*FWHM* / cm^{-1}	λ_{max} / nm ($\tilde{\nu}_{max}$ / cm^{-1})	
Pyrl**D5**tBu**A5**	479 (20880)	764 (1300)	850[d)]	478 (20920)	n/a[e)]
nPr**D5**tBu**A5**	746 (13400)	749 (13350)	480	489/736 (20450/13590)	50
nHe**D5**tBu**A5**	750 (13330)	753 (13280)	330	489/746 (20450/13400)	50

[a)] Measured with emission and excitation bandwidths of 12 nm; [b)] Excitation at 480 nm; [c)] Emission at 800 nm; [d)] *FWHM* was was derived as twice the distance between the emission maximum to the closest edge at half maximum to prevent falsification by the offset at higher wavelengths caused by the detector; [e)] No Stokes shift is given as no clear J-band was observed in absorption measurements.

The excitation spectra (emission monitored at 800 nm) show the H-type (Pyrl**D5**tBu**A5**) as well as H- and J-type features (nPr**D5**tBu**A5**, nHe**D5**tBu**A5**), which correlate well to the respective absorption spectra. This demonstrates that excitation into the lowest (J-band) as well as highest excited state (H-band) is possible, indicating that the H- and J-bands are lying within one exciton band. Additonally, the large spectral overlap for the J-coupled dyes should induce a high reabsorption probability χ, which can be estimated by equation (21),[101] with $I_{Fl}(\lambda)$ being the fluorescence spectra normalized to $\int_0^\infty I_{Fl}(\lambda)\,d\lambda = 1$ and $A(\lambda)$ the absorption spectra of the thin film. Note, that this equation is derived for fluorescence spectra without contamination by reabsorption, however, as the films are already very thin, an assessment is made based on the obtained spectra:

$$\chi = \int_0^\infty I_{Fl}(\lambda)\,(1 - 10^{-A(\lambda)})\,d\lambda\,. \qquad (21)$$

Calculating the reabsorption probabilities leads to values of 11 % (nPr**D5**tBu**A5**) and 30 % (nHe**D5**tBu**A5**), confirming that already for thin films of only 10 nm (OD of 0.1-0.3), the reabsorption probability is high. As noted, the spectra used for this estimation are already contaminated by reabsorption effects and thus the calculated values are only a lower estimate of the real reabsorption probabilities which should be even larger. Based on these considerations, it seems not surprising that an estimation of the quantum yield within an integrating sphere setup was unfortunately not possible. Here, the design of the integrating sphere with multiple reflections of the light beam might result in even stronger

reabsorption of the emitted light. Alongside, the low signal intensity could also be not sufficient for the sensitivity of the integrating sphere setup of about 5 % and does account also for the fact that no lifetime measurements could be performed.

Comparing the *FWHM* and the Stokes shift of the thin film spectra of nHe**D5**tBu**A5** (330 cm^{-1} and 50 cm^{-1}, respectively) to J-aggregates of other well-known dyes, similar Stokes shifts of 54 cm^{-1} are found for J-aggregates of pseudoisocyanine dyes in thin films.[102] However, J-aggregates of thiacarbocyanine and perylene dyes in solution show either higher or lower values of the Stokes shift of 290 cm^{-1} (perylenes)[103] or even down to 40 cm^{-1} (thiacarbocyanines).[104] The *FWHM* of the fluorescence for these aggregates is higher for J-aggregates of perylene dyes with 880 cm^{-1},[103] but lower for cyanine dyes with values between 220 cm^{-1} and 60 cm^{-1}.[104] This comparison to other archetype J-aggregates demonstrates clearly that the thin film of nHe**D5**tBu**A5** shows model-like J-type coupling. Due to the high reabsorption of at least 30 %, the Stokes shift and *FWHM* of spectra without contamination by reabsorption effects should be even lower.

Although all dyes show different absorption spectra, it is quite remarkable that the H- and J-bands appear at similar positions for the whole series of molecules and that the same J-type emission band is observed irrespective of the excitation wavelength (489 nm or 736/746 nm). This indicates that strong coupling between the dyes in the solid state generates an exciton band from ~480 nm to ~750 nm (20830-13330 cm^{-1}), corresponding to an energy difference of 7500 cm^{-1} (0.93 eV).

3.3.3 Conversion to the Crystalline State

To monitor the irreversible formation of the crystalline state and to rationalize the annealing procedure described in the last section, UV-vis absorption spectra were recorded in-situ for different heating processes on a precision hot stage in reflection mode. As the H-band of Pyrl**D5**tBu**A5** and Pip**D5**tBu**A5** is already present after spin coating, the conversion was monitored exemplarily for thin films of nHe**D5**tBu**A5**, showing the highest intensity for the J-band absorption (note that due to the different experimental setups, the absorption values in this section differ slightly from those in section 3.3.2).

First, spin-coated samples of nHe**D5**tBu**A5** were heated up to 150 °C with a heating rate of 2 K min^{-1} and the in-situ monitored absorption spectra at different temperatures are shown in Figure 50. With rising temperature, the absorption intensity of the J-band increases and reaches its maximum at 130 °C while afterwards slightly decreasing for

heating up to 150 °C. Furthermore, the maximum of absorption shows a shift from 733 nm (25 °C) up to 750 nm (130 °C). The absorption at 677 nm, indicative of amorphous material, decreases from 25 °C to 130 °C, while increasing again for higher temperatures approaching the melting point of 159 °C. An isosbestic point at 711 nm can be observed in the temperature range 25-100 °C, whereas for temperatures higher than 100 °C, this isosbestic point does not prevail due to a sharpening of the J-type absorption band.

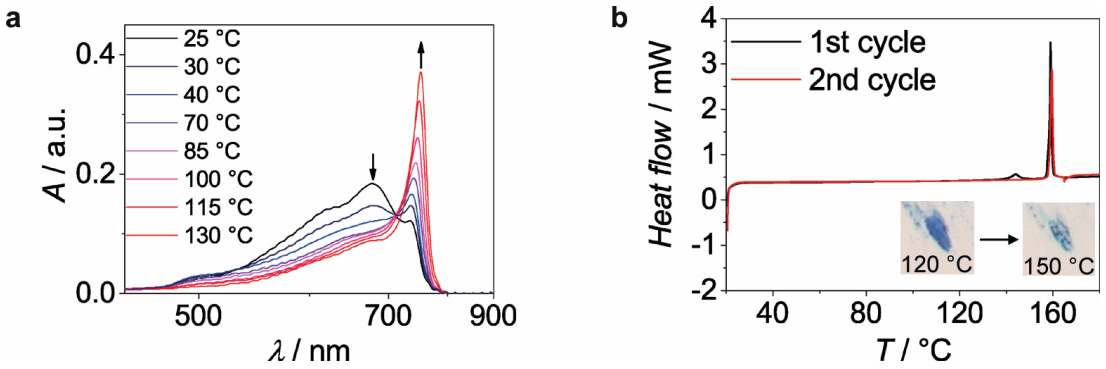

Figure 50. (a) UV-vis absorption spectra of a thin film of nHe**D5**tBu**A5** on quartz for different temperatures during a heating process with a heating rate of 2 K min^{-1}; (b) DSC heating curves of 2 mg powder of nHe**D5**tBu**A5** for two consecutive cycles with a heating rate of 2 K min^{-1} (Inset: Microscopy image of powder of nHe**D5**tBu**A5** showing an irreversible color change within the temperature range of 120-150 °C; Images scale to 50×50 µm).

While an isosbestic point suggests a transition between two species, in this case presumably the amorphous and crystalline state, the loss of such a point in thin film spectra upon heating does not necessarily imply the presence of an additional species. The sharpening of the J-band upon heating to 60% of its initial value instead suggests an increase of the coherence length, meaning that molecules first assemble in small aggregates at lower temperatures and only upon futher heating, larger two-dimensional domains are formed. The absence of other species can also be deduced from DSC measurements which show only one small signal in the first cycle (at 144 °C) before the melting temperature for a powder of nHe**D5**tBu**A5** (Figure 50b). Additionally, a color change of powder of nHe**D5**tBu**A5** can be observed in this temperature regime with a microscope which corresponds well to the color change of the thin films. The temperature in the DSC measurements is slightly higher than the temperature applied for annealing of the thin films, however, the two different experimental approaches with different setups and samples have to be taken into account, surely leading to different heat flows for the transition. These experimental results again indicate an amorphous to crystalline transition which is also supported by the diffraction and AFM results (see section 3.3.5).

Second, the same transition was recorded for an isothermal heating process and is shown for a temperature of 130 °C in Figure 51a. The recorded UV-vis absorption spectra demonstrate the fast formation of the J-band which is almost fully evolved after already 60 s, validating the annealing procedure of 5 min at 130 °C.

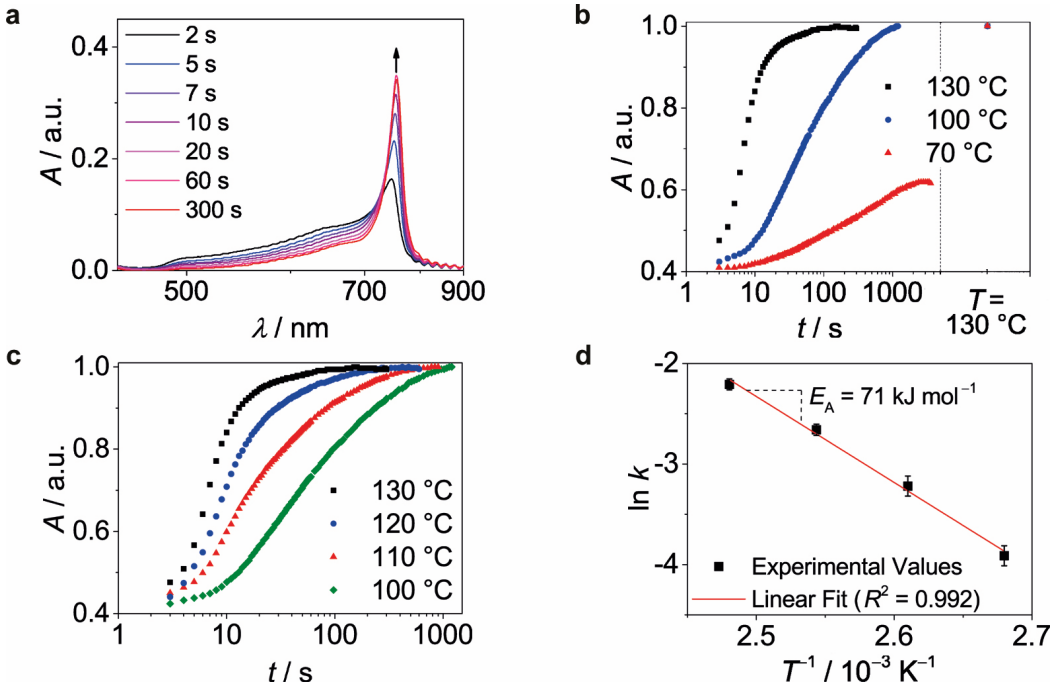

Figure 51. (a) UV-vis absorption spectra of a thin film of nHe**D5**tBu**A5** for different times during an isothermal heating process at 130 °C; (b,c) Time-dependent evolution of the absorption of the J-band of thin films of nHe**D5**tBu**A5** on quartz at different temperatures normalized to the absorption of the fully formed J-band; (d) Arrhenius plot of the rate constants derived from the data in (c) with linear fit (red line) to calculate the activation energy.

To gain insight into the kinetics of the process, the formation was also monitored for temperatures of 70 °C, 100 °C, 110 °C and 120 °C. For $T \geq 100$ °C, a full conversion to the J-coupled species can be observed in contrast to a lower temperature of 70 °C, where a full conversion is only reached by additional heating to 130 °C (Figure 51b). The formation of the fully converted crystalline state can be described by a first order kinetic process with the absorption maximum increasing by e^{-kt} in time, with k being the rate constant. From the data of Figure 51c, rate constants in the range of 0.019 s^{-1} (100 °C) to 0.114 s^{-1} (130 °C) are calculated. By plotting ln k against T^{-1} in an Arrhenius plot, the activation energy E_A of the formation of the J-band can be estimated to be 71 kJ mol^{-1}. This value is in the same range as that for the amorphous to crystalline transition of thin film rubrene,[105] which is as expected for the formation of the crystalline state.

3.3.4 Crystallographic Analysis

To clarify, if the significantly different optical signatures can be attributed to H-/J-type coupling arising from different solid state packing arrangements, single crystal structures of six compounds, namely Pyrl**D5**tBu**A5**, Et**D5**tBu**A5**, EtBu**D5**tBu**A5**, nPr**D5**tBu**A5**, nBu**D5**nBu**A5** as well as Ph**D5**tBu**A5**, could be successfully determined. These structures were also verified for the thin films by XRD and SAED. To quantify the slipping between the molecules, DFT calculations were performed to visualize the transition dipole moment of the molecules (see Figure 52).

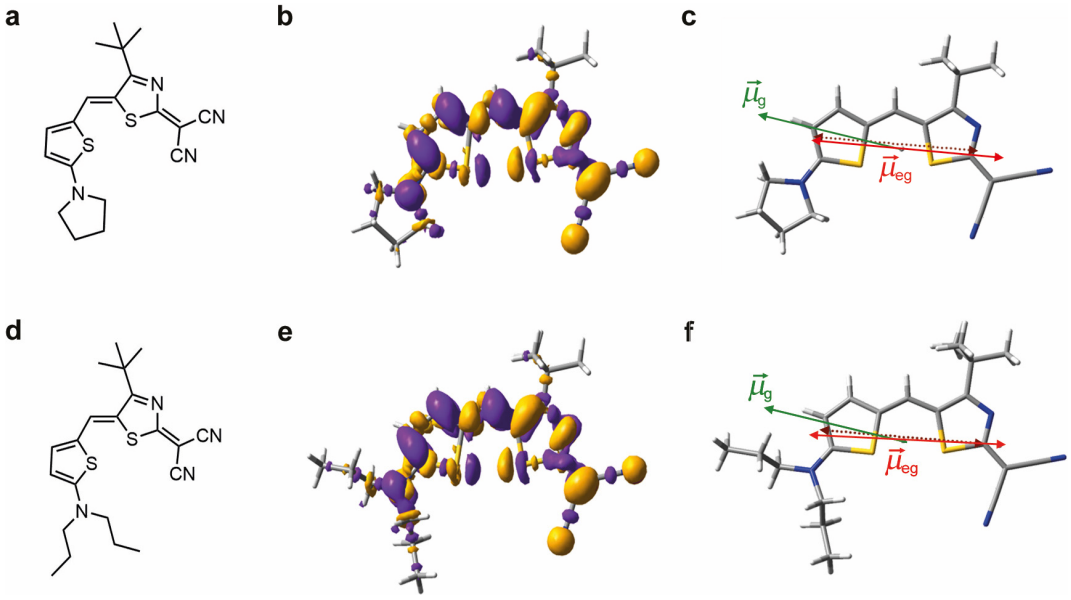

Figure 52. Results of DFT calculations for merocyanine dyes Pyrl**D5**tBu**A5** (a-c) and nPr**D5**tBu**A5** (d-f) with molecular structure (a,d) as well as the transition densities for the transition from the ground to the first excited state with an isovalue of 0.0015 a.u. (TD-DFT, ωB97/def2-SVP) (b,e). Additionally, the ground-state dipole moments μ_g (DFT, ωB97/def2-SVP, green arrow) and transition dipole moments μ_{eg} (TD-DFT, ωB97/def2-SVP, solid red arrow) for the transition from the ground state to the first excited state are shown. Moreover, the approximated transition dipole moments (dashed dark red arrow) for the calculations of the slip angle θ (c,f) are given.

The single crystal structures of all dyes are depicted in Figure 53 and Figure 54. Driven by electrostatic interactions between these dipolar molecules, centrosymmetric dimers with antiparallel arrangement of neighboring molecules can be observed in all cases. However, these dimers exhibit different lateral slips with slip angles θ in the range of 23-77°.

Originating from this primary dimer motif, the single crystal structures can be described as follows: For Pyrl**D5**tBu**A5** the dimer units stack cofacially on top of each other with

the molecules being slightly tilted to the (001) layer and packing in a card stack fashion, yielding equidistant spacing of the molecular layers with close distances of 3.35 Å. Accordingly, there are two nearest neighbors for each molecule and the stacking sequence can be described by two repeating layers ABAB. For Et**D5**tBu**A5**, the molecules again pack in the card stack fashion with an equidistant layer spacing of 3.50 Å for a repeating unit of two layers ABAB. However, within one layer, the molecules show an alternating tilt to the (010) layer, yielding a zig-zag pattern along the *c*-axis within the single crystal structure.

By substituting one ethyl chain with a *n*-butyl chain, the dimer for dye EtBu**D5**tBu**A5** exhibits a significantly larger lateral slip with a slip angle of 23°/35° (the slip angles depends on the molecule at which the angle was determined, see section 2.3; note that for another dimer in the crystal structure, slip angles of 29°/36° were determined). Again, an equidistant layer arrangement ABAB is found with layer distances of 3.83 Å. Within one of these layers, the molecules are twisted with respect to each other and zig-zag patterns are found with the molecules being tilted by 40°. Considering the crystal structure of nPr**D5**tBu**A5**, the layer sequence is now described by four different molecular layers ABCD while as for the other dyes, the molecular layers are equidistant with a layer distance of 3.86 Å. Here, the slipped dimers do not stack on top of each other but form zig-zag strands throughout the crystal lattice with the molecular axes twisted by 33°. For the dye with phenyl substituents Ph**D5**tBu**A5**, alternating distances between the layers are found with layer distances of 3.88 Å and 4.48 Å with an ABCD layer architecture. While the two molecules forming the dimer unit correspond to the layers with larger distance, two of these dimers again do not stack on top of each other but form zig-zag strands with the molecules being twisted by 61°. Additionally, these molecules exhibit the closer layer distance compared to the dimer. Lastly, the dye with the *n*-butyl chain at the acceptor (nBu**D5**nBu**A5**) shows a repeating unit of four layers ABCD and again, the layers show an alternating layer spacing with distances of 3.29 Å and 3.75 Å. This time, the molecules pack on top of each other and due to the alternation, four different layers ABCD are given and thus two dimer units can be distinguished in the crystal structure with slip angles of 44° (Figure 54c) and 59°. Therefore, although the dyes show a layer-like packing with antiparallel dimer synthons as commonly observed for dipolar dyes,[56b] the diversity of packing structures for the same chromophore backbone is unique for this series of molecules.

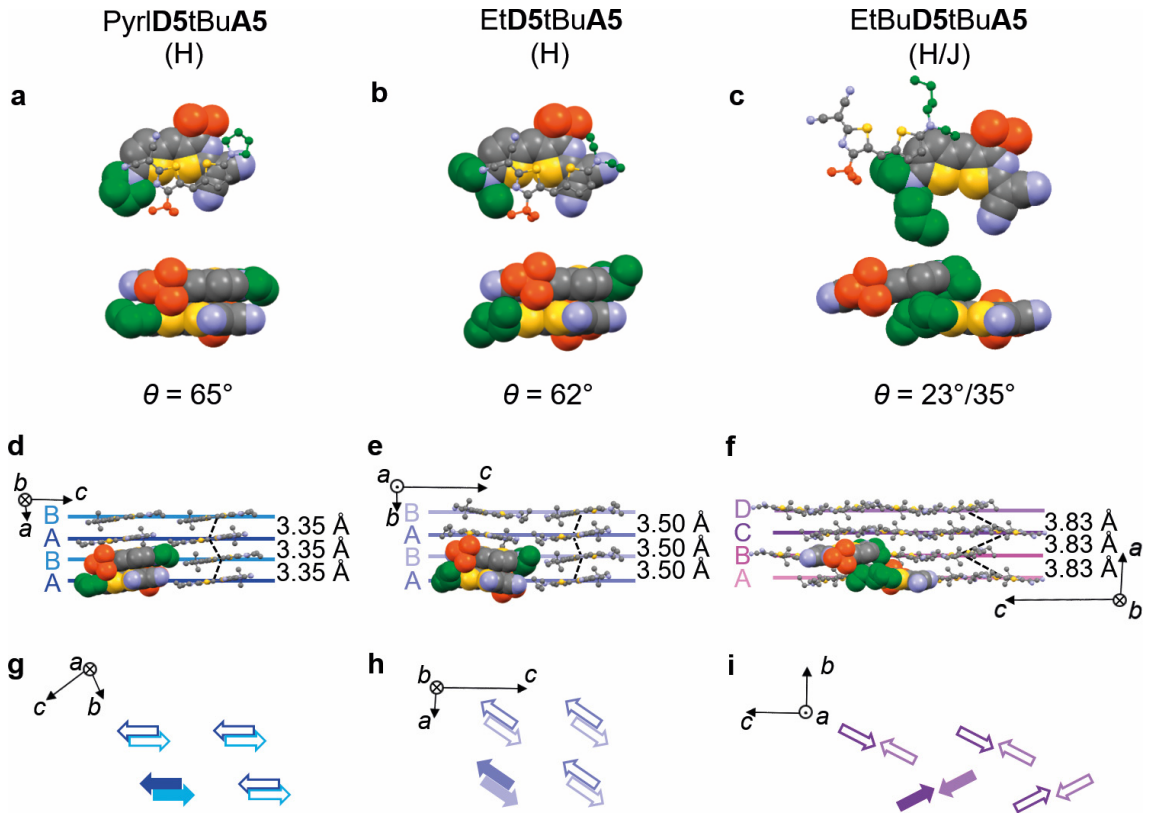

Figure 53. Single crystal structures of the three merocyanines PyrlD5tBuA5 (a,d,g), EtD5tBuA5 (b,e,h) and EtBuD5tBuA5 (c,f,i) with the aliphatic substituents at the acceptor/donor moiety marked in orange/green (for the other atoms, the color code N: blue, C: grey and S: yellow applies). (a-c) top and side view onto the antiparallel dimer unit representing the π-π-overlap together with the slip angle θ; (d-f) side view on the crystal structure with illustrated crystallographic layers formed by the molecules, layer sequence, the respective layer-to-layer distance, center-to-center distances of the molecules (dashed black line) and the closest dimer in spacefill representation; (g-i) schematic top view on the layers with the molecules' ground state dipole moment sketched as arrows to visualize the packing in the single crystal (the respective dimers of (a-c) are highlighted with filled arrows). Hydrogens are omitted for clarity.

An explanation for the observed packing motifs bearing dimers with different lateral slips can be made in terms of sterical demand of the *tert*-butyl/*n*-butyl groups at the acceptor and the substituents at the donor (Figure 53a-c and Figure 54a-c). For the acceptors bearing a *tert*-butyl group, this group partially fits into the void between the cyano group and the compact pyrrolidino or ethyl groups of the donor (PyrlD5tBuA5 and EtD5tBuA5) and thus a small lateral slip with close cofacial stacking of the dyes becomes possible. If the aliphatic chain is enlarged, the sterics of the *n*-butyl and *n*-propyl chains at the donor (EtBuD5tBuA5 and nPrD5tBuA5) as well as the bulky *tert*-butyl group at the acceptor prohibit the formation of a dense crystal composed of cofacially stacked dimers and instead demand a larger lateral slip.

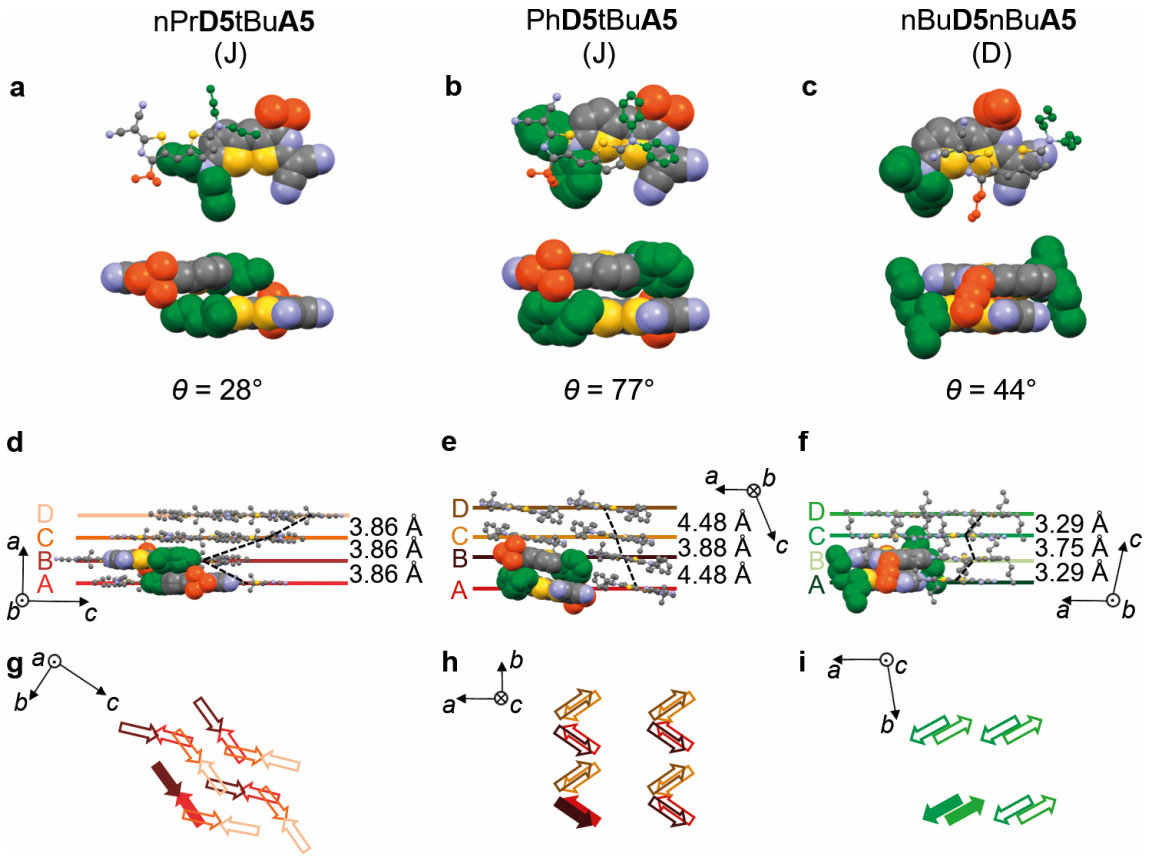

Figure 54. Single crystal structures of the three merocyanines nPr**D5**tBu**A5** (a,d,g), Ph**D5**tBu**A5** (b,e,h) and nBu**D5**nBu**A5** (c,f,i) with the aliphatic/aryl substituents at the acceptor/donor moiety marked in orange/green (for the other atoms, the color code N: blue, C: grey and S: yellow applies). (a-c) top and side view onto the antiparallel dimer unit representing the π-π-overlap together with the slip angle *θ*; (d-f) side view on the crystal structure with illustrated crystallographic layers formed by the molecules, layer sequence, the respective layer-to-layer distance, center-to-center distances of the molecules (dashed black line) and the closest dimer in spacefill representation; (g-i) schematic top view on the layers with the molecules' ground state dipole moment sketched as arrows to visualize the packing in the single crystal (the respective dimers of (a-c) are highlighted with filled arrows). Hydrogens are omitted for clarity.

In the case of dye Ph**D5**tBu**A5**, there is a large sterical demand of the phenyl substituent and accordingly, the π-π-distance of the molecules is significantly enlarged with a value above 4 Å. With this, a small lateral slip within the dimer moiety is retained. For nBu**D5**nBu**A5**, although the *n*-butyl chains at the donor exhibit a large sterical demand, the flexible *n*-butyl chain at the acceptor fits into the void between the acceptor cyano group and the donor *n*-butyl chains, enabling a cofacial packing. As this arrangement is not symmetrical to both sides of the molecules, alternating distances are consequently found in the crystal structure, which is rather common for merocyanines where the close cofacial antiparallel arrangement to one neighbor molecule is optimized at the expense of the other.[34b] It may be hypothesized that the dimer structure formed upon self-association

of nBu**D5**nBu**A5** in concentrated solution exhibits indeed a similar structure like the closest dimer found for this molecule in the solid state.

The reasoning of the further growth of such card stack and zig-zag like crystal structures can be visualized exemplarily by the electrostatic potentials on the van-der-Waals surface of monomers and dimers of dyes PyrI**D5**tBu**A5** and nPr**D5**tBu**A5** (Figure 55).

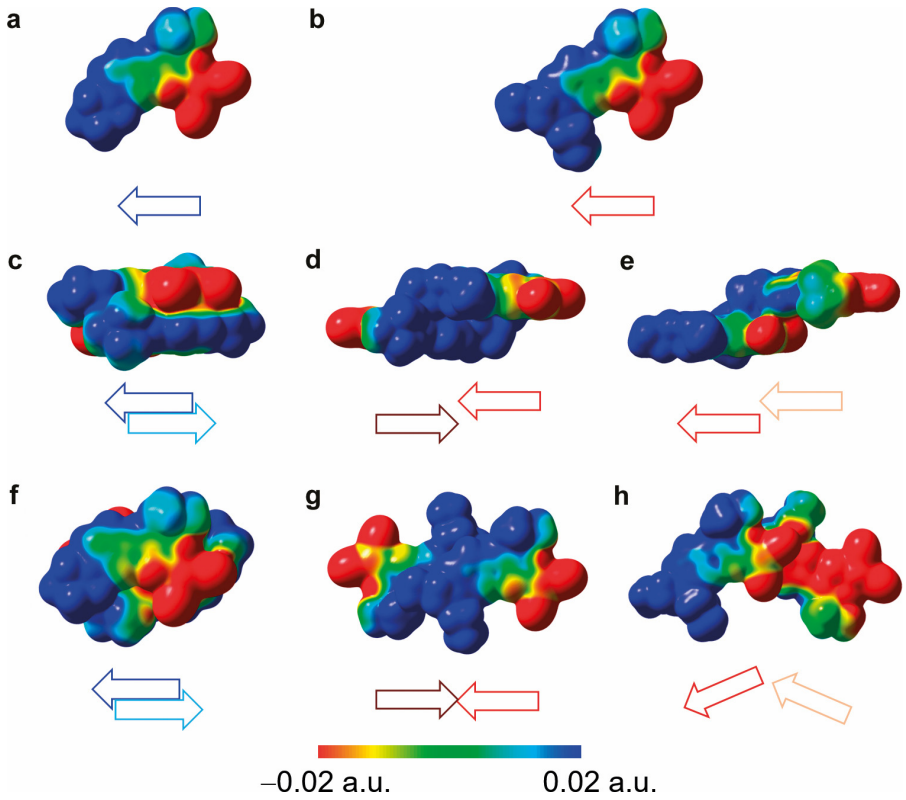

Figure 55. Electrostatic potentials on the van-der-Waals surface for an isovalue of 0.001 a.u. and schematic orientation of dipole moments of monomers (a,b) and dimers (c-h) of PyrI**D5**tBu**A5** (a,c,f) and nPr**D5**tBu**A5** (b,d,e,g,h) with side views (c-e) and top views (f-h) of the dimers.

For PyrI**D5**tBu**A5**, the card stack packing is directed by the retained dipolarity within the dimer moiety which directs a further growth of the stack. For dye nPr**D5**tBu**A5**, where such a dimer packing is not possible due to the combination of the sterical demanding *tert*-butyl group and the flexible *n*-propyl chains, a larger lateral slip is obtained for the dimer and additionally a zig-zag packing of other neighboring dyes is formed which might originate from the alternation of the molecules in one molecular layer (Figure 54). As one zig-zag strand would lead to a macroscopic dipole in a crystal which is energetically unfavorable, another zig-zag strand has to point in the opposite direction which is indeed the case.

3.3.5 Thin Film Characterization

To ensure that the thin film structures comply with the packing observed in single crystal structures, XRD and SAED experiments were done. The TEM images showed structured films for all dyes and thus the SAED measurements yielded polycrystalline diffraction cycles. Remarkably, by using a high resolution TEM, even single crystalline diffraction patterns were observed when selecting small regions in the range of 3 μm^2 (Figure 56). In the case of dye nBu**D5**nBu**A5**, the annealing step caused a complete loss of crystallinity as no diffraction pattern was observed after heating (Figure 57), which leads to the conclusion that the UV-vis spectrum of the annealed thin film can indeed be assigned to the dyes' absorption in the amorphous solid state.

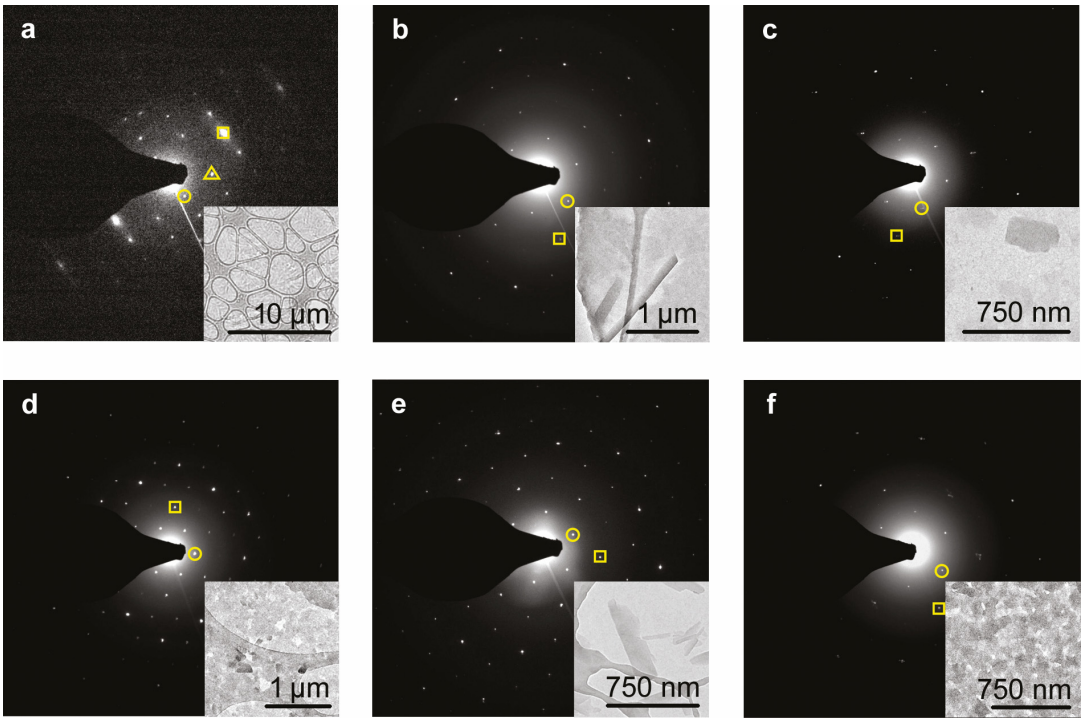

Figure 56. SAED patterns of single crystalline regions (< 3 μm^2) of annealed thin films of Pyrl**D5**tBu**A5** (a), Et**D5**tBu**A5** (b), EtBu**D5**tBu**A5** (c), nPr**D5**tBu**A5** (d), Ph**D5**tBu**A5** (e) and nBu**D5**nBu**A5** (f) with marked reflexes (a: circle (010), square (200), triangle (110); b: circle (110), square (214); c: circle (110), square (200); d: circle (020), square (400)); e: circle (011), square (120); f: circle (d = 6.3 Å), square (d = 3.8 Å); Insets: TEM image of the respective thin films on Lacey carbon film).

For all other dyes as well as for nBu**D5**nBu**A5** before heating, the observed single crystalline patterns correlate to the single crystal structures which is shown by simulation of the single crystalline diffraction patterns from the crystal structure with the program *JEMS*.[106]

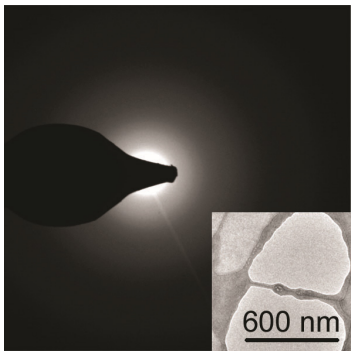

Figure 57. SAED pattern of the annealed thin film of nBu**D5**nBu**A5** confirming its non-crystalline structure.

Additionally, by XRD, clear reflexes can be seen at diffraction angles in the range of 5.1-6.4° for all dyes (Figure 58, Table 11), while upon heating, the intensity of these reflexes increased and even the second order is observed for dyes Pyrl**D5**tBu**A5**, Et**D5**tBu**A5** and nPr**D5**tBu**A5**. By comparing the XRD patterns with a powder pattern simulated from the crystal structure with the program *Mercury*,[84] the reflexes can be assigned (Table 11). The molecular orientation on the substrate is then deduced from the XRD results and yields an edge-on packing for the molecules of Pyrl**D5**tBu**A5**, Et**D5**tBu**A5** and EtBu**D5**tBu**A5** while the molecules of dyes nPr**D5**tBu**A5** and Ph**D5**tBu**A5** adopt a face-on packing. For nBu**D5**nBu**A5**, the peak cannot be clearly assigned due to close lying reflexes and therefore no molecular orientation on the substrate is deduced.

Table 11. Reflex positions of first reflexes of XRD patterns of all dyes for the as fabricated and annealed thin films as well as the closest matching reflex from the powder pattern simulated with the program *Mercury*[84] together with its index.

Dye	Reflex position / °			Index
	Thin film as fabricated	Thin film annealed	Simulation	Simulation
Pyrl**D5**tBu**A5**	5.6	6.0	6.1	(001)
Et**D5**tBu**A5**	6.1	6.2	6.2	(002)
EtBu**D5**tBu**A5**	5.7	5.8	6.1[a)]	(010)[a)]
nPr**D5**tBu**A5**	5.6	5.7	5.7[a)]	(100)[a)]
Ph**D5**tBu**A5**	n/a	5.1	5.3[a)]	(001)[a)]
nBu**D5**nBu**A5**	6.4	n/a	6.4 or 6.6	(001) or (010)

[a)] Systematic absence

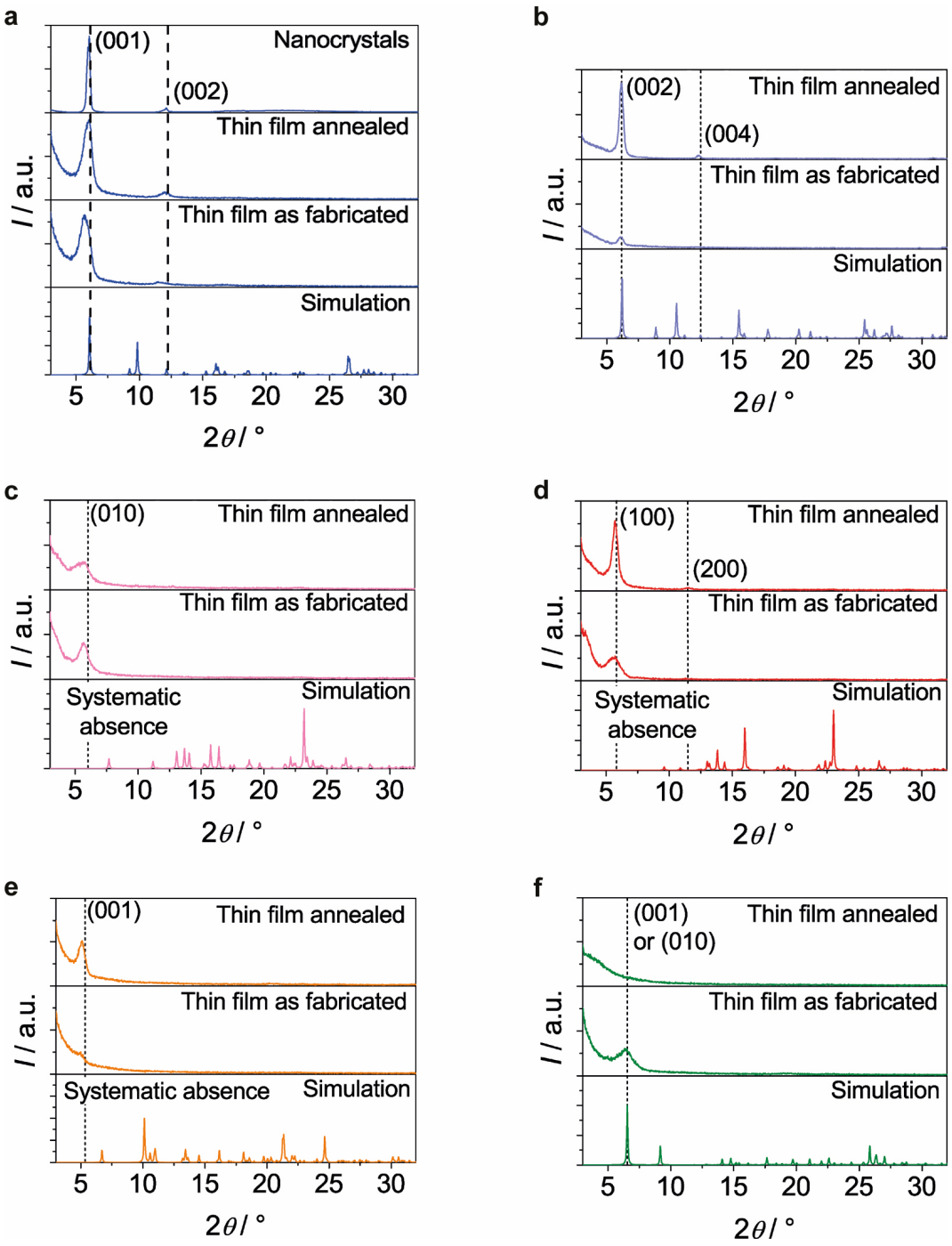

Figure 58. XRD patterns of thin films of dyes Pyrl**D5**tBu**A5** (a), Et**D5**tBu**A5** (b), EtBu**D5**tBu**A5** (c), nPr**D5**tBu**A5** (d), Ph**D5**tBu**A5** (e) and nBu**D5**nBu**A5** (f) in the as fabricated and annealed state together with powder patterns simulated from the crystal structure with the program *Mercury*[84] and indexed reflexes.

Moreover, AFM measurements of the thin films were conducted (Figure 59) and here, the thin film of dye nBu**D5**nBu**A5** shows an unstructured and smooth surface as expected from the UV-vis and diffraction results that show the presence of amorphous material in the film.

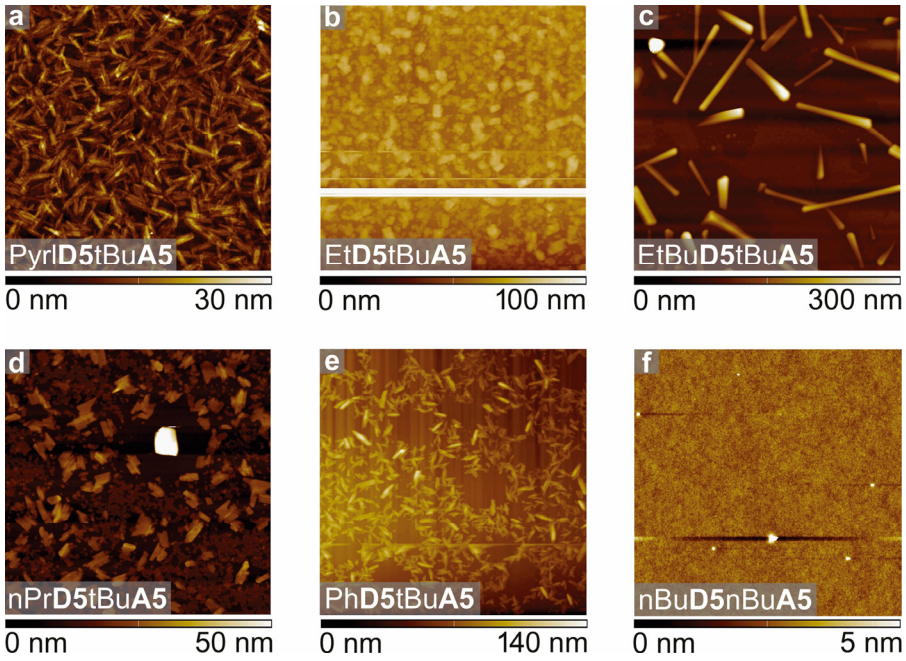

Figure 59. AFM images of thin films of Pyrl**D5**tBu**A5** (a), Et**D5**tBu**A5** (b), EtBu**D5**tBu**A5** (c), nPr**D5**tBu**A5** (d), Ph**D5**tBu**A5** (e) and nBu**D5**nBu**A5** (f) on quartz in the annealed state (a-e) or as fabricated (f).

In contrast, the annealed thin films of dyes Pyrl**D5**tBu**A5**, EtBu**D5**tBu**A5** and Ph**D5**tBu**A5**n exhibit structured surfaces with rod-like as well as more block-like features for the thin films of dyes Et**D5**tBu**A5** and nPr**D5**tBu**A5**. This is in accordance with the results from SAED and XRD which showed polycrystalline signals for the thin films. These results strongly indicate that the unique thin film spectra with H- or J-type coupling are a direct result of exciton couplings within the described single crystal structures.

3.3.6 Nanocrystals

In order to validate the assignment of the pronounced spectral shifts to exciton coupling and to elucidate which structural arrangement provokes these different couplings, nanocrystals of Pyrl**D5**tBu**A5** and nPr**D5**tBu**A5** as representative examples for the H- and J-type absorption could be grown onto quartz substrates with thicknesses of about 100-500 nm (Figure 60). Unfortunately, nanocrystals of other dyes were not of sufficient quality or thin enough to provide good experimental data. The correspondence of the nanocrystals to the thin film structure was verified by XRD for Pyrl**D5**tBu**A5** (Figure 58a), while for nPr**D5**tBu**A5**, the obtained crystals were too small and few to give a diffraction signal. Thus, crystals with similar absorption spectra as the thin films were chosen which also exhibited a rod-like or block-like morphology (dyes Pyrl**D5**tBu**A5** or nPr**D5**tBu**A5**,

respectively) as seen in AFM measurements. Accordingly, the nanocrystals show absorption maxima at 475 nm (Pyrl**D5**tBu**A5**) as well as 488 nm and 741 nm (nPr**D5**tBu**A5**) which corresponds well to the thin film absorption with absorption maxima of 479 nm (Pyrl**D5**tBu**A5**) and 746 nm (nPr**D5**tBu**A5**) as well as the additional feature around 480-490 nm in the thin film absorption of nPr**D5**tBu**A5** (Figure 47, Table 9).

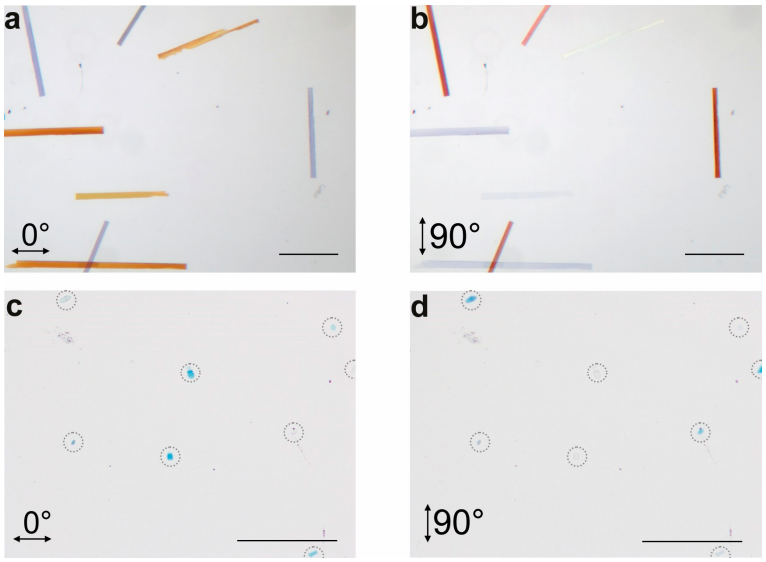

Figure 60. Polarized optical microscopy images of nanocrystals of Pyrl**D5**tBu**A5** (a,b) and nPr**D5**tBu**A5** (c,d) on quartz for different orientations of the nanocrystals to the polarization axis of the incident light (scale bars: 100 µm). In (c,d) the nanocrystals are highlighted by grey dotted circles for visibility.

When measuring the crystals' absorption with polarized light, significant changes are observed upon turning the crystals where the H-/J-bands either disappear completely or remain only partially (Figure 61). For Pyrl**D5**tBu**A5**, the rod-like nanocrystal appears yellow when the long axis of the nanocrystal is perpendicular to the polarization axis of the light and becomes completely transparent when the axes are oriented parallel (Figure 61a,e). When comparing the crystal morphology to the BFDH morphology simulated from the crystal structure (Figure 61c),[84] it becomes evident that this is due to the orientation of the transition dipole moments which lie perpendicular to the long axis of the nanocrystal. For nPr**D5**tBu**A5**, the block-like crystal appears blue when the nanocrystal is oriented with its longer axis perpendicular to the polarization axis of the light and both H- and J-bands are present (Figure 61b,f). When turned by 90°, the J-band disappears and the crystal becomes almost transparent while the intensity of the H-band decreases but does not disappear completely.

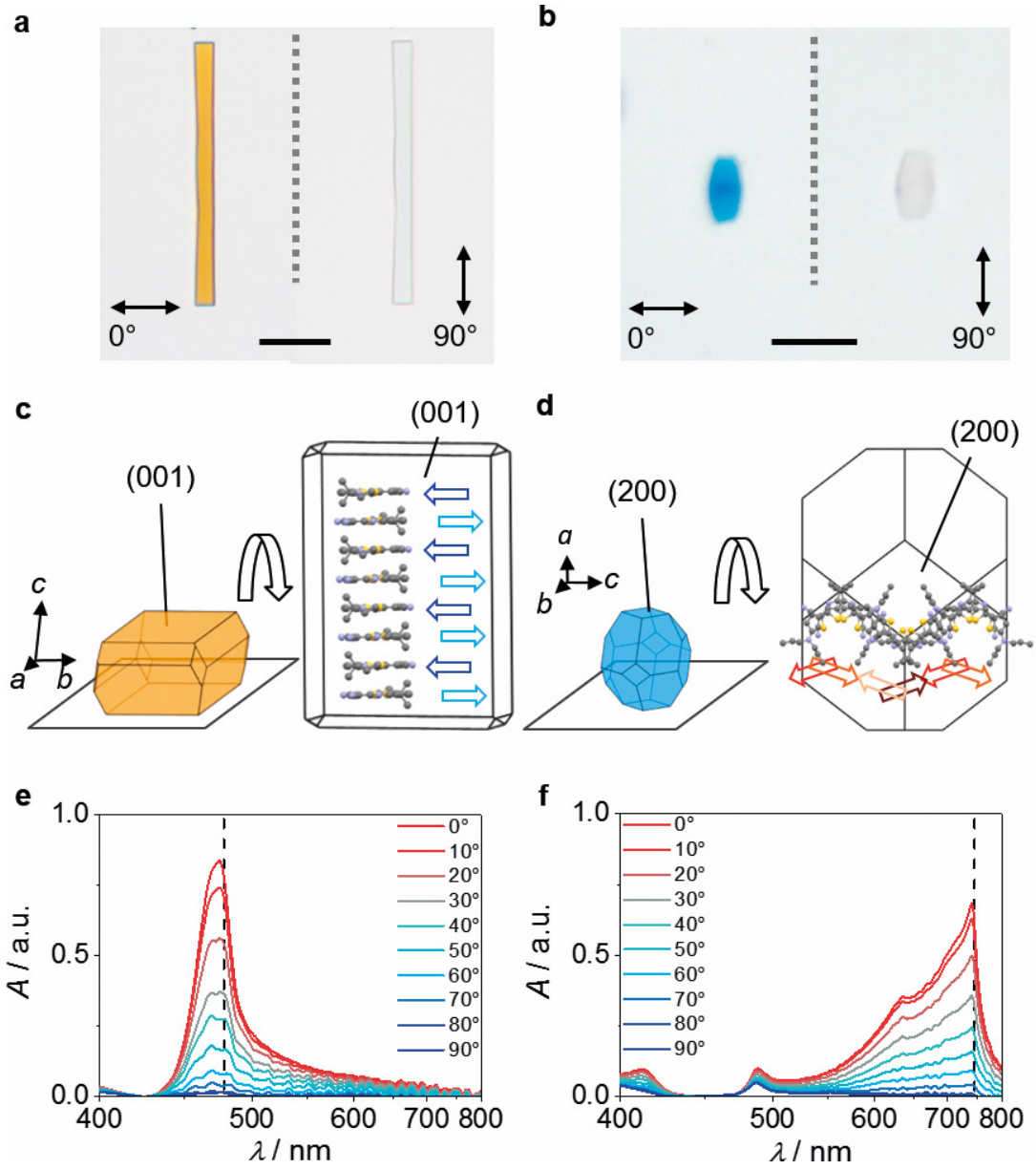

Figure 61. (a,b) Polarized optical microscopy images of nanocrystals of Pyrl**D5**tBu**A5** (a) and nPr**D5**tBu**A5** (b) for different orientations of the nanocrystals to the polarization axis of the incident light (scale bars: 20 µm); (c,d) BFDH morphologies of corresponding crystals on the substrate with top views on (001) (c) and (200) (d) facets with schematic molecular ordering in the nanocrystal to illustrate the orientation of the molecules to the incident light. (e,f) UV-vis/NIR absorption spectra of nanocrystals measured in different orientations to the polarized incident light with indicated position of the thin film absorption maxima (dashed vertical lines).

A comparison with the BFDH morphology (Figure 61d) shows that the short axis of the crystal corresponds to the elongation direction of the zig-zag strands within the single crystal and thus when the J-band is apparent, the strands are oriented parallel to the polarized incident light. In contrast, when the J-band disappears, the strands are perpendicular to the incident light. This deduced polarization-dependent absorption is in

good accordance with the structural description of H-/J-aggregates by Kasha who described a card stack like packing as the archetype for H-aggregates and attributed the appearance of both H- and J-bands to a zig-zag packing structure (see Figure 16 in section 2.3).[26]

3.3.7 Calculation of Exciton Coupling

From the experimental data on nanocrystals, the card stack like packing of Pyrl**D5**tBu**A5** and the zig-zag type packing of nPr**D5**tBu**A5** were identified to yield the spectral signatures of the H- and J-bands. Whereas for Pyrl**D5**tBu**A5**, there is only one intermolecular coupling to nearest neighbor molecules within the card stack structure, in the zig-zag strand of nPr**D5**tBu**A5** various couplings originate to neighboring molecules. To relate the observed spectral shifts to the respective packing arrangements and the concomitant intermolecular couplings, theoretical studies were performed for three approaches of increasing sophistication.

In a first basic approach, the intermolecular coupling energies J were derived for arrangements taken from the single crystal structures. Here, J was calculated for two next neighbors around one central molecule within the stack of Pyrl**D5**tBu**A5** and for the four next neighbors around one central molecule within the strand of nPr**D5**tBu**A5** by means of the point dipole approximation (PDA) as in equation (12), which is often applied for aggregates in solution (Figure 62 and Table 12, for coordinates of the molecular centers and transition dipole moments within the crystal structure, see appendix).

Table 12. Exciton coupling energies J calculated for molecular pairs of next neighbors of Pyrl**D5**tBu**A5** and nPr**D5**tBu**A5** around a central molecule (see Figure 62).[a)]

Dye	Next neighbor #	J_{PDA} / cm^{-1}	J_{TC} / cm^{-1}	$J_{TD\text{-}DFT}$ / cm^{-1}
Pyrl**D5**tBu**A5**	1	+3605	+1859	+2219
	2	+3891	+1863	+2216
nPr**D5**tBu**A5**	1	−594	−580	−676
	2	−594	−580	−676
	3	−1148	−151	−244
	4	−277	−441	−471

[a)] Exciton coupling energies J_i were calculated within the point dipole approximation (PDA), the transition charge method (TC) and the TD-DFT method. The sign (+/−) denotes if the most prominent transition is of H- (+) or J-type (−) nature.

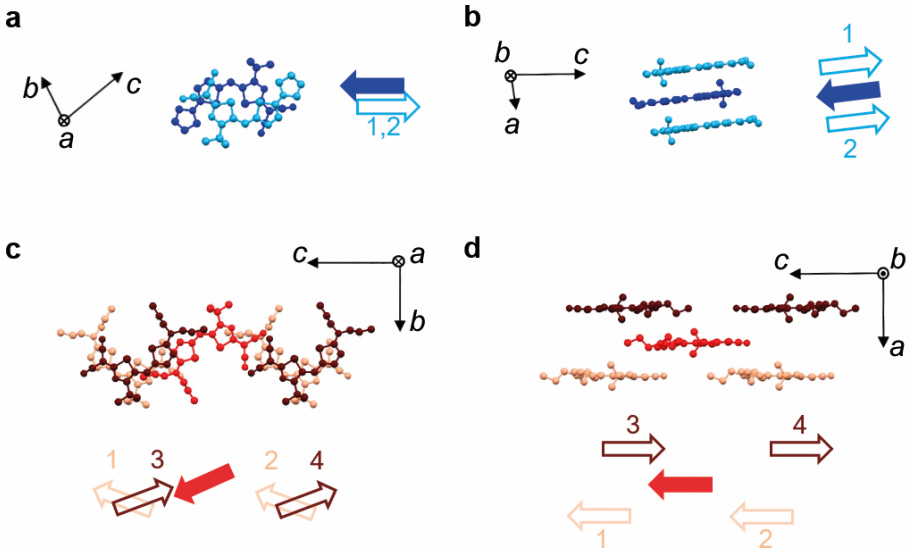

Figure 62. Next neighbors (numbered) around a central molecule (filled arrows) in the card stack structure of Pyrl**D5**tBu**A5** (a,b) and the zig-zag strand of nPr**D5**tBu**A5** (c,d) with top (a,c) and side views (b,d) as well as schematic views according to the crystal structures (see Figure 53 and Figure 54).

These coupling energies show a good qualitative agreement with the experiment by correctly describing the shift of the absorption bands as of H- and J-type nature for Pyrl**D5**tBu**A5** and nPr**D5**tBu**A5**, respectively. Nevertheless, the derived values are too large and confirm the limitations of the PDA for close intermolecular distances.[107] Thus, in a second more sophisticated approach, the intermolecular coupling energies were derived for the same structures by decomposition of the transition densities obtained by TD-DFT calculations (ωB97/def2-SVP) into point charges localized on atomic sites by a Mulliken population analysis. Subsequently, the intermolecular coupling energies were calculated as the Coulomb energy of the molecular pairs according to equation (22) (see Figure 62, Table 12):[40, 107-108]

$$J_{TC} = \frac{1}{4\pi\varepsilon_0} \sum_i \sum_j \frac{Q_i Q_j}{r_{ij}} \quad . \tag{22}$$

In the case of crystals of Pyrl**D5**tBu**A5**, it can be seen that the intermolecular couplings to the two next neighbors are of equal magnitude and show values of about 1860 cm^{-1} which is half of the values calculated within the PDA. In the case given in crystals of nPr**D5**tBu**A5**, the highest coupling value is not the one of the antiparallel dimer ($J_{TC} = -150\ cm^{-1}$), but of the head-to-tail oriented zig-zag packing structure ($J_{TC} = -580\ cm^{-1}$), again with the same value to both next neighbors. As the dominant values within the stack and strand structure of Pyrl**D5**tBu**A5** and nPr**D5**tBu**A5** are equal

to both next neighbors, the total exciton splitting of an infinite stack or strand structure can be estimated as $|4J|$,[28] yielding values around 7400 cm^{-1} (Pyrl**D5**tBu**A5**) and 2300 cm^{-1} (nPr**D5**tBu**A5**). To verify these values derived from next neighbor interactions, TD-DFT calculations (ωB97/def2-SVP) were conducted in the third approach for the same structures as for the other approaches. The calculated values are slightly higher than for the transition charge method, but match well, thus confirming these values in contrast to the exciton couplings obtained by PDA which are too high (Table 12).

In order to estimate the UV-vis spectra as well as the corresponding transition densities of the most prominent transitions, TD-DFT calculations (ωB97/def2-SVP) were also done for larger ensembles: a π-stack as given in the crystal of Pyrl**D5**tBu**A5**, a zig-zag strand as given in the crystal of nPr**D5**tBu**A5**, and a closely π-stacked dimer moiety as given in the crystal of nBu**D5**nBu**A5** (Figure 63). Due to computational effort, the extent of the structures of Pyrl**D5**tBu**A5** and nPr**D5**tBu**A5** were limited to eight molecules and the results can be found in Figure 64, Figure 65 and Table 9.

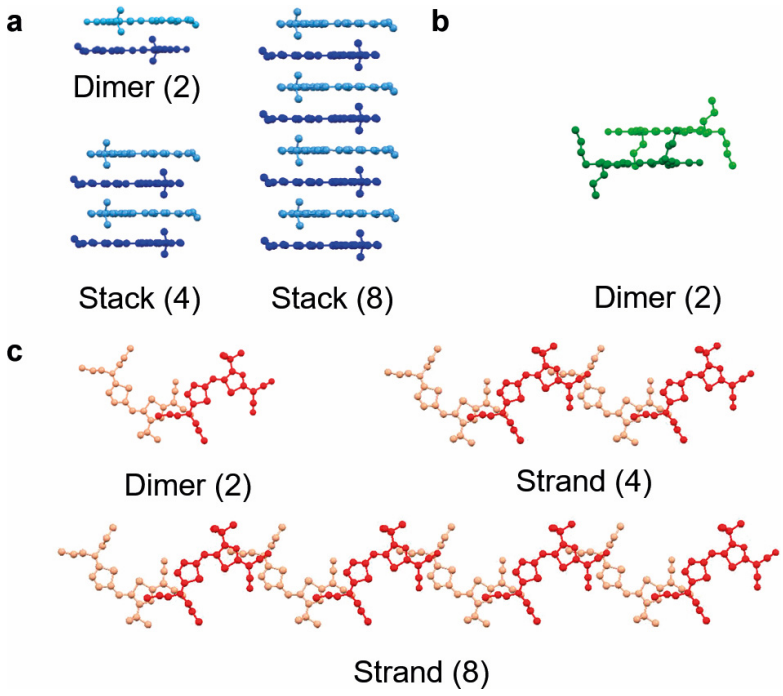

Figure 63. Molecular assemblies of dyes for which TD-DFT calculations (ωB97/def2-SVP) were performed: (a) Pyrl**D5**tBu**A5**, (b) nBu**D5**nBu**A5**, (c) nPr**D5**tBu**A5**.

For Pyrl**D5**tBu**A5** and nBu**D5**nBu**A5**, the most prominent transitions with an in-phase coupling of the transition dipole moments (Figure 64) are hypsochromically shifted compared to the monomer absorption with absorption maxima at 521 nm (Pyrl**D5**tBu**A5**)

as well as 618 nm (nBu**D5**nBu**A5**, see Figure 65). For the zig-zag strand of nPr**D5**tBu**A5**, two transitions are most prominent: one being bathochromically shifted to 755 nm with an in-phase coupling of the transition dipole moments, the other being hypsochromically shifted to 622 nm and showing an out-of-phase and ten-fold lower oscillator strength (Figure 65). In both cases, these findings comply with the description of H- and J-type transitions in such π-stacks and zig-zag strands by Kasha as stated before.[26a]

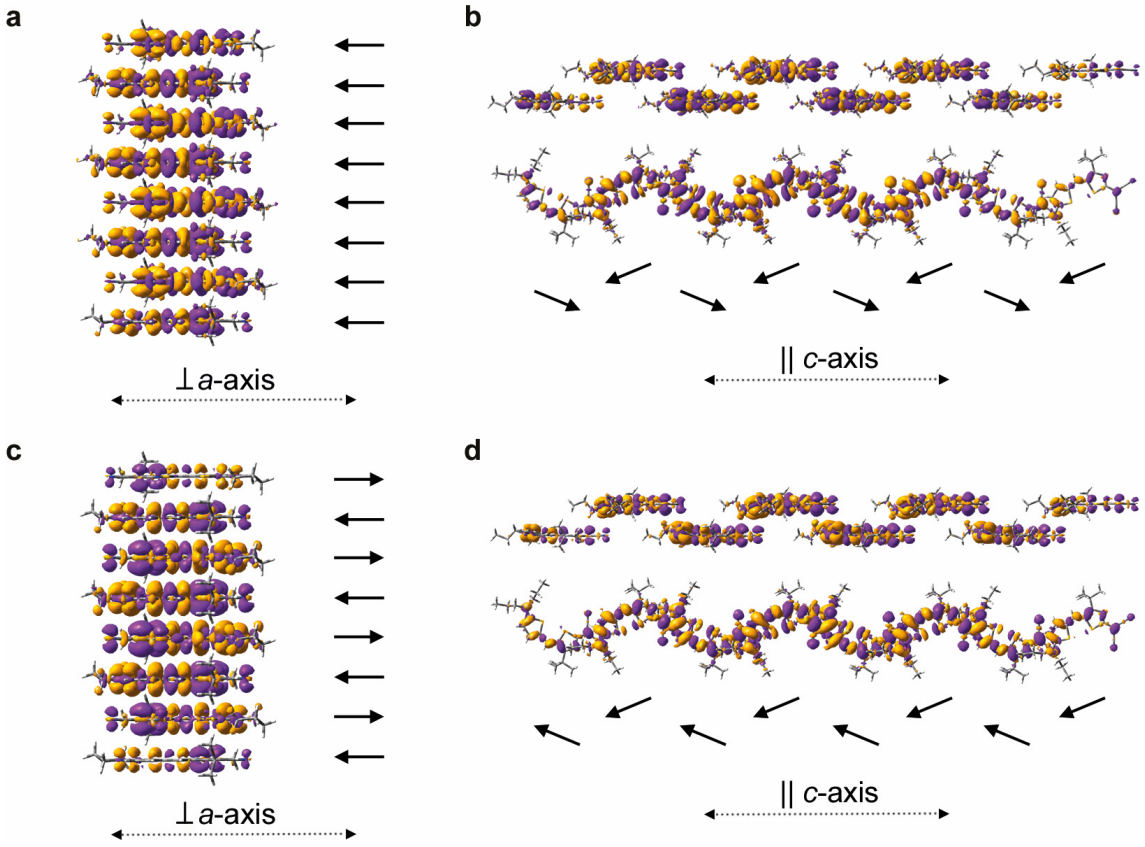

Figure 64. Transition densities for highest (a,b) and lowest (c,d) energetic transitions of a stack of eight molecules of Pyrl**D5**tBu**A5** (a,c) and a strand of eight molecules of nPr**D5**tBu**A5** (b,d); all transition densities are shown with an isovalue of 0.0004 a.u. and a classical schematic illustration of phase relations of transition dipole moments (solid arrows) together with orientation of the resulting optical transition (dashed arrows).

Additionally, it becomes evident that already with an assembly size of two or eight molecules, respectively, the experimental absorption maxima of the dimer (nBu**D5**nBu**A5**) and J-type (nPr**D5**tBu**A5**) bands from the experiments as well as the energetic difference of 7500 cm^{-1} (0.93 eV) of the H-band of Pyrl**D5**tBu**A5** and the J-band of nPr**D5**tBu**A5** are well reproduced with a value of 6000 cm^{-1} (0.74 eV).

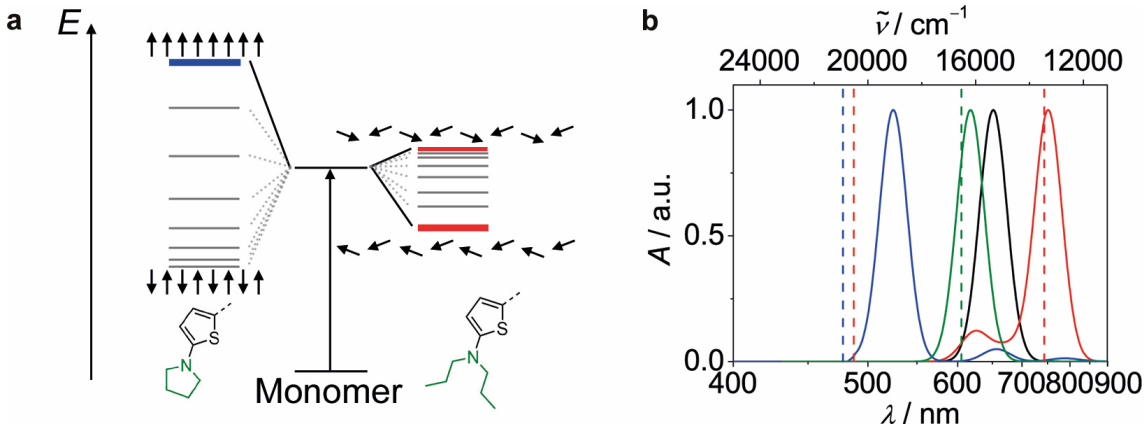

Figure 65. (a) Schematic illustration of the exciton band diagrams for a stack and strand of eight molecules of Pyrl**D5**tBu**A5** and nPr**D5**tBu**A5**, together with schematic phase relations of transition dipole moments for the highest and lowest energetic state (adapted from ref. [26a]); the thickness of the lines of the energetic states illustrates the magnitude of oscillator strength of the optical transition (see appendix); (b) Simulated absorption spectra in solid lines calculated for a monomer of nPr**D5**tBu**A5** (black), a stack of Pyrl**D5**tBu**A5** (blue) and strand of nPr**D5**tBu**A5** (red) of eight molecules as well as a dimer moiety of nBu**D5**nBu**A5** (green). The segments were taken from the crystal structures and all spectra were shifted by 5400 cm^{-1} towards lower energies to adjust for the difference given for the calculated and experimental monomer absorption band (see ref. [40]). The dashed lines denote the absorption maxima of the H- or J-bands of thin films of dyes Pyrl**D5**tBu**A5** (blue) and nPr**D5**tBu**A5** (red) as well as the dimer band of nBu**D5**nBu**A5** (green).

However, in the case of the H-bands of Pyrl**D5**tBu**A5** and nPr**D5**tBu**A5**, the calculated absorption maxima do not match the experimental values as precisely. Calculations for larger assemblies are expected to provide even better results as demonstrated with the evolution of the shift from monomer over dimer to the ensembles of four and eight molecules (Figure 66 and Figure 67, for a list of the calculated values, see appendix).

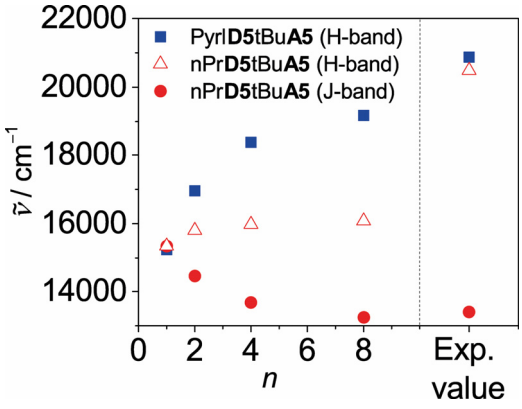

Figure 66. Evolution of the energetic levels of the H- and J-band absorption maxima of dyes Pyrl**D5**tBu**A5** and nPr**D5**tBu**A5** for different sizes of the stack and strand structures with a number of molecules *n* as resulting from TD-DFT calculations. The experimentally observed maxima values of the annealed thin films are given as comparison (for the H-band of nPr**D5**tBu**A5**, the value for the nanocrystal is given as for the thin film, no defined maximum was observed).

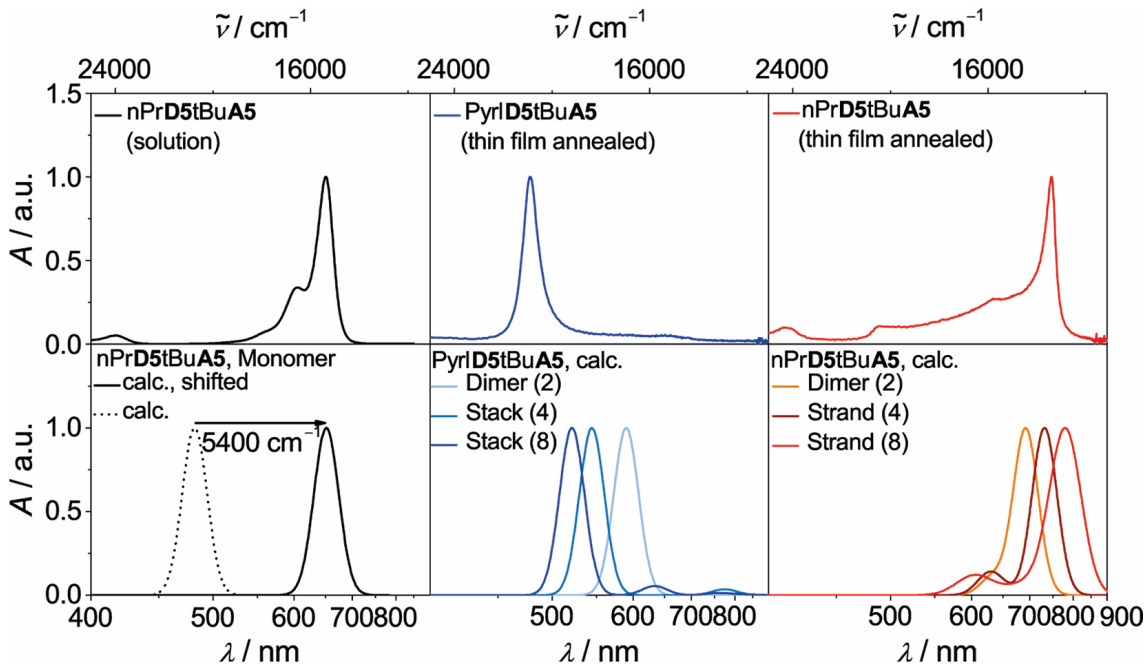

Figure 67. UV-vis absorption spectra of a monomer of nPr**D5**tBu**A5** in solution ($CHCl_3$, 10^{-5}, 298 K) and calculated by TD-DFT (ωB97/def2-SVP, original values and values shifted by 5400 cm^{-1} towards lower energies to account for the difference to the experimental value)[40] as well as the experimental spectra of the annealed thin films of Pyrl**D5**tBu**A5** and nPr**D5**tBu**A5** compared to the UV-vis/NIR spectra of Pyrl**D5**tBu**A5** and nPr**D5**tBu**A5** obtained by TD-DFT (ωB97/def2-SVP) calculations for a dimer as well as for assemblies of four and eight molecules of Pyrl**D5**tBu**A5** and nPr**D5**tBu**A5** (all calculated spectra were shifted by 5400 cm^{-1} as for the monomer spectrum).

Note that for the obtained results, the calculated spectra were shifted by 5400 cm^{-1} towards lower energies to account for the difference of measured and calculated monomer absorption.[40] Additionally, an evaluation of the intermolecular coupling for all next neighbors around a central molecule within the PDA as well as by the transition charge method shows that for Pyrl**D5**tBu**A5**, the strongest coupling is clearly within the card stack packing structure. For nPr**D5**tBu**A5**, there are several couplings of equal magnitude which are also not within the zig-zag strand structure (see appendix). Especially for this complex structure, calculations of larger ensembles would lead to a better understanding of the intermolecular coupling of J-type nature. However, this was beyond the scope of this thesis.

3.3.8 Mixtures of Dyes

The studied merocyanine dyes show intriguing H- or J-bands in the solid state despite their almost identical molecular properties due to the same chromophore. Hence, the question arises, if dye mixtures show social self-sorting phenomena and incorporate one dye into another's packing structure or rather behave narcissistically and form separate domains. To investigate this issue, the two molecules with the most distinct H- and J-bands (Pyrl**D5**tBu**A5** and nHe**D5**tBu**A5**) were chosen. The mixed thin films were prepared by spin coating onto quartz substrates from mixtures combined of equimolar solutions of the dyes in $CHCl_3$ ($c = 4 \cdot 10^{-3}$ M) with varying volumetric mixing ratios. Then, the thin films were annealed at 130 °C for 5 min to induce a higher crystallinity (see section 3.3.2).
The single component thin films of Pyrl**D5**tBu**A5** and nHe**D5**tBu**A5** exhibit only a H- or J-band, respectively, and do not show any absorption at the position of the other band. Thus, the absorption at 479 nm and 750 nm can be used to deduce the amount of H- and J-type coupled chromophores. With regard to correct interpretation of the results, two control experiments were performed. First, the single components were spin coated from diluted solutions of the same concentration as in the respective mixtures to account for the reduced concentration in the mixed solutions and here the absorption indeed showed, as expected, a linear decrease with lower concentration. Second, the ratio of the molecules in the thin films was verified as the different solubilities of the dyes might lead to a change of the ratio during the rapid spin coating process. Thus, thin films deposited from a 50:50 mixture were rinsed off twenty coated substrates and this mixture was investigated by NMR spectroscopy together with the mixture used for spin coating (see Figure 68).

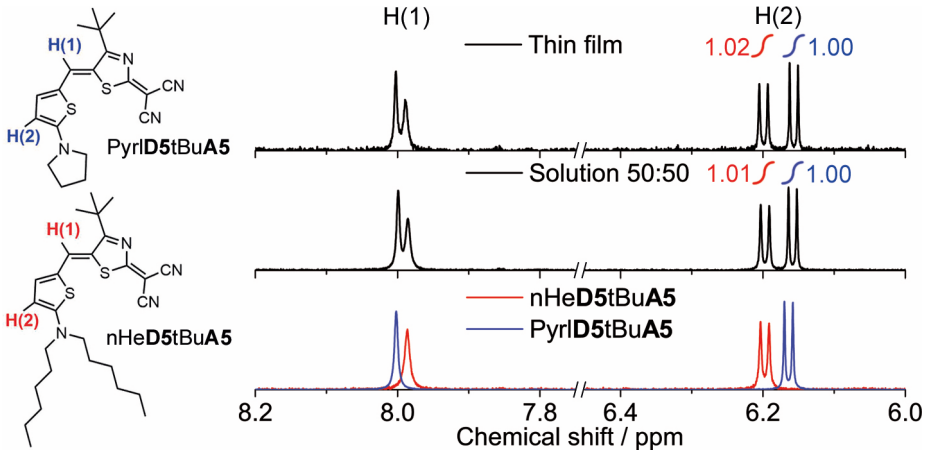

Figure 68. ^{1}H NMR signals of protons at positions (1) and (2) of dyes Pyrl**D5**tBu**A5** (blue) and nHe**D5**tBu**A5** (red) in $CDCl_3$ at 298 K for the single dyes (bottom), the solution of a 50:50 mixture (middle) and the mixture rinsed off the spin-coated substrates (top).

The dye ratio calculated from the integrals of proton signals at the thiophene ring for both mixtures indeed matches the 50:50 ratio of the mixed solution. Therefore it can be stated, that the ratio of the two components in the thin films does not change by the fast spin coating process.

Figure 69a exemplarily shows the absorption spectrum of a thin film prepared from a 50:50 mixture of PyrlD5tBuA5 : nHeD5tBuA5 in addition to their single component spectra. Here it can be clearly seen that the absorption of the mixture shows an enhanced H-band with a slight red shift of 1 nm while the J-band is strongly diminished and slightly blue shifted by 2 nm. In Figure 69b, the absorption at the maxima of H- and J-band is shown with respect to the molar fraction of nHeD5tBuA5 in the mixtures. It can be clearly seen that for all mixtures, the absorption at the given wavelengths shows a nonlinear behavior.

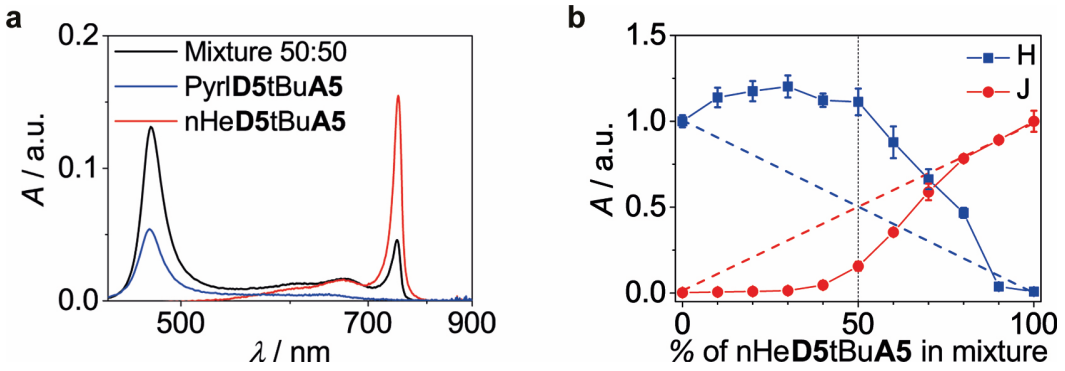

Figure 69. (a) UV-vis absorption spectra of a thin film processed from a 50:50 mixture of PyrlD5tBuA5 : nHeD5tBuA5 after spin coating and annealing (black line) as well as of thin films of the single components processed from solutions of the same concentration of the dyes in the mixture; (b) Normalized values of maximum absorption of the H- (blue) and J-band (red) of thin films with varying mixing ratios (values are normalized to the absorption of the 100 % single component spectra, respectively, and given as average of three measurements with the standard deviation as error bars). The solid lines serve as guide to the eye and the dashed colored lines show the linear decrease of absorption due to a lower amount of the dyes within the mixture.

For mixtures of PyrlD5tBuA5 : nHeD5tBuA5 varying from 100:0 to 50:50, the J-type absorption is almost absent, while then showing an increase for higher molar fractions of nHeD5tBuA5. In contrast, for mixtures varying from 20:80 to 0:100, the maximum absorption values of the J-band are in good accordance with the values estimated from the single component thin films and show a linear increase. On the other hand, the absorption of the H-band does not decrease for mixing ratios of PyrlD5tBuA5 : nHeD5tBuA5 varying from 100:0 to 50:50 as expected from the single component thin films. It is quite remarkable that for these mixing ratios, the absorption of the H-band is in all cases even

higher than that of the thin film of pure Pyrl**D5**tBu**A5** with a maximum increase of up to 20 % in absorbance for the mixing ratio 70:30. Up to a molar fraction of 80 % of nHe**D5**tBu**A5**, the H-type absorption remains higher than for thin films of the pure compound. These results suggest that nHe**D5**tBu**A5** can be socially incorporated in the card stack like packing of Pyrl**D5**tBu**A5** and enhances the absorption of the H-band up to a ratio of about 40-50 %, while for an excess of nHe**D5**tBu**A5**, this compound behaves rather narcissistically.

To evaluate, if the spectral signatures of H- and J-bands can be attributed to different domains and if the enhanced H-type absorption is caused by social self-sorting, further UV-vis, AFM, XRD and SAED studies were performed. First, the absorption of the thin film with a mixing ratio of 50:50 was measured under a microscope equipped with a spectrometer on a spot size resolution of 4 μm^2 (see Figure 70). Here, the same absorption spectra as observed from measurements on a larger area of 0.5 cm^2 (Figure 69) are retained for measurements on ten randomly chosen spots, meaning that both couplings either arise from the same packing structure or that the domains are smaller than the spot size.

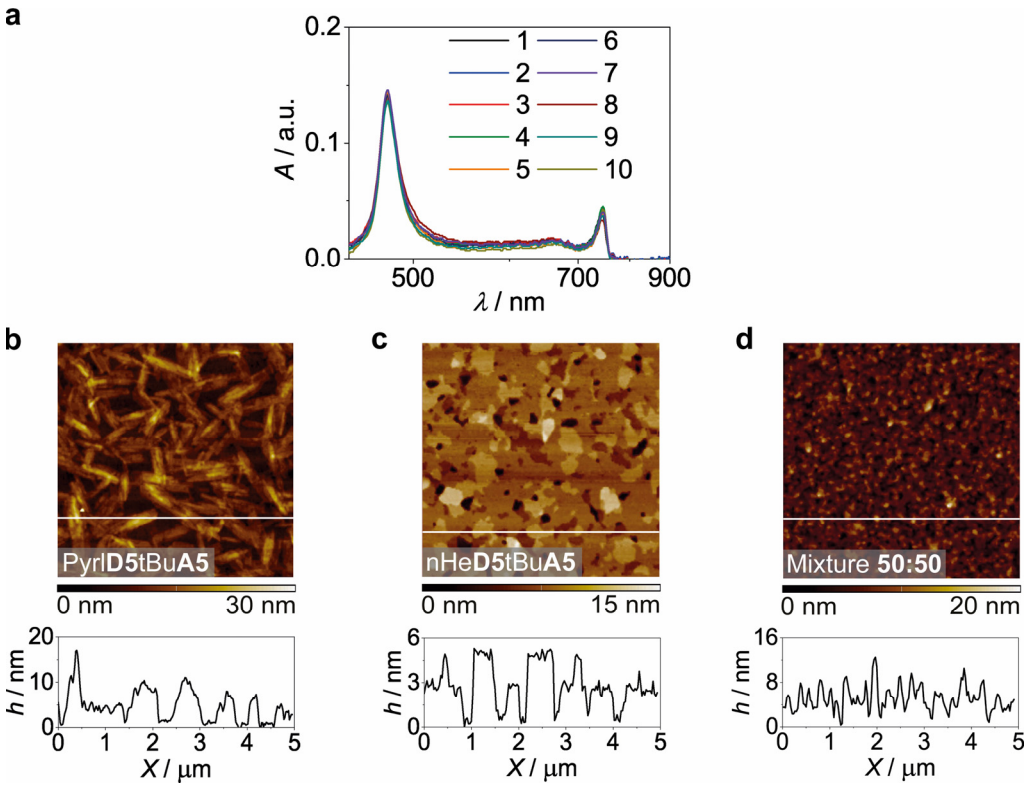

Figure 70. (a) UV-vis absorption spectra of a thin film processed from a 50:50 mixture of Pyrl**D5**tBu**A5** : nHe**D5**tBu**A5** measured on ten random spots of 4 μm^2; (b-d) AFM images (top) and cross sections (bottom, at the position of the white lines) of thin films of Pyrl**D5**tBu**A5** (b), nHe**D5**tBu**A5** (c) and a 50:50 mixture of Pyrl**D5**tBu**A5** : nHe**D5**tBu**A5** (d) on quartz in the annealed state. Each image scales to 5×5 μm^2.

Elaborating this implication, AFM measurements of the thin films were performed (see Figure 70b-d). The layers of the single components as well as the mixed thin film show all a structured surface with rod-like structures for Pyrl**D5**tBu**A5** and more block-like features for nHe**D5**tBu**A5**. In contrast, the thin film of the mixture exhibits much smaller domains, suggesting that the thin film is of crystalline nature (see below) and that by the UV-vis absorption measurements on a spot size of 4 μm^2, it cannot be distinguished if there are different domains present.

Next, XRD measurements of the thin films of various mixing ratios were performed to gain insight into the molecular packing of the domains (Figure 71; for a better understanding, the respective UV-vis absorption spectra of the mixed thin films are depicted as well). The XRD signals of the single component thin films show distinct peaks at 4.1° (Pyrl**D5**tBu**A5**) and 6.0° (nHe**D5**tBu**A5**). For mixing ratios of 80:20 and 50:50 (Pyrl**D5**tBu**A5** : nHe**D5**tBu**A5**), only one peak is observed at 2θ values of 5.2° and 5.0°, respectively, while for a mixing ratio of 20:80, two peaks at 4.2° and 5.5° are present.

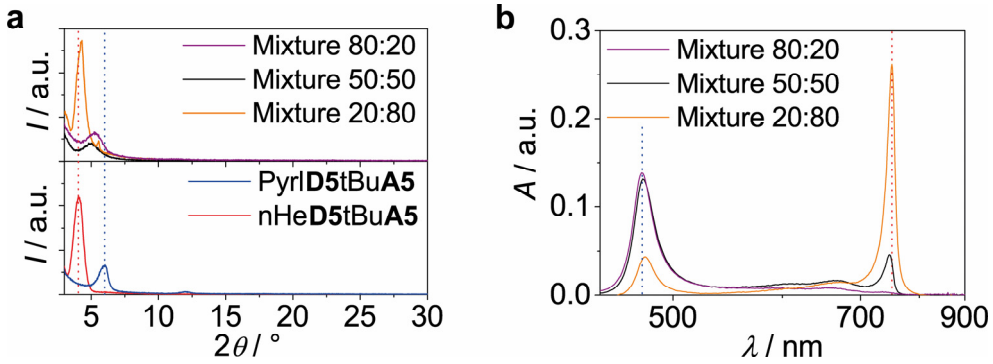

Figure 71. XRD diffractograms (a) and UV-vis absorption spectra (b) of thin films of 80:20, 50:50 and 20:80 mixtures of Pyrl**D5**tBu**A5** : nHe**D5**tBu**A5**. In (a), the diffractograms of the single component thin films are given as well. The dashed lines denote the reflex positions (a) as well as absorption maxima (b) of Pyrl**D5**tBu**A5** (blue) and nHe**D5**tBu**A5** (red).

From these reflexes, the corresponding interplanar distances can be calculated, yielding values of 21.5 Å (nHe**D5**tBu**A5**) and 14.7 Å (Pyrl**D5**tBu**A5**) for the single component thin films, while for the Pyrl**D5**tBu**A5** : nHe**D5**tBu**A5** mixtures, values of 17.0 Å (80:20), 17.7 Å (50:50), as well as 16.0 Å and 21.0 Å (20:80) are obtained. These results suggest that for an excess of Pyrl**D5**tBu**A5**, only one crystalline domain is present, while for an excess of nHe**D5**tBu**A5**, there are cleary two crystalline domains. Assuming that for the mixed thin films, slight deviations in XRD signals can occur due to e.g. reorientation of domains or minor changes in crystalline packing because of the presence of the other

component, it seems reasonable that the reflex at 4.2° originates from single component domains of nHe**D5**tBu**A5**, which narcissistically separate from the Pyrl**D5**tBu**A5** molecules. However, the origin of the reflex of the mixtures in the region of 5.0°-5.5° cannot be attributed to such slight changes as it lies just in between the two single component reflexes. If one dye is incorporated into the structure of the other and the distances are consequently altered, also crystallographic axes and thus the reflexes will change.

To evaluate this hypothesis of incorporation, SAED experiments of the mixed thin films were performed. For thin films of Pyrl**D5**tBu**A5** and mixing ratios of Pyrl**D5**tBu**A5** : nHe**D5**tBu**A5** 80:20 and 50:50, six polycrystalline diffraction rings can be observed, while in contrast, the diffraction pattern of the thin film of nHe**D5**tBu**A5** shows only three clear diffraction rings (Figure 72).

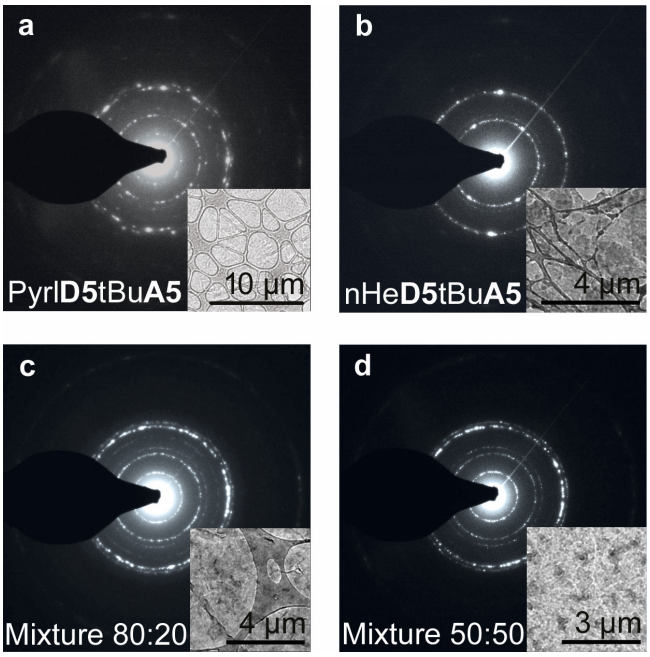

Figure 72. SAED patterns of polycrystalline regions of annealed thin films of Pyrl**D5**tBu**A5** (a), nHe**D5**tBu**A5** (b), and 80:20 (c) as well as 50:50 mixtures (d) of Pyrl**D5**tBu**A5** : nHe**D5**tBu**A5**; Insets: TEM image of the respective thin films on Lacey carbon film.

From these diffraction patterns, the corresponding layer distances were calculated and are given in Table 13. Due to the lack of crystal structures for nHe**D5**tBu**A5** and the mixtures, the layer distances are not assigned to distinct layers. In particular for the mixtures, a growth of co-crystals was not possible as crystal growth experiments from solution always lead to crystals of the single dyes, probably due to their different solubilities. Additionally, crystal growth by co-sublimation of both dyes did not yield any crystals at all.

Table 13. Layer distances calculated from the SAED patterns of thin films of Pyrl**D5**tBu**A5**, nHe**D5**tBu**A5** as well as 80:20 and 50:50 mixtures of Pyrl**D5**tBu**A5** : nHe**D5**tBu**A5**.

Thin film	Layer distances / Å					
Pyrl**D5**tBu**A5**	9.8	5.6	5.0	4.0	3.4	3.2
nHe**D5**tBu**A5**	5.8	5.1	3.5	/	/	/
Mixture 80:20	10.0	5.7	5.1	4.0	3.5	3.3
Mixture 50:50	10.0	5.6	5.0	4.0	3.5	3.2

While the lattice spacing values for the single component thin films are both very similar to those obtained for the mixed thin films, XRD results suggest that only one crystalline phase exists in these thin films and all six reflexes of the mixture observed in SAED can only be explained by the packing of Pyrl**D5**tBu**A5**. As the diffraction pattern of both mixed thin films is almost identical to that of Pyrl**D5**tBu**A5**, their orientation on the substrate is the same as for Pyrl**D5**tBu**A5** (a visualization is given below).

The presented results clearly show that nHe**D5**tBu**A5** can be incorporated into the H-type packing of Pyrl**D5**tBu**A5**. To visualize a structure of the mixed stack, the amount of incorporated material in the H-type domains α_H can be calculated from the UV-vis experiments by equation (23) with A_H and A_J being the maximum absorption of the H- and J-band, respectively, of the single component spectra and $A_{Mix,J}$ being the maximum J-type absorption of the mixture:[109]

$$\alpha_H = \frac{A_J - A_{Mix,J}}{A_H + A_J - A_{Mix,J}}. \quad (23)$$

This calculation yields a maximum incorporation of 41 % in the domains with H-type coupling for thin films prepared from a 50:50 mixture of both dyes, meaning that every second to third molecule of the H-stack in the mixed thin film is a nHe**D5**tBu**A5** molecule (Figure 73a). From the calculated α_H values, the fraction of H- and J-type domains X_H and X_J in the mixed thin films can be calculated by equations (24) and (25), with X_{nHe} being the fraction of nHe**D5**tBu**A5** in the mixture used for spin coating process:

$$X_J = \frac{X_{nHe} - \alpha_H}{1 - \alpha_H}; \quad (24)$$

$$X_H + X_J = 1. \quad (25)$$

The results of this calculation are shown in Figure 73b and demonstrate that, when for example spin coating from a 50:50 mixture, the ratio of H- and J-type coupled domains results in 82:18.

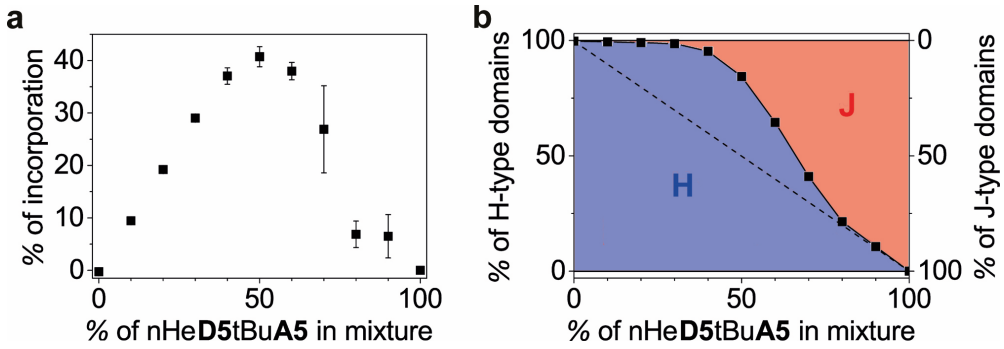

Figure 73. (a) Calculated incorporation of nHe**D5**tBu**A5** into the card stack structure of Pyrl**D5**tBu**A5** as average of three measurements with the standard deviation as error bars; (b) Calculated fractions of H- and J-type domains in mixed thin films in dependence on the fraction of nHe**D5**tBu**A5** in the mixed solution used for preparation. The solid line serves as guide to the eye and the dashed line corresponds to the values expected for a totally narcissistic behavior.

Combining the results from UV-vis absorption and diffraction experiments, a model for the packing of the mixed stack (deposited from a 50:50 mixture) on the substrate is proposed and shown in Figure 74. Here, about 40 % of the stacked molecules are of the compound nHe**D5**tBu**A5** and the XRD results, which give information about the lattice spacings of layers parallel to the substrate, show that this layer spacing is enlarged by about 19 % for the mixture in comparison to the crystal structure of Pyrl**D5**tBu**A5**. This increase can probably be attributed to the flexible *n*-hexyl chains of nHe**D5**tBu**A5** which point roughly into the <001> direction as another arrangement would alter the distances of other layers, which would have been observed in the SAED pattern. Additionally, these results demonstrate that the enhanced H-type absorption does not arise from a mere reorientation of whole H-stack on the substrate but might be caused by a slight twist of the molecules within the mixed H-stack.

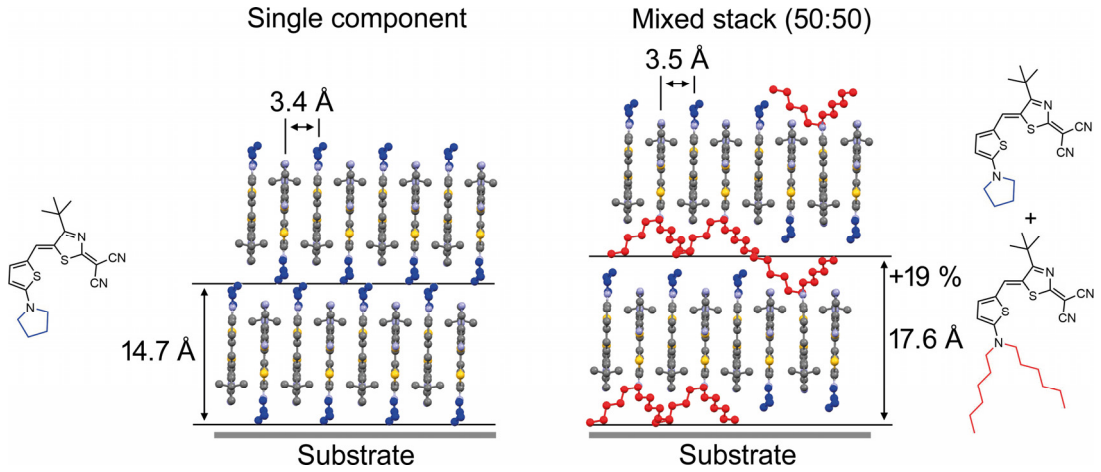

Figure 74. Packing of Pyrl**D5**tBu**A5** on the substrate as well as proposed packing of a mixed thin film of Pyrl**D5**tBu**A5** and nHe**D5**tBu**A5** on the substrate with indicated layer distances.

In contrast, no evidence for the incorporation of Pyrl**D5**tBu**A5** into the structure of nHe**D5**tBu**A5** is observed. This preference of the card stack like packing yielding an H-type coupling is in correspondence to the fact that this structural motif is most commonly observed for dipolar merocyanines due to their inherent dipolarity and concomitant antiparallel alignment.[37] Furthermore, it is shown that by mixing these two components, the intensity of the H- and J-band can be continuously tuned by varying the mixing ratio and an increase of the H-type absorption can be induced by just a small fraction of 10 % of nHe**D5**tBu**A5** in the mixture.

3.3.9 Conclusion

In summary, a series of ten highly dipolar merocyanine dyes bearing the same **D5A5** chromophore backbone but decorated with different aliphatic substituents show almost identical absorption spectra and electronic properties in solution whereas those for thin films and nanocrystals are entirely different with either narrow H- or J-type absorption bands around 480 and 750 nm, respectively (for a schematic summary, see Figure 75). Interestingly, the thin films show a weak emission at 750 nm-765 nm irrespective of the irradiation wavelength, demonstrating the formation of an exciton band with a large energetic offset of 0.93 eV between the H- and J-band.

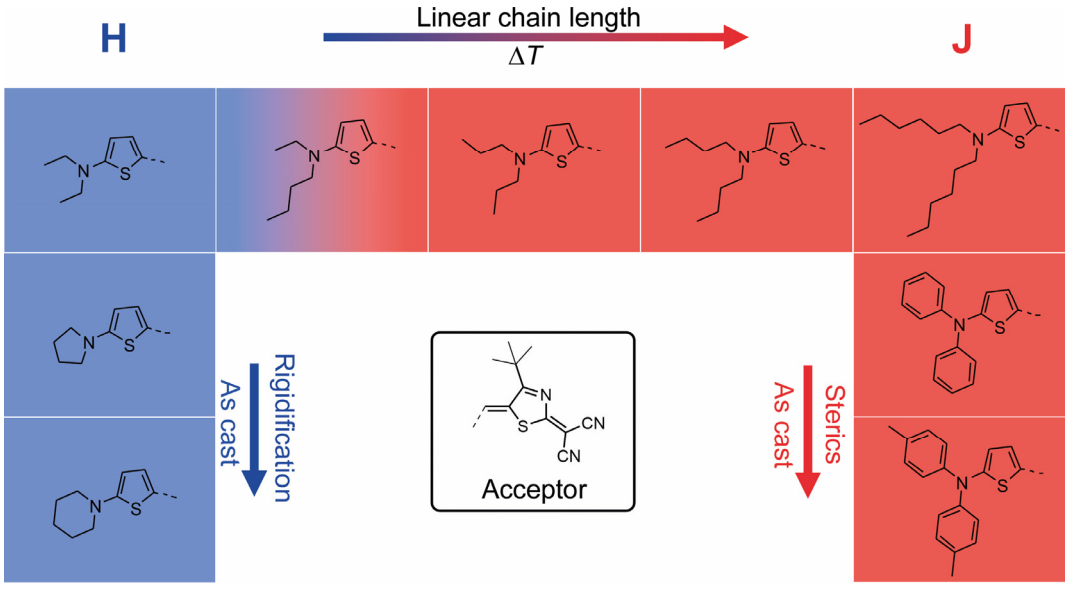

Figure 75. Schematic depiction of investigated dyes with their H- or J-type coupling in spin-coated thin films upon annealing (ΔT) or as cast.

The appearance of these bands as well as the energetic difference is related to different packing arrangements of the dyes within the single crystal structures, with either cofacially stacked or zig-zag type arrangements leading to distinct H-type or J-type exciton couplings which correspond to the archetype situations of H- and J-aggregates as described by Kasha. For mixtures of two dyes showing either H- or J-type coupling, it is shown that dyes exhibiting J-type coupling can be incorporated into the preferred H-type card stack like structure up to a molar ratio of almost 50 %. This suggests, that almost every second position in a π-stack can be occupied by a molecule with more bulky alkyl substituents.

So far, this is the first example where modulation from H-type to J-type coupling is demonstrated in the solid state for a merocyanine chromophore by means of a crystal engineering approach, i.e. substituent-directed adjustment of the slipping angle.

Chapter 4
-
Summary

The demand for new (opto-)electronic devices and materials is constantly rising and predicted to increase even further in the near future because of a rapid progression in interconnecting almost all sectors of our society (e.g. “internet of things”). To account for these needs, low-cost accessible and versatile processable semiconducting materials are required and here organic semiconductors aim to compete with traditional inorganic materials. In particular, merocyanine dyes are long known for their straightforward synthetic access and intense absorption, but were almost absent in the field of organic electronics due to their inherent ground state dipole moments. Only few studies on the dyes’ potential for charge carrier transport as well as their unique absorption properties in the solid state with exciton coupling have been shown. In all cases, the studies were limited to either one molecule or rather special experimental conditions, which did not allow for conclusions on the pure material. Consequently, the aim of this thesis was to establish structure-property relationships of merocyanine dyes concerning their charge transport as well as their solid state absorption with exciton coupling. Therefore, 30 different merocyanine dyes based on five different donor and acceptor heterocycles, respectively, were investigated and structure-property relationships could be established for the optoelectronic subjects within two different series of merocyanine dyes (Chart 7).

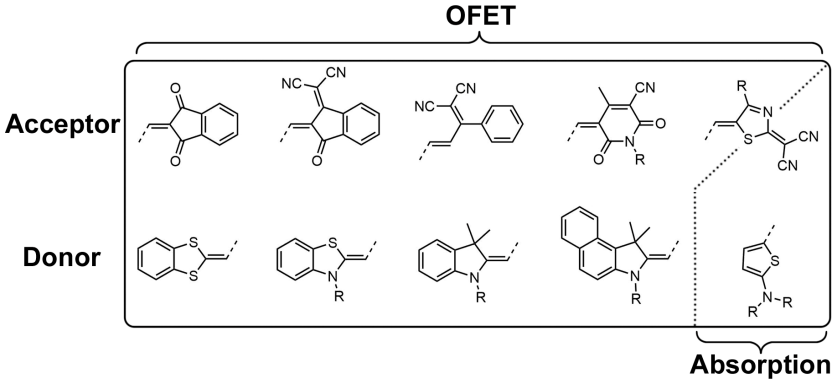

Chart 7. Donor and acceptor moieties of the merocyanine dyes investigated in this thesis.

The first part of this thesis focuses on the investigation of the charge transport properties of merocyanine dyes. Here, twenty merocyanines with different donor and acceptor heterocycles were investigated in vacuum processed organic thin film transistors (OTFTs). All investigated dyes showed HOMO levels suitable for p-type OTFTs with Au electrodes and, in devices on Si/SiO_2 substrates, also exhibited either similar p-type mobility values of the order 10^{-5}-10^{-6} $cm^2\ V^{-1}\ s^{-1}$, or no field-effect at all. On these substrates with a high surface energy, the molecule-substrate interactions superimposed the intermolecular interactions and therefore all dyes formed amorphous thin films, which was confirmed by AFM as well as XRD measurements. By using *n*-tetradecylphosphonic acid (TPA) modified Si/SiO_2 substrates with a low-energy surface, the intermolecular dipole-dipole interactions now could dominate the molecule-substrate interactions and accordingly two groups of dyes were found, which exhibited either low performance, as on the Si/SiO_2 substrates, or high mobility values up to 0.21 $cm^2\ V^{-1}\ s^{-1}$. By analysis of representative single crystal structures, it could be shown that the dyes' performance as organic semiconductors in OTFTs depends highly on the solid state structure (Figure 76).

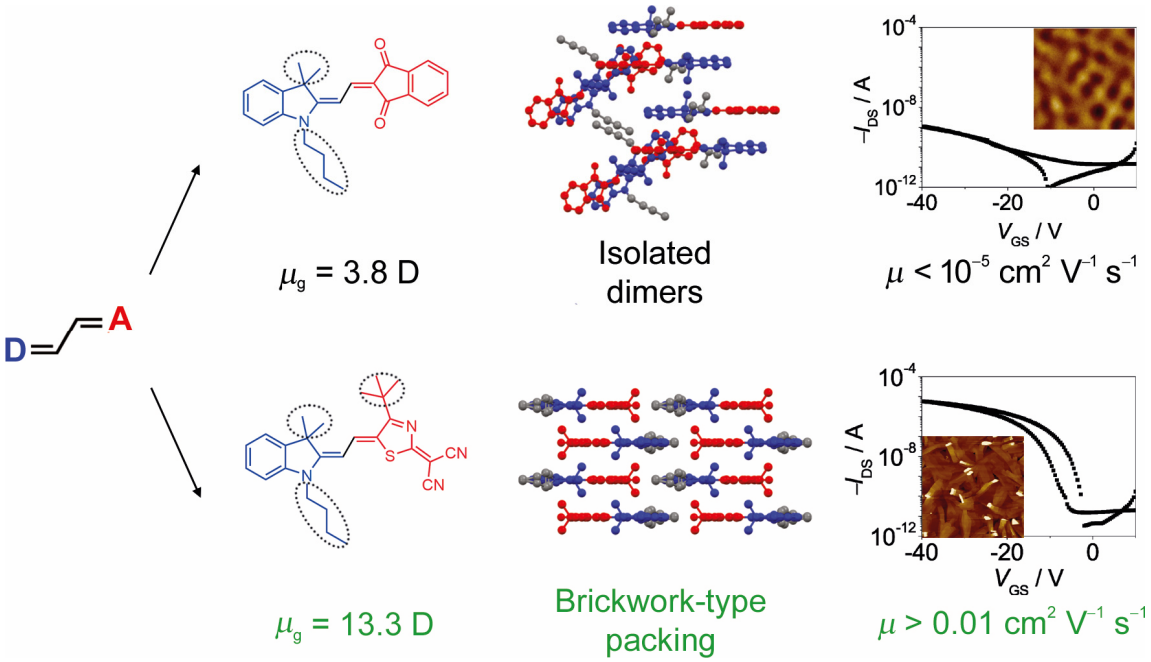

Figure 76. Different single crystal packing structures of merocyanine dyes resulting from their ground state dipole moment μ_g and the sterical design (dotted lines) with the performance in OTFT devices and their thin film morphology.

Whereas all dyes exhibited an antiparallel dimer motif in the solid state due to their intrinsic dipolarity, the two groups differed within the long-range order.

For dyes which showed the typically observed cofacial dimer arrangement with a low lateral slip as well as low dipolarities, the ground state dipole moments were annihilated by the dimer formation and the long-range order in the single crystal structure showed alternating layer spacings where the dimers appeared isolated or in stacks. With AFM and XRD measurements, it could be shown that these dyes formed amorphous thin films even on the TPA modified substrates due to the lack of further electrostatic interactions after dimer formation, thus explaining the low mobility values.

On the other hand, dyes which showed high mobility values up to 0.21 $cm^2 V^{-1} s^{-1}$ exhibited high ground state dipole moments and crystallized into dimer units with large lateral slip. This slip was caused by a properly positioned sterically demanding *tert*-butyl group which prohibited the typical cofacial dimer arrangement. Thus, free π-surfaces were retained and the molecules' dipolarity was not fully annihilated upon dimer formation, which directed a further growth into a brickwork-type arrangement with equidistant spacing of the single molecules. Accordingly, on the TPA modified substrates, highly crystalline layers were formed, giving rise to the high mobility values with the best values observed for dyes with an indolenine donor and thiazole acceptor.

For the best performing dye with an OTFT mobility value of 0.21 $cm^2 V^{-1} s^{-1}$, single crystal field-effect transistor (SCFET) devices were built to examine charge transport directions in the material as well as to investigate intrinsic mobility values without the influence of grain boundaries. In this study, average mobility values of 1.05 $cm^2 V^{-1} s^{-1}$ with the highest value reaching 2.34 $cm^2 V^{-1} s^{-1}$ could be achieved under ambient conditions (Figure 77).

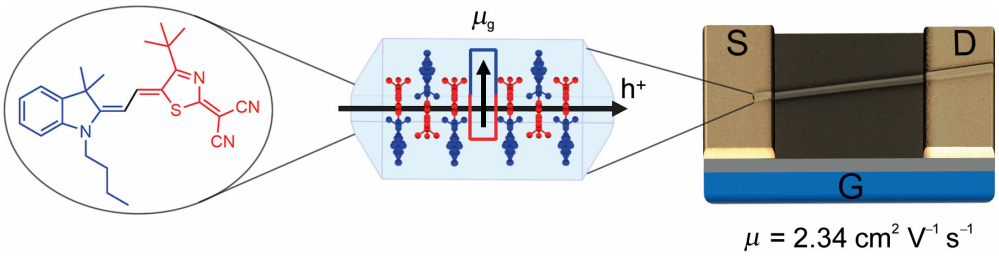

Figure 77. Application of a merocyanine dye in a SCFET device with resulting maximum hole mobility and depicted charge transport direction in the single crystal. Adapted from ref. [110] with permission by The Royal Society of Chemistry.

Thus, for the first time, transistor devices of a highly dipolar material with mobility values exceeding 1.00 $cm^2 V^{-1} s^{-1}$ could be demonstrated, which is similar to the mobility values of SCFETs of typical p-type organic semiconductors like tetracene (2.4 $cm^2 V^{-1} s^{-1}$),[111] TIPS-pentacene (5.0 $cm^2 V^{-1} s^{-1}$)[112] and copper phthalocyanine (1.0 $cm^2 V^{-1} s^{-1}$).[113] Higher values were only reported for dinaphthothienothiophene (DNTT, 9.9 $cm^2 V^{-1} s^{-1}$),[114] pentacene (40 $cm^2 V^{-1} s^{-1}$)[115] and rubrene (40 $cm^2 V^{-1} s^{-1}$),[116] however, these results were obtained by fabrication of the devices in a clean room (rubrene) or measurements under inert conditions (DNTT, pentacene). In contrast, the SCFETs in this thesis were prepared and characterized under ambient conditions.

The suitability of highly dipolar materials for high mobility applications should be clearly reassessed. To recapitulate, the difficulty in applying D–A molecules in organic electronics is rather the formation of large crystalline domains on planar substrates than the molecules' intrinsic dipolarity. By solving this issue, materials with very close intimate π-π-distances due to their dipole-dipole interactions might exhibit even higher charge carrier mobilities in OFETs, thus placing them among the best organic semiconductors.

The second part of this thesis focuses on optical phenomena resulting from different solid state packing arrangements, for which a series of ten merocyanine dyes with aminothiophene donor and thiazole acceptor has been investigated (see Chart 7). While these dyes all showed similar molecular properties due the same chromophore backbone (with the exception of two dyes with aryl substituents), their solid state absorption in thin films yielded narrow and strongly shifted H- or J-type absorption bands (Figure 78) with an energy difference of 0.93 eV. Additionally, a weak fluorescence was observed irrespective of the irradiation wavelength, showing only a small Stokes shift of 50 cm^{-1}.

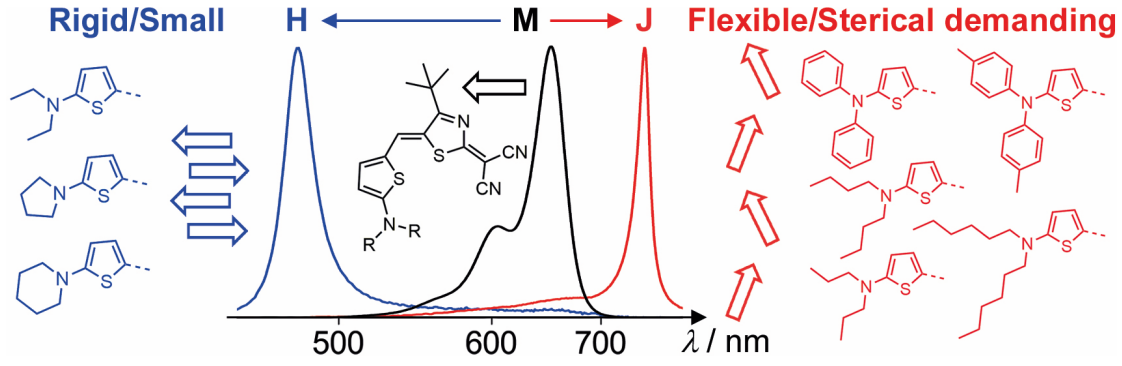

Figure 78. Shift of the absorption band in merocyanine thin films due to different packing structures with card stack (H) or zig-zag type (J) packing, arising from rigid and small or flexible/sterical demanding donor substituents.

In this regard, the rigid and small donor substituents with low sterical demand such as ethyl chains or compact pyrrolidino and piperidin groups gave rise to the H-type absorption. Dyes with longer flexible alkyl chains and sterically demanding phenyl or tolyl substituents exhibited a J-band. An intermediate case with one ethyl and one *n*-butyl chain at the donor showed both bands with similar intensity, whereas substituting the acceptor's *tert*-butyl group with a *n*-butyl chain yielded only a broad absorption band with lower hypsochromic shift. By the analysis of six crystal structures and polarization-dependent absorption of nanocrystals, it was demonstrated that the absorption properties originated from different solid state packing arrangements. In this regard, the broad dimer-like absorption was caused by crystallization of the respective dye into a dimer-like arrangement with alternating layer distances. On the other hand, the narrow and intense hypsochromically (H) and bathochromically (J) shifted bands were shown to arise from a card stack like packing or a zig-zag type arrangement of the dyes in the crystal structure, which is directed by the donor substituents. Additionally, calculations of the exciton coupling by the point dipole approximation, the transition charge method as well as TD-DFT calculations could confirm the observed results. Investigations on mixtures of H- and J-type coupling dyes showed the incorporation of the J-type coupling dye into the preferred card stack structure with H-type coupling, while there was no evidence for an incorporation of a molecule originally preferring an H-stack into the zig-zag structure with J-type coupling. As J-type coupling of merocyanine dyes was so far only observed under rather special experimental conditions,[42a, 42c, 44-46] this is the first time that such a coupling could be realised for the pure solid state and rationalized by crystallographic data.

Concluding, this thesis demonstrates the importance of the molecular design as well as crystal engineering with regard to the solid state properties of merocyanine dyes for charge carrier transport as well as their absorption. Here, the aim of this thesis was to establish structure-property relationships with regard to the two described subjects. While all investigated dyes exhibit the commonly observed antiparallel dimer motif in the solid state structure, crystalline materials with an equidistant layer spacing are shown to be crucial in both fields. By choosing the right molecular design, hole mobilities up to 2.34 $cm^2 V^{-1} s^{-1}$ and the change of exciton coupling from H- to J-type could be accomplished. Here, a fine balance of high dipolarities together with well-defined sterics play the key roles: By specifically avoiding the typical dimer arrangement with low lateral

slip by introducing sterically demanding groups, the π-surfaces remain accessible and the high ground state dipole moments are not fully annihilated, leading to a further, regular growth of the molecular aggregate to the solid state material in two-dimensional layers with equidistant spacing between the single molecules. Thus, this thesis elucidates how to control packing arrangements to precisely tune the charge transport and absorption properties by crystal engineering. In addition to the cheap and easy synthesis and versatile processing possibilities of these small molecules, this knowledge can guide directions towards new tailored materials for a broad variety of applications.

Chapter 5
-
Zusammenfassung

Aufgrund der stetig wachsenden Nachfrage für (opto-)elektronische Materialien im Zuge der Vernetzung aller Bereiche unserer Gesellschaft („Internet der Dinge“) steigt auch das Interesse an organischen Halbleitern. Diese bieten im Gegensatz zu konventionellen anorganischen Materialien die Vorteile von günstiger Verfügbarkeit und Prozessierung. Insbesondere Merocyanine sind schon lange für ihre einfache Synthese und intensive Absorption bekannt, wurden aber aufgrund der hohen Grundzustandsdipolmomente im Bereich der organischen Elektronik bislang vernachlässigt. So existieren nur wenige Studien zu den Eigenschaften dieser Moleküle im Hinblick auf Ladungsträgertransport und deren Festkörperabsorption. Zusätzlich wurde immer nur ein einzelnes Molekül untersucht, oder die Experimente wurden unter besonderen Bedingungen durchgeführt, welche keine Rückschlüsse auf das reine Material zulassen. Daher war das Ziel dieser Arbeit, Struktur-Eigenschafts-Beziehungen für Merocyaninfarbstoffe im Hinblick auf den Ladungsträgertransport sowie ihre Festkörperabsorption mit Exzitonenaufspaltung aufzustellen. Hierzu wurden 30 verschiedene Merocyanine untersucht, welche durch Kombination von jeweils fünf verschiedenen Donor- und Akzeptorheterozyklen hergestellt wurden. Für zwei Serien konnten so Struktur-Eigenschafts-Beziehungen für die optoelektronischen Fragestellungen aufgestellt werden (Schaubild 7).

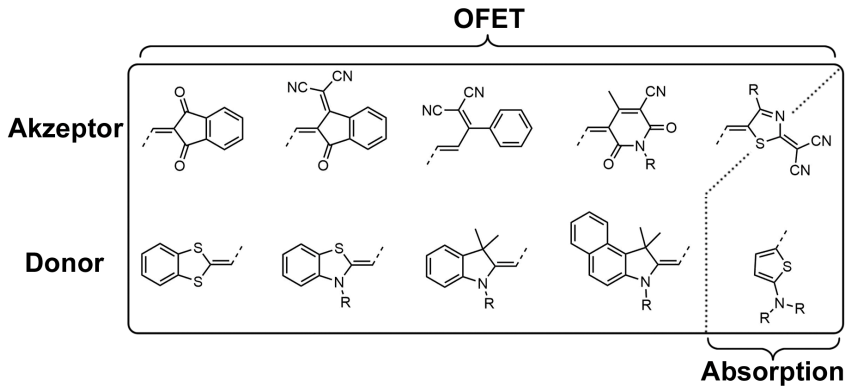

Schaubild 7. Donor- und Akzeptorheterozyklen der in dieser Arbeit untersuchten Merocyanine.

Der erste Teil dieser Dissertationsschrift behandelt die Untersuchung der Ladungstransporteigenschaften von Merocyaninfarbstoffen. Hierbei wurden zwanzig Farbstoffe mit verschiedenen Donor- und Akzeptorheterozyklen in vakuum-prozessierten organischen Dünnschichttransistoren (engl. *organic thin film transistors*, OTFTs) untersucht. Alle Farbstoffe zeigten HOMO Niveaus, welche sich für den Einsatz in p-halbleitenden OTFTs mit Goldelektroden eigneten, und wiesen in Bauteilen auf Si/SiO_2 Substraten entweder ähnliche Lochmobilitätswerte im Bereich von 10^{-5}-10^{-6} $cm^2\ V^{-1}\ s^{-1}$, oder aber gar keinen Feldeffekt auf. Auf diesen Substraten mit hoher Oberflächenenergie überlagerten die Molekül-Substrat-Wechselwirkungen die intermolekularen Wechselwirkungen und somit bildeten alle Farbstoffe amorphe Schichten aus (verifiziert durch Rasterkraftmikroskopie und Röntgenbeugung). Hingegen konnten beim Einsatz von *n*-Tetradecylphosphonsäure (engl. *n-tetradecylphosphonic acid*, TPA) modifizierten Si/SiO_2 Substraten mit einer niedrigen Oberflächenenergie zwei Gruppen von Molekülen identifiziert werden, welche entweder geringe Mobilitätswerte - wie auf Si/SiO_2 - oder hohe Mobilitäten bis zu 0.21 $cm^2\ V^{-1}\ s^{-1}$ aufwiesen. Diese hohen Werte wurden auf die zwischenmolekularen Dipol-Dipol-Wechselwirkungen zurückgeführt, die auf diesem Substrat mit geringer Oberflächenenergie nun die Molekül-Substrat-Wechselwirkungen überlagern konnten. Weiterhin konnte die Ausbildung zweier Gruppen schließlich mit den Einkristallstrukturen der Farbstoffe korreliert werden (Abbildung 76).

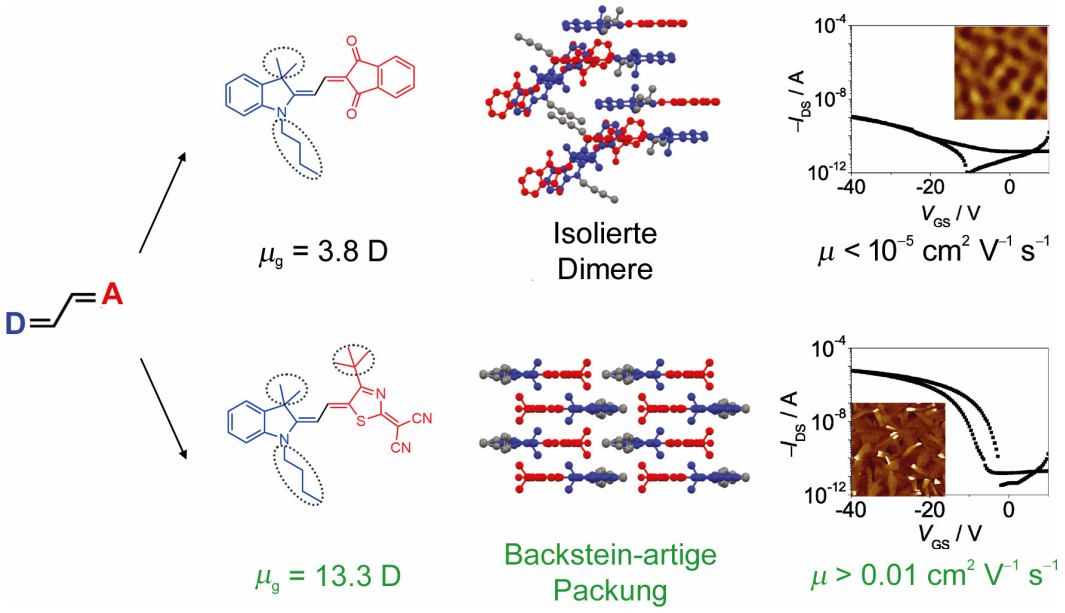

Abbildung 76. Verschiedene Einkristallpackungsstrukturen von Merocyaninen, welche sich aufgrund der Grundzustandsdipolmomente μ_g und dem sterischen Design (gepunktete Linien) ergeben und der resultierenden Leistung in OTFT Bauteilen sowie ihrer Dünnschichtmorphologie.

Alle untersuchten Farbstoffe zeigten in ihrer Einkristallstruktur ein antiparalleles Dimermotiv aufgrund ihrer inhärenten Dipolarität. Die beiden identifizierten Gruppen wiesen allerdings Unterschiede hinsichtlich ihrer langreichweitigen Ordnung auf.
Hierbei zeigten Farbstoffe, die geringe Mobilitätswerte oder gar keinen Feldeffekt aufwiesen, antiparallele Dimere mit geringem lateralem Versatz in der Einkristallstruktur. Innerhalb dieser Packung wurden so die Grundzustandsdipolmomente ausgelöscht. Folglich zeigte die langreichweitige Ordnung der Einkristallstruktur alternierende Ebenenabstände, wobei die Dimere entweder isoliert oder in Stapeln auftraten. Durch Rasterkraftmikroskopie sowie Röntgenbeugung konnte außerdem gezeigt werden, dass diese Farbstoffe sogar auf den TPA modifizierten Oberflächen amorphe Dünnschichten ausbildeten. Dies wurde auf das Fehlen von weiteren elektrostatischen Wechselwirkungen nach Bildung eines Dimers zurückgeführt und erklärt die niedrigen Mobilitätswerte.
Die zweite Gruppe zeigte hingegen hohe Mobilitätswerte bis zu 0.21 $cm^2 V^{-1} s^{-1}$ und kristallisierte in Dimereinheiten mit großem lateralem Versatz, der durch das Einbringen sterisch anspruchsvoller *tert*-Butyl Gruppen bewirkt wurde. Somit blieben freie π-Kontaktflächen der Moleküle nach Bildung eines Dimers teilweise erhalten und die Dipolarität wurde nicht vollständig ausgelöscht, was ein weiteres Wachstum in eine Backstein-Struktur dirigierte. In dieser zeigten die Moleküle äquidistante Abstände und entsprechend bildeten sich auch hochkristalline Schichten auf dem TPA modifizierten Substrat aus, was die hohen Mobilitätswerte erklärt. Die besten Lochmobilitäten wurden hierbei für eine Kombination aus Indolenin-Donor und Thiazol-Akzeptor beobachtet.
Für den besten Farbstoff mit Mobilitätswerten von 0.21 $cm^2 V^{-1} s^{-1}$ in OTFTs wurden Einkristalltransistoren hergestellt, um die intrinsische Mobilität ohne Einflüsse der Korngrenzen sowie die verschiedenen Ladungstransportrichtungen zu untersuchen. In dieser Studie wurden Durchschnittswerte von 1.05 $cm^2 V^{-1} s^{-1}$ sowie ein maximaler Wert von 2.34 $cm^2 V^{-1} s^{-1}$ unter ambienten Bedingungen erreicht (Abbildung 77). Dies ist das erste Mal, dass Transistorbauteile eines hoch dipolaren Materials hohe Mobilitäten über 1.00 $cm^2 V^{-1} s^{-1}$ aufweisen. Weiterhin sind diese Werte mit jenen vergleichbar, welche für Einkristalltransistoren konventioneller organischer p-Halbleiter berichtet wurden, wie z.B. für Tetracen (2.4 $cm^2 V^{-1} s^{-1}$),[111] TIPS-Pentacen (5.0 $cm^2 V^{-1} s^{-1}$)[112] und Kupfer-Phthalocyanin (1.0 $cm^2 V^{-1} s^{-1}$).[113] Nur für sehr wenige Moleküle, z. B. Dinaphthothienothiophen (DNTT, 9.9 $cm^2 V^{-1} s^{-1}$),[114] Pentacen (40 $cm^2 V^{-1} s^{-1}$)[115] und Rubren (40 $cm^2 V^{-1} s^{-1}$),[116] konnten höhere Mobilitäten realisiert werden. Hierbei ist

aber zu sagen, dass die Bauteile mit den höchsten Mobilitätswerten entweder in einem Reinraum gefertigt (Rubren) oder unter inerten Bedingungen charakterisiert wurden (DNTT und Pentacen), wohingegen die Prozessierung und Charakterisierung der hier untersuchten Bauteile unter ambienten Bedingungen erfolgte.

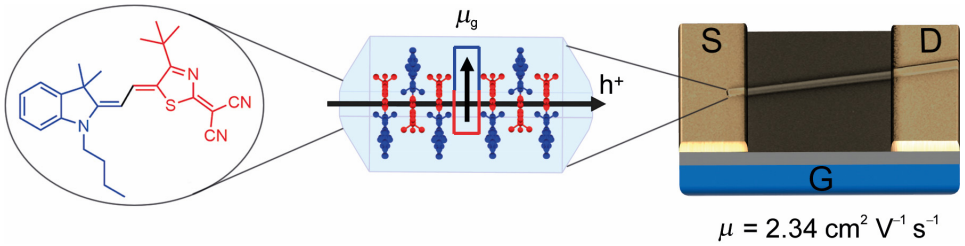

Abbildung 77. Anwendung eines dipolaren Merocyaninfarbstoffs in einem Einkristalltransistor mit der maximal erreichten Lochmobilität sowie eingezeichneter Ladungstransportrichtung im Kristall. Adaption aus Lit. [110] mit Erlaubnis von The Royal Society of Chemistry.

Aufgrund der vorliegenden Ergebnisse sollte die Eignung von hoch dipolaren Materialien für Anwendungen mit hohen Mobilitäten überdacht werden. Es scheint, dass die Schwierigkeit der Anwendung von D−A Molekülen im Feld der organischen Elektronik nicht in der Dipolarität der Moleküle, sondern vielmehr im Aufbringen hochkristalliner Schichten auf planaren Substraten liegt. Durch das Lösen dieses Problems könnten organische Halbleitermaterialien zugänglich werden, welche aufgrund ihrer elektrostatischen Dipol-Dipol-Wechselwirkung mit noch kleineren π-π-Abständen kristallisieren. Da dies den Ladungsträgertransport begünstigt, würden dadurch noch höhere Mobilitäten möglich werden, welche vergleichbar oder sogar besser als die der momentan besten organischen Halbleiter wären.

Der zweite Teil dieser Dissertationsschrift befasst sich mit optischen Phänomenen, welche durch verschiedene Festkörperpackungsstrukturen hervorgerufen werden. Hierzu wurde eine Serie von zehn Merocyaninfarbstoffen mit Aminothiophen-Donor sowie Thiazol-Akzeptor untersucht (Schaubild 7). Während diese Farbstoffe aufgrund des gleichen Chromophorgrundgerüsts ähnliche molekulare Eigenschaften aufwiesen (mit Ausnahme der beiden Farbstoffe mit Aryl-Substituenten), wies die Festkörperabsorption der Dünnschichten schmale sowie stark verschobene H- oder J-Banden auf, welche einen Versatz von 0.93 eV zeigten (Abbildung 78). Zusätzlich konnte eine schwache, von der Anregungswellenlänge unabhängige Fluoreszenz mit einer kleinen Stokes-Verschiebung von 50 cm^{-1} beobachtet werden.

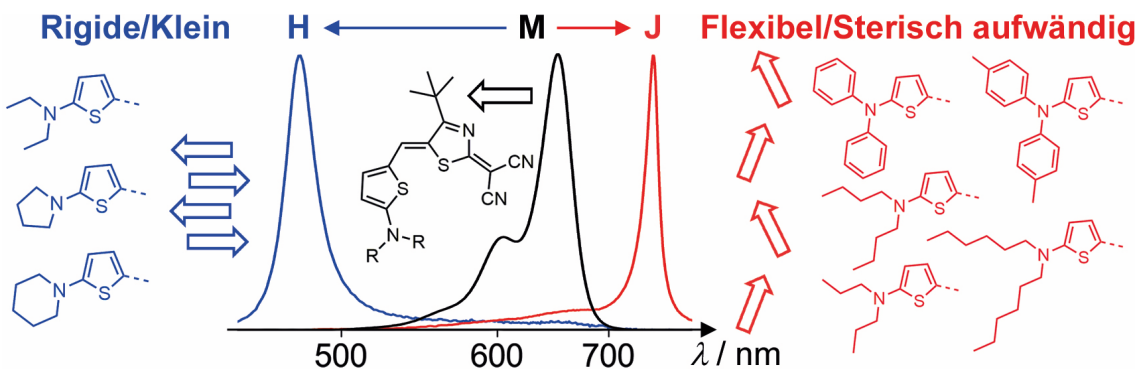

Abbildung 78. Verschiebung der Absorptionsbande von Merocyaninen in Dünnschichten aufgrund verschiedener Packungstrukturen mit Kartenstapel-artiger (H) sowie Zick-Zack-artiger (J) Packung, die durch kleine rigide bzw. flexible oder sterisch anspruchsvolle Donor-Substituenten bedingt werden.

Hierbei zeigten die Farbstoffe mit kleinen rigiden Substituenten am Donor, d. h. Ethyl-Ketten oder kompakten Pyrrolidino- und Piperidin-Gruppen, eine H-Bande, wohingegen Farbstoffe mit längeren flexiblen Alkylketten oder sterisch anspruchsvollen Phenyl- sowie Tolyl-Gruppen eine J-Bande aufwiesen. Ein Derivat mit einer Ethyl- sowie einer *n*-Butyl-Kette am Donor zeigte zudem beide Banden mit vergleichbarer Intensität, wohingegen das Substituieren der *tert*-Butyl Gruppe am Akzeptor durch eine *n*-Butyl-Kette eine breite Absorptionsbande mit nur schwacher hypsochromer Verschiebung aufwies. Durch die Analyse von sechs Einkristallstrukturen und polarisationsabhängigen Absorptionsmessungen von Nanokristallen konnte demonstriert werden, dass die Absorptionseigenschaften von verschiedenen Packungsstrukturen hervorgerufen wurden. Hierbei wurde die breite Dimer-Absorption durch eine Kristallisation des entsprechenden Farbstoffs zu einer Dimer-artigen Packung mit alternierenden Ebenenabständen bedingt. Die schmalen und intensiven hypsochrom (H) oder bathochrom (J) verschobenen Banden hingegen wurden von einer Kartenstapel-artigen sowie einer Zick-Zack-artigen Struktur im Festkörper hervorgerufen, welche durch die Sterik des Donorsubstituenten dirigiert wurden. Zusätzlich konnten diese Ergebnisse durch Berechnungen der Exzitonenkopplung mit Hilfe der Punkt-Dipol-Näherung, durch Berechnung der Übergangsladungen sowie durch TD-DFT Rechnungen belegt werden. Weiterhin wurde durch Untersuchungen von Mischungen dieser Farbstoffe gezeigt, dass Farbstoffe, welche J-Kopplung zeigen, in die präferierte Kartenstapel-artige Packung mit H-Kopplung eingebaut werden können, während es hingegen keine Hinweise für den Einbau eines H-Stapel präferierenden Moleküls in die Zick-Zack-Packung mit J-Kopplung gab. Da J-Kopplungen von Merocyaninfarbstoffen bislang nur unter

speziellen experimentellen Bedingungen beobachtet werden konnten,[42a, 42c, 44-46] ist dies das erste Mal, dass solch eine Kopplung im reinen Festkörper realisiert wurde und mit kristallographischen Daten erklärt werden konnte.

Zusammenfassend wird innerhalb der vorliegenden Dissertationsschrift die Wichtigkeit des molekularen Designs sowie des gezielten Einstellens von Packungsmotiven (engl. *crystal engineering*) im Hinblick auf Ladungsträgertransport und Festkörperabsorption von Merocyaninen gezeigt. Das Ziel dieser Arbeit war es, Struktur-Eigenschafts-Beziehungen für die beiden Themenkomplexe aufzustellen. Während alle untersuchten Farbstoffe das üblicherweise beobachtete antiparallele Dimermotiv in der Festkörperstruktur aufweisen, sind kristalline Materialien mit äquidistanten Ebenenabständen innerhalb der molekularen Packung für beide Felder von hoher Bedeutung. Dadurch konnten Ladungsträgermobilitäten bis zu 2.34 $cm^2 V^{-1} s^{-1}$, sowie Exzitonenkopplung im Festkörper mit schmalen und intensiven H- und J-Absorptionsbanden realisiert werden. Zum Erreichen dieser Eigenschaften nehmen eine hohe Dipolarität sowie eine gut definierte Sterik, um einen gewissen lateralen Versatz zu induzieren, die Schlüsselrollen ein: Durch das gezielte Verhindern der typischen Dimeranordnung mit geringem lateralen Versatz mit Hilfe sterisch aufwändiger Gruppen werden antiparallelen Dimere mit hohem lateralem Versatz generiert. Die π-Flächen bleiben dadurch zugänglich und die Grundzustandsdipolmomente werden nicht vollständig ausgelöscht, sodass ein weiteres geordnetes Wachstum vom Molekülaggregat zum Festkörper mit äquidistanten Abständen zwischen den einzelnen Molekülen in zweidimensionalen Schichten erfolgt. Durch diese Arbeit wird gezeigt, wie die molekulare Packung im Hinblick auf Ladungsträgertransport und Festkörperabsorption gezielt kontrolliert werden kann. Zusätzlich zu der günstigen sowie einfachen Synthese und Prozessierbarkeit der Moleküle können so neue maßgeschneiderte Materialien für breite Anwendungsmöglichkeiten zugänglich werden.

Chapter 6
-
Experimental Part

6.1 Materials

In this section, all materials used for this thesis are described, including organic dye molecules, substrates as well as commercially obtained solvents and materials (Table 14).

Used Merocyanines

All merocyanines are composed of various donor and acceptor heterocycles (Scheme 2). The studied molecules are shown in Chart 8. All dyes were synthesized in the group of Prof. Dr. Frank Würthner by Dr. Alhama Arjona Esteban, Dr. Hannah Bürckstümmer, Thorsten Günder, Fabian Holzmeier and Dr. Elena Tulyakova. The syntheses of all dyes was reported in the given references: **D3A1**,[73] **D3A2**,[13] **D3A4**,[9] nBu**D3**tBu**A5**,[73] nHe**D3**tBu**A5**,[76] Bn**D3**tBu**A5**,[13] nBu**D3**nBu**A5**,[77] bPr**D3**tBu**A5**[14], nPr**D5**tBu**A5**,[117] nBu**D5**tBu**A5**,[61] nBu**D5**nBu**A5**,[117] Ph**D5**tBu**A5**,[71] Pyrl**D5**tBu**A5**[117] and all other dyes with donors **D1-D4**[118] as well as the **D5A5** family[119].

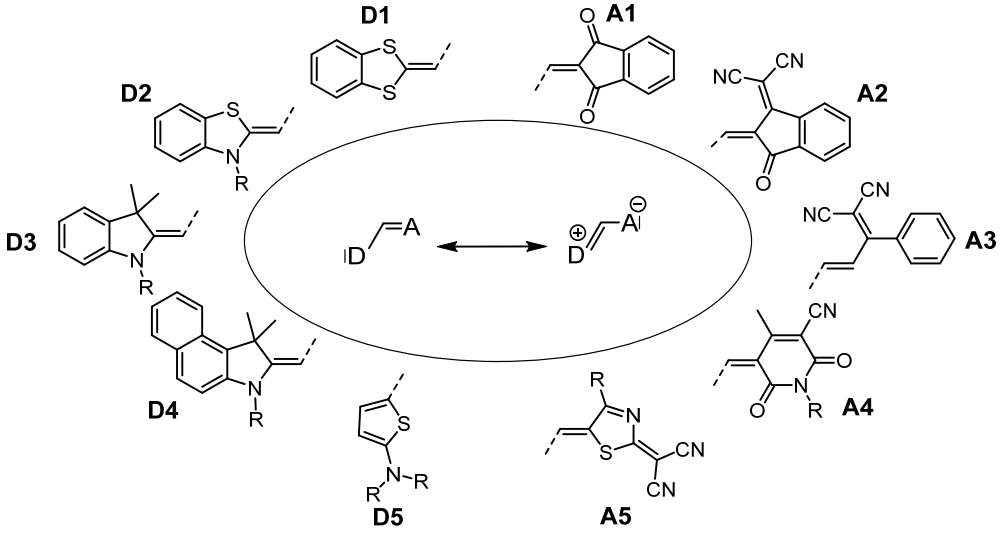

Scheme 2. Merocyanine dyes based on five different donor and acceptor heterocycles employed in this thesis as well as mesomeric structures (in oval circle).

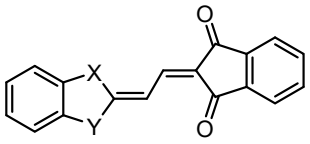

D1A1: X = Y = S
D3A1: X = CMe_2, Y = N*n*Bu

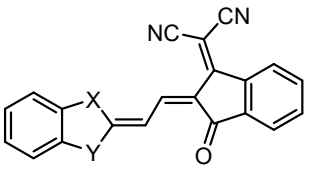

D1A2: X = Y = S
D3A2: X = CMe_2, Y = N*n*Bu

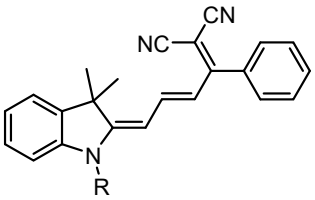

D3A3: R = *n*Bu

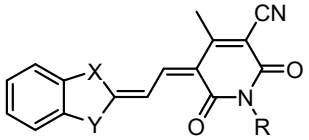

D1A4: X = Y = S, R = Me
D3A4: X = CMe_2, Y = NMe, R = *n*Bu

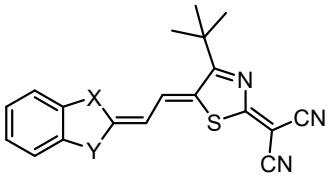

D1A5: X = Y = S
D2A5: X = S, Y = N*n*Bu

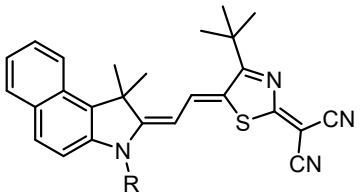

D4A5: R = *n*Bu

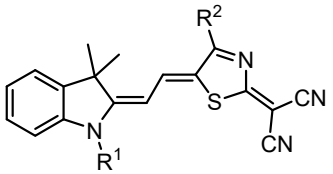

Me**D3**tBu**A5**: R^1 = Me R^2 = *t*Bu
nPr**D3**tBu**A5**: R^1 = *n*Pr R^2 = *t*Bu
iPr**D3**tBu**A5**: R^1 = *i*Pr R^2 = *t*Bu
nBu**D3**tBu**A5**: R^1 = *n*Bu R^2 = *t*Bu
nPe**D3**tBu**A5**: R^1 = *n*Pen R^2 = *t*Bu
nHe**D3**tBu**A5**: R^1 = *n*Hex R^2 = *t*Bu
Bn**D3**tBu**A5**: R^1 = Bn R^2 = *t*Bu
nBu**D3**nBu**A5**: R^1 = *n*Bu R^2 = *n*Bu

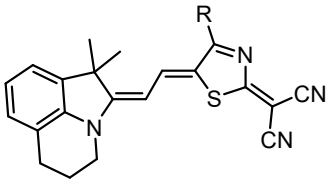

bPr**D3**tBu**A5**: R = *t*Bu
bPr**D3**Ph**A5**: R = Ph
(bPr: bridged propyl)

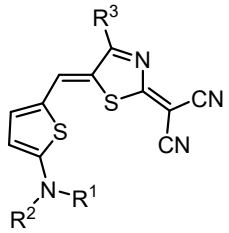

Et**D5**tBu**A5**: R^1 = R^2 = Et R^3 = *t*Bu
EtBu**D5**tBu**A5**: R^1 = Et, R^2 = *n*Bu R^3 = *t*Bu
nPr**D5**tBu**A5**: R^1 = R^2 = *n*Pr R^3 = *t*Bu
nBu**D5**tBu**A5**: R^1 = R^2 = *n*Bu R^3 = *t*Bu
nHe**D5**tBu**A5**: R^1 = R^2 = *n*Hex R^3 = *t*Bu
nBu**D5**nBu**A5**: R^1 = R^2 = *n*Bu R^3 = *n*Bu

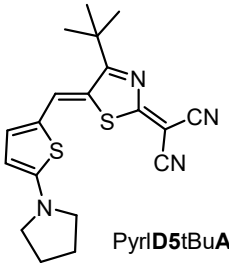

Pyrl**D5**tBu**A5**

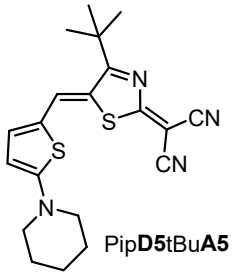

Pip**D5**tBu**A5**

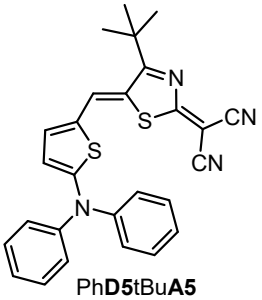

Ph**D5**tBu**A5**

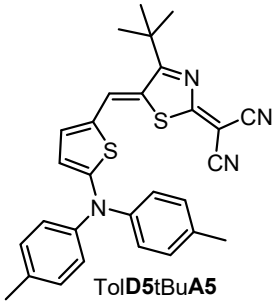

Tol**D5**tBu**A5**

Chart 8. Chemical structures of merocyanine dyes investigated in this thesis.

Solvents and Materials

Table 14. Solvents and materials used for the experiments described in this thesis.

Solvents and materials	Company
Toluene, p.a. grade	*VWR Chemicals*, *BDH Prolabo®*
Acetone, semiconductor grade	*Aldrich® Chemistry*
Isopropanol, semiconductor grade	*Aldrich® Chemistry*
Chloroform, anhydrous (≥ 99 %)	*Sigma Aldrich®*
Methanol, p.a. grade	*VWR Chemicals*, *BDH Prolabo®*
Methanol, anhydrous (≥ 99 %)	*Sigma Aldrich®*
1,4-Dioxane, anhydrous (≥ 99 %)	*Sigma Aldrich®*
Poly(3,4-ethylenedioxythiophene):Polystyrene sulfonate (PEDOT:PSS), Clevios™ P VP Al 4083	*Heraeus*
Gold, 99.99%	*Umicore Materials AG*
Gold wire, diameter of 25 μm or 12.7 μm	*VWR*

Substrates

Si/SiO_2 wafers: Boron-doped p-type Si(100) wafers with a thickness of 525 ± 25 μm and 100 nm SiO_2 as gate dielectric (C_i = 34.0 nF cm^{-1}) were obtained from *SiMat*.

TPA modified substrates: *N*-tetradecylphosphonic acid (TPA) modified Si/SiO_2/AlO_x substrates were prepared by atomic layer deposition of an 8 nm thick AlO_x layer onto the Si/SiO_2 wafers and subsequent immersion of the Si/SiO_2/AlO_x substrates into isopropanol solutions of TPA yielding a 1.7 nm thick monolayer of TPA. The substrates (C_i = 32.4 nF cm^{-1}) were kindly provided by Dr. Hagen Klauk & Dr. Ute Zschieschang (Max-Planck-Institute Stuttgart).

Quartz substrates: 1.3 mm thick quartz substrates (*SUPRASIL®*) with a diameter of 14 mm were obtained from *Hellma® Analytics*.

ITO substrates: Glass substrates (25.8 mm x 25.8 mm x 1 mm) with an indium tin oxide (ITO) spot of 16 mm diameter and 150 nm thickness were obtained from *Soluxx GmbH*.

SEM substrates: For SEM measurements, Lacey Carbon Films on 200 Mesh copper grids were obtained from *Agar Scientific Ltd*.

6.2 Sample Preparation

Cleaning Procedure

The cleaning of the wafer, quartz and ITO substrates was performed on a spin coater (*SPIN 150*, *SPS Europe*) with rinsing of the substrates with toluene, acetone and isopropanol at a velocity of 3000 rpm for 30 s. The Si/SiO_2 and ITO substrates were afterwards cleaned in a UVO-Cleaner (*Model 42A-220*, *Jelight Company Inc.*) for 5 min. The SEM substrates were used as received due to their small size.

OTFTs

Merocyanine films of 30 nm thickness were sublimed under vacuum (pressure < 10^{-6} mbar) in a sublimation system *Auto306 with FL400 vacuum chamber* (*BOC Edwards*) onto Si/SiO_2 substrates as well as TPA modified $Si/SiO_2/AlO_x$ substrates. A growth rate of 0.2-1.0 nm min^{-1} was adjusted by monitoring the film growth with a quartz crystal microbalance and the substrate temperature was fixed in the range of 50-125 °C to yield devices with optimized performance. To form source and drain electrodes, 30 nm gold were evaporated through steel shadow masks onto the films with a rate of 0.03-0.05 nm s^{-1} at a pressure of below $3 \cdot 10^{-6}$ mbar. By this procedure, devices with a channel length *L* and width *W* of 100 and 200 μm, respectively, were obtained.

SCFETs and Nanocrystals

The growth of nanocrystals was carried out as follows: First, solutions of the dyes in $CHCl_3$ were prepared, which were then filtered with a 0.2 μm polytetrafluoroethylene (PTFE) syringe filter and mixed with MeOH if needed to induce more nucleation sites and thus fabricate smaller crystals (for experimental conditions, see Table 15). Then, a substrate was placed onto a PTFE plate in a closable container (50 mm diameter, 30 mm height). Additionally, a small PTFE piece was put in the middle of the substrate and two screw caps, each filled with 250 μl of either $CHCl_3$ (Pyrl**D5**tBu**A5**, nPr**D5**tBu**A5**) or a $CHCl_3$:MeOH mixture (volume ratio 1:1; nBu**D3**tBu**A5**) were placed next to the substrate. The container was sealed with parafilm® and heated to 30 °C for 1 h. Afterwards, the solution was deposited on the substrate and the container was sealed again with parafilm®. After 3 d, the solvent evaporated and thin nanocrystals were retained on the substrate.

Table 15. List of the preparation conditions for the growth of nanocrystals of dyes nBu**D3**tBu**A5**, Pyrl**D5**tBu**A5** and nPr**D5**tBu**A5**.

#	c / 10^{-3} mol L^{-1}	Volumetric mixing ratio $CHCl_3$:MeOH	Substrate
nBu**D3**tBu**A5**	7.0	2:1 or 3:2	TPA modified Si/SiO_2/AlO_x, Quartz
Pyrl**D5**tBu**A5**	2.7	1:0	Quartz
nPr**D5**tBu**A5**	2.5	2:1	Quartz

For the fabrication of SCFETs of nBu**D3**tBu**A5**, residual solvent was first removed from the substrates by heating for 1 h to 40 °C under vacuum. Afterwards, a gold wire with a diameter 25 µm or 12.7 µm (the diameter depended on the nanocrystals' size) was placed onto the single crystals as shadow mask. Then, 100 nm gold were evaporated in a sublimation system *Auto306 with FL400 vacuum chamber* (*BOC Edwards*) with a rate of 0.03-0.05 nm s^{-1} and a pressure below $3 \cdot 10^{-6}$ mbar to yield source and drain electrodes. The schematic preparation of nanocrystals and SCFETs is shown in Figure 79.

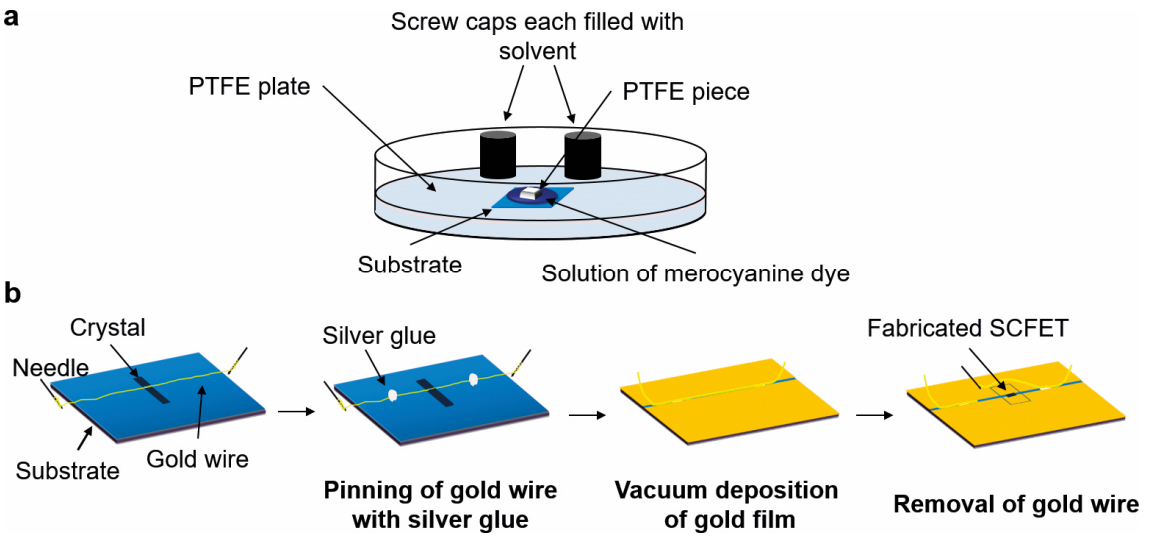

Figure 79. (a) Schematic drawing of nanocrystal growth procedure; (b) Schematic drawing of fabrication of gold source and drain electrodes onto a grown nanocrystal; Adapted from ref. [110] with permission by The Royal Society of Chemistry.

Thin Films for UV-vis/XRD/SAED Studies

D3A5 group

For XRD measurements, the transistor devices were used. The preparation of the samples for SAED was performed by deposition of the dye onto the respective substrate and subsequent deposition of a thin carbon film as support layer. By immersion of the substrate into 10 % HF solution, the films were separated from the substrate and transferred onto a copper grid.[120]

D5A5 group

The thin films for UV-vis and XRD experiments were fabricated by a spin coating process: Here, 25 µl of a $4 \cdot 10^{-3}$ M solution in $CHCl_3$ were deposited onto a rotating quartz substrate (3000 rpm, 30 s spin time) with a *SPIN 150* spin coater (*SPS Europe*). With this procedure, there is no variation of the concentration due to varying times between deposition of the solution and starting of the spin coater. Afterwards, the UV-vis absorption was measured for the as cast films as well as films after an additional annealing step (130 °C, 5 min) on a precision hot plate (*PZ28-2*, *Harry Gestigkeit GmbH*).

The thin films for the TEM/SAED experiments were prepared in a similar fashion onto PEDOT:PSS coated ITO substrates, which were also fabricated by spin coating (2000 rpm, 4000 rpm s^{-1}, 30 s). Here, the thin films were spin coated from 200 µl of a $4 \cdot 10^{-3}$ M solution in $CHCl_3$ (3000 rpm, 3000 rpm s^{-1}, 30 s) and then additionally annealed as described above. To obtain the merocyanine film, the substrates were immersed in purified water, where the PEDOT:PSS layer dissolved, and the floating merocyanine film could be retrieved with carbon-covered copper grids for TEM.

6.3 Methods

Atomic Force Microscopy

Atomic force microscopy (AFM) of the vacuum deposited thin films of the **D3A5** group was performed in tapping mode with a *Bruker AXS MultiMode Nanoscope IV* instrument. AFM of all nanocrystals and thin films of dyes of the **D5A5** group was carried out in tapping mode with a *NT-MDT SOLVER NEXT* instrument. In both cases, silicon cantilevers with a spring constant of 42 N m^{-1} and a resonance frequency of ~300 kHz were used (*OMCL-AC160TS*, *Olympus*).

Calculations

The calculations of the Braivais-Friedel-Donnay-Harker (BFDH) morphologies from the crystal structures were performed with the program *Mercury*.[84] The density functional theory (DFT) calculations of the electrostatic potentials, ground state dipole moments, transition dipole moments, transition densities and UV-vis spectra of segments taken from crystal structures were performed with the *Gaussian 09* program package.[121] All calculations were performed as single-point calculations on geometries taken from the respective crystal structures. For the dyes of the **D3A5** group, the functional B3LYP[122] and the basis set 6-31G(d) were used while for dyes of the **D5A5** group, ωB97[123] was used as functional and def2-SVP[124] as basis set. The transition densities were analyzed with *Multiwfn*[125] and all visualizations were done with *GaussView 5*.[126]

Cyclic Voltammetry

Cyclic voltammetry (CV) was carried out in a three electrode single-compartment cell on a standard electrochemical analyzer (*EC epsilon*, *BAS instruments*) (working electrode: Pt disc; reference electrode: Ag/AgCl; auxiliary electrode: Pt wire). The experiments were performed with a scanning rate of 100 mV s^{-1} under argon in a 10^{-4} M CH_2Cl_2 (HPLC grade, *J.T. Baker*, dried over calcium hydride and degassed) solution. Ferrocene was used as internal standard and Tetrabutylammonium hexafluorophosphate (TBAHFP) as supporting electrolyte.

Electrical Characterization of Transistor Devices

The electrical characterization of transistor devices was done by measuring the transistor current voltage characteristics with a *Micromanipulator 4060* and *4155C semiconductor parametric analyzer* (*Agilent Technologies, Inc.*) under ambient conditions at room temperature. By scratching the semiconducting film around the device with a needle of the Micromanipulator, the device was electrically isolated before the characterization.

Electro-Optical Absorption Measurements (EOAM)

With electro-optical absorption spectroscopy, the dipole moments of the ground state μ_g and the dipole moment difference $\Delta\mu = \mu_e - \mu_g$ (μ_e: excited state dipole moment) of the chromophores were determined. Here, measuring the difference of the absorption of a solution with ($\varepsilon^E(\varphi,\tilde{\nu})$) and without ($\varepsilon(\tilde{\nu})$) an applied external electric field **E** was done with polarized light, which was oriented parallel ($\varphi = 0°$) and perpendicular ($\varphi = 90°$) to the direction of the electric field.[56b] Uniaxial phases were induced in a solution with an alternating and a constant electric field of about $3 \cdot 10^6$ V m^{-1}. Here, the dichroism $\varepsilon^E(\varphi,\tilde{\nu}) - \varepsilon(\tilde{\nu})$ depends on several factors, such as the orientational order of the molecules because of their ground state dipole moment μ_g, the shift of the absorption band which is proportional to the dipole moment difference $\Delta\mu$, and on the dependence of the electric transition dipole moment μ_{eg} on the electric field **E**. For determining the integral absorption μ_{eg}^2, UV-vis absorption spectra were recorded on a *Perkin-Elmer Lambda 950* spectrometer at 298 K. Anhydrous 1,4-dioxane was used as solvent for all measurements.

Nuclear Magnetic Resonance

Nuclear magnetic resonance (NMR) experiments were performed on a Bruker Avance III HD 400 spectrometer in $CDCl_3$ at 298 K.

Scanning Electron Microscopy

Scanning electron microscopy (SEM) experiments were done on a *Zeiss Ultra Plus FE-SEM* with a *GEMINI* e-Beam column, which was operated at 3-5 kV. For the images obtained with an energy selective backscattered detector, a grid voltage of 530 V was set.

Single Crystal X-ray Diffraction

Crystallographic data was collected on a *Bruker X8 APEX* diffractometer for dyes **D3A1**, **D3A2**, while the crystal structure of dye **D3A4** was measured on a *Nonius KappaCCD* instrument. On both diffractometers, Mo K_α radiation ($\lambda = 0.71073$ Å) and a CCD area detector were used. The data of all other dyes was recorded on a *Bruker D8 Quest* diffractometer with a *Photon 100 CMOS APS* detector. Here, Mo K_α radiation ($\lambda = 0.71073$ Å; nBu**D5**nBu**A5**) or Cu K_α radiation ($\lambda = 1.54056$ Å; all other dyes of the **D5A5** and the **D3A5** family) was used. Refinement of the structures was done with the SHELX software package and expanding using Fourier techniques.[127] Non-hydrogen atoms were refined anisotropically and calculations of the structure factors included hydrogen atoms which were assigned idealized positions.

Transmission Electron Microscopy / Selected Area Electron Diffraction

The selected area electron diffraction (SAED) and transmission electron microscopy (TEM) for dyes of the **D3A5** group were performed on a *JEOL JEM-1011* transmission electron microscope with an accelerating voltage of 100 kV. In order to achieve a weaker-intensity beam and high contrast, dark field was used for the experiments.
For dyes of the **D5A5** group, TEM and SAED measurements were carried out on a *FEI Titan 80-300* transmission electron microscope at 150 kV and 300 kV.

UV-vis and Fluorescence Characterization

Optical absorption spectra in solution were recorded on a *PerkinElmer Lambda 950* UV-vis/NIR, *Lambda 35* UV-vis or *JASCO V670* UV-vis spectrometer in quartz cuvettes (*SUPRASIL®*) from *Hellma® Analytics*. Thin film absorption spectra were measured in transmission mode on a *PerkinElmer Lambda 950* UV-vis/NIR spectrometer which was equipped with an integration sphere. UV-vis spectra of the nanocrystals were recorded with a *Nikon Eclipse LV100Pol* optical polarizing microscope equipped with a *Black-Come*t spectrometer (*StellarNet*). The in-situ UV-vis experiments were done in reflectance mode with an *OceanOptics Maya2000 Pro* spectrometer on a precision hot plate (*PZ28-2*, *Harry Gestigkeit GmbH*). Localized UV-vis absorption was measured in transmission mode on a *Zeiss Axio Imager* microscope equipped with a *Zeiss* CCD spectrometer and customized by *A.S. & Co*. Emission properties were measured at room

temperature on an *Edinburgh Instruments FLS980* spectrometer with front face geometry setup (22.5°).

X-ray Diffraction

X-ray diffraction (XRD) was done with Cu K_α radiation ($K_{\alpha1}$ and $K_{\alpha2}$ doublet, mean wavelength $\lambda = 154.19$ pm) on a *Bruker D8 Discover* diffractometer with a *LynxEye-1D-Detector*.

6.4 Single Crystal Data

Table 16. Crystallographic data for dyes **D3A1**, **D3A2** and **D3A4**.

Compound	**D3A1**	**D3A2**	**D3A4**
Chemical formula	$C_{25}H_{25}NO_2$	$C_{28}H_{25}N_3O$	$C_{24}H_{27}N_3O_2$
M / g mol^{-1}	371.46	419.51	389.49
T / K	167(2)	173(2)	100(2)
Crystal description	needle	block	block
Crystal color	red	red	red
Crystal system	monoclinic	monoclinic	monoclinic
Space group	P21/n	P21/c	P21/c
a / Å	9.315(8)	10.281(3)	10.8848(2)
b / Å	11.178(9)	21.738(6)	15.0436(3)
c / Å	19.178(16)	10.040(3)	12.8829(2)
α / °	90	90	90
β / °	96.267(13)	96.970(4)	101.2440(10)
γ / °	90	90	90
V_{UC} / Å^3	1985(3)	2227.3(12)	2069.04(6)
Z	4	4	4
ρ_{cal} / g cm^{-3}	1.243	1.251	1.250
μ_{abs} / mm^{-1}	0.078	0.077	0.081
F(000)	792	888	832
Measurement range of θ / °	2.81-27.85	2.77-27.95	2.91-31.51
Completeness / %	99.9	100.0	99.5
Number of independent reflections	3907	4405	6865
Parametres / restraints	256/0	292/0	267/0
Goodness of fit for F^2	1.176	1.075	1.033
$R(I > 2\sigma(I))$	$R_1 = 0.0545$ $wR_2 = 0.1081$	$R_1 = 0.0402$ $wR_2 = 0.0992$	$R_1 = 0.0401$ $wR_2 = 0.1072$
R(all data)	$R_1 = 0.0630$ $wR_2 = 0.1117$	$R_1 = 0.0455$ $wR_2 = 0.1035$	$R_1 = 0.0455$ $wR_2 = 0.1117$

Table 17. Crystallographic data for dyes Me**D3**tBu**A5**, nBu**D3**tBu**A5** and nHe**D3**tBu**A5**.

Compound	Me**D3**tBu**A5**	nBu**D3**tBu**A5**	nHe**D3**tBu**A5**
Chemical formula	$C_{23}H_{24}N_4S$	$C_{26}H_{30}N_4S$	$C_{28}H_{34}N_4S$
M / g mol^{-1}	388.52	430.60	458.65
T / K	233(2)	223(2)	302(2)
Crystal description	needle	prism	needle
Crystal color	purple	blue	violet
Crystal system	orthorhombic	monoclinic	triclinic
Space group	Pcbm	P21/m	P–1
a / Å	13.0012(5)	12.6293(5)	7.0840(5)
b / Å	24.1266(9)	7.2565(3)	17.5050(17)
c / Å	6.8589(2)	14.1271(6)	23.0478(17)
α / °	90	90	111.082(5)
β / °	90	113.2000(10)	92.440(3)
γ / °	90	90	97.604(2)
V_{UC} / Å^3	2151.46(13)	1189.98(8)	2630.7(4)
Z	4	2	4
ρ_{cal} / g cm^{-3}	1.199	1.202	1.158
μ_{abs} / mm^{-1}	1.44	1.348	1.247
F(000)	824	460	984
Measurement range of θ / °	3.40-68.20	3.81-70.26	2.74-74.48
Completeness / %	100.0	98.5	99.9
Number of independent reflections	2151	2425	10621
Parametres / restraints	166/68	199/14	648/20
Goodness of fit for F^2	1.053	1.058	1.017
$R(I > 2\sigma(I))$	$R_1 = 0.0306$ $wR_2 = 0.0868$	$R_1 = 0.0446$ $wR_2 = 0.1186$	$R_1 = 0.0492$ $wR_2 = 0.1145$
R(all data)	$R_1 = 0.0336$ $wR_2 = 0.0895$	$R_1 = 0.0484$ $wR_2 = 0.1224$	$R_1 = 0.0827$ $wR_2 = 0.1312$

Table 18. Crystallographic data for dye bPr**D3**tBu**A5**.

Compound	bPr**D3**tBu**A5**
Chemical formula	$C_{25}H_{26}N_4S$, $CHCl_3$
M / g mol^{-1}	533.92
T / K	100(2)
Crystal description	block
Crystal color	violet
Crystal system	monoclinic
Space group	P21/n
a / Å	11.4349(3)
b / Å	6.7966(2)
c / Å	33.3287(9)
α / °	90
β / °	90.8879(10)
γ / °	90
V_{UC} / Å^3	2589.94(12)
Z	4
ρ_{cal} / g cm^{-3}	1.369
μ_{abs} / mm^{-1}	4.129
F(000)	1112
Measurement range of θ / °	2.65-72.20
Completeness / %	99.5
Number of independent reflections	5081
Parametres / restraints	312/0
Goodness of fit for F^2	1.038
$R(I > 2\sigma(I))$	$R_1 = 0.0325$ $wR_2 = 0.0824$
R(all data)	$R_1 = 0.0365$ $wR_2 = 0.0862$

Table 19. Crystallographic data for dyes Pyrl**D5**tBu**A5**, Et**D5**tBu**A5** and EtBu**D5**tBu**A5**.

Compound	Pyrl**D5**tBu**A5**	Et**D5**tBu**A5**	EtBu**D5**nBu**A5**
Chemical formula	$C_{19}H_{20}N_4S_2$, 0.335 H_2O	$C_{19}H_{22}N_4S_2$	$C_{21}H_{26}N_4S_2$
M / g mol^{-1}	374.55	370.52	398.58
T / K	100(2)	100(2)	100(2)
Crystal description	needle	block	block
Crystal color	blue	blue	green
Crystal system	triclinic	monoclinic	monoclinic
Space group	P–1	P21/c	P21
a / Å	6.7620(4)	9.9527(18)	7.6747(6)
b / Å	9.8326(7)	6.9941(13)	14.4919(11)
c / Å	15.0722(10)	28.499(5)	18.8693(15)
α / °	76.998(4)	90	90
β / °	82.280(4)	93.565(5)	92.764(2)
γ / °	88.894(4)	90	90
V_{UC} / Å^3	967.52(11)	1980.0(6)	2096.2(3)
Z	2	4	4
ρ_{cal} / g cm^{-3}	1.286	1.243	1.263
μ_{abs} / mm^{-1}	2.575	2.496	2.392
F(000)	395	784	848
Measurement range of θ / °	3.04-77.37	3.11-74.74	2.34-74.76
Completeness / %	99.8	99.9	100.0
Number of independent reflections	4033	4053	8524
Parametres / restraints	261 / 0	231 / 0	497 / 1
Goodness of fit for F^2	1.056	1.065	1.104
$R(I > 2\sigma(I))$	$R_1 = 0.0334$ $wR_2 = 0.0871$	$R_1 = 0.0352$ $wR_2 = 0.0921$	$R_1 = 0.0239$ $wR_2 = 0.0612$
R(all data)	$R_1 = 0.0377$ $wR_2 = 0.0905$	$R_1 = 0.0386$ $wR_2 = 0.0940$	$R_1 = 0.0248$ $wR_2 = 0.0618$

Table 20. Crystallographic data for dyes nPr**D5**tBu**A5**, Ph**D5**tBu**A5** and nBu**D5n**Bu**A5**.

Compound	nPr**D5**tBu**A5**	Ph**D5**tBu**A5**	nBu**D5**nBu**A5**
Chemical formula	$C_{21}H_{26}N_4S_2$	$C_{27}H_{22}N_4S_2$	$C_{23}H_{30}N_4S_2$
M / g mol^{-1}	398.58	466.61	426.64
T / K	100(2)	100(2)	100(2)
Crystal description	block	blade	needle
Crystal color	green	blue	blue
Crystal system	orthorhombic	monoclinic	triclinic
Space group	Pbca	P21/c	P–1
a / Å	15.4428(5)	14.2098(8)	12.1822(5)
b / Å	14.3273(4)	10.2441(5)	13.6493(6)
c / Å	19.1045(5)	18.0188(10)	14.0809(5)
α / °	90	90	91.1920(10)
β / °	90	112.0340(10)	101.5670(10)
γ / °	90	90	98.295(2)
V_{UC} / Å^3	4226.9(2)	2431.4(2)	2266.81(16)
Z	8	4	4
ρ_{cal} / g cm^{-3}	1.253	1.275	1.250
μ_{abs} / mm^{-1}	2.373	2.151	0.252
F(000)	1696	976	912
Measurement range of θ / °	4.63-74.83	3.36-68.20	2.42-26.84
Completeness / %	100.0	99.8	99.9
Number of independent reflections	4332	4431	9685
Parametres / restraints	327 / 11	301 / 87	529 / 0
Goodness of fit for F^2	1.217	1.039	1.061
$R(I > 2\sigma(I))$	$R_1 = 0.0572$ $wR_2 = 0.1330$	$R_1 = 0.0290$ $wR_2 = 0.0766$	$R_1 = 0.0358$ $wR_2 = 0.0889$
R(all data)	$R_1 = 0.0601$ $wR_2 = 0.1344$	$R_1 = 0.0294$ $wR_2 = 0.0769$	$R_1 = 0.0476$ $wR_2 = 0.0951$

Appendix

SCFETs of Dye nBu**D3**tBu**A5**

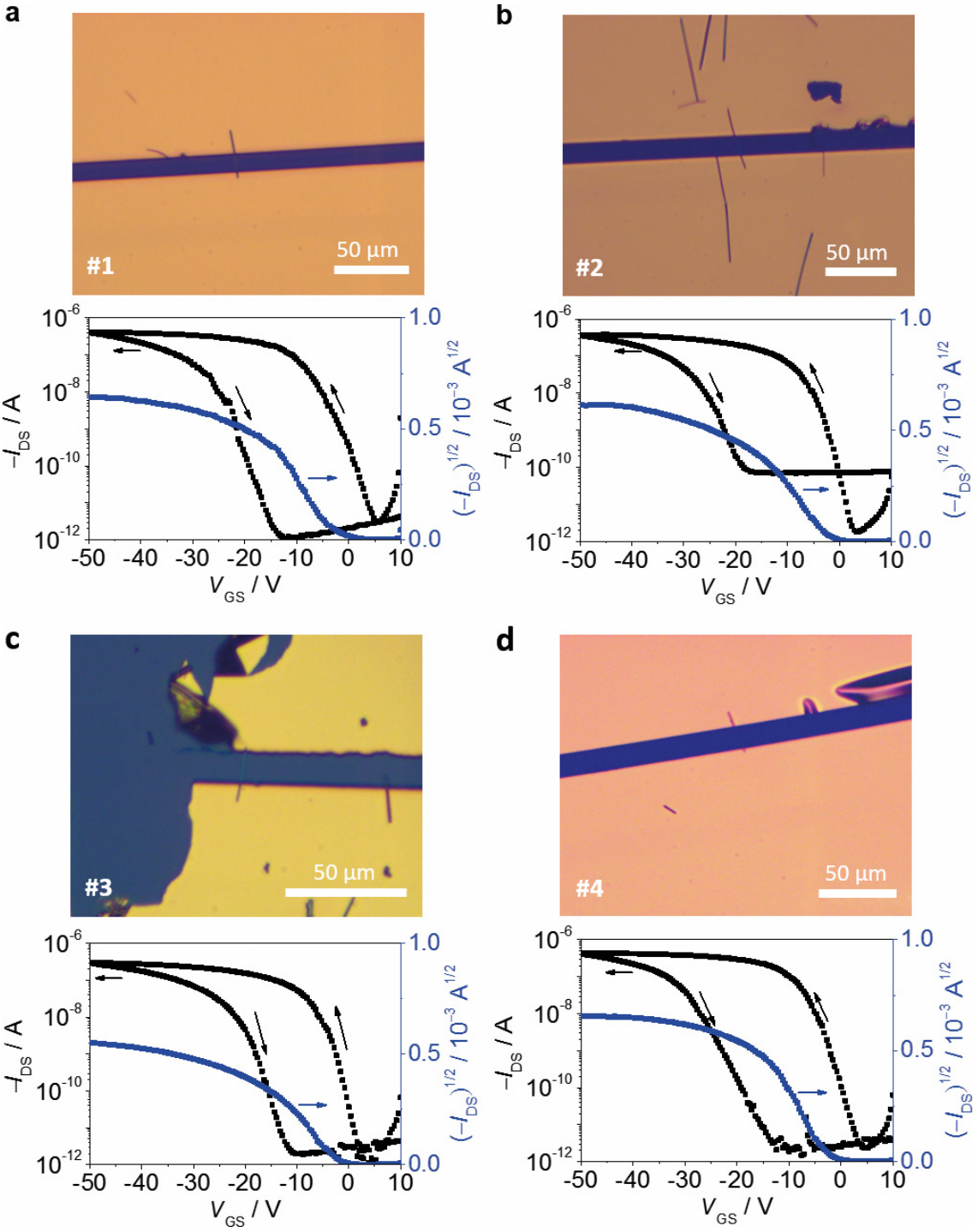

Figure 80. Optical microscopy images and corresponding transfer characteristics of SCFET devices #1 (a), #2 (b), #3 (c) and #4 (d). The devices are numbered according to Table 6.

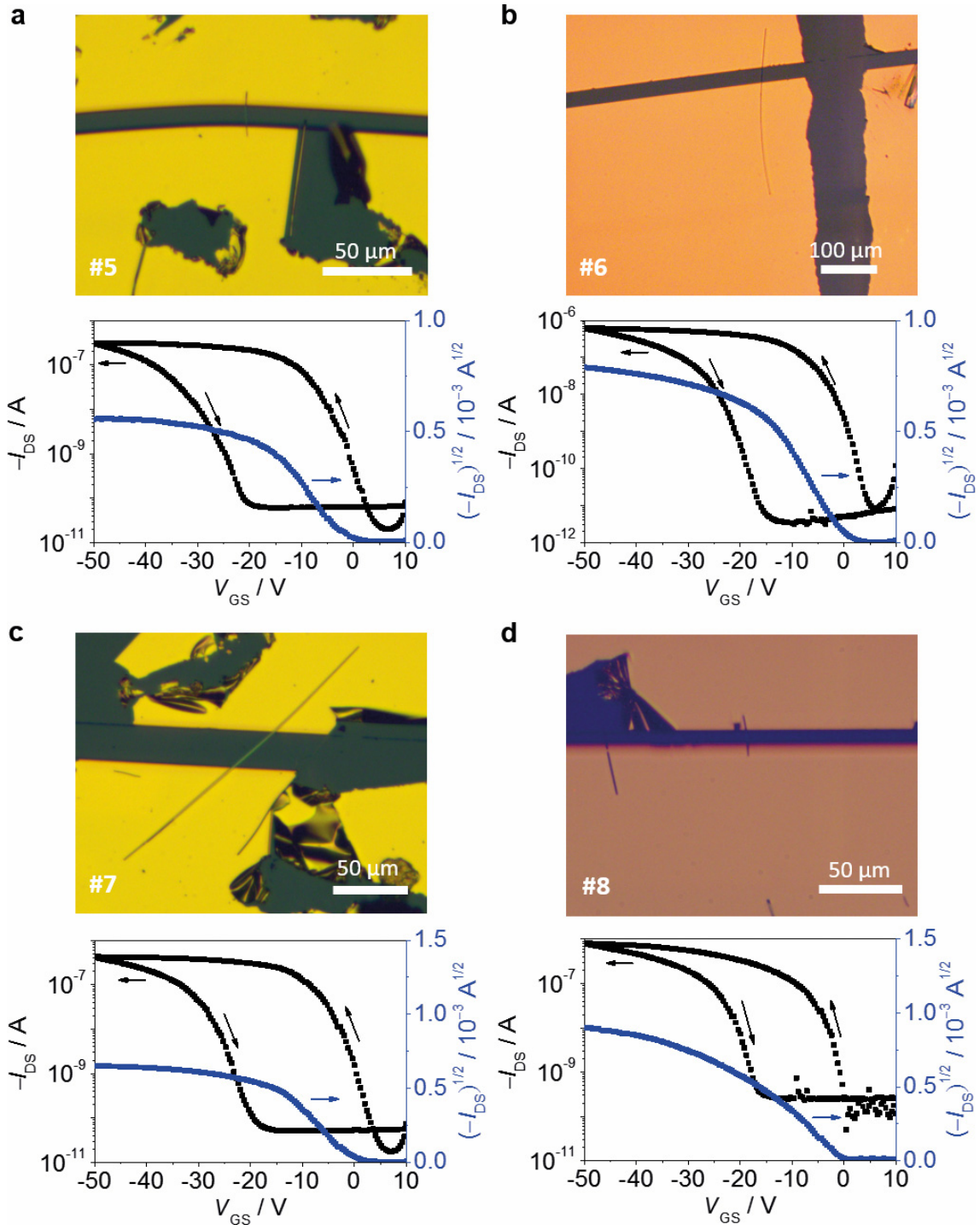

Figure 81. Optical microscopy images and corresponding transfer characteristics of SCFET devices #5 (a), #6 (b), #7 (c) and #8 (d). The devices are numbered according to Table 6.

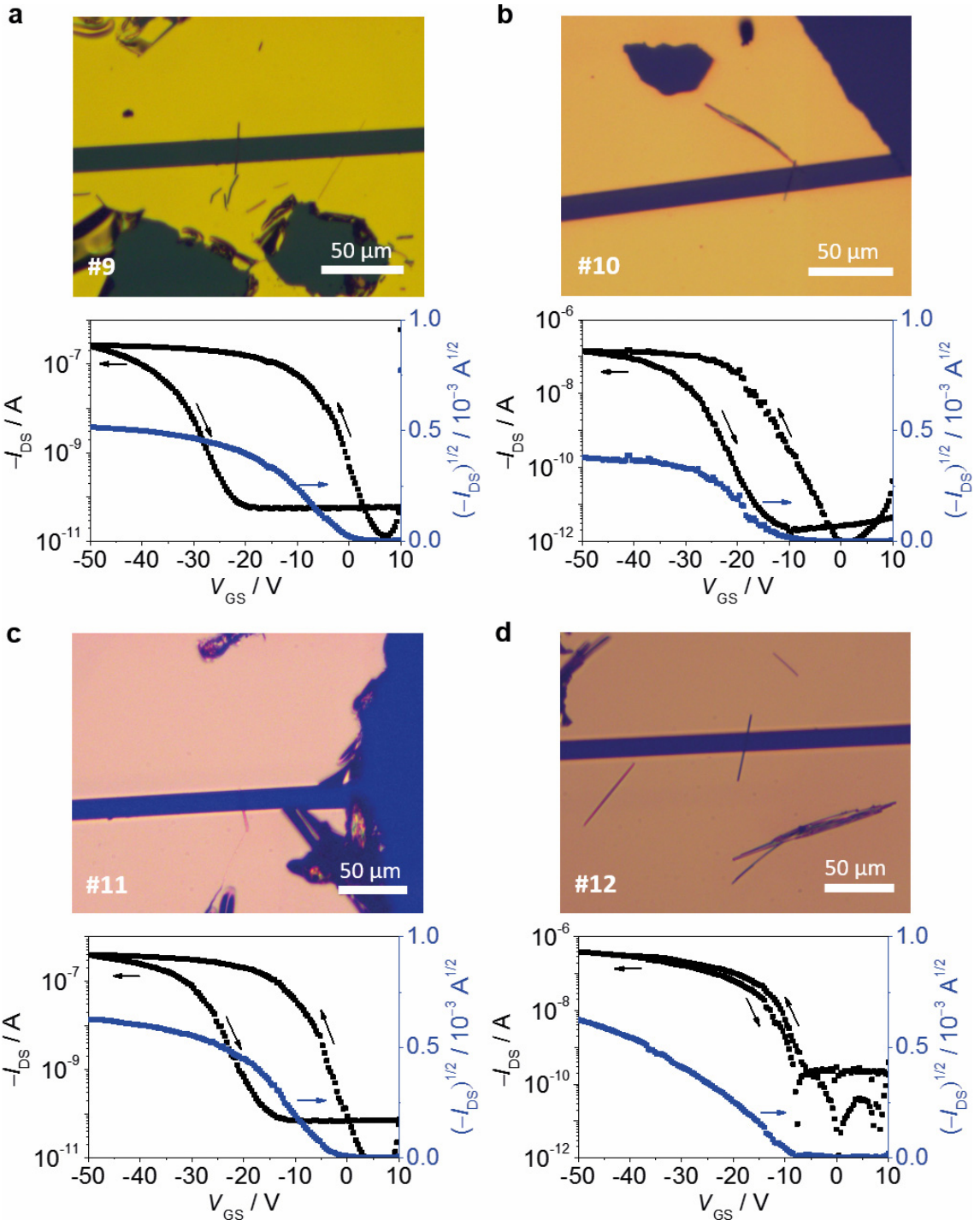

Figure 82. Optical microscopy images and corresponding transfer characteristics of SCFET devices #9 (a), #10 (b), #11 (c) and #12 (d). The devices are numbered according to Table 6.

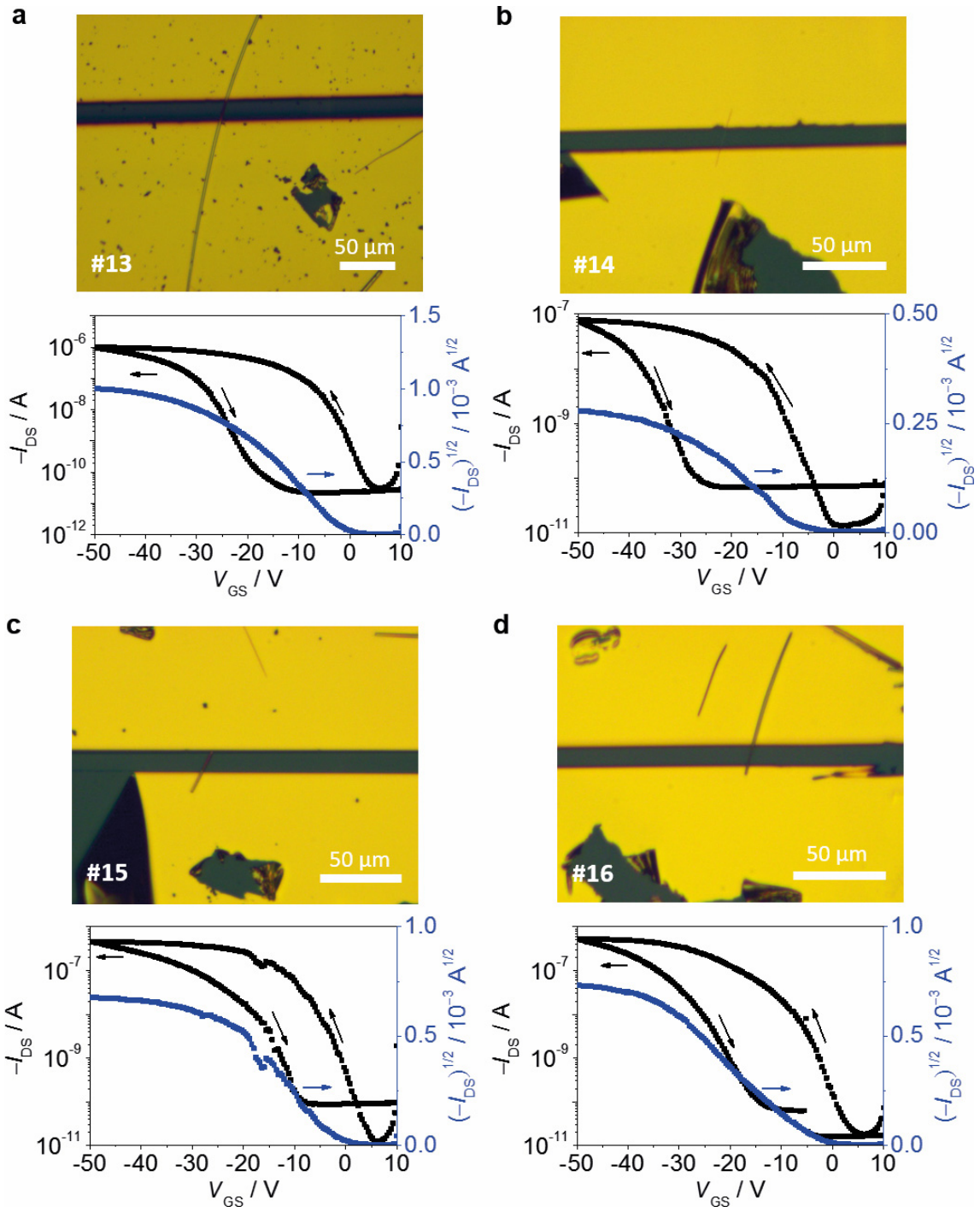

Figure 83. Optical microscopy images and corresponding transfer characteristics of SCFET devices #13 (a), #14 (b), #15 (c) and #16 (d). The devices are numbered according to Table 6.

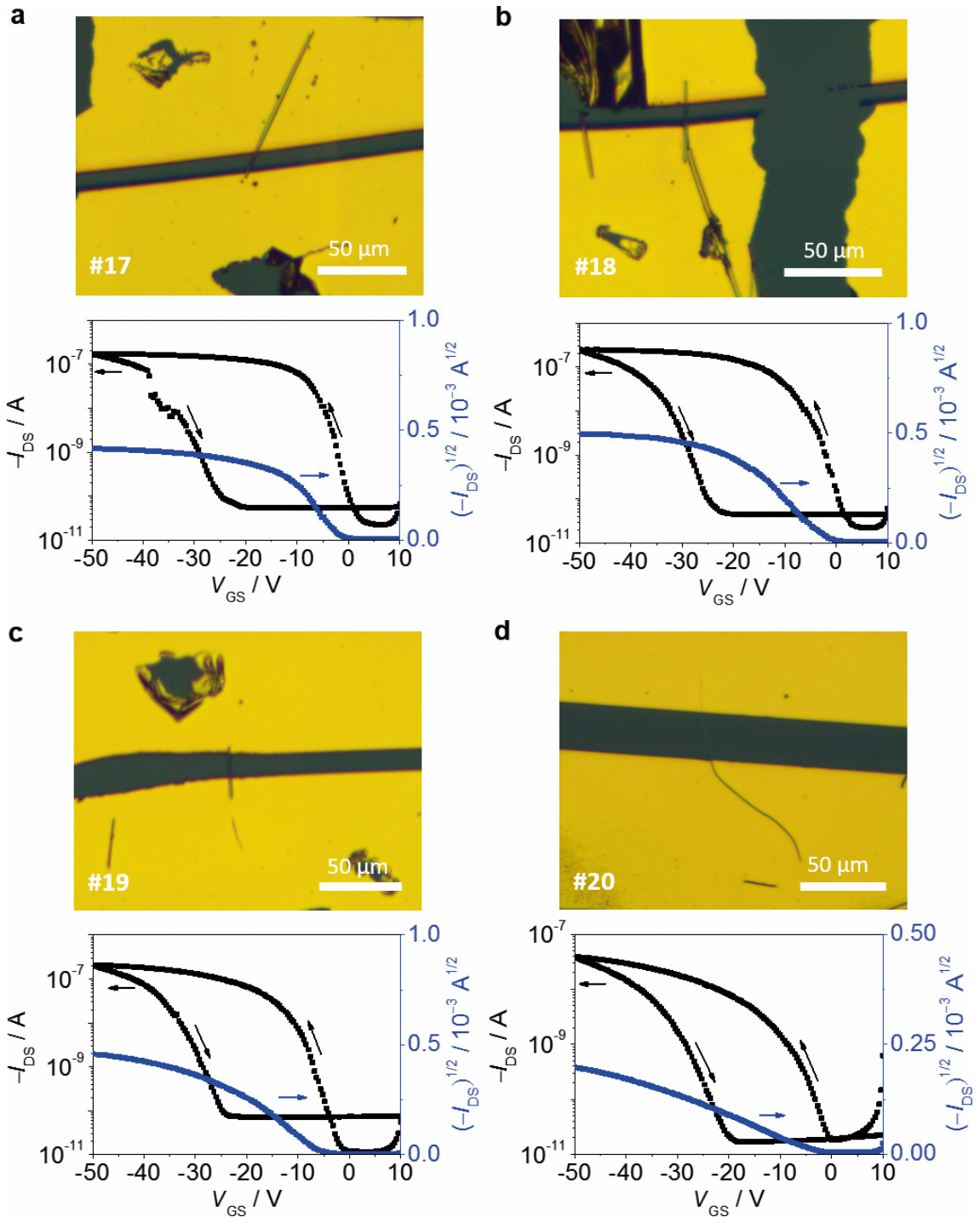

Figure 84. Optical microscopy images and corresponding transfer characteristics of SCFET devices #17 (a), #18 (b), #19 (c) and #20 (d). The devices are numbered according to Table 6.

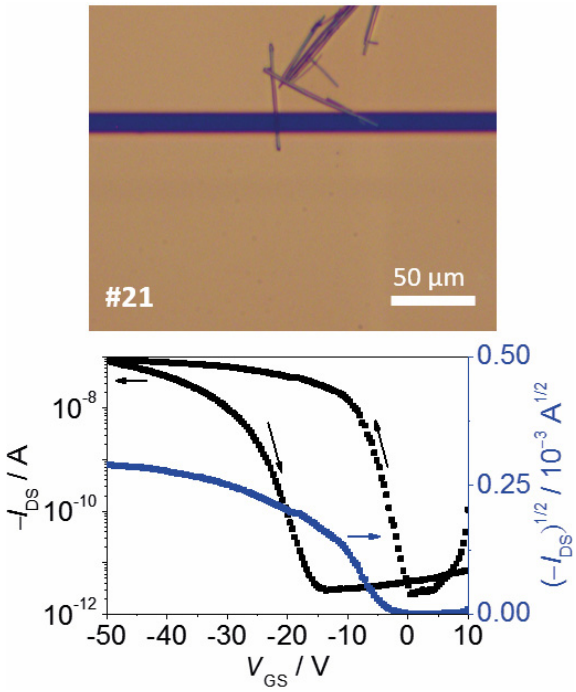

Figure 85. Optical microscopy image and corresponding transfer characteristic of SCFET device #21. The device is numbered according to Table 6.

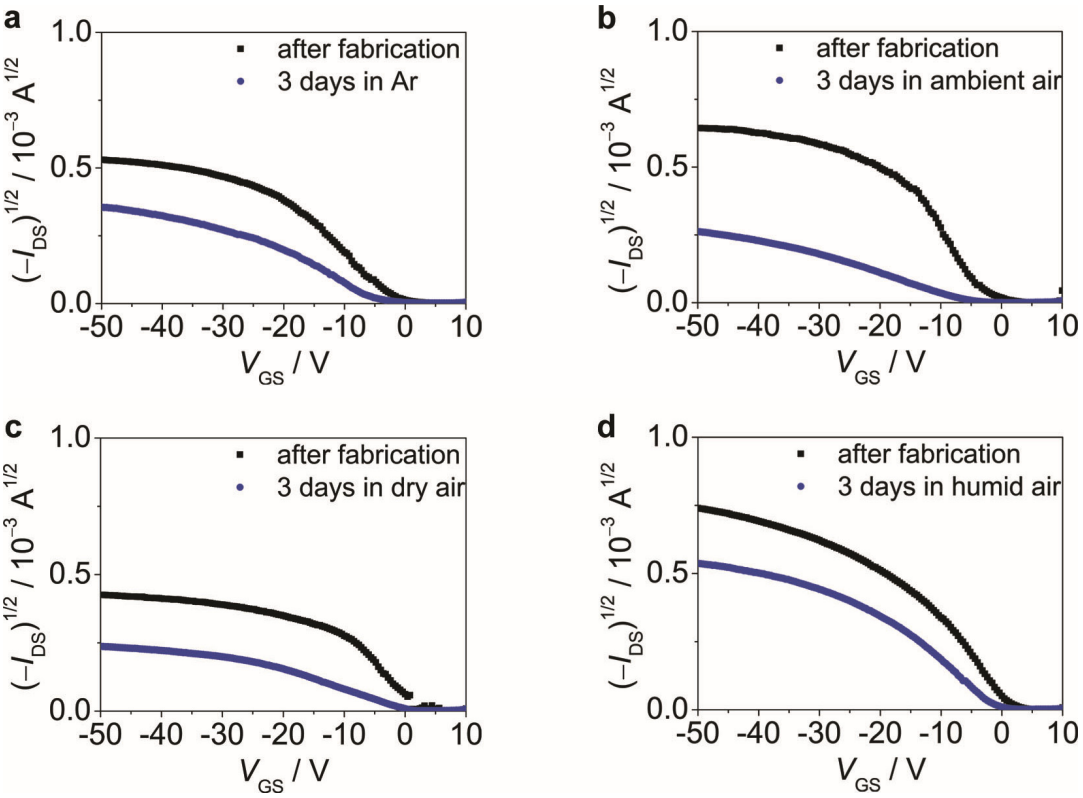

Figure 86. Square root of the drain current of different devices after fabrication and storage for 3 d in argon (a), ambient air (b), dry air (c) as well as air with 100 % relative humidity (d).

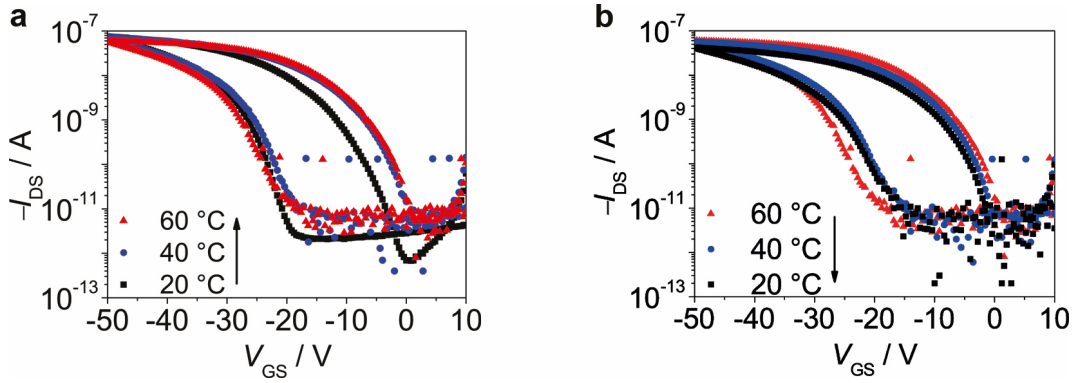

Figure 87. Transfer characteristics of device #3 measured at different device temperatures upon heating (a) and cooling (b) of the device.

Calculation of Exciton Coupling

Table 21. Coordinates of molecular centers and endpoints of transition dipole moments for dye Pyrl**D5**tBu**A5** and nPr**D5**tBu**A5**.[a)]

Dye	Axis	Molecular center	Transition dipole moment endpoints	
Pyrl**D5**tBu**A5**	*a*	0.757	0.816	0.706
	b	0.114	0.351	−0.149
	c	0.477	0.269	0.659
nPr**D5**tBu**A5**	*a*	0.624	0.623	0.624
	b	0.434	0.385	0.520
	c	0.316	0.146	0.483

[a)] Coordinates given for central molecules for which the exciton coupling with all next neighbors was calculated in the case of dyes Pyrl**D5**tBu**A5** and nPr**D5**tBu**A5**. The coordinates are given in the respective crystallographic coordinate system of the single crystal structures as fraction of the crystallographic axes.

Table 22. Absorption maxima of optical transitions of monomers of dyes Pyrl**D5**tBu**A5**, nBu**D5**nBu**A5** and nPr**D5**tBu**A5** as resulting from experiments in solution ($CHCl_3$, 10^{-5}, 298 K, see Table 8) as well as from TD-DFT calculations (ωB97/def2-SVP).

Dye	λ_{exp} / nm	$\tilde{\nu}_{exp}$ / cm^{-1}	$\lambda_{TD\text{-}DFT}$ / nm	$\tilde{\nu}_{TD\text{-}DFT}$ / cm^{-1}
Pyrl**D5**tBu**A5**	651	15361	484	20645
nBu**D5**nBu**A5**	648	15432	482	20762
nPr**D5**tBu**A5**	651	15361	482	20749

Table 23. Optical transitions resulting from TD-DFT calculations (ωB97/def2-SVP) of a dimer of nBu**D5**nBu**A5**.[a)]

Segment	Value	Transition	
		1	2
Dimer (2)	$\tilde{\nu}^{b)}$ / cm^{-1}	13314	**16192**
	λ / nm	751	**618**
	f / 1	0	**1**

[a)] In bold, the most prominent transition is marked; [b)] Given wavenumbers were shifted by 5400 cm^{-1} towards lower energies.

Table 24. Optical transitions resulting from TD-DFT calculations (ωB97/def2-SVP) of a dimer, a stack of four as well as a stack of eight molecules of Pyrl**D5**tBu**A5**.[a)]

Segment	Value	Transition							
		1	2	3	4	5	6	7	8
Dimer (2)	$\tilde{\nu}$[b)] / cm^{-1}	12521	**16958**	-	-	-	-	-	-
	λ / nm	799	**590**	-	-	-	-	-	-
	f / 1	0	**1**	-	-	-	-	-	-
Stack (4)	$\tilde{\nu}$[b)] / cm^{-1}	12022	12918	15158	**18368**	-	-	-	-
	λ / nm	832	774	660	**544**	-	-	-	-
	f / 1	0	0.035	0	**1**	-	-	-	-
Stack (8)	$\tilde{\nu}$[b)] / cm^{-1}	11808	12063	12501	13172	14261	15790	17567	**19183**
	λ / nm	847	829	800	759	701	633	569	**521**
	f / 1	0	0.004	0	0.013	0	0.055	0	**1**

[a)] In bold, the most prominent transition is marked; [b)] Given wavenumbers were shifted by 5400 cm^{-1} towards lower energies.

Table 25. Optical transitions resulting from TD-DFT calculations (ωB97/def2-SVP) of a dimer, a strand of four as well as a strand of eight molecules of nPr**D5**tBu**A5**.[a)]

Segment	Value	Transition							
		1	2	3	4	5	6	7	8
Dimer (2)	$\tilde{\nu}$[b)] / cm^{-1}	**14452**	**15804**	-	-	-	-	-	-
	λ / nm	**692**	**632**	-	-	-	-	-	-
	f / 1	**1**	**0.110**	-	-	-	-	-	-
Strand (4)	$\tilde{\nu}$[b)] / cm^{-1}	**13680**	14838	15600	**15980**	-	-	-	-
	λ / nm	**731**	674	641	**626**	-	-	-	-
	f / 1	**1**	0.004	0.038	**0.093**	-	-	-	-
Strand (8)	$\tilde{\nu}$[b)] / cm^{-1}	**13244**	13885	14524	15061	15469	15760	15955	**16080**
	λ / nm	**755**	720	689	664	646	635	627	**622**
	f / 1	**1**	0.001	0.060	0.002	0.015	0.009	0.004	**0.101**

[a)] In bold, the most prominent transitions are marked; [b)] Given wavenumbers were shifted by 5400 cm^{-1} towards lower energies.

Table 26. Exciton coupling energies calculated for molecular pairs of next neighbors of Pyrl**D5**tBu**A5** and nPr**D5**tBu**A5** around a central molecule (see Figure 88 below).[a)]

Next neighbor #	Pyrl**D5**tBu**A5**		nPr**D5**tBu**A5**	
	J_{PDA} / cm^{-1}	J_{TC} / cm^{-1}	J_{PDA} / cm^{-1}	J_{TC} / cm^{-1}
1	−68	−70	+122	+108
2	−237	−329	−446	−201
3	+74	+204	−104	−240
4	−68	−70	+81	+108
5	−237	−329	−104	−240
6	+74	+204	−446	−201
7	+3605	+1859	+708	+585
8	+3891	+1863	−594	−580
9	-	-	+708	+587
10	-	-	−594	−580
11	-	-	+593	+565
12	-	-	−277	−441
13	-	-	+593	+565
14	-	-	−1148	−151

[a)] Exciton couplings energies *J* were calculated within the point dipole approximation (PDA) and the transition charge method (TC). The sign (+/−) denotes if the most prominent transition is of H- (+) or J-type (−) nature.

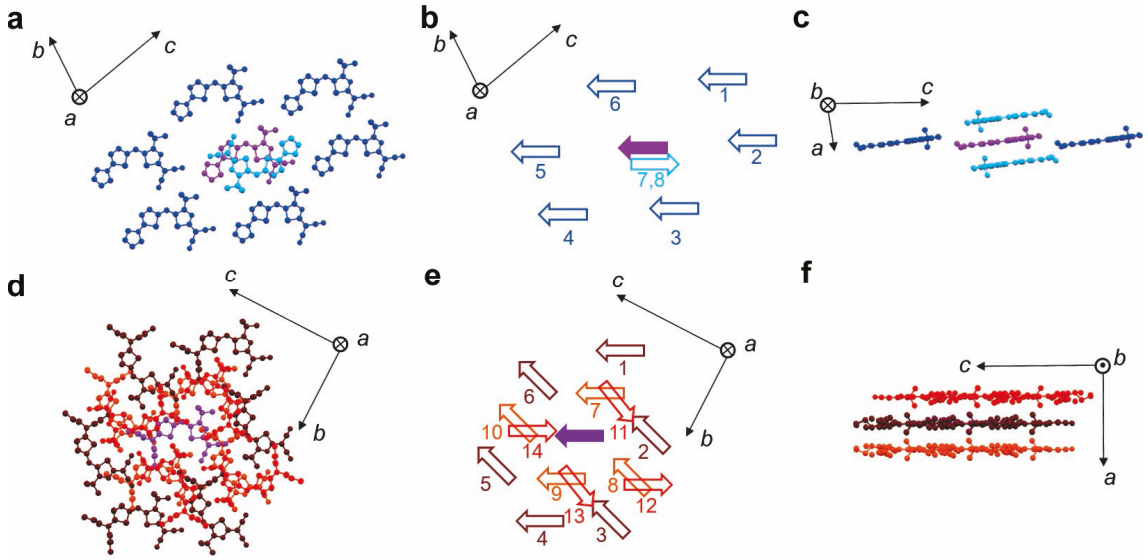

Figure 88. Next neighbors around a central molecule (purple) in the crystal structure of Pyrl**D5**tBu**A5** (a-c) and nPr**D5**tBu**A5** (d-f) with top (a,d) and side view (c,f) as well as schematic top view (b,e).

References

[1] Broadband commission for sustainable development (ITU, UNESCO), *The State of Broadband: Broadband catalyzing sustainable development*, **2016**.

[2] a) T. Heeg, So cool ist Virtual Reality schon jetzt, http://www.faz.net/aktuell/wirtschaft/netzwirtschaft/vr-brillen-virtual-reality-soll-das-naechste-grosse-ding-werden-14414639.html, accessed: 02/11/2016, **2016**; b) A. Steiner, Diese Technologien ändern unseren Alltag, http://www.faz.net/aktuell/wirtschaft/smarte-arbeit/smart-home-technologien-veraendern-alltag-der-zukunft-13944271.html, accessed: 02/11/2016, **2015**.

[3] a) S. C. Mukhopadhyay, N. K. Suryadevara, in *Internet of Things: Challenges and Opportunities* (Ed.: S. C. Mukhopadhyay), Springer International Publishing, Switzerland, **2014**, pp. 1-18; b) H. Schweitzer, Der Laster wird zum Hightechgerät, http://www.zeit.de/mobilitaet/2016-09/autonomes-fahren-logistik-lkw-iaa-speditionen, accessed: 02/11/2016, **2016**.

[4] Results based on IHS Markit, Technology Group, *IoT platforms: Enabling the Internet of Things Whitepaper*, **2016**. Legal Disclaimer: Results are not an endorsement. Any reliance on these results is at the third party's own risk. Visit technology.ihs.com for more details.

[5] F. Li, A. Nathan, Y. Wu, B. S. Ong, *Organic Thin Film Transistor Integration: A Hybrid Approach*, Wiley-VCH Verlag GmbH & Co. KGaA, Weinheim, Germany, **2011**.

[6] a) H. Sirringhaus, *Adv. Mater.* **2014**, *26*, 1319-1335; b) J. Mei, Y. Diao, A. L. Appleton, L. Fang, Z. Bao, *J. Am. Chem. Soc.* **2013**, *135*, 6724-6746.

[7] A. Armin, R. D. Jansen-van Vuuren, N. Kopidakis, P. L. Burn, P. Meredith, *Nat. Commun.* **2015**, *6*, 6343.

[8] C. Liu, K. Wang, X. Gong, A. J. Heeger, *Chem. Soc. Rev.* **2016**, *45*, 4825-4846.

[9] F. Würthner, R. Wortmann, R. Matschiner, K. Lukaszuk, K. Meerholz, Y. DeNardin, R. Bittner, C. Bräuchle, R. Sens, *Angew. Chem.* **1997**, *109*, 2933-2936.

[10] a) K. Kudo, T. Moriizumi, *Jpn. J. Appl. Phys.* **1981**, *20*, L553; b) K. Kudo, M. Yamashina, T. Moriizumi, *Jpn. J. Appl. Phys.* **1984**, *23*, 130; c) D. L. Morel, A. K. Ghosh, T. Feng, E. L. Stogryn, P. E. Purwin, R. F. Shaw, C. Fishman, *Appl. Phys. Lett.* **1978**, *32*, 495-497.

[11] a) J. E. Anthony, *Angew. Chem. Int. Ed.* **2008**, *47*, 452-483; b) Y. Yuan, G. Giri, A. L. Ayzner, A. P. Zoombelt, S. C. B. Mannsfeld, J. Chen, D. Nordlund, M. F. Toney, J. Huang, Z. Bao, *Nat. Commun.* **2014**, *5*, 3005.

[12] a) H. Bässler, *Phys. Status Solidi B* **1993**, *175*, 15-56; b) D. Hertel, H. Bässler, *ChemPhysChem* **2008**, *9*, 666-688.

[13] N. M. Kronenberg, M. Deppisch, F. Würthner, H. W. A. Lademann, K. Deing, K. Meerholz, *Chem. Commun.* **2008**, 6489-6491.

[14] L. Huang, M. Stolte, H. Bürckstümmer, F. Würthner, *Adv. Mater.* **2012**, *24*, 5750-5754.

[15] F. Würthner, K. Meerholz, *Chem. Eur. J.* **2010**, *16*, 9366-9373.

[16] D. Braga, G. Horowitz, *Adv. Mater.* **2009**, *21*, 1473-1486.

[17] P. V. Pesavento, R. J. Chesterfield, C. R. Newman, C. D. Frisbie, *J. Appl. Phys.* **2004**, *96*, 7312-7324.

[18] Z. Bao, J. Locklin, *Organic Field-Effect Transistors*, CRC Press, Boca Raton, U. S. A., **2007**.

[19] a) G. Baccarani, P. Ostoja, *Solid-State Electron.* **1975**, *18*, 579-580; b) D. C. Cronemeyer, *Phys. Rev.* **1957**, *105*, 522-523.

[20] a) O. D. Jurchescu, J. Baas, T. T. M. Palstra, *Appl. Phys. Lett.* **2004**, *84*, 3061-3063; b) W. Warta, R. Stehle, N. Karl, *Appl. Phys. A* **1985**, *36*, 163-170.

[21] a) C. D. Dimitrakopoulos, P. R. L. Malenfant, *Adv. Mater.* **2002**, *14*, 99-117; b) G. Horowitz, *Adv. Mater.* **1998**, *10*, 365-377.

[22] S. Stafström, *Chem. Soc. Rev.* **2010**, *39*, 2484-2499.

[23] A. Miller, E. Abrahams, *Phys. Rev.* **1960**, *120*, 745-755.

[24] M. Sugiuchi, H. Nishizawa, *J. Imaging Sci. Technol.* **1993**, *37*, 245-250.

[25] A. Dieckmann, H. Bässler, P. M. Borsenberger, *J. Chem. Phys.* **1993**, *99*, 8136-8141.

[26] a) M. Kasha, *Radiat. Res.* **1963**, *20*, 55-70; b) M. Kasha, H. R. Rawls, M. Ashraf El-Bayoumi, *Pure Appl. Chem.* **1965**, *11*, 371-392.

[27] A. S. Davydov, *Phys.-Usp.* **1964**, *7*, 145-178.

[28] E. G. McRae, M. Kasha, in *Physical Processes in Radiation Biology* (Eds.: L. Augenstein, R. Mason, B. Rosenberg), Academic Press, New York, U. S. A., **1964**, pp. 23-42.

[29] C. E. Mortimer, U. Müller, *Chemie: das Basiswissen der Chemie*, 8 ed., Georg Thieme Verlag, Stuttgart, Germany, **2007**.

[30] a) S. R. Marder, C. B. Gorman, F. Meyers, J. W. Perry, G. Bourhill, J.-L. Brédas, B. M. Pierce, *Science* **1994**, *265*, 632-635; b) J. J. Wolff, R. Wortmann, in *Advances in Physical Organic Chemistry, Vol. 32* (Ed.: D. Bethell), Academic Press, London, UK, **1999**, pp. 121-218.

[31] F. Würthner, G. Archetti, R. Schmidt, H.-G. Kuball, *Angew. Chem. Int. Ed.* **2008**, *47*, 4529-4532.

[32] P. W. Atkins, J. de Paula, *Physikalische Chemie*, 4 ed., Wiley-VCH Verlag GmbH & Co. KGaA, Weinheim, Germany, **2007**.

[33] L. R. Dalton, A. W. Harper, B. H. Robinson, *Proc. Natl. Acad. Sci. U. S. A.* **1997**, *94*, 4842-4847.

[34] a) F. Würthner, S. Yao, *Angew. Chem. Int. Ed.* **2000**, *39*, 1978-1981; b) F. Würthner, S. Yao, T. Debaerdemaeker, R. Wortmann, *J. Am. Chem. Soc.* **2002**, *124*, 9431-9447.

[35] A. Lohr, T. Gress, M. Deppisch, M. Knoll, F. Würthner, *Synthesis* **2007**, 3073-3082.

[36] F. Würthner, T. E. Kaiser, C. R. Saha-Möller, *Angew. Chem. Int. Ed.* **2011**, *50*, 3376-3410.

[37] F. Würthner, *Acc. Chem. Res.* **2016**, *49*, 868-876.

[38] S. Yao, U. Beginn, T. Gress, M. Lysetska, F. Würthner, *J. Am. Chem. Soc.* **2004**, *126*, 8336-8348.

[39] a) A. Lohr, M. Grüne, F. Würthner, *Chem. Eur. J.* **2009**, *15*, 3691-3705; b) A. Lohr, S. Uemura, F. Würthner, *Angew. Chem. Int. Ed.* **2009**, *48*, 6165-6168.

[40] D. Bialas, A. Zitzler-Kunkel, E. Kirchner, D. Schmidt, F. Würthner, *Nat. Commun.* **2016**, *7*, 12949.

[41] A. Zitzler-Kunkel, E. Kirchner, D. Bialas, C. Simon, F. Würthner, *Chem. Eur. J.* **2015**, *21*, 14851-14861.

[42] a) K. Ikegami, C. Mingotaud, M. Lan, *J. Chem. Phys. B* **1999**, *103*, 11261-11268; b) K. Iriyama, F. Mizutani, M. Yoshiura, *Chem. Lett.* **1980**, *9*, 1399-1402; c) S.-i. Kuroda, *Adv. Colloid Interface Sci.* **2004**, *111*, 181-209.

[43] H. Kuhn, C. Kuhn, in *J-Aggregates* (Ed.: T. Kobayashi), World Scientific, Singapore, **1996**, pp. 1-40.

[44] Y. Ueda, K. Nitta, *Jpn. J. Appl. Phys.* **2001**, *40*, 6951-6955.

[45] S. Yagai, M. Higashi, T. Karatsu, A. Kitamura, *Chem. Commun.* **2006**, 1500-1502.

[46] S. Yagai, K. Iwai, T. Karatsu, A. Kitamura, *Angew. Chem. Int. Ed.* **2012**, *51*, 9679-9683.

[47] P. A. Franken, A. E. Hill, C. W. Peters, G. Weinreich, *Phys. Rev. Lett.* **1961**, *7*, 118-119.

[48] J. L. Oudar, D. S. Chemla, *J. Chem. Phys.* **1977**, *66*, 2664-2668.

[49] a) C. B. Gorman, S. R. Marder, *Proc. Natl. Acad. Sci. U. S. A.* **1993**, *90*, 11297-11301; b) S. R. Marder, D. N. Beratan, L.-T. Cheng, *Science* **1991**, *252*, 103-106; c) S. R. Marder, L.-T. Cheng, B. G. Tiemann, A. C. Friedli, M. Blanchard-Desce, J. W. Perry, J. Skindhøj, *Science* **1994**, *263*, 511-514.

[50] a) T.-D. Kim, J.-W. Kang, J. Luo, S.-H. Jang, J.-W. Ka, N. Tucker, J. B. Benedict, L. R. Dalton, T. Gray, R. M. Overney, D. H. Park, W. N. Herman, A. K.-Y. Jen, *J. Am. Chem. Soc.* **2007**, *129*, 488-489; b) L. R. Dalton, P. A. Sullivan, D. H. Bale, *Chem. Rev.* **2009**, *110*, 25-55.

[51] I. D. L. Albert, T. J. Marks, M. A. Ratner, *J. Am. Chem. Soc.* **1998**, *120*, 11174-11181.

[52] V. Parthasarathy, R. Pandey, M. Stolte, S. Ghosh, F. Castet, F. Würthner, P. K. Das, M. Blanchard-Desce, *Chem. Eur. J.* **2015**, *21*, 14211-14217.

[53] A. Maser, B. Gmeiner, T. Utikal, S. Götzinger, V. Sandoghdar, *Nat. Photon.* **2016**, *10*, 450-453.

[54] a) W. E. Moerner, S. M. Silence, F. Hache, G. C. Bjorklund, *J. Opt. Soc. Am. B* **1994**, *11*, 320-330; b) K. Meerholz, B. L. Volodin, Sandalphon, B. Kippelen, N. Peyghambarian, *Nature* **1994**, *371*, 497-500.

[55] S. Beckmann, K.-H. Etzbach, P. Krämer, K. Lukaszuk, R. Matschiner, A. J. Schmidt, P. Schuhmacher, R. Sens, G. Seybold, R. Wortmann, F. Würthner, *Adv. Mater.* **1999**, *11*, 536-541.

[56] a) F. Würthner, R. Sens, K.-H. Etzbach, G. Seybold, *Angew. Chem. Int. Ed.* **1999**, *38*, 1649-1652; b) F. Würthner, S. Yao, J. Schilling, R. Wortmann, M. Redi-Abshiro, E. Mecher, F. Gallego-Gomez, K. Meerholz, *J. Am. Chem. Soc.* **2001**, *123*, 2810-2824.

[57] G. Archetti, A. Abbotto, R. Wortmann, *Chem. Eur. J.* **2006**, *12*, 7151-7160.

[58] A. Jäger-Waldau, in *Encyclopedia of Inorganic and Bioinorganic Chemistry*, John Wiley & Sons, Ltd., **2015**, pp. 1-10.

[59] C. W. Tang, *Appl. Phys. Lett.* **1986**, *48*, 183-185.

[60] G. Yu, J. Gao, J. C. Hummelen, F. Wudl, A. J. Heeger, *Science* **1995**, *270*, 1789-1791.

[61] H. Bürckstümmer, E. V. Tulyakova, M. Deppisch, M. R. Lenze, N. M. Kronenberg, M. Gsänger, M. Stolte, K. Meerholz, F. Würthner, *Angew. Chem. Int. Ed.* **2011**, *50*, 11628-11632.

[62] V. Steinmann, N. M. Kronenberg, M. R. Lenze, S. M. Graf, D. Hertel, K. Meerholz, H. Bürckstümmer, E. V. Tulyakova, F. Würthner, *Adv. Energy Mater.* **2011**, *1*, 888-893.

[63] N. M. Kronenberg, V. Steinmann, H. Bürckstümmer, J. Hwang, D. Hertel, F. Würthner, K. Meerholz, *Adv. Mater.* **2010**, *22*, 4193-4197.

[64] A. Arjona-Esteban, J. Krumrain, A. Liess, M. Stolte, L. Huang, D. Schmidt, V. Stepanenko, M. Gsänger, D. Hertel, K. Meerholz, F. Würthner, *J. Am. Chem. Soc.* **2015**, *137*, 13524-13534.

[65] a) Y. Chen, Y. Zhu, D. Yang, Q. Luo, L. Yang, Y. Huang, S. Zhao, Z. Lu, *Chem. Commun.* **2015**, *51*, 6133-6136; b) S. Paek, H. Choi, H. Jo, K. Lee, K. Song, S. A. Siddiqui, G. D. Sharma, J. Ko, *J. Mater. Chem. C* **2015**, *3*, 7029-7037; c) J. Roncali, *Acc. Chem. Res.* **2009**, *42*, 1719-1730.

[66] U. Mayerhöffer, K. Deing, K. Gruß, H. Braunschweig, K. Meerholz, F. Würthner, *Angew. Chem. Int. Ed.* **2009**, *48*, 8776-8779.

[67] Y.-H. Chen, L.-Y. Lin, C.-W. Lu, F. Lin, Z.-Y. Huang, H.-W. Lin, P.-H. Wang, Y.-H. Liu, K.-T. Wong, J. Wen, D. J. Miller, S. B. Darling, *J. Am. Chem. Soc.* **2012**, *134*, 13616-13623.

[68] S.-W. Chiu, L.-Y. Lin, H.-W. Lin, Y.-H. Chen, Z.-Y. Huang, Y.-T. Lin, F. Lin, Y.-H. Liu, K.-T. Wong, *Chem. Commun.* **2012**, *48*, 1857-1859.

[69] O. L. Griffith, X. Liu, J. A. Amonoo, P. I. Djurovich, M. E. Thompson, P. F. Green, S. R. Forrest, *Phys. Rev. B* **2015**, *92*, 085404.

[70] Q. Miao, M. Lefenfeld, T.-Q. Nguyen, T. Siegrist, C. Kloc, C. Nuckolls, *Adv. Mater.* **2005**, *17*, 407-412.

[71] A. Lv, M. Stolte, F. Würthner, *Angew. Chem. Int. Ed.* **2015**, *54*, 10512-10515.

[72] M. Gsänger, E. Kirchner, M. Stolte, C. Burschka, V. Stepanenko, J. Pflaum, F. Würthner, *J. Am. Chem. Soc.* **2014**, *136*, 2351-2362.

[73] S. Krause, M. Stolte, F. Würthner, N. Koch, *J. Phys. Chem. C* **2013**, *117*, 19031-19037.

[74] H. Bürckstümmer, N. M. Kronenberg, M. Gsänger, M. Stolte, K. Meerholz, F. Würthner, *J. Mater. Chem.* **2010**, *20*, 240-243.

[75] F. Würthner, S. Yao, R. Wortmann, *Polym. Mater. Sci. Eng.* **2000**, *83*, 186-187.

[76] A. Ojala, H. Bürckstümmer, M. Stolte, R. Sens, H. Reichelt, P. Erk, J. Hwang, D. Hertel, K. Meerholz, F. Würthner, *Adv. Mater.* **2011**, *23*, 5398-5403.

[77] A. Ojala, H. Bürckstümmer, J. Hwang, K. Graf, B. von Vacano, K. Meerholz, P. Erk, F. Würthner, *J. Mater. Chem.* **2012**, *22*, 4473-4482.

[78] L. Onsager, *J. Am. Chem. Soc.* **1936**, *58*, 1486-1493.

[79] a) C. M. Cardona, W. Li, A. E. Kaifer, D. Stockdale, G. C. Bazan, *Adv. Mater.* **2011**, *23*, 2367-2371; b) N. G. Connelly, W. E. Geiger, *Chem. Rev.* **1996**, *96*, 877-910; c) W. N. Hansen, G. J. Hansen, *Phys. Rev. A* **1987**, *36*, 1396-1402.

[80] R. P. Shibaeva, E. B. Yagubskii, *Chem. Rev.* **2004**, *104*, 5347-5378.

[81] a) F. Würthner, R. Wortmann, R. Matschiner, K. Lukaszuk, K. Meerholz, Y. DeNardin, R. Bittner, C. Bräuchle, R. Sens, *Angew. Chem. Int. Ed. Engl.* **1997**, *36*, 2765-2768; b) F. Würthner, R. Wortmann, K. Meerholz, *ChemPhysChem* **2002**, *3*, 17-31.

[82] a) L. Beverina, G. A. Pagani, *Acc. Chem. Res.* **2014**, *47*, 319-329; b) S. R. Marder, B. Kippelen, A. K.-Y. Jen, N. Peyghambarian, *Nature* **1997**, *388*, 845-851; c) A. Mishra, R. K. Behera, P. K. Behera, B. K. Mishra, G. B. Behera, *Chem. Rev.* **2000**, *100*, 1973-2011.

[83] G. R. Desiraju, *Angew. Chem. Int. Ed. Engl.* **1995**, *34*, 2311-2327.

[84] C. F. Macrae, P. R. Edgington, P. McCabe, E. Pidcock, G. P. Shields, R. Taylor, M. Towler, J. van de Streek, *J. Appl. Crystallogr.* **2006**, *39*, 453-457.

[85] S. Yogev, R. Matsubara, M. Nakamura, U. Zschieschang, H. Klauk, Y. Rosenwaks, *Phys. Rev. Lett.* **2013**, *110*, 036803.

[86] A. Amassian, V. A. Pozdin, T. V. Desai, S. Hong, A. R. Woll, J. D. Ferguson, J. D. Brock, G. G. Malliaras, J. R. Engstrom, *J. Mater. Chem.* **2009**, *19*, 5580-5592.

[87] T. He, X. Zhang, J. Jia, Y. Li, X. Tao, *Adv. Mater.* **2012**, *24*, 2171-2175.

[88] Q. Tang, H. Li, M. He, W. Hu, C. Liu, K. Chen, C. Wang, Y. Liu, D. Zhu, *Adv. Mater.* **2006**, *18*, 65-68.

[89] L. Jiang, W. Hu, Z. Wei, W. Xu, H. Meng, *Adv. Mater.* **2009**, *21*, 3649-3653.

[90] M. Egginger, S. Bauer, R. Schwödiauer, H. Neugebauer, N. S. Sariciftci, *Monatsh. Chem.* **2009**, *140*, 735-750.

[91] a) G. Paasch, S. Scheinert, A. Herasimovich, I. Hörselmann, T. Lindner, *Phys. Status Solidi A* **2008**, *205*, 534-548; b) M. Qu, H. Li, R. Liu, S.-L. Zhang, Z.-J. Qiu, *Nat. Commun.* **2014**, *5*, 3185; c) A. Salleo, R. A. Street, *Phys. Rev. B* **2004**, *70*, 235324; d) R. A. Street, A. Salleo, M. L. Chabinyc, *Phys. Rev. B* **2003**, *68*, 085316.

[92] G. Schweicher, V. Lemaur, C. Niebel, C. Ruzié, Y. Diao, O. Goto, W.-Y. Lee, Y. Kim, J.-B. Arlin, J. Karpinska, A. R. Kennedy, S. R. Parkin, Y. Olivier, S. C. B. Mannsfeld, J. Cornil, Y. H. Geerts, Z. Bao, *Adv. Mater.* **2015**, *27*, 3066-3072.

[93] a) H. Ephardt, P. Fromherz, *J. Chem. Phys.* **1989**, *93*, 7717-7725; b) R. F. Khairutdinov, N. Serpone, *J. Chem. Phys. B* **1997**, *101*, 2602-2610.

[94] a) Z. B. Henson, K. Müllen, G. C. Bazan, *Nat. Chem.* **2012**, *4*, 699-704; b) M. Kirkus, L. Wang, S. Mothy, D. Beljonne, J. Cornil, R. A. J. Janssen, S. C. J. Meskers, *J. Phys. Chem. A* **2012**, *116*, 7927-7936.

[95] I. G. Scheblykin, O. P. Varnavsky, M. M. Bataiev, O. Sliusarenko, M. Van der Auweraer, A. G. Vitukhnovsky, *Chem. Phys. Lett.* **1998**, *298*, 341-350.

[96] a) E. Rousseau, M. Van der Auweraer, F. C. De Schryver, *Langmuir* **2000**, *16*, 8865-8870; b) E. W. Knapp, *Chem. Phys.* **1984**, *85*, 73-82.

[97] a) K. Ikegami, *J. Chem. Phys.* **2004**, *121*, 2337-2347; b) G. Busse, B. Frederichs, N. K. Petrov, S. Techert, *Phys. Chem. Chem. Phys.* **2004**, *6*, 3309-3314.

[98] I. G. Scheblykin, M. M. Bataiev, M. Van der Auweraer, A. G. Vitukhnovsky, *Chem. Phys. Lett.* **2000**, *316*, 37-44.

[99] D. Möbius, *Adv. Mater.* **1995**, *7*, 437-444.

[100] J. Gierschner, L. Lüer, B. Milián-Medina, D. Oelkrug, H.-J. Egelhaaf, *J. Phys. Chem. Lett.* **2013**, *4*, 2686-2697.

[101] T.-S. Ahn, R. O. Al-Kaysi, A. M. Müller, K. M. Wentz, C. J. Bardeen, *Rev. Sci. Instrum.* **2007**, *78*, 086105.

[102] T. Kobayashi, J. Du, Y. Kida, in *J-Aggregates, Vol. 2* (Ed.: T. Kobayashi), World Scientific, Singapore, **2012**, pp. 1-47.

[103] T. E. Kaiser, H. Wang, V. Stepanenko, F. Würthner, *Angew. Chem. Int. Ed.* **2007**, *46*, 5541-5544.

[104] I. G. Scheblykin, O. Y. Sliusarenko, L. S. Lepnev, A. G. Vitukhnovsky, M. Van der Auweraer, *J. Chem. Phys. B* **2001**, *105*, 4636-4646.

[105] S.-W. Park, J.-M. Choi, K. H. Lee, H. W. Yeom, S. Im, Y. K. Lee, *J. Chem. Phys. B* **2010**, *114*, 5661-5665.

[106] P. Stadelmann, JEMS Java Electron Microscopy Software V4, **2014**.

[107] P.-A. Plötz, T. Niehaus, O. Kühn, *J. Chem. Phys.* **2014**, *140*, 174101.

[108] a) J. C. Chang, *J. Chem. Phys.* **1977**, *67*, 3901-3909; b) K. A. Kistler, F. C. Spano, S. Matsika, *J. Chem. Phys. B* **2013**, *117*, 2032-2044; c) J. Megow, M. I. S. Röhr, M. Schmidt am Busch, T. Renger, R. Mitrić, S. Kirstein, J. P. Rabe, V. May, *Phys. Chem. Chem. Phys.* **2015**, *17*, 6741-6747.

[109] S. Ghosh, X.-Q. Li, V. Stepanenko, F. Würthner, *Chem. Eur. J.* **2008**, *14*, 11343-11357.

[110] A. Liess, M. Stolte, T. He, F. Würthner, *Mater. Horiz.* **2016**, *3*, 72-77.

[111] C. Reese, W.-J. Chung, M.-m. Ling, M. Roberts, Z. Bao, *Appl. Phys. Lett.* **2006**, *89*, 202108.

[112] G. Xue, C. Fan, J. Wu, S. Liu, Y. Liu, H. Chen, H. L. Xin, H. Li, *Mater. Horiz.* **2015**, *2*, 344-349.

[113] R. Zeis, T. Siegrist, C. Kloc, *Appl. Phys. Lett.* **2005**, *86*, 022103.

[114] W. Xie, K. Willa, Y. Wu, R. Häusermann, K. Takimiya, B. Batlogg, C. D. Frisbie, *Adv. Mater.* **2013**, *25*, 3478-3484.

[115] O. D. Jurchescu, M. Popinciuc, B. J. van Wees, T. T. M. Palstra, *Adv. Mater.* **2007**, *19*, 688-692.

[116] J. Takeya, M. Yamagishi, Y. Tominari, R. Hirahara, Y. Nakazawa, T. Nishikawa, T. Kawase, T. Shimoda, S. Ogawa, *Appl. Phys. Lett.* **2007**, *90*, 102120.

[117] A. Liess, A. Lv, A. Arjona-Esteban, D. Bialas, A.-M. Krause, V. Stepanenko, M. Stolte, F. Würthner, *Nano Lett.* **2017**, *17*, 1719-1726.

[118] A. Liess, L. Huang, A. Arjona-Esteban, A. Lv, M. Gsänger, V. Stepanenko, M. Stolte, F. Würthner, *Adv. Funct. Mater.* **2015**, *25*, 44-57.

[119] A. Arjona Esteban, *Merocyanine Dyes as Organic Semiconductors for Vacuum-processed Solar Cell and Transistor Devices (PhD Thesis)*, Julius-Maximilians-Universität Würzburg, **2015**.

[120] L. Huang, F. Zhu, C. Liu, H. Wang, Y. Geng, D. Yan, *Org. Electron.* **2010**, *11*, 195-201.

[121] M. J. Frisch, G. W. Trucks, H. B. Schlegel, G. E. Scuseria, M. A. Robb, J. R. Cheeseman, G. Scalmani, V. Barone, B. Mennucci, G. A. Petersson, H. Nakatsuji, M. Caricato, X. Li, H. P. Hratchian, A. F. Izmaylov, J. Bloino, G. Zheng, J. L. Sonnenberg, M. Hada, M. Ehara, K. Toyota, R. Fukuda, J. Hasegawa, M. Ishida, T. Nakajima, Y. Honda, O. Kitao, H. Nakai, T. Vreven, J. A. Montgomery Jr., J. E. Peralta, F. Ogliaro, M. J. Bearpark, J. Heyd, E. N. Brothers, K. N. Kudin, V. N. Staroverov, R. Kobayashi, J. Normand, K. Raghavachari, A. P. Rendell, J. C. Burant, S. S. Iyengar, J. Tomasi, M. Cossi, N. Rega, N. J. Millam, M. Klene, J. E. Knox, J. B. Cross, V. Bakken, C. Adamo, J. Jaramillo, R. Gomperts, R. E. Stratmann, O. Yazyev, A. J. Austin, R. Cammi, C. Pomelli, J. W. Ochterski, R. L. Martin, K. Morokuma, V. G. Zakrzewski, G. A. Voth, P. Salvador, J. J. Dannenberg, S. Dapprich, A. D. Daniels, Ö. Farkas, J. B. Foresman, J. V. Ortiz, J. Cioslowski, D. J. Fox, Gaussian 09, revision D.01, Wallingford, Connecticut, U. S. A., **2009**.

[122] a) A. D. Becke, *Phys. Rev. A* **1988**, *38*, 3098-3100; b) A. D. Becke, *J. Chem. Phys.* **1993**, *98*, 5648-5652; c) C. Lee, W. Yang, R. G. Parr, *Phys. Rev. B* **1988**, *37*, 785-789.

[123] J.-D. Chai, M. Head-Gordon, *J. Chem. Phys.* **2008**, *128*, 084106.

[124] F. Weigend, R. Ahlrichs, *Phys. Chem. Chem. Phys.* **2005**, *7*, 3297-3305.

[125] T. Lu, F. Chen, *J. Comput. Chem.* **2012**, *33*, 580-592.

[126] R. Dennington, T. Keith, J. Millam, GaussView, Version 5, Semichem Inc., Shawnee Mission, Kansas, U. S. A., **2009**.

[127] G. M. Sheldrick, *Acta Crystallogr. Sect. A: Found. Crystallogr.* **2008**, *A64*, 112-122.

Danksagung

Hiermit möchte ich mich bei allen denjenigen bedanken, die mich in den letzten Jahren unterstützt haben.

Zuallererst möchte ich mich besonders bei meinem Doktorvater Prof. Dr. Frank Würthner bedanken, der mir die Möglichkeit gegeben hat, diese spannenden Themen in seinem Arbeitskreis zu bearbeiten. Hierbei haben sein Vertrauen, das bereit gestellte hervorragende Arbeitsumfeld sowie die vielen fachlichen Diskussionen und Ratschläge in hohem Maß zum Gelingen dieser Arbeit beigetragen.

Ein weiterer besonderer Dank geht an Dr. Matthias Stolte, der auch in den unpassendsten Situationen immer ein offenes Ohr hatte. Danke auch für das Vertrauen und den sehr angenehmen humorvollen Umgang miteinander über die ganze Zeit. Und natürlich für die Elektrooptik-Messungen.

Weiterhin möchte ich mich bei Dr. Christian Burschka, Dr. Marcel Gsänger, Ana-Maria Krause sowie Dr. David Schmidt für die kristallographischen Messungen bedanken. Dr. David Schmidt danke ich außerdem für die vielen durchgeführten XRD Experimente.

Bei Dr. Vladimir Stepanenko möchte ich mich für die Aufnahme von AFM-Bildern sowie die Einführung in die Methode bedanken. Weiterhin danke ich ihm herzlich für das Durchführen der TEM- und SAED-Messungen sowie die Hilfe bei deren Auswertung.

Bei Dr. Tao He, Dr. Lizhen Huang und Dr. Aifeng Lv bedanke ich mich für die gute Zusammenarbeit und die vielen Hilfestellungen sowie die Einführung in die Transistorherstellung und Messung während meiner Doktorarbeit.

Prof. Dr. Matthias Lehmann danke ich für die Möglichkeit der Durchführung der Absorptionsmessungen von Nanokristallen.

Mein Dank gilt außerdem Dr. Alhama Arjona Esteban und David Bialas für die theoretischen Berechnungen sowie die Unterstützung bei diesen.

Ich bedanke mich weiterhin bei Astrid Kudzus für die vielen Hilfestellungen beim Herstellen und Messen verschiedenster Proben. Ihr und Reinhard Hecht möchte ich außerdem für den humorvollen Umgang in unserem alten Büro danken.

Bei Dr. Alhama Arjona Esteban, Dr. Hannah Bürckstümmer, Thorsten Günder, Fabian Holzmaier, Manuela Kaiser, Christian Simon sowie Dr. Elena Tulyakova bedanke ich mich für die durchgeführten Synthesen sowie die Charakterisierung der Moleküle in Lösung.

Dr. Hagen Klauk und Dr. Ute Zschieschang vom MPI Stuttgart danke ich außerdem für das Bereitstellen der TPA modifizierten Substrate.
Für die Unterstützung bei den jeweiligen Themen bedanke ich mich bei Julia Zillner, die im Rahmen Ihrer Bachelorarbeit und eines Praktikums einen Beitrag geleistet hat, sowie bei den von mir betreuten Praktikanten Thomas Niepel, Thomas Ferschke, Benjamin Arensmayer, Florian Hirsch, Arthur Turkin sowie Martin Mattenheimer.
Ein herzlicher Dank geht ebenfalls an alle, die beim Korrekturlesen dieser Arbeit geholfen haben: Dr. Alhama Arjona Esteban, Reinhard Hecht, Stefanie Herbst, Eva Kirchner, Valentin Kunz, Dr. Marcus Schulze und Dr. Matthias Stolte.
Christiana Toussaint und Eleonore Klaus danke ich für die Hilfe bei allen bürokratischen Dingen, Bernd Brunner für die Hilfe bei allen Computerproblemen. Weiterhin bedanke ich mich bei Markus Braun und Michael Ramold für die Unterstützung bei allen technischen Angelegenheiten im Labor bzw. an Laborgeräten.
Dem gesamten Arbeitskreis möchte ich außerdem für die angenehme und lustige Arbeitsatmosphäre während der Doktorarbeit danken. Für die vielen schönen Abende und diverse Unternehmungen möchte ich mich insbesondere bei Alhama, Anni, Ayan, Eva, Jana, Marcus, Reinhard, Sabine, Steffi, Valentin und Viki bedanken.
Zuletzt danke ich meiner Familie sowie Freunden für die gesamte Unterstützung während dieser Zeit und darüber hinaus. Ein besonderer Dank gilt auch meiner Frau Anna, die immer an mich glaubt und mich in allen Dingen unterstützt.

List of Publications

Exciton Coupling of Merocyanine Dyes in the Solid State from H- to J-type
A. Liess, A. Lv, A. Arjona-Esteban, D. Bialas, A.-M. Krause, V. Stepanenko, M. Stolte, F. Würthner
Nano Lett. **2017**, *17*, 1719-1726.

Single-Crystal Field-Effect Transistors of a Highly Dipolar Merocyanine Dye
A. Liess, M. Stolte, T. He, F. Würthner
Mater. Horiz. **2016**, *3*, 72-77.

Influence of Solid-State Packing of Dipolar Merocyanine Dyes on Transistor and Solar Cell Performances
A. Arjona-Esteban, J. Krumrain, A. Liess, M. Stolte, L. Huang, D. Schmidt, V. Stepanenko, M. Gsänger, D. Hertel, K. Meerholz, F. Würthner
J. Am. Chem. Soc. **2015**, *137*, 13524-13534.

Organic Thin Film Transistors Based on Highly Dipolar Donor-Acceptor Polymethine Dyes
A. Liess, L. Huang, A. Arjona-Esteban, A. Lv, M. Gsänger, V. Stepanenko, M. Stolte, F. Würthner
Adv. Funct. Mater. **2015**, *25*, 44-57.

Synthesis and Structural Analysis of Thiophene-Pyrrole-Based S,N-Heteroacenes
C. Wetzel, A. Mishra, E. Mena-Osteritz, A. Liess, M. Stolte, F. Würthner, P. Bäuerle
Org. Lett. **2014**, *16*, 362-365.

Domain Fragmentation during Cyclic Fatigue in 94%($Bi_{1/2}Na_{1/2}$)TiO_3-6%$BaTiO_3$
H. Simons, J. Glaum, J. E. Daniels, A. J. Studer, A. Liess, J. Rödel, M. Hoffman
J. Appl. Phys. **2012**, *112*, 044101.

List of Used Substances

(including internal number)

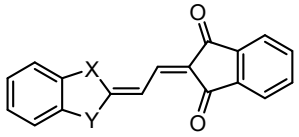

D1A1: X = Y = S (**AAE093**)
D3A1: X = CMe_2, Y = N*n*Bu (**HB248**)

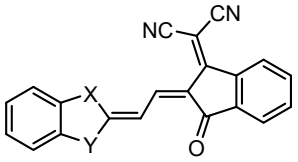

D1A2: X = Y = S (**AAE094**)
D3A2: X = CMe_2, Y = N*n*Bu (**MD376**)

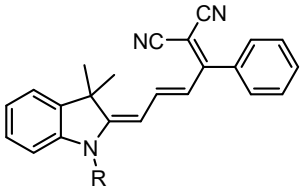

D3A3: R = *n*Bu (**HB312**)

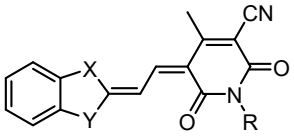

D1A4: X = Y = S, R = Me (**AAE095**)
D3A4: X = CMe_2, Y = NMe, R = *n*Bu (**IDOP1**)

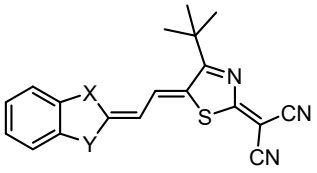

D1A5: X = Y = S (**AAE112**)
D2A5: X = S, Y = N*n*Bu (**EL32**)

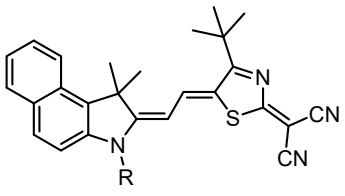

D4A5: R = *n*Bu (**EL53**)

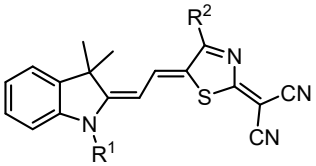

Me**D3**tBu**A5**: R^1 = Me R^2 = *t*Bu (**EL64**)
nPr**D3**tBu**A5**: R^1 = *n*Pr R^2 = *t*Bu (**HB174**)
iPr**D3**tBu**A5**: R^1 = *i*Pr R^2 = *t*Bu (**MD530**)
nBu**D3**tBu**A5**: R^1 = *n*Bu R^2 = *t*Bu (**HB170**)
nPe**D3**tBu**A5**: R^1 = *n*Pen R^2 = *t*Bu (**HB181**)
nHe**D3**tBu**A5**: R^1 = *n*Hex R^2 = *t*Bu (**HB183**)
Bn**D3**tBu**A5**: R^1 = Bn R^2 = *t*Bu (**MD304**)
nBu**D3**nBu**A5**: R^1 = *n*Bu R^2 = *n*Bu (**HB364**)

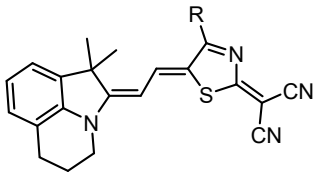

bPr**D3**tBu**A5**: R = *t*Bu (**HB255**)
bPr**D3**Ph**A5**: R = Ph (**HB256**)
(bPr: bridged propyl)

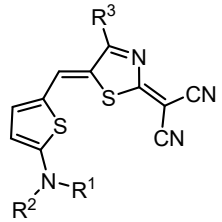

Et**D5**tBu**A5**: R^1 = R^2 = Et R^3 = *t*Bu (**CS258**)
EtBu**D5**tBu**A5**: R^1 = Et, R^2 = *n*Bu R^3 = *t*Bu (**CS254**)
nPr**D5**tBu**A5**: R^1 = R^2 = *n*Pr R^3 = *t*Bu (**CS264**)
nBu**D5**tBu**A5**: R^1 = R^2 = *n*Bu R^3 = *t*Bu (**HB238**)
nHe**D5**tBu**A5**: R^1 = R^2 = *n*Hex R^3 = *t*Bu (**CS194**)
nBu**D5**nBu**A5**: R^1 = R^2 = *n*Bu R^3 = *n*Bu (**HB432**)

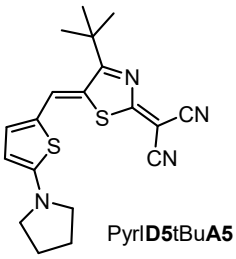

Pyrl**D5**tBu**A5** (**TG008**)

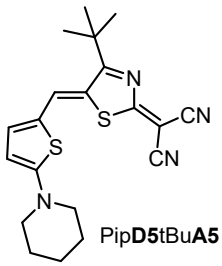

Pip**D5**tBu**A5** (**CS195**)

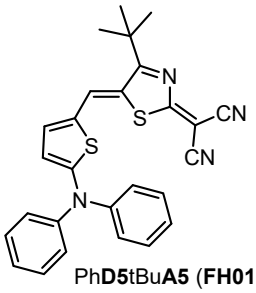

Ph**D5**tBu**A5** (**FH01**)

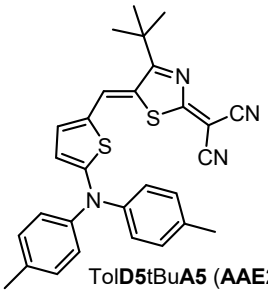

Tol**D5**tBu**A5** (**AAE291**)